Application of laser-plasma accelerated beams to high dose-rate radiation biology

Marco Cavallone

INSTITUT POLYTECHNIQUE DE PARIS

NNT : 2020IPPAX063

Thèse de doctorat

Application of laser-plasma accelerated beams to high dose-rate radiation biology

Thèse de doctorat de l'Institut Polytechnique de Paris
préparée à l'École Polytechnique

École doctorale n°626 de l'Institut Polytechnique de Paris (ED IP-Paris)
Spécialité de doctorat : Optique, lasers et plasma

Thèse présentée et soutenue à Palaiseau, le 16/11/2020, par

MARCO CAVALLONE

Composition du Jury :

Sandrine Dobosz Dufrénoy Chercheur, CEA-Saclay	Président
Leonida Antonio Gizzi Directeur de recherche, laboratoire ILIL, CNR Pise (Italie)	Rapporteur
Raphaël Moeckli Directeur de recherche et PD-MER, IRA (Suisse)	Rapporteur
Ludovic De Marzi Chercheur, Institut Curie	Examinateur
Alessandro Flacco Enseignant-chercheur, LOA, ENSTA	Directeur de thèse
Victor Malka Directeur de recherche, Schwartz/Reisman Center for Intense Laser Physics, Institut Weizmann (Israel)	Invité

Dedicated to my mother.

Remerciements

Je tiens d'abord à remercier Antoine Rousse, ancien directeur du LOA, pour m'avoir accueilli au sein de son laboratoire ainsi que pour m'avoir permis de m'initier à cette aventure. Dans le même état d'esprit, je veux adresser un remerciement spécial à tout le LOA, dont l'ambiance conviviale, sans compétition ni arrogance, m'a permis de me sentir comme chez moi.

Un remerciement tout particulier à Victor Malka, qui a toujours gardé un oeil sur moi, même quand il était loin. Merci pour l'affection et le confort que tu m'as transmis, mais aussi et surtout pour les encouragements et félicitations que tu m'as adressées à la fin de cette thèse. Ton avis positif et ton soutient ont été très importants pour moi.

Un remerciement spécial aussi à Émilie Bayart, pour l'empathie dont elle a fait preuve et pour l'inconditionnel support qu'elle m'a apporté pendant ces trois années.

Voglio rivolgere il ringraziamento più sentito al mio direttore di tesi, Alessandro Flacco, che oggi fatico ad identificare unicamente come tale. Hai svolto il ruolo di direttore di tesi in modo impeccabile, ma soprattutto sei stato per me un punto di riferimento, una persona in cui ho sempre potuto riporre la mia fiducia. Le tantissime cose che ho potuto imparare da te, non solo sotto l'aspetto tecnico ma anche in termini di approccio alla ricerca, sono infatti soltanto una piccola parte del tuo apporto in questa tesi. Hai saputo lasciarmi lo spazio necessario a fare ricerca in modo autonomo e a collaborare liberamente con altri laboratori e ricercatori. Allo stesso tempo, sei stato sempre presente e vigile, hai saputo indirizzarmi quando la strada da prendere era per me meno evidente, hai saputo aiutarmi a vedere il grande disegno dietro un lavoro di ricerca in cui ho spesso faticato a trovare il filo conduttore. Soprattutto, nei momenti in cui mi sono sentito più incerto, hai saputo ascoltare, capire e condividere i miei turbamenti, e hai impiegato tante delle tue energie per la buona riuscita di questo dottorato. Il tuo impegno in tal senso è stato per me uno stimolo in più, e se oggi posso dire di sentirmi fiero del mio lavoro un grande

merito va a te. Grazie di cuore.

J'adresse ensuite un remerciement à toutes les personnes avec lesquelles j'ai pu avoir la chance de collaborer et qui m'ont permis de mener d'enrechissants travaux expérimentaux durant ces trois ans.
D'abord, une pensée pour ceux qui ont travaillé avec moi au LOA. Merci à Olivier Delmas, qui au tout début de ce doctorat m'a consacré beaucoup de son temps et avec qui j'ai pu mener les ultimes expériences en salle SAPHIR. De même, merci à Daniel Adjei, qui m'a permis de participer à son expérience, toujours en salle SAPHIR, et de collaborer avec lui sur l'analyse des données. Pour moi, ces deux semaines de manips avec toi et Olivier resteront un très beau souvenir.
Merci à Olena Kononenko et Sébastien Corde pour la semaine qu'ils m'ont accordée en salle Jaune et pour leur précieuse aide pendant cette première manip'.
Merci à Julius Huijts, Lucas Rovige, Aline Vernier et Jérôme Faure. J'ai de tout coeur apprécié votre engagement pendant la manip radiobio, qui n'aurait pas été possible sans votre apport fondamental. Ces deux semaines avec vous ont été pour moi très agréables et riches d'enseignements. Merci aussi à Thomas Lavergne, pour son impeccable travail sur le support des cellules, mais aussi à toutes les personnes de l'atelier de la mécanique qui m'ont offert leur support pendant ces trois ans.

Je tiens aussi à remercier le personnel du secrétariat: Sandrine Tricaud, Catherine Buljore, Patricia Toullier, Carole Gratpanche. Votre disponibilité et votre remarquable travail d'administration est selon moi un important atout pour le laboratoire. J'ai toujours pu trouver une aide et un support à chaque occasion qui m'a été donnée d'entrer dans votre secrétariat.

Un remerciement à ceux qui m'ont donné la possibilité de mener des expériences dans d'autres laboratoires: l'équipe du CNR-INO de Pise, Alberto Fazzi et Dario Giove, et l'équipe de l'Oriatron à Lausanne. Merci à Vincent Favaudon pour le temps qu'il m'a accordé au Kinétron au tout début de ce doctorat.
Un remerciement spécial à Rachel Delorme, pour les courbes que nous avons peut-être réussi à aligner et les centaines de films analysés. Merci pour tes enseignements sur la physique médicale mais aussi pour tous les agréables moments passés ensemble pendant les campagnes expérimentales.

Un remerciement à tout le groupe de Doc'union pour les bons moment passés ensem-

ble pendant cette aventure.
Merci à Safir, pour les pizzas à Camille Claudel et les séries Netflix. Nous devons toujours aller voir ce qu'il y a à Saint-Rémy-Lès-Chevreuse.
Grazie ad Ambra, il mio riferimento femminile a Parigi, per aver osservato - senza giudicare - le diverse versioni di me e aver ascoltato i miei complessi lambiccamenti mentali. E soprattutto per le quanto mai indispensabili e gustosissime cene italiane.
Merci à Pierre, pour toutes les réflexions philosophiques que nous avons eues sur un banc, et surtout pour toutes les réponses que nous n'avons jamais trouvées. J'ai appris grâce à toi à toujours regarder les choses du point de vue le moins attendu.
Grazie a Francesco, per avermi accolto al LOA, per tutti i consigli preziosi e la tua vicinanza nei momenti in cui ne avevo bisogno.
Merci à Kosta, mon office-mate, pour m'avoir permis de comprendre ces français qui n'articulent jamais... et aussi pour la compagnie et les rires lors de ces trois années. J'ai bien aimé partager le bureau avec toi.
Merci à Céphise, pour tous les films super bizarres qu'on a vus au cinéma.

Merci à la ville de Paris, envers laquelle je sens un lien profond.
Merci à tous les français que j'ai pu croiser pendant ces trois ans, qui ont su m'accueillir avec respect et amour. En particulier, je veux adresser un sincère remerciement à Christian et Anne, les propriétaires de mon magnifique studio du Boulevard Arago, et qui en vérité ont représenté à mon coeur bien plus que cela. Surtout, un très grand merci pour avoir pris soin de moi pendant le confinement et pour m'avoir gâté avec des si délicieux plats et desserts.

A Stefano, che occupa il primo posto per spazio dati nel mio WhatsApp. Nonostante la distanza, la nostra amicizia rimane per me un'ancora fondamentale nella mia vita. Lo è stata in particolare in questi ultimi tre anni, fatti di grandi cambiamenti, nuove domande, profonde riflessioni filosofico-esistenziali, tormenti e gioie infinite. Vorrei tanto che venissi qui, ma poi ti immagino parlare francese e ci ripenso.

A Chiara, per quel biglietto aereo che per fortuna decidesti di comprare, per quegli occhi lucidi e quelle parole in un prato. Per aver stravolto (piano piano e poi... profondamente) il mio equilibrio instabile offrendomi in cambio quel conforto profondo che, senza volerlo ammettere, io andavo cercando.

A mia madre, senza la quale tutto ciò non sarebbe stato possibile.

Contents

Acronyms

- CAP: Conventional Accelerated Protons
- CPA: Chirped Pulsed Amplification
- DPP: Dose-Per-Pulse
- DSB: Double Strand Break
- FLASH-RT: FLASH Radiation Therapy
- FWHM: Full Width at Half Maximum
- GA: Genetic Algorithm
- HDR: High Dose-Rate
- HWHM: Half Width at Half Maximum
- IC: Ionisation Chamber
- IMRT: Intensity Modulated Radiation Therapy
- LET: Linear Energy Transfer
- LPA: Laser-Plasma Accelerated (particles, beams)
- LPAE: Laser-Plasma Accelerated Electrons
- LPAP: Laser-Plasma Accelerated Protons
- MC: Monte Carlo
- OD: Optical Density
- PMQ: Permanent Magnet Quadrupole

- RBE: Relative Biological Effectiveness
- RCF: RadioChromic Film
- RNC: Razor Nano Chamber
- ROI: Region Of Interest
- SOBP: Spread-Out Bragg Peak
- SS: Scattering System
- SSB: Single Strand Break
- SSD: Source-to-Surface Distance
- TIC: Transmission Ionisation Chamber
- TNSA: Target Normal Sheath Acceleration
- TOF: Time Of Flight
- TP: Thomson Parabola
- TVA: Two Voltage Analysis
- UHDR: Ultra High Dose-Rate
- VHEE: Very High-Energy Electrons

Résumé

Cette thèse décrit l'utilisation de protons et électrons produits par interaction laser-plasma dans le cadre d'expériences biologiques. En focalisant une impulsion laser ultra intense ($>10^{18}\,\mathrm{W/cm^2}$) sur une cible solide ou gazeuse, il est possible de produire des faisceaux de protons et électrons ayant une durée de l'impulsion inférieure à la nanoseconde. Cela permet d'atteindre un débit de dose dans l'impulsion pouvant dépasser $10^9\,\mathrm{Gy/s}$, supérieur de plusieurs ordres de grandeur au débit de dose typiquement utilisé en radiothérapie conventionnelle ($\sim$Gy/min).
L'effet du débit de dose élevé sur la réponse biologique a fait l'objet de nombreux travaux de recherche dans les dernières années. Notamment, plusieurs études *in-vivo* ont montré que l'administration d'une dose en un temps très court ($<$ 500 ms) et avec un débit de dose élevé ($>$ 40 Gy/s) peut augmenter la sélectivité du traitement, en réduisant le risque d'effets secondaires sur les tissus sains tout en gardant le même effet sur la tumeur. Bien que les causes de ce phénomène soient encore à l'étude, le protocole FLASH a été testé avec succès sur le premier patient en 2019. Or, l'utilisation de ces protocoles demande une compréhension plus approfondie des processus physico-chimiques et biologiques déclenchés par un dépôt de dose rapide. Dans ce contexte, les faisceaux de particules accélérées par laser représentent un outil unique pour mettre en lumière les processus régissant la réponse biologique suite à une irradiation à haut débit de dose.

Le manuscrit présente des études expérimentales et théoriques réalisées avec des faisceaux de particules produits avec différents lasers de très haute puissance. Il montre les aspects critiques liés à l'application de ces faisceaux à des études de radiobiologie et définit des stratégies potentielles ainsi que des protocoles d'irradiation. Il aborde notamment les problèmes liés à la caractérisation et la mise en forme de ces faisceaux ainsi qu'à leur dosimétrie.
La réalisation d'expériences de radiobiologie nécessite un contrôle précis des conditions d'irradiation, telles que le spectre et la distribution de la dose. Pour y parvenir sont nécessaires une caractérisation précise des propriétés de telles sources ainsi qu'une mise

en forme spectrale et spatiale de ces dernières à l'aide d'un système de transport. Cet aspect est particulièrement critique pour les protons qui présentent une large divergence à la source dépendant de l'énergie et un spectre polychromatique exponentiel. Afin d'obtenir le spectre et la divergence des protons, une technique de déconvolution à partir des mesures de spectroscopie par films radiochromiques a été développée et validée, ce qui a permis une caractérisation rigoureuse de ces faisceaux et, à son tour, des études détaillées de la ligne de transport. La simulation du transport et de l'interaction radiation-matière avec un seul outil Monte Carlo tel que Geant4 a permis l'étude directe de différentes lignes de transport en fonction des conditions d'irradiation, ainsi que l'étude d'une nouvelle approche par algorithme génétique qui permet d'optimiser le design d'un diffuseur à insérer dans le système de transport en fonction des contraintes sur la cible biologique.

L'évaluation de la dose délivrée dans l'échantillon biologique est un autre aspect particulièrement critique en raison du débit de dose très élevé qui produit des effets de saturation dans les instruments de dosimétrie couramment utilisés dans les protocoles de radiothérapie. Le manuscrit discute en particulier les aspects liés à l'utilisation de chambres d'ionisation, qui représentent l'instrument de dosimétrie de référence en radiothérapie classique. Lors de l'utilisation d'une chambre d'ionisation avec des faisceaux ayant un débit de dose très élevés, un phénomène de recombinaison entre les charges produites dans le volume sensible entraine une diminution de la charge collectée aux électrodes qui dépend du profil temporel du faisceau ainsi que de la géométrie de la chambre. Le manuscrit décrit les bases théoriques de ce processus et présente la caractérisation d'une nano-chambre Razor (IBA) avec des impulsions d'électrons de durées microsecondes délivrées par un prototype de LINAC (Oriatron eRT6). Les résultats montrent que le volume extrêmement petit de cette chambre réduit la recombinaison, bien qu'il semble entraîner une plus grande sensibilité à la durée de l'impulsion.

Le manuscrit décrit enfin les études théoriques et expérimentales de radiobiologie menées avec des protons et des électrons, et en présente les résultats. Les applications décrites couvrent un large éventail d'installations laser, des lasers à haute énergie (100 J/impulsion) et faible taux de répétition (mHz) aux lasers kHz délivrant quelques mJ sur cible, en passant par les lasers J–10 Hz. Ces études ont permis d'explorer différentes modalités temporelles d'administration de la dose avec différents types d'accélérateurs laser-plasma et de fournir ainsi une description détaillée du potentiel et des limitations de ces sources.

Introduction

Scientific background Cancer is the second leading cause of death globally, accounting for an estimated 9.6 million deaths, or one in six deaths, in 2018. Besides surgery and chemotherapy, radiotherapy is one of the major treatment modality. It consists in the use of ionising radiation to kill cancerous cells by depositing energy into the tumour and destroying the genetic material that controls how cells grow and divide. While both cancerous and healthy cells are damaged by radiation, the goal of radiotherapy is to increase the treatment selectivity by sparing as much as possible the healthy tissues. Optimisation of the selectivity reposes on several aspects, including dose conformity, resolution of imaging techniques, use of different radiations and temporal structures of dose delivery. In particular, the impact of dose-rate and total irradiation time on the treatment selectivity has not been extensively explored yet.

Clinical accelerators typically deliver the dose with a dose-rate around a few Gy/min, leading to exposure times in the order of few minutes to deliver a therapeutic dose. While the effect of a reduction of the dose-rate in the order of cGy/min is well known, the effect of high dose-rate, short exposure time irradiation on living cells still needs to be elucidated. Evidences of an effect of the high dose-rate on the biological response have been recently observed in many studies. In particular, *in-vivo* studies performed with electrons and photons produced by accelerator prototypes have shown that delivering the prescribed dose in a short time (< 500 ms) and at a high dose-rate (> 40 Gy/s) increases the treatment selectivity by reducing the occurrence of secondary effects on healthy tissues compared to conventional treatments with the same total dose [64]. Although theoretical explanations underpinning such phenomenon are still under discussion, the so-called FLASH protocol has been successfully tested with the first human patient in 2019 [33], paving the way for further research in this domain. These results highlight the importance of the dose delivery modality and the potential benefit that high dose-rate protocols may bring to clinics, asking for a deeper understanding of the physico-chemical and biological processes following fast dose deposition. In this scenario, Laser-Plasma Accelerated (LPA) beams represent a unique tool to shed some light on the radiobiological response following high-

dose rate irradiation. LPA particles are produced by focusing an ultra-short (∼fs) and ultra-intense (>10^{19} W/cm^2) laser pulse on a solid or gaseous thin target (∼µm), producing proton and electron bunches with a duration of respectively a few picoseconds and a few femtoseconds. These characteristics allow the reach of extremely high peak dose-rates in the pulse larger than 10^9 Gy/s, i.e. irradiation conditions that are extremely different compared to both conventional and FLASH treatment protocols. For this reason, LPA beams have been receiving great attention in the last decade, but their radiobiological effect on living cells is still debated and further systematic studies are required.

Thesis overview The thesis investigates the possible applications of both Laser-Plasma Accelerated Protons (LPAP) and Electrons (LPAE) produced by different types of high-power laser systems to radiation biology. It addresses some of the main challenges and define potential strategies and irradiation protocols enabling systematic and robust radiobiology studies. In particular, three main issues, summarised in the schematic draft of Fig. 1, are discussed and tackled in this thesis.

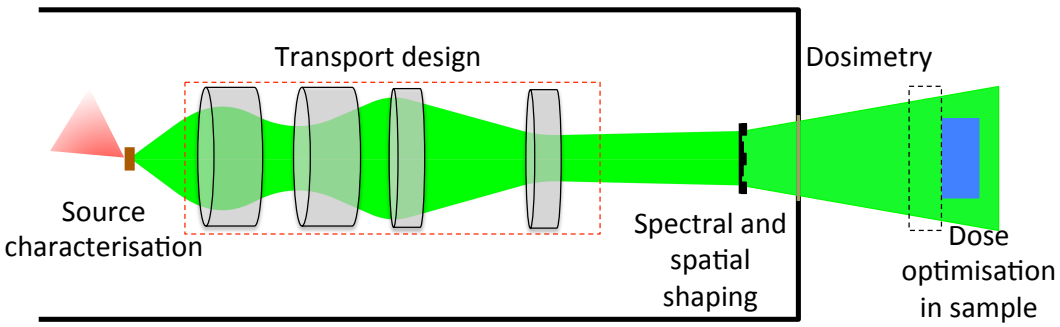

Figure 1: Crucial aspects tackled in the thesis to perform radiation biology experiments.

Firstly, the definition of techniques enabling accurate characterisation of LPA beams (I) in terms of source spectrum and divergence is necessary to design proper beamlines and perform spatial and spectral shaping of such beams. This aspect is for instance crucial for LPAP, which feature an exponential spectrum at the source and a large divergence (several degrees) that is a function of the proton energy. To address this issue, a technique to characterise the source spectrum and divergence through film stack spectroscopy has been developed and validated, which allowed accurate design of LPAP beamlines for radiation biology applications.
Secondly, besides a precise characterisation of the source, spectral and spatial shaping (II) [163] of the beam needs to be performed in order to make such beams suitable for such applications. One of the main concerns that drives the design of the beamline is

the delivery of an homogeneous dose at the biological target to approach the constraints of radiation biology. Since LPAE feature a small divergence at the source and a higher penetration depth compared with LPAP, they can be used for direct irradiation of biological samples without particular spectral shaping. On the contrary, LPAP need a transport beamline to collect as much charge as possible, transport it to the irradiation site in air and shape the beam in order to optimise the delivered dose distribution in the biological target. This aspect is particularly relevant for irradiation of 3D biological targets, since both the transverse and the depth-dose uniformity need to be optimised. In this case, the large spectrum at the source represents an asset, but it needs to be properly tailored in order to reach the required in-depth and transverse homogeneity. The strategy employed in this thesis to optimise the beam shaping consists in the use of Permanent Magnet Quadrupole (PMQ) transport systems coupled with Scattering Systems (SS). The transport system can be configured to transport the desired spectral bandwidth to the irradiation site, whereas an SS of proper thickness can be used to spread the beam and optimise the dose distribution in the sample. In particular, the thesis presents a novel strategy consisting in the use of a non-flat SS positioned in the transport beamline to take advantage of the chromaticity of the PMQs and to further optimise the dose uniformity. A genetic algorithm approach coupled with Monte Carlo simulations has been developed to optimise the SS design according to given requirements on the biological sample such as total dose and dose homogeneity. The method allows improvement of the dose homogeneity on both 2D (*in-vitro*) and 3D (*in-vivo*) biological target.

Finally, precise evaluation of the dose (III) delivered to the biological target is a crucial aspect. Dosimetry of LPA beams and, in general, of high dose-rate beams is a challenging task, since most of the instruments employed in dosimetry protocols for conventional radiotherapy treatments are not suitable for such conditions. The reference dosimetry instrument in clinics is the Ionisation Chamber (IC), which suffers from saturation at high dose-rate caused by recombination between the charges generated in the sensitive volume. In particular, IC recombination with pulsed beam is a complex phenomenon that depends on the interplay between the dose-per-pulse (DPP), the dose-rate and the pulse duration. Therefore, the response of IC to short pulsed beams delivering high DPP needs to be carefully characterised prior to their transfer to high dose-rate irradiation protocols. In this thesis, recombination in a small Razor nano-chamber[1]has been investigated. The extremely small active volume of this chamber compared to larger

[1]https://www.iba-dosimetry.com/product/razor-nano-chamber/

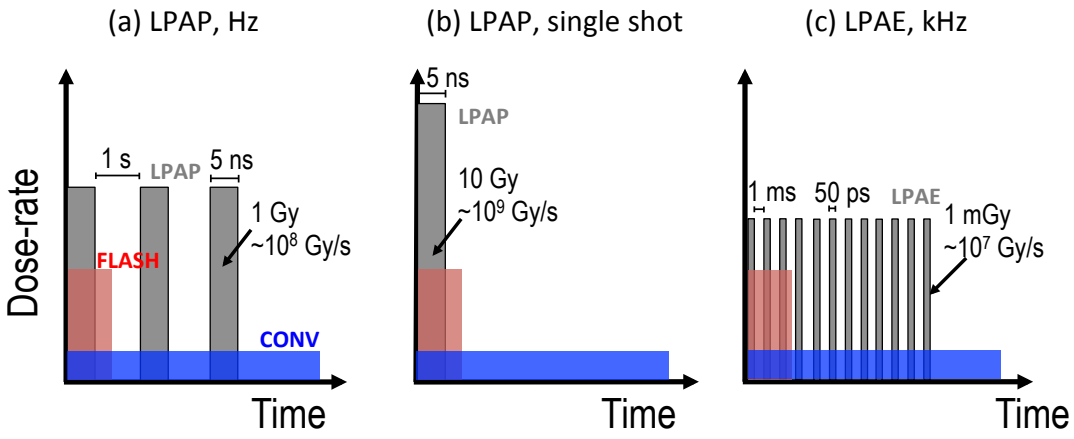

Figure 2: Different temporal structures of the LPA beams investigated in this thesis compared to FLASH and conventional treatments. The figures are not to scale.

chambers typically used in clinics may reduce the impact of recombination because of the shorter time spent by the charges to reach the electrodes. The chamber response has been characterised with µs electron pulses delivered by the LINAC prototype eRT6 Oriatron [105] available at the CHUV of Lausanne and with fs LAEs produced with the Salle Jaune TW laser system available at the LOA.

All together, these studies enabled the design of beamlines and radiation biology experiments with different types of LPA beams. Depending on the combination of laser and target parameters, laser-plasma accelerators can indeed generate beams with different qualities and temporal profiles. In particular, the thesis presents experimental and theoretical studies carried out with three different types of LPA beams allowing different temporal modalities of dose delivery that are relevant for radiation biology applications (Fig. 2):

a) Laser-plasma accelerated protons with cut-off energies of few MeV delivering a dose-per-pulse of ∼1 Gy at repetition rate of 1 Hz (generated by J-class), which have been widely employed for *in-vitro* radiation biology experiments. With such source, the dose is applied in several pulses with a considerable DPP and a peak dose-rate in the pulse in the order of 10^8 Gy/s, whereas the mean dose-rate is comparable to those employed in clinics. Promising results obtained at the Laboratoire d'Optique Appliquée (LOA) during the SAPHIR project [17] showed that the delay at which the proton bunches are applied has a strong impact on cell survival, demonstrating that the temporal structure of LPA bunches might play a key role on the radiobiological response. However, more studies are needed to clarify the role of the different parameters such as DPP and peak

dose-rate on the onset of this phenomenon.
In the framework of a collaboration with the CNR-INO of Pisa and the INFN of Milan, an experimental campaign has been devoted to the characterisation of the proton source of the ILIL-PW facility, which will be dedicated in the next years to radiation biology experiments with LPAP in conditions similar to those obtained at the LOA. The experiment allowed preliminary designs of transport beamlines to define the irradiation conditions that can be achieved.

b) Laser-plasma accelerated protons delivering a DPP $>$ 10 Gy and running at a repetition rate of $\sim 10^{-3}$ Hz (generated by high-energy lasers delivering tens of joules at the target). With this type of source a therapeutic dose can be delivered in a single shot, thus reaching irradiation conditions even harder than those employed in FLASH-RT (Fig. 2.b).
The pico2000 laser system of the LULI laboratory at the École Polytechnique can produce high charge (tens of nC/bunch) LPAP bunches with a cut-off energy above 10 MeV, which allows to investigate the FLASH effect in *in-vivo* biological targets of $\sim$1 mm thickness (e.g. zebrafish embryos). An experimental campaign is scheduled in December 2020 to demonstrate the production of FLASH-like irradiation conditions using a single pulse laser-driven proton beam. The thesis presents the design and optimisation of the beamline to deliver a 3D homogeneous dose in single-shot irradiation. The results showed that a homogeneous dose higher than 10 Gy can be delivered in a single shot over a surface of 5 x 5 mm^2.

c) Laser-plasma accelerated electrons delivering a low DPP of about 1 mGy at a high repetition rate of 1 kHz (generated by low energy lasers delivering few millijoules at the target). This type of laser plasma accelerator has been developed in the last years and no radiation biology studies have been reported so far in such conditions. The asset of this source lies in the high repetition rate that can bring remarkable benefits in terms of beam stability between irradiations compared to typical Hz LPAE beams. In fact, since the desired dose is applied by integrating a higher number of shots, the effect of shot-to-shot instabilities that typically affect LPAE beams is reduced.
A radiation biology experiment has been carried out with the kHz, low energy (1-3 MeV) electron source produced by the laser system of the Salle Noire (LOA) [88] to perform a first validation of the dosimetry arrangement and to investigate the effect of different dose fractionation modalities with kHz LPAE on the radiobiological response of *in-vitro* cancer cells.

The manuscript is organised as follows:

- Chapter 1 presents the main aspects related to the use of ionising radiations for cancer treatment and the mechanisms underpinning the biological response. At the end of the chapter, the role of the temporal modality of dose delivery and recent results on the biological effects of high dose-rate irradiation are discussed.

- Chapter 2 introduces the physics of laser-plasma acceleration and discusses the properties of these sources relevant to their application to radiation biology. Finally, the chapter provides a review of the results obtained in radiobiology experiments reported in literature and discusses the results obtained at the SAPHIR facility of the LOA on *in-vitro* response to LPAP.

- Chapter 3 describes the approaches used to takle some of the issues related to the application of LPAP to radiation biology. Notably, it describes the tools and techniques used to characterise, transport and shape these beams.

- Chapter 4 includes theoretical and experimental studies carried out with LPAP generated by two types of lasers. The first section presents the experiment carried out at the ILIL-PW facility with a J-class laser and preliminary design of the transport beamline for *in-vitro* irradiation. The second section presents the design of a beamline for the pico2000 multi-J laser facility in view of *in-vivo* radiation biology experiments in FLASH conditions.

- Chapter 5 focuses on high dose-rate dosimetry with ionisation chambers. In particular, the chapter presents the experiment carried out at the ert6 Oriatron LINAC of the *Centre Hospitalier Universitaire Vaudois* (CHUV, Lausanne) to characterise the response of an IBA Razor Nano Chamber with ∼µs electron bunches delivering a dose-per-pulse up to 10 Gy and discusses the transfer of ICs to LPA beam dosimetry.

- Chapter 6 presents the radiation biology experiment carried out with the kHz, low energy LPAE beam at the *Salle Noire* of the LOA. After description of of the source and of the dosimetry protocol, preliminary results on the response of *in-vitro* cancer cells are discussed.

Chapter 1

Medical application of ionising radiations - scientific background

Contents

1.1 Scientific rationale of radiotherapy

Radiotherapy consists in the use of ionising radiation to kill cancerous cells by depositing energy into the tumour. Optimisation of the dose[1] delivered to the tumor and healthy tissues is one of the crucial aspects of a radiotherapy treatment, since, to a first approximation, the radiobiological response is proportional to the absorbed dose. Indeed, as the delivered dose increases, both the probability of tumour control and the risk of side effects increase, the shape of the curves being usually a sigmoid, as shown in Fig. 1.1. The application of high doses to the tumour relies on the ability to protect surrounding healthy tissues from radiation harmful effects. In this sense, a radiotherapy treatment must always consider the balance between benefits on tumour control and the risk of side effects on healthy tissues. The relative displacement of the two dose-response curves determines the tolerance on the maximum dose that can be delivered to the tumour with an acceptable level of side-effect risks. It is quantified by the therapeutic index (see Fig 1.1), defined as the ratio between the probability of tumour control and the probability of side effects for a fixed value of tolerance dose. Its value reposes on numerous aspects, including anatomy of the tumour and relative position of surrounding healthy tissues, physiological characteristics such as tumour oxygenation and radiosensitivity, radiation quality, dosimetry accuracy and dose delivery modality. Improvement of the therapeutic effect of cancer treatments over the last decades have resulted in a strong research activity on all the aformentioned aspects [44]. However, many tumours remain radioresistant to tolerance doses and novel approaches are needed to further improve the curative power of radiotherapy. In particular, temporal aspects of dose delivery, such as dose rate modulation, irradiation time and fractionation have not been extensively explored outside typical time scales of clinical radiotherapy. Indeed, recent promising results on FLASH-RT [64] suggest that high dose-rate, pulsed, irradiation may bring important benefits to future clinical radiotherapy protocols.

This chapter provides a review of the mechanisms of interaction between radiation and matter. It then describes the spatial dynamics of various radiations at a macroscopic scale and the techniques used in clinics to spatially optimise the delivered dose. Thus, it discusses some key concepts of radiation biology, showing how the different ionisation pattern of radiations at a molecular scale may affect the cell response and, therefore, the treatment efficiency. To conclude, temporal aspects of dose delivery are discussed. In par-

[1] Dose is the physical quantity employed to quantify the energy that is deposited in matter by directly or indirectly ionising radiation (see section 1.3). It is defined as the energy delivered in a given volume divided by its mass and is expressed in Gy (1 Gy = 1 J/Kg).

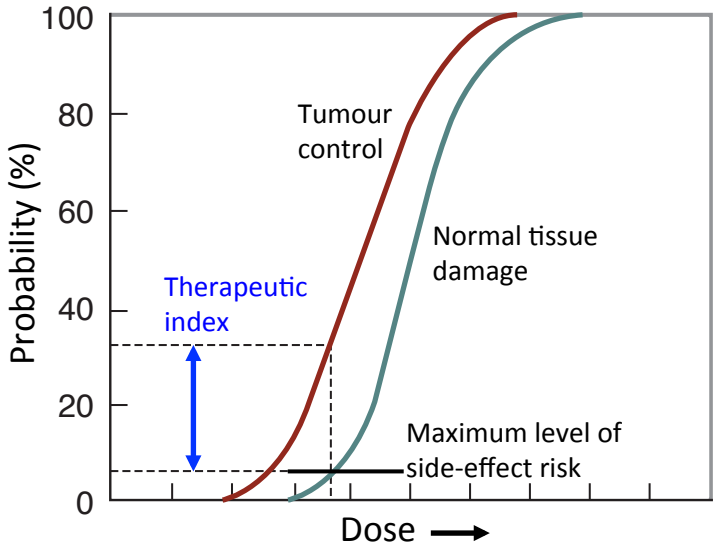

Figure 1.1: Typical dose-response curves and therapeutic index concept. Modified from E. J. Hall (2012) [92].

ticular, section 1.5.2 presents the recent findings on high dose-rate irradiation protocols (FLASH-RT) and discusses the role that laser-plasma sources may play in the research on fast dose deposition radiation biology.

1.2 Mechanisms of interaction between radiation and matter

Many phenomena may occur when matter is exposed to radiation. In general, radiation interaction with matter leads to an energy transfer to the atomic structure of the traversed material. For low-energy, non-ionising radiations the energy transfer may simply promote an electron to a higher energy level (excitation). The exact energy treshold below which radiation is non-ionising is not well defined since different atoms and molecules have a different ionisation potential[2]. Usually, radiations with energy lower than 33 eV (ionisation potential of air) are considered non-ionising. Instead, ionising radiations (energy greater than a few tens of electronvolts) may transfer a sufficient amount of energy when interacting with an atom and expel orbital electrons. Ionising radiations are divided into two categories, depending on the nature of the interaction:

- Directly ionising radiations: this category includes all charged particles such as

[2]The ionisation potential is defined as the minimum energy required to remove an electron from an atom.

electrons, protons and heavy ions. They continuously interact with matter through Coulomb interaction with orbital electrons and nuclei, although the frequency of the latter event is normally negligible. Depending on the distance of the interaction, the Coulomb force between the orbital electron and the charged particle may cause excitation or ejection of the electron. The energy loss per event is a small fraction of the total energy of the incident particles, resulting in a continuous slowing down.

- Indirectly ionising radiations: this category includes neutral particles such as neutrons and photons, which are not subject to Coulomb force. Instead, these radiations undergo a rather more "catastrophic" interaction in a single event, which drastically alters the properties of the primary radiation, such as its energy and nature. In the case of photons, the interaction process leads to the emission of secondary electrons that continuously transfer their energy to the medium through directly ionising events.

1.2.1 Charged particle interaction with matter

Heavy charged particle interaction The transfer of energy during the Coulomb interaction results in the excitation or ejection of the traversed material's orbital electrons, as well as in a decrease of the primary particle kinetic energy along its path. Since the primary particle interacts with many electrons at any given time, its energy loss is treated as continuous. It is expressed by the linear stopping power $S = -dE/dx$, which represents the differential energy loss per unit path length for a given particle in a specific medium, and is given by the following Bethe-Bloch formula [113, 162]:

$$-dE/dx = S = \frac{4\pi z^2}{m_0 v^2} \cdot \left(\frac{e^2}{4\pi\varepsilon_0}\right) NB \tag{1.1}$$

where

$$B = Z\left[\ln\frac{2m_0v^2}{I} - \ln\left(1-\frac{v^2}{c^2}\right) - \frac{v^2}{c^2}\right] \tag{1.2}$$

In these expressions, z and v are the atomic number and the velocity of the incident particle respectively, e is the electron charge, m_0 is the electron mass at rest, N and Z are the atomic density (atoms/m^3) and the atomic number of the traversed medium, respectively, c is the speed of light in vacuum and ε_0 the vacuum permittivity. The parameter I represents the average energy needed to ionise an atom of the material and is usually determined through experiments. The Bethe-Bloch formula is valid for

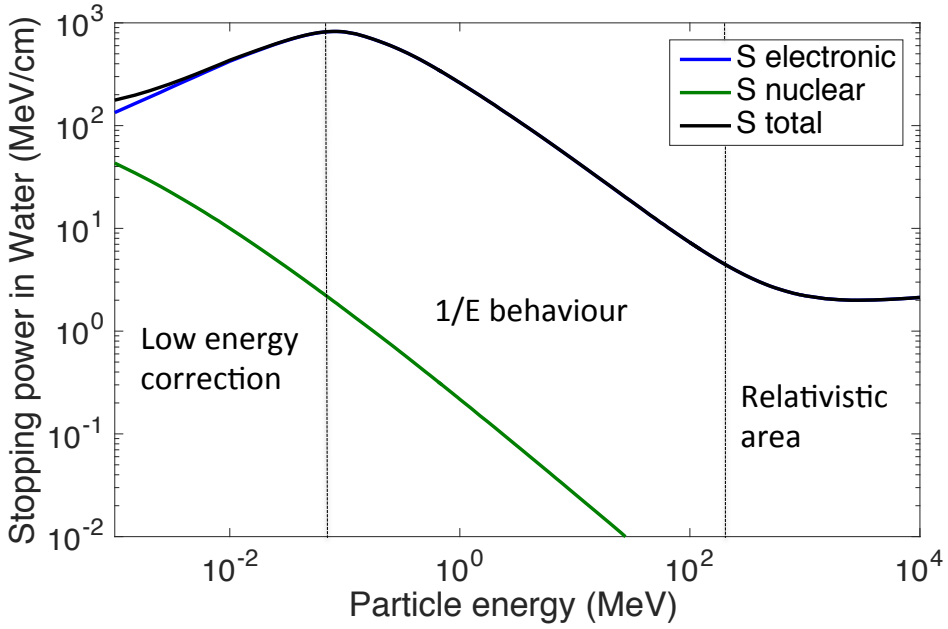

Figure 1.2: Stopping power of a proton in water as a function of its energy. The graph is obtained using the NIST tables (https://www.nist.gov/pml/stopping-power-range-tables-electrons-protons-and-helium-ions)

all charged particles and for all energies. In particular, the terms containing v^2/c^2 are relativistic corrections and are negligible for a particle energy lower than its mass at rest. For very low energies, comparable with the electron orbital velocity, an additional "Shell correction" factor should be applied [214]. The energy loss per unit length for a given particle energy ($\propto v^2$) is proportional to z^2, therefore particles with higher charge undergo a greater energy loss. Also, if both the numerator and the denominator are multiplied by the mass of the incident particle, we notice that particles with the same energy and charge but higher mass undergo a higher energy loss. Therefore, protons release more energy per unit length than electrons.

The stopping power for protons in water is shown in Fig. 1.2. The expression for B varies slowly with the particle energy and, to a first approximation, the behaviour of the stopping power can be inferred from the multiplicative factor $4\pi e^4 z^2 N/m_0 v^2$. In the non-relativistic zone, dE/dx varies as $1/v^2 \propto 1/E$. The $1/E$ behaviour can be easily explained by noting that the lower the velocity the greater the amount of time that the particle spends in the proximity of a given electron, thus the impulse and energy transfers are largest. This implies that the energy loss increases as the proton moves forward in the medium and reaches a maximum, the so-called Bragg-peak, immediately before it comes to rest. The position of the Bragg-peak in depth is a function of the initial proton energy: the higher

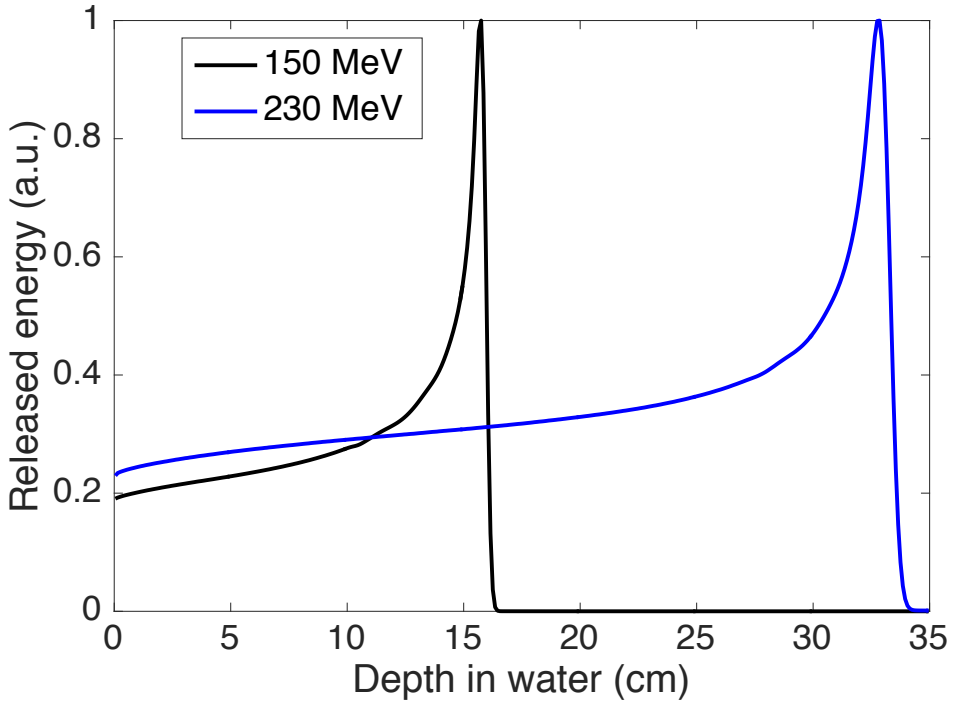

Figure 1.3: In-depth profile of the energy released in water by 150 MeV and 230 MeV proton beams obtained through Monte Carlo (Geant4) simulations.

the initial energy the deeper the particle penetrates in the medium, as shown in Fig. 1.3. The larger Bragg-peak of the 230 MeV protons in comparison with 150 MeV protons is due to two phenomena. First, the interaction between charged particles and orbital electrons is a stochastic process, i.e. the energy loss varies randomly in each interaction. As a consequence, an initial monoenergetic beam undergoes an energy spread while traversing a medium (energy straggling). Secondly, during the interaction process, charged particles experience stochastic deviations (scattering) from the initial direction. Although this effect is somewhat negligible for protons, whose mass is higher than the orbital electron mass, it results in a slightly different penetration depth (measured along the initial proton direction) of protons having the same initial energy (range straggling). The combination of this two effects causes the expansion of the Bragg-peak, which is more pronounced for higher energy protons as they experience more stochastic events along their path.

Electron interaction Any charged particle radiates energy when accelerated or decelerated. This phenomenon, known as Bremsstrahlung emission, is described by the Larmor formula:

$$P = \frac{q^2 a^2}{6\pi\epsilon_0 c^3} \tag{1.3}$$

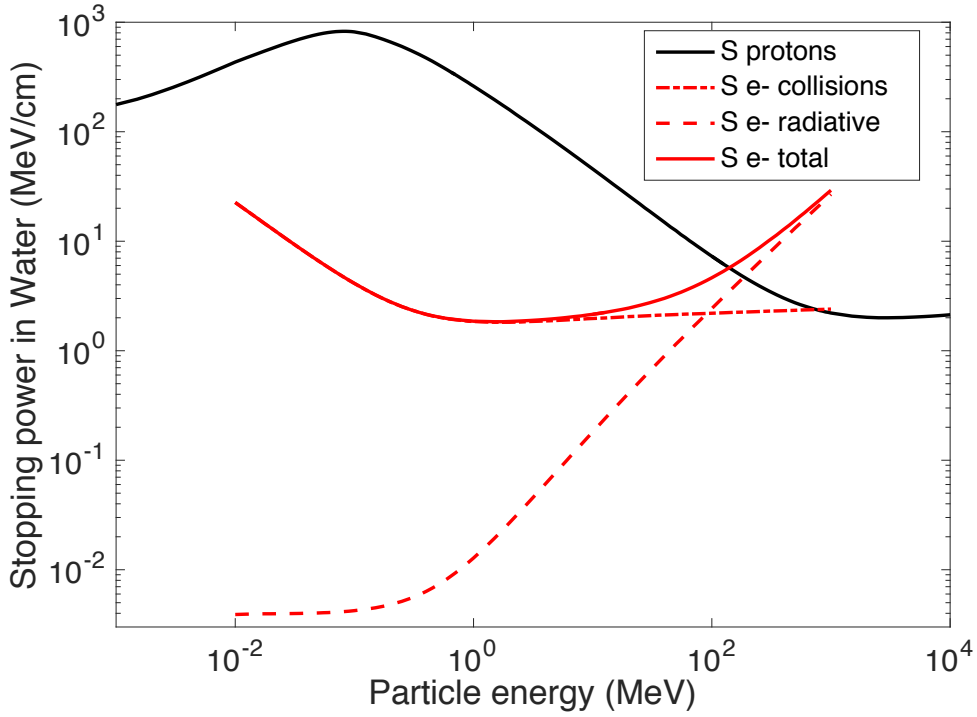

Figure 1.4: Stopping power of an electron in water. The stopping power of protons is also reported for comparison.

where P is the radiative emitted power for a particle of charge q that undergoes an acceleration $a = F/m$. Since acceleration is inversely proportional to the particle mass, radiative emission is significant for charged particles with a low mass, such as electrons, while is negligible for protons and heavier ions. Therefore, the energy loss of electrons is the sum of Bremsstrahlung emission and electron collisions, described by the Bethe-Bloch formula[3]. Figure 1.4 shows the stopping power of electrons in water as a function of the energy. Electron energy loss is dominated by Coulomb collisions up to energies around few tens of MeV, after which radiative emission becomes non negligible. In this energy range, electrons have a lower stopping power compared to protons since, as mentioned above, S is proportional to the incident particle mass. This means that electrons lose their energy at a lower rate compared to protons with the same energy and, therefore, feature a larger penetration depth. Furthermore, since their mass is equal to that of the orbital electrons of the traversed medium, electrons experience larger deviations from the

[3]The logarithmic part of the Bethe-block formula needs a correction, since the mass of the primary particle equals that of orbital electrons. The correction can be found in G. F. Knoll (2000) [113]. Moreover, the $1/v^2$ non-relativistic behaviour is valid only below 0.5 MeV. For higher energies, the velocity of the relativistic electrons can be considered constant, which explains the flatness of the collisional stopping power.

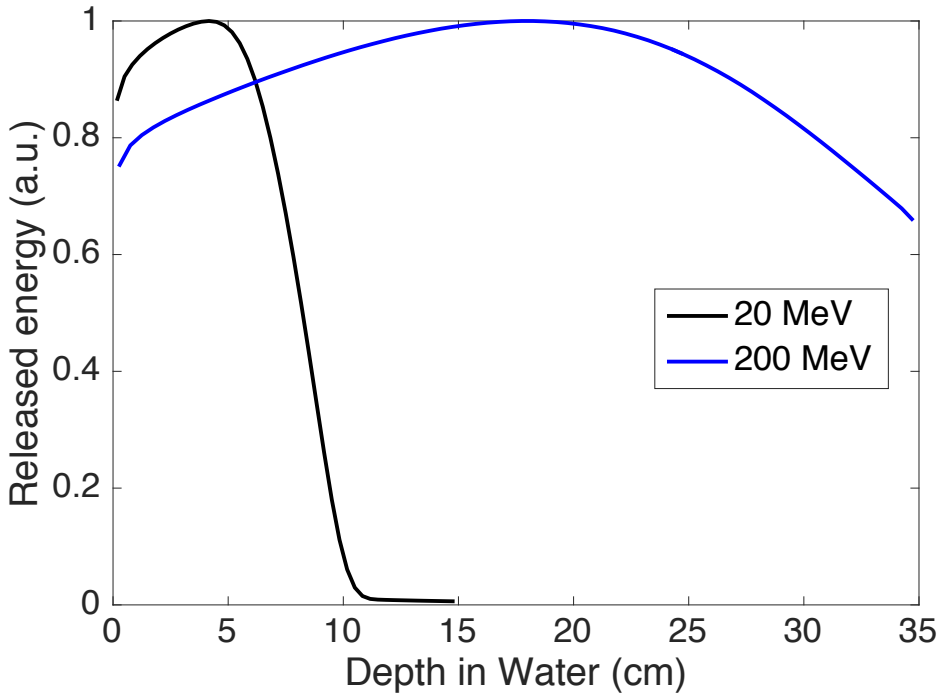

Figure 1.5: In-depth profile of the energy released in water by low energy (20 MeV) and high energy (200 MeV) electron beams obtained through Monte Carlo (Geant4) simulations.

initial direction compared to protons. As a consequence, they exhibit stronger range and energy straggling as well as a larger beam diffusion in depth. Overall, these characteristics deeply affect the in-depth energy loss of electrons, which does not feature any Bragg-peak or steep fall-off, as shown in Fig. 1.5.

1.2.2 Photon interaction with matter

Photons with energy exceeding a few tens of electronvolts (X-rays and gamma ray) can indirectly ionise matter, as previously mentioned. Their interaction with matter is quite different from that of charged particles. The interaction process normally results in an abrupt change of the properties of the incident photon, which either disappears or undergoes a significant deflection that removes it from the beam envelope. Therefore, while charged particle beams are degradated in energy through a continuous slowing down process, photon beams are degradated in intensity through single and catastrophic events such as absorption, annihilation or deflection.

The attenuation of a photon beam traversing a medium is exponential and depends on both the medium properties and the photon energy. The beam intensity at a given depth

$I(x)$ can be described by the following exponential formulation:

$$I(x) = I_0 e^{-\mu x} = I_0 e^{-\left(\frac{\mu}{\rho}\right)(\rho x)} \tag{1.4}$$

Where I_0 is the initial beam intensity, μ is the linear attenuation coefficient, usually tabulated as mass attenuation coefficient μ/ρ, and ρ is the density of the traversed medium. The mass attenuation coefficient does not change with the physical state of the traversed medium and depends on the type of material and the photon energy. It physically represents the rate of photon interaction per unit area mass.
Three main stochastic processes can occurr when a photon interacts with an atom of the traversed material:

- Photoelectric effect: in this process, the photon interacts with one of the bound electrons of an atom and transfer all its energy. The incident photon is absorbed and the electron is ejected from the atom with the initial photon energy minus the electron binding energy[4].

- Compton scattering: in this process, the photon transfers part of its energy to a bound electron and moves forward with a reduced energy that depends on the deflection angle θ, according to:

$$E'_{ph} = \frac{E_{ph}}{1 + E_{ph}\left(\frac{1-\cos\theta}{m_e c^2}\right)} \tag{1.5}$$

  where E_{ph} and E'_{ph} are respectively the photon energy before and after the interaction and m_e is the electron mass at rest. From the law of energy conservation, the energy of the secondary electron is given by:

$$E_e = E_0 + (E_{ph} - E'_{ph}) \tag{1.6}$$

  where $E_0 = m_e c^2$ is the electron energy at rest. The spectrum of the generated secondary electrons is therefore continuous between the energy at rest (no photon deflection, $\theta = 0°$) and the maximum energy (maximum photon deflection, $\theta = 180°$) given by:

$$E_e = E_0 + E_{ph} \cdot (1 - \frac{1}{1 + 2E_{ph}/m_e c^2}) \tag{1.7}$$

- Pair production: in this process, the photon interacts with the Couloumb field of

[4]The binding energy is the energy required to free an electron from the atom.

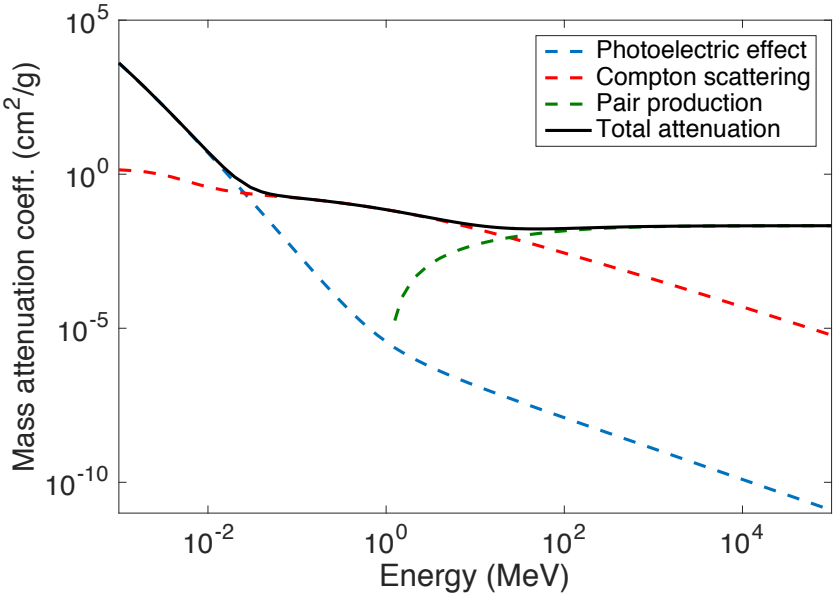

Figure 1.6: Photon attenuation coefficients in water. Data taken from NIST tables (https://physics.nist.gov/PhysRefData/Xcom/html/xcom1.html)

the nucleus and disappears, giving rise to an electron-positron pair. The event is energetically possible only if the photon energy exceeds twice the electron mass at rest, i.e. 1.02 MeV, and its probability at typical energies of medical interest (few MeV) is negligible. All the photon energy exceeding 1.02 MeV is shared, as kinetic energy, between the positron and the electron.

All of these events occur with a given probability that depends on the photon energy and the medium material. The total probability of interaction per unit length μ is simply the sum of the three probabilities associated to each event:

$$\mu = \mu_{ph} + \mu_{co} + \mu_{pp} \tag{1.8}$$

The attenuation coefficients in water as a function of the photon energy are shown in Fig. 1.6.

It is important to bear in mind that, in all these processes, the photon energy is transferred to the medium by the secondary electrons generated during the interaction. Therefore, the energy is released progressively along the secondary electron path, "far" from the interaction point. To provide some indicative values, the average energy of electrons produced by a 10 MeV photon is 0.8 MeV, whose range in water is $\sim$ 3mm. The energy released in depth from a photon beam features an initial increase followed by an exponential decay, due to the exponential attenuation of the beam intensity (Fig. 1.7). The initial increase is

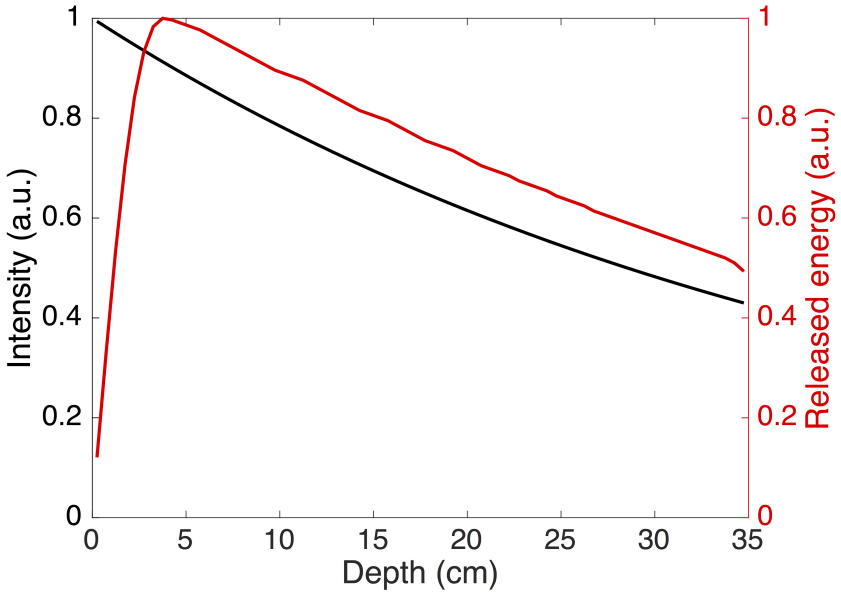

Figure 1.7: Exponential attenuation in water of 8 MeV photon beam (black line, left axis) and total energy released obtained through Monte Carlo Simulations (red line, right axis)

explained by considering that the first interaction events in depth produce electrons that deliver their energy far from the interaction point. A minimum thickness called "equilibrium thickness" is required to reach the so-called electronic equilibrium, defined as the condition in which as many electrons are stopped as set in motion in a given volume. Once the electronic equilibrium is reached, the in-depth profile of the deposited energy follows the exponential decay of the beam intensity.

1.3 Radiation spatial dynamics

The dose is the physical unit used to quantify the energy delivered by radiation. It is expressed in Gray (Gy = J/kg) and theoretically defined as the ratio between the energy delivered in a given volume and its mass, as the mass tends to zero:

$$D = \lim_{m \to 0} \frac{\Delta E}{\Delta m} \tag{1.9}$$

Knowing the fluence of particles (charged particles only) and under the assumption that radiative photons escape the volume of interest and that secondary electrons are absorbed in this volume (or that charged particle equilibrium is verified) the dose can be computed

through the use of the collisional stopping power, expressed in $\mathrm{J} \cdot \mathrm{cm}^2/\mathrm{kg}$, as:

$$D = \int \Phi(E) \cdot S_{col}(E) dE \tag{1.10}$$

Because of the stochastic nature of radiation interaction with matter, dose deposition is not homogeneous at a molecular scale. However, classical dosimetry employed in clinics does not deal with the microsopic nature of energy deposition[5] and considers the deposited dose as a macroscopic quantity. It is experimentally measured with dosimetry instruments that rely on different processes to convert the deposited dose into a readable signal[6]. In this sense, dose can be simply considered as the energy deposited in a given volume divided by its mass, for a given resolution of the measurement voxel.
The primary goal of a radiotherapy treatment planning is to increase the so-called "dose conformity", i.e. to deliver an homogeneous dose within the tumour volume while sparing as much as possible the surrounding healthy tissues. The ability to improve dose conformity depends both on technological advances in dose delivery techniques, imaging and dosimetry, and on the intrinsic physical properties of radiations. In particular, the last factor affects the 3D dose deposition spatial profile in matter and therefore plays a crucial role in assessing the suitability of a specific radiation for the treatment of a given tumour geometry.

1.3.1 Dose profiles

In the previous section we explained the physical phenomena leading to different in-depth energy deposition profiles for various radiations, which are presented in the same graph in Fig. 1.8. The energy deposition is calculated with the Geant4 Monte Carlo code by simulating a collimated beam and shooting it in the direction of a water phantom containing the entire transverse beam section. The phantom is divided into slices perpendicular to the beam propagation axis to integrate the energy deposited in depth over the entire transverse section. Consequently, the resulting 1D energy profiles shown in Fig. 1.8 do not take into account the transverse beam dimension and the beam diffusion, and can be read as the energy profiles generated by a single particle.
However, a real radiotherapy treatment employs particle beams of a given transverse sec-

[5] Microdosimetry is the branch of radiation biophysics that systematically studies the stochastic nature of energy deposition processes in microscopic structures.

[6] Dosimetry instruments are typically classified by their status (solid, liquid, gaseous) or by the type of process they rely on. The most employed instruments rely on the ionisation process (ionisation chambers), on temperature changes (calorimeters) or on radiation induced chemical changes of their properties, such as color or radical concentration (radiochromic films, alanine detectors).

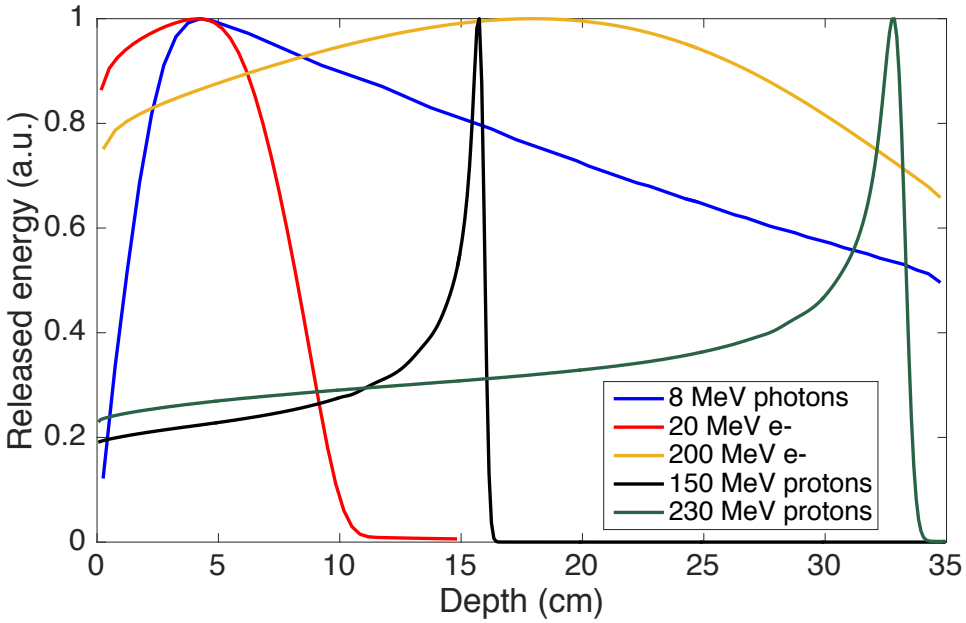

Figure 1.8: In-depth profile of deposited energy in water for different radiations.

tion that evolves as the beam penetrates in the body. The in-depth behaviour of the transverse beam section depends on both the beam dimension and its diffusion, and is a crucial parameter as it affects the 3D dose distribution and the depth-dose profile. To illustrate this concept, Fig. 1.9 shows a 2D horizontal cut of the dose distribution on the beam axis inside a water phantom for three different radiation qualities and for two different beam transverse dimensions:

- Left column of Fig. 1.9: collimated beam with a transverse diameter of 5 cm impinging on a $25 \times 25 \times 35$ cm^3 wather phantom;
- Right column of Fig. 1.9: collimated beam with a transverse diameter of 1 cm impinging on a $5 \times 5 \times 35$ cm^3 whater phantom;

In the two geometries, the transverse dimensions of both the beam and the phantom are rescaled by a factor of 5 while the number of transverse pixels (125×125 pixels) and shooted particles (10^8 particles) is kept equal in order to maintain the same resolution in term of particles per transverse pixel. As it is shown, when the beam dimension is reduced to around 1 cm or below, the diffusion of the beam due to the scattering with matter has a major effect on the dose distribution. Since in clinics and radiation biology the target volume must receive an homogeneous dose[7], it is relevant to study the in-depth profile of

[7]The maximum acceptable error on dose inhomogeneity inside the irradiated sample in radiation biology is normally 10% [116, 55]

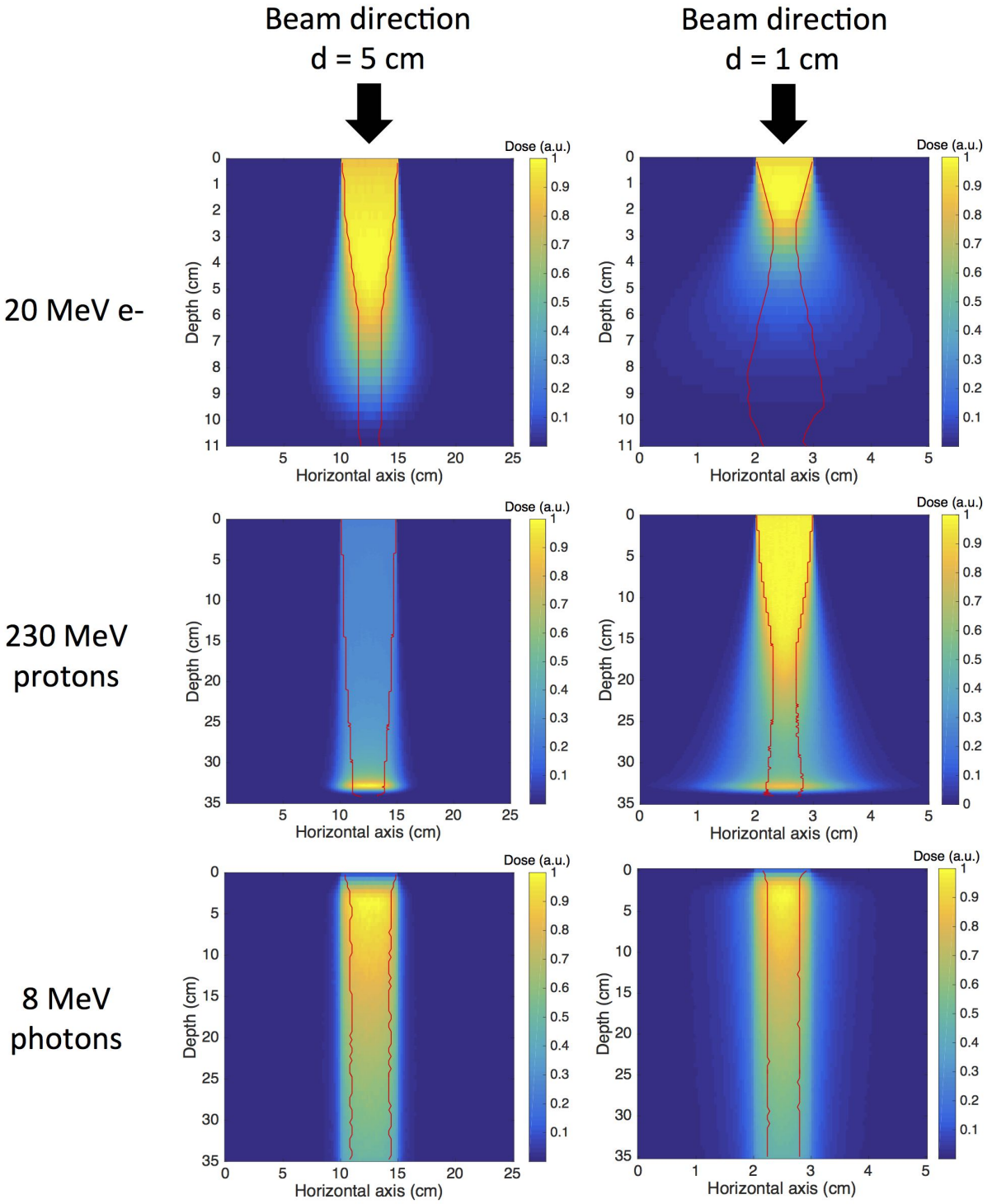

Figure 1.9: Top view of the 2D in-depth dose profile for different radiation qualities and two different geometries: beam diameter of 5 cm (left column) and beam diameter of 1 cm (righ column). The red lines indicate the 90% isodose limits over the transverse section (i.e. the transverse dimension inside of which the dose is higher than 90% of the maximum dose of the same transverse section). The results are obtained with Geant4 monte carlo simulations using 10×10^8 particles. In each figure the dose is normalised to its maximum value.

the dose within a fixed transverse uniformity region, e.g. the 90% isodose surface[8]. The behaviour of the 90% isodose surface in depth is showed by the red lines in the images of Fig. 1.9 and the resulting depth-dose profiles are shown in Fig. 1.10. For all radiations, the depth-dose profile of the 5 cm beams (continuous lines in Fig. 1.10) is very similar to the in-depth energy profile of Fig. 1.8, since the collective effect of diffusion for such dimension is negligible and does not affect the characteristic feature of the different in-depth energy profiles. If the beam size is reduced to ∼1 cm, the isodose surface of charged particles tends to shrink and then widen again in depth (Fig. 1.9). This effect is due to the higher ratio between the typical diffusion length and the beam initial dimension, and gets more and more pronounced as the beam size is reduced. Also, a smaller beam size causes an increase of the beam penumbra[9]. The isodose surface of photons depends to a small degree on the beam dimension, since photon diffusion is less pronounced and the energy deposition is due to the low-energy secondary electrons. The only effect of the reduced beam dimension is a larger penumbra region (Fig. 1.9), due to the higher ratio between the average range of the secondary electrons and the beam dimension.
All together, these effects may significantly alter the depth-dose profile of small beams (dashed lines in Fig. 1.10). Electron and photon beams present a dose peak closer to the phantom entrance, whereas the effect of diffusion is cathastrophic for small proton beams, as the typical Bragg-peak feature is completely degradated[10] (green dashed line of Fig. 1.10).
These examples show that, for a given radiation, the location of dose peak in depth depends not only on the initial energy of the beam but also on its transverse dimension and diffusion. In general, the depth-dose profile of the 5 cm beam case is representative of clinical scenarios, since typical dimensions of the beams employed in radiotherapy treatments do normally exceed 1 cm. In the following sections, we will briefly describe the use of such radiations in radiotherapy and the techniques developed to adapt their characteristic dose distribution to the tumour volume.

[8]For each slice of the water phantom, perpendicular to the beam axis, the 90% isodose is computed with respect to the maximum value of the dose in the slice. The isodose surface delimit, therefore, the transverse region with an homogeneity of ±5% for each slice. It gives an indication of how the beam section, precisely the same isodose area, evolves while the beam penetetrates in the phantom.

[9]The rapid decrease of the transverse dose distribution at the edges of the beam is called the penumbra region. It is usually defined as the space between the 80% and 20% isodose lines.

[10]The degradation of the Bragg-peak feature of proton beams is well known in the field of Mini Beam Radiation Therapy (MBRT) [165], which uses beams having a transverse dimension of hundreds of microns.

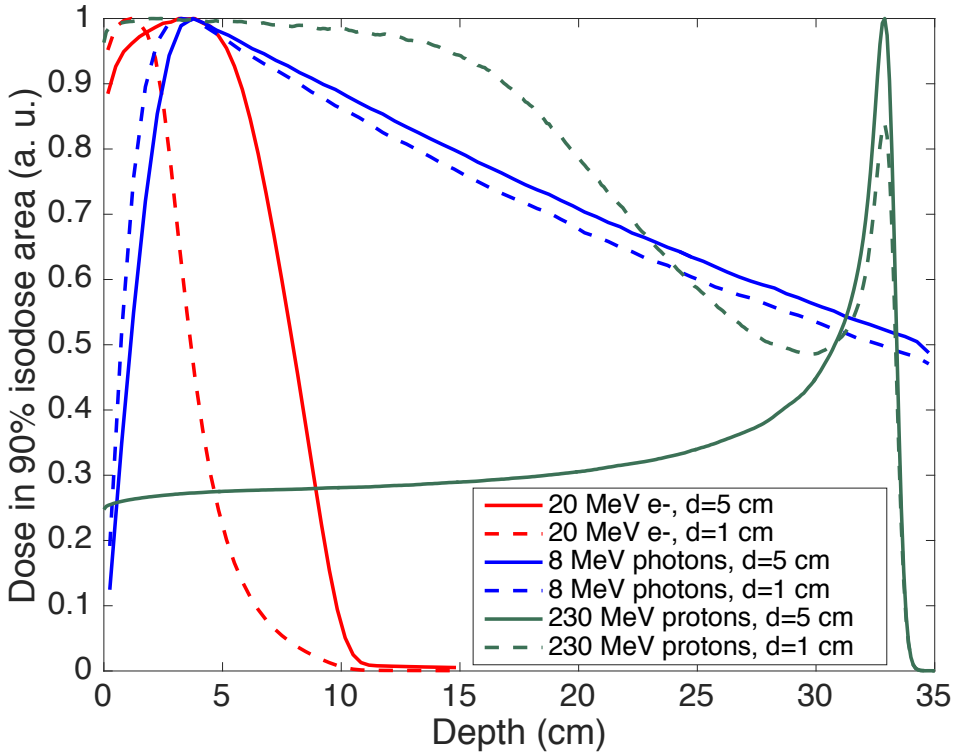

Figure 1.10: In-depth dose deposition for the examples in Fig. 1.9. The y-axis represents the dose delivered inside the 90% isodose surfaces for each slice in depth (dotted lines in Fig. 1.9). The in-depth resolution, i.e. the thickness of the phantom slices, is 3.5 mm for the photon and electron curves and 1 mm for the proton curve to obtain a sufficient resolution of the Bragg-peak.

1.3.2 Geometrical aspects in clinics

As already mentioned, optimisation of the treatment selectivity is the main issue of radiotherapy. One of the strategies employed to increase the treatment selectivity is to spatially concentrate the dose into the tumour, thus allowing the delivery of high tumour doses for a given tolerance dose on the healthy tissues. Spatial optimisation of the delivered dose is strongly affected by the radiation spatial dynamics and is performed with proper techniques. This section briefly discusses the use of photons, protons and electrons in clinics and presents the techniques developed to control such beams and spatially optimise the dose.

Use of photons in radiotherapy Radiotherapy with photons is widely employed in clinics, since X-rays are quite easy to produce and control[11]. Complex dose delivery techniques have been developed to overcome the unfavorable exponential attenuation of photons and to concentrate the dose in tumors located deep inside the body. Intensity Modulated Radiation Therapy (IMRT) is the most commonly used technique [169, 34]. Dose conformity is obtained by positioning the patient at the center of a rotating gantry that delivers the X-ray beam. During the treatment, the patient is irradiated using multiple exposure angles. In this way, the tumour is crossed multiple times by the beam while surrounding tissues receive a lower dose. Moreover, at each specified gantry angle, the photon flux is also properly shaped to obtain a more conformal dose distribution. Fig. 1.11. shows a schematic draft of the IMRT technique and a picture of a typical gantry. The dynamic control of the beam flux shape is performed through the use of multiple remotely controlled absorber leaves. The multileaf collimator (MLC) is usually the last stage of a series of collimators mounted in the head of the rotating gantry and ensures the fine shaping of the beam flux (Fig. 1.12). The movement of MLCs and the number of gantry angles are programmed through inverse treatment planning techniques [201].
Thanks to technological and computational advances, IMRT has evolved in more complex versions such as rotational IMRT techniques. In these techniques (VMAT, helical tomotherapy) the gantry continuously rotates around the patient and the multileaf movement is programmed as a continuous function of time. IMRT techniques are steadily evolving and are considered today the standard for many tumour treatments.

[11] X-rays are normally produced by electrons accelerated with classical linear accelerators (LINAC). These electrons strikes a tungsten target producing X-ray bremsstrahlung radiation.

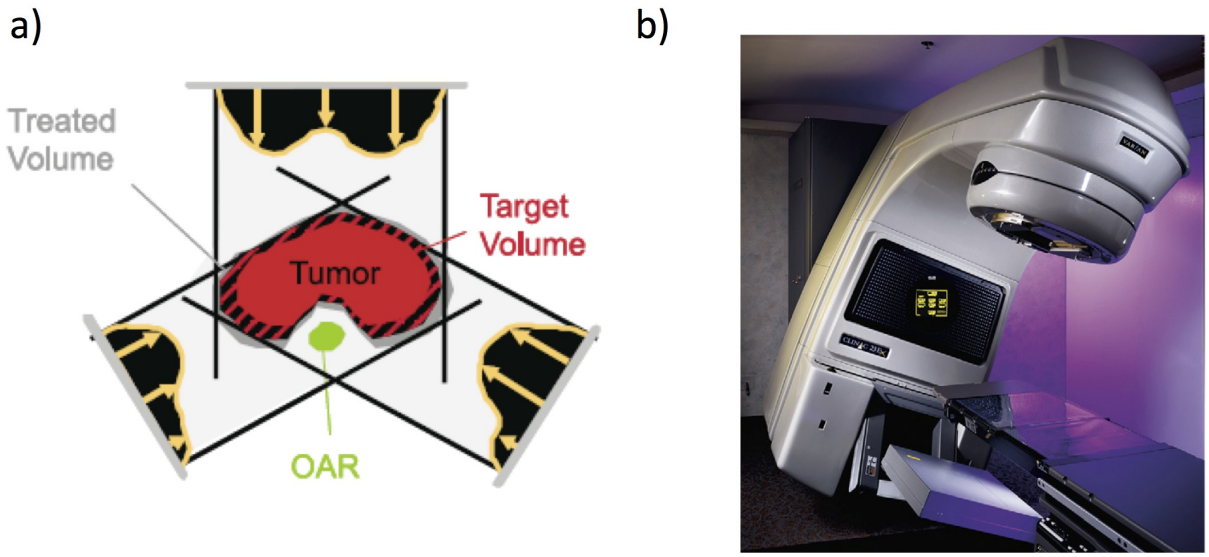

Figure 1.11: a) Schematic draft of an Intensity Modulated Radiation Therapy with 3 exposure angles. The flux modulation allow sculpting the dose to a complex concave tumour shape while sparing the Organ At Risk (OAR). Taken from T. Bortfeld (2006) [31]. b) External view of a rotating gantry, taken from D. Baatar et al. (2018) [12].

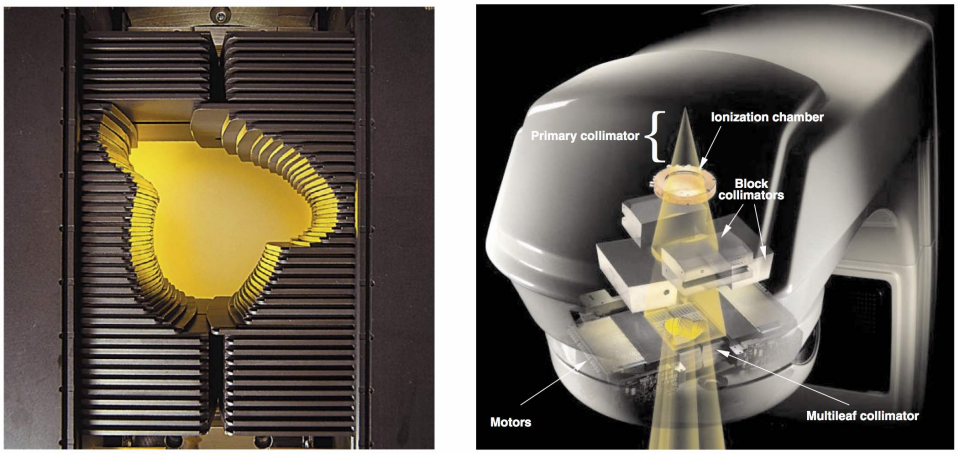

Figure 1.12: Left: picture of a multileaf collimator. Right) Internal view of a gantry head. The multileaf collimator is the last stage of a collimator system. The pictures are taken from D. Baatar et al. (2018) [12] and A. L. Boyer (2002) [34].

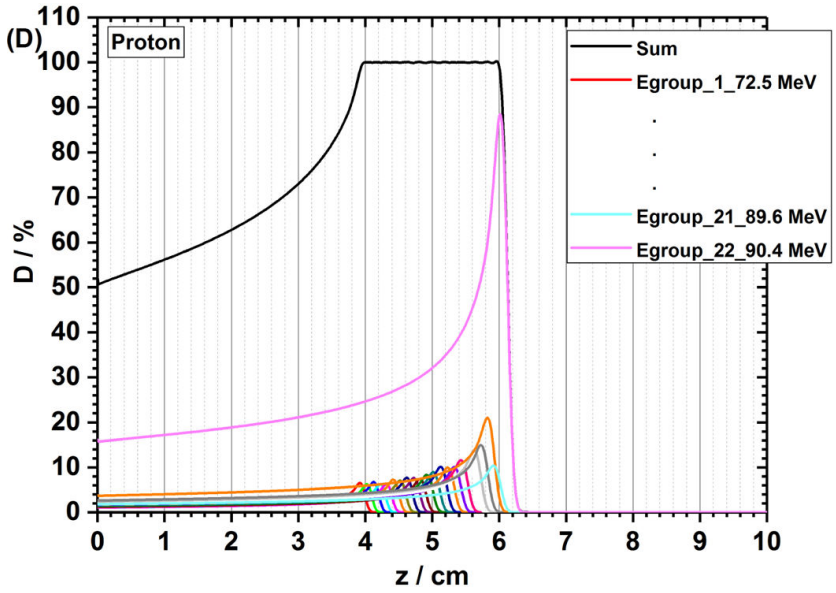

Figure 1.13: Spread-out Bragg-peak (black line) obtained by spectrally tailoring proton energies ranging from 72.5 MeV to 90.4 MeV. Taken from C. Geng et al. (2018) [73].

Protontherapy The geometrical complexity of a treatment planning using photons is necessary to tackle their unfavorable depth-dose profile and sculpt the dose to the tumour. Protons offer in this sense an undeniable ballistic advantage thanks to their peculiar depth-dose profile, which allows better sparing of the entry tissue and of the organs at risk located after the distal dose falloff (Fig. 1.10).

Protons used in clinics (typical energies between 70 MeV and 250 MeV) are generated by synchrotrons or cyclotrons, and are guided towards the head of the gantry system. To irradiate large tumour volumes, the Bragg-peak must be longitudinally and transversally spread. The longitudinal spread is obtained through spectral shaping of the initially monoenergetic beam leaving the accelerator. As mentioned in Section 1.2.1, the Bragg-peak position depends on the initial energy of the proton beam. Therefore, by properly tuning the yield of each energetic component, a flat Spread-Out Bragg-Peak (SOBP) can be obtained at a specific depth defined by the spectral bandwidth selected [73], as shown in Fig. 1.13. Altough the ratio between the peak and the entrance dose is significantly reduced, the depth-dose profile still allows a significant sparing of the entry tissues compared to photons, as well as complete sparing the organs located after the distal falloff.

The SOBP can be experimentally obtained through many different techniques, whose extreme forms are passive systems and active scanning [180, 139]. In the first case, the beam is shaped in three dimensions and adapted to the tumour contours by passive scattering systems. In the second case, the tumour is divided in voxels, each of which is irradiated

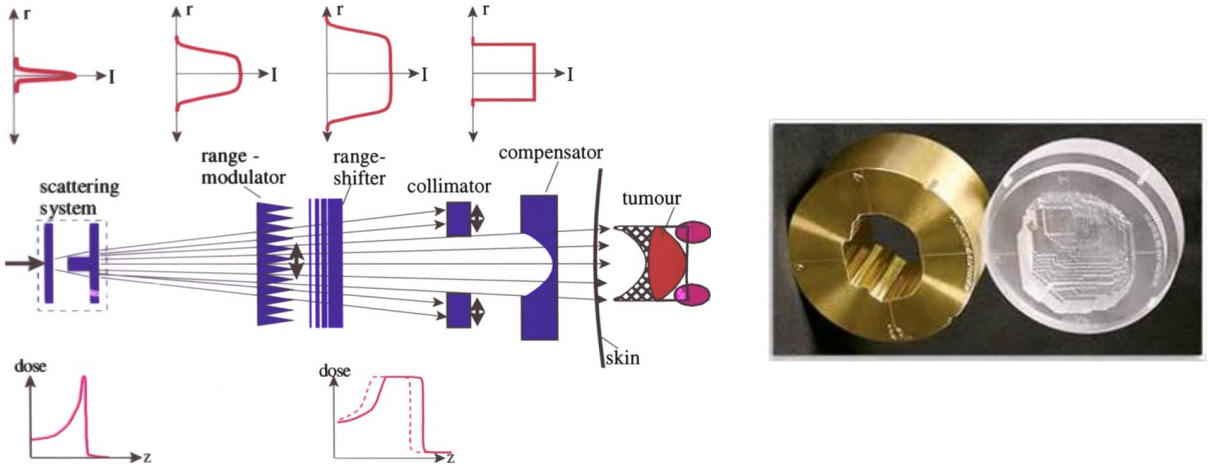

Figure 1.14: Experimental set-up of a typical passive proton beam shaping system. Left: the Bragg-peak is transversally (top draft) and longitudinally (bottom draft) spread by different scattering systems providing the required dose conformity to the tumour volume. Taken from D. Schardt et al. (2010) [180]. Right: image of a patient specific collimator and compensator. Taken from A. Klyachko (2017) [112].

separately by a small pencil-beam delivering the prescribed dose. A detailed discussion of the techniques employed in clinics would be out of the scope of this manuscript. However, as an introduction to activities conducted during this thesis and described in the following sections, a typical passive beam shaping system used in clinics is here briefly described. After the accelerator exit, flat scattering systems are first used to flatten the transverse beam profile (Fig. 1.14). The Bragg-peak is then longitudinally spread through the use of a Ridge filter [6] or a rotating modulation wheel [179] so as to cover the entire tumour length. Both strategies introduce homogeneous energy losses over the transverse cross-section of the beam so as to widen the initial monoenergetic spectrum equally over the transverse beam section and longitudinally spread the Bragg-peak uniformly over the beam section. Once the SOBP of the desired length is created, the beam passes through an absorber called "range shifter" that produces an in-depth shift of the SOBP by introducing an equal energy loss over the transverse beam section. Ultimately, in order to sculpt the dose to complex tumour shapes, a set of two patient-specific devices, a collimator and a compensator, finally adapts the transversal beam area to the largest target contour as seen in beam view and adjust the varying in-depth position of the SOBP over a transverse plane.

If on the one hand the depth-dose characteristic of protons constitutes their main asset, on the other hand the sharp distal falloff makes the delivered dose more sensitive to uncertainties regarding treatment planning parameters, such as tissue composition, as

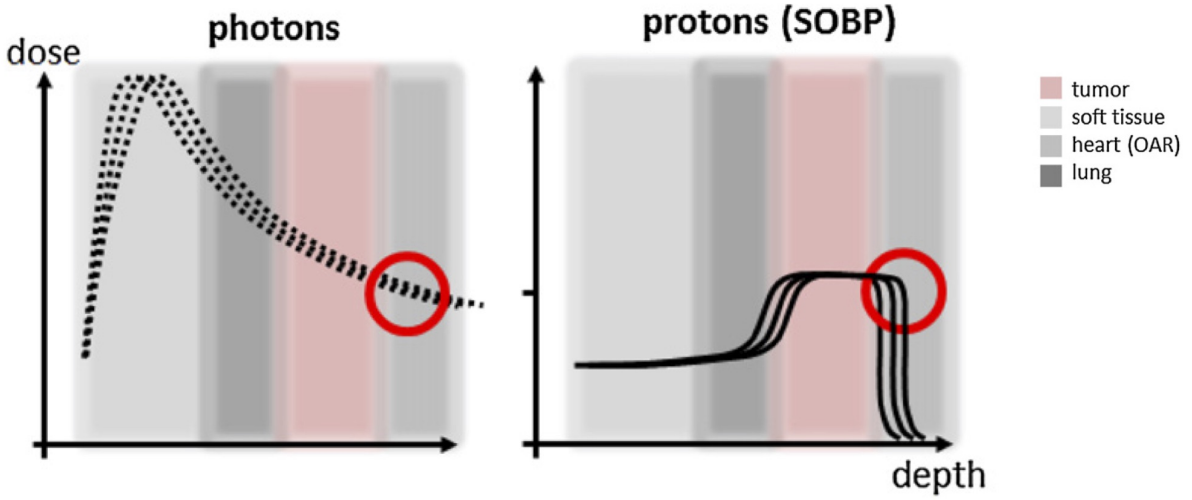

Figure 1.15: Influence of uncertainty on in-depth dose curves of photons and protons. An uncertainty on the photon attenuation coefficients would cause a small error on the dose distribution, while an uncertainty on the proton range would shift the SOBP and result in a tremendous error in the dose delivered to the adjacent healthy tissues.Taken from A. C. Knopf et al. [114].

well as to inter- and intra-fraction anatomy variations (see Fig. 1.15). In other words, the attractive depth-dose profile is at the same time the advantage and the challenging aspect of protontherapy [114]. In order to reduce dose errors and fully exploit the proton potential, protontherapy treatments require highly efficient imaging technology, robust treatment planning techniques and a more frequent tumour follow-up to constantly re-adapt the treatment planning to the evolving tumour shape. All of these aspects result in high operating costs of a protontherapy facility, which is also subject to high installation costs due to the large accelerators required. For these reasons, the number of facilities worldwide is limited (57 operating facilities in 2017). Clinical trials require therefore more time and coordination of multiple protontherapy centres, and the overall number of patients treated with protontherapy is to date significantly lower compared to the number of patients treated with photon therapy. As a consequence, the clinical advantage of protontherapy is still being debated for most of the cancer diseases. Despite these limitations, protontherapy has already proven to be highly effective for some malignancies such as skull based cancers and ocular melanoma. In addition, it is widely used to treat many pediatric cancers, since the reduction of the dose delivered to the healthy tissues reduces the risk of long-term side effects [7, 192, 139].

Use of electrons in radiotherapy Given their short range (Fig. 1.10), low energy electrons (4-20 MeV) are typically used in specific treatments requiring a high dose deliv-

ered in the first centimeters of tissues. For example, external electron beam therapy has proven to be effective for treatment of skin cancers such as melanoma and carcinoma [177] and for IntraOperative Electron Radiation Therapy (IOERT), consisting in the application of a single dose fraction during a surgical removal of the tumour mass [151, 160].
On the contrary, applications of Very High-Energy Electron (VHEE) has been limited to theoretical studies. VHEE (50-250 MeV) could offer a promising alternative to photons for irradiation of deep-seated tumours as they feature a comparable penetration depth (see Fig. 1.8) and, additionally, they could be delivered through pencil beam active scanning approaches. Furthermore, VHEE beams could be easily focused (for example with quadrupoles having field gradients of few tens of Tesla) to reduce both the entrance and exit doses [82, 115] and increase the resolution of active scanning techniques. For these reasons, many theoretical studies on VHEE have been conducted in the last decades, leading to the conclusion that they may offer clinical advantages in terms of healthy tissue sparing for many cancer diseases [209, 54, 71, 19, 154]. However, very few experiments have been published [189] and the higher cost of VHEE accelerators compared to X-rays [155] hinders their clinical implementation. To conclude, although the feasibility of a clinical application is still being debated, VHEE therapy is an active domain of research.

1.4 Radiobiology basics

Dose optimisation is the central aspect of radiotherapy treatment plannings, as the response of tumours and healthy tissues is proportional to the absorbed dose. Nevertheless, dose is a macroscopic quantity and does not account for the effect of energy deposition modality at a molecular scale. Indeed, delivering the same dose with different radiation qualities produces different biological responses [45]. Other quantities are therefore employed in radiobiology to account for the specific effect of radiations at a molecular scale and the consequent cellular damage.

1.4.1 Processes following irradiation - DNA damage

Irradiation of biological systems generates a sequence of processes that can be divided in three main phases: physical, chemical and biological. These stages enormously differ in time-scale, as shown in Fig. 1.16, and also exibhit a growing complexity.
The physical phase lasts $10^{-18} - 10^{-14}$ seconds and consists in the excitation and ionisation of atoms and molecules within the cell, through the mechanisms described in section 1.2.1. The hypothesis that has been made during the last decades to explain the biological con-

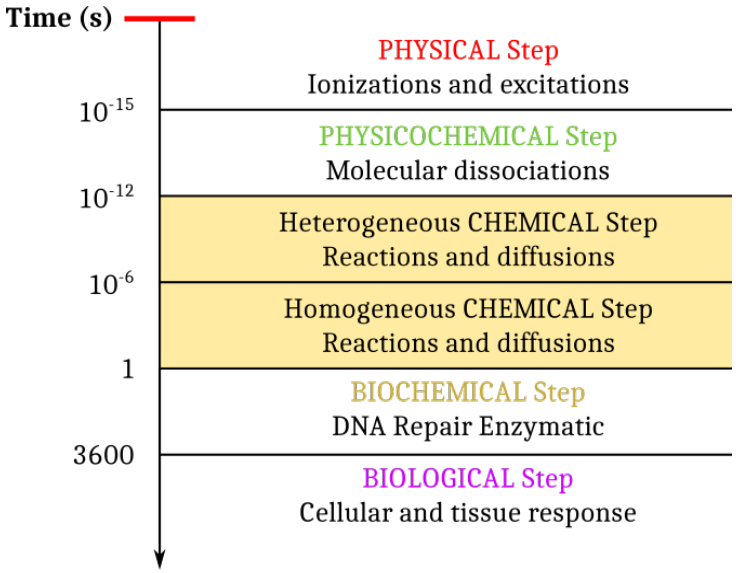

Figure 1.16: Time-scale of phenomena following irradiation of a biological system.

sequences of irradiation is based on the central role of DNA damage [107, 200]. According to this assumption, DNA lesions are more important than damage to other cell components to induce cell death. In fact, while most of cell molecules are present in multiple copies (water, mRNA, proteins), DNA is present in only two copies and, moreover, it is central to cellular activity and reproduction. During the last years, however, the approach to explain cell mortality mechanisms evolved, moving from the emphasis on DNA damage to more complex biochemical mechanisms, involving other cell components and non targeted effects [36, 9]. It is therefore important to bear in mind that the description of cell mortality as a response to DNA damage is a simplified view, although it is essential to explain many radiobiological phenomena. Reviews on complex cell damage and non targeted effects can be found in O. Desouky et al. (2015) [53] and I. Mavragani et al. (2017) [132]. A division can be made between direct and indirect DNA damage, as schematically shown in Fig. 1.17. Direct damage consists in energy deposition occurring through excitation or ionisation of the DNA components (sugars, bases etc). This direct energy deposition can lead to break-up of a strand, producing a Single Strand Break (SSB). If two SSBs are located on opposite strands and are close enough, that is few pairs, the damage is called Double Strand Break (DSB) (see Fig. 1.18, right image) and it is believed to be a very important radiation-induced lesion. Cells have indeed trouble dealing with DSBs and this results in a high likelihood of cell killing. Indirect damage consists in energy deposition through interaction with other molecules than the DNA, which in turn generates free electrons or radicals that can chemically attack the DNA.

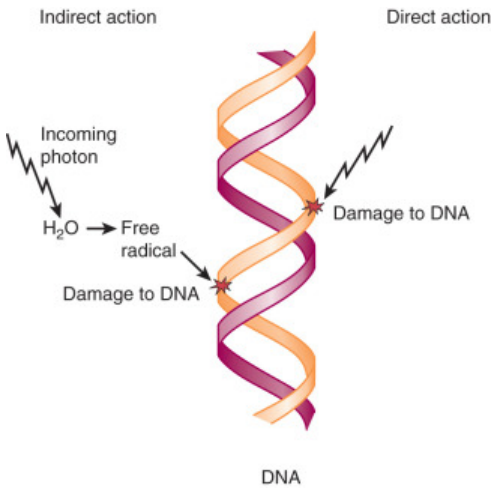

Figure 1.17: Schematic of DNA direct and indirect damage. Taken from C. M. Yashar (2018) [208].

Therefore, while direct DNA damage occurs in the first physical phase, indirect DNA damage is the result of complex chemical reactions involving free electrons and reactive radicals that are complete whitin $\sim$ 1 ms.
The chemical phase is then followed by the biological phase, which includes all the subsequent processes ranging from the repair mechanisms activated by the cells to late effects on the organism.
Altough the biological response is the consequence of complex phenomena encompassing physics, chemistry and biology, the type of physical interaction at a molecular scale between radiation and living matter determines the onset of all the subsequent processes and therefore plays a key role in causing cell death, as discussed in the following sections.

1.4.2 Energy transfer at molecular scale: the LET

The specific submicrometric pattern of ionisations produced by different radiations within the cell is closely related to the severity of induced damage. In other words, the same dose delivered with two "radiation qualities"[12] induces different subsequent chemical processes and cell damage. Therefore, the dose alone seems not adequate to completely capture the effect of irradiation.
The Linear Energy Transfer (LET) is the parameter used to quantify the spatial rate at which energy is transferred to matter and is strongly related to the severity of the

[12]The term radiation quality refers to those features of the micrometric spatial distribution of energy transfer that play a role in the effectiveness of radiations, when other factors such as the total delivered dose are kept constant.

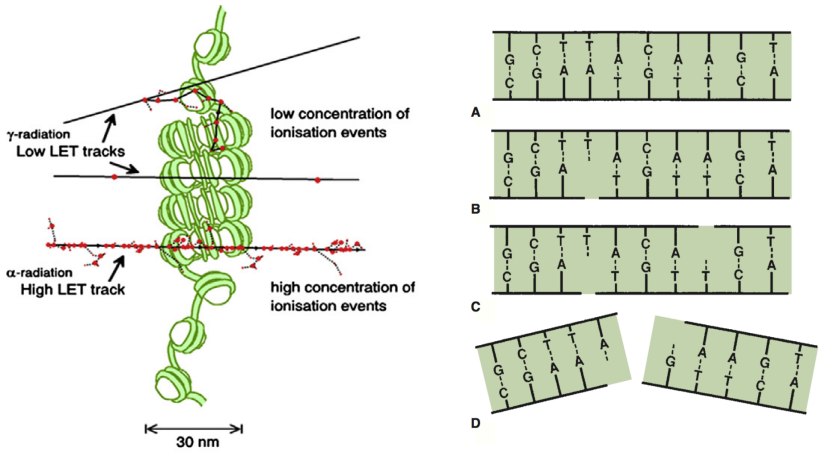

Figure 1.18: Left: draft of different ionisation density of low-LET (photon) and high-LET (alpha particle) radiations on a chromatin (package of a DNA molecule wrapped around histone proteins). The dense ionising pattern of high-LET radiation more likely induces close single strand breaks that finally lead to double strand breaks. Taken from M. E. Lomax et al (2013) [122]. Right: schematic of Double Strand Break (DSB). Taken from E. J. Hall et al. (2012) [92].

induced damage (see Fig. 1.17). The International Commission on Radiation Units and Measurements (ICRU) defines the LET as [1, 118]:

$$L[\mathrm{keV}/\mu\mathrm{m}] = \frac{dE_L}{dl} \tag{1.11}$$

Where dE_L is the energy released locally in the medium by a particle traversing the distance dl. Typical values of LET for various radiations are shown in Fig. 1.19. The term locally is arbitrary and depends on the application. The ICRU suggests to use a more formal definition of LET, called "restricted LET", as it can be easily related to the stopping power. It is defined as that part of the total energy loss of a particle transmitted to the medium by collisions generating secondary particles carrying a maximum energy Δ, expressed in electronvolts:

$$L_\Delta = \left(\frac{dE}{dl}\right)_\Delta \tag{1.12}$$

If $\Delta = \infty$, then all energy losses are included and the restricted LET would be equal to the collisional stopping power. The choice of the Δ is arbitrary and depends on the specific situation. The quantity LET_{100}, however, is often employed to characterise the spatial rate at which energy is deposited "locally", assuming that secondary electrons carrying more than 100 eV do not deliver the energy locally. A detailed discussion on theoretical model and experimental techniques to compute the radiation LET can be found in the ICRU report of 1970 [1].

Radiation		Linear Energy Transfer
Type	Energy	[keV · µm^{-1}]
Cobalt-60 γ-rays	1.2 MeV	0.2
x-rays	250 keV	2.0
Electrons	4 to 20 MeV	0.2
	100 keV	0.42
	10 keV	2.3
	1 keV	12
Protons	150 MeV	0.5
	10 MeV	4.7
	3 MeV	12
	1.5 MeV	20
	1 MeV	27
	0.1 MeV	93
Neutrons	14 MeV	75
α-particles	2.5 MeV	166
Fe ions	2 GeV	1000

Figure 1.19: Typical LET values for various radiations. Taken from L. Pommarel (2017) [162].

Several studies have demonstrated the relation between LET and cell mortality (Section 1.4.3). In particular, higher LET radiations produce more severe damage such as DSB and clustered lesions (Fig. 1.18), thus causing a higher cell mortality for the same delivered dose [184, 103].

1.4.3 Cell survival curves

Surviving fraction A cell survival curve quantifies the percentage of cells that have survived after irradiation as a function of the delivered dose. However, cell survival can be defined in many different ways, depending on the type of cells and the context. Therefore, before introducing the concept of survival curve for *in vitro* radiobiology analysis, a precise definition of "cell survival" is essential.

Cells can be divided into two main groups: non-proliferating and proliferating cells. In the case of a non-proliferating cell, such as muscle cells, death can be simply defined as a loss of function, while in the case of a proliferating cell, such as stem cells or cancer cells, death can be defined as a loss of reproductive ability. T. T. Puck et. al (1956)[166] defined cell

death as the loss of its ability to multiply into a macroscopic colony[13]. This "reproductive death" is usually the end-point of *in vitro* radiobiology assays, called "clonogenic assays", whose goal is to quantify the colonies formed by a given number of treated cells as a function of the delivered dose.
In a typical clonogenic assay, cells of the analysed cell line culture are placed in separate dishes containing a proper culture medium and divided into two groups: the control group and the test group. After a given incubation time following irradiation of the test group, the number of colonies formed within the two group dishes are counted. The control group is used to quantify the Plating Efficiency (PE), which is defined as the fraction of control cells that have formed colonies:

$$PE = \frac{\text{Counted colonies (control group)}}{\text{Seeded cells (control group)}} \tag{1.13}$$

The PE is normally lower than one, because of several reasons including growth medium imperfection and cell handling. It is employed to normalise the percentage of irradiated cells that have formed colonies in the test group, leading to the following definition of Surviving Fraction (SF):

$$\text{SF} = \frac{\text{Counted colonies (test group)}}{\text{Seeded cells (test group)} \cdot PE} \tag{1.14}$$

Survival curve shape - linear quadratic model The bio-physical processes underpinning the relation between the dose delivered and the surviving fraction are numerous. Many attempts have been made to establish theoretical models that match the experimental curves and contain parameters that are descriptive of the underlying processes. The reference theory that has been used for many years to model cell mortality is the so-called "target theory". It assumes that cell mortality following irradiation is due to direct hit of a cell sensitive target, primarily the DNA. However, as we mentioned in section 1.4.1, the assumption of DNA damage as the main cause of cell death has been questioned during last years, driving the biology community towards the elaboration of more complex models, including "multi-target" and "non-targeted" effects[14]. Despite the complexity of cell killing processes, the target theory still provides a sufficiently compre-

[13]Colony is usually defined as a group of more than 50 descending cells. This number corresponds to 5-6 generations of proliferation and is used to exclude stem cells whose reproductive potential has been damaged by sub-lethal damage.

[14]Recent evidences of non-targeted effects due to cell to cell communication mechanisms, such as the bystander effects [53], demonstrated that biological effects of radiation are also detected in non directly hit cells.

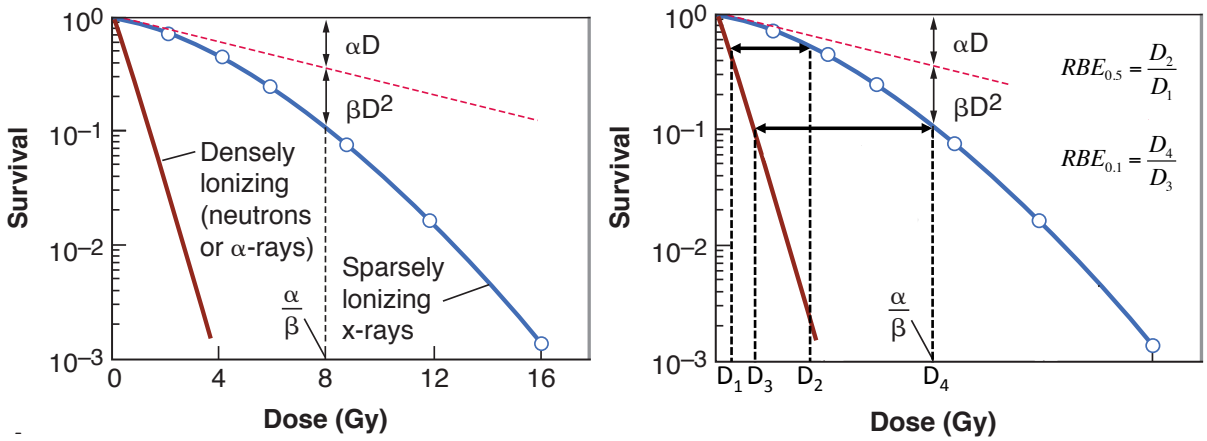

Figure 1.20: Typical survival curves for mammalian cells exposed to high-LET and low-LET radiation, modeled with the linear quadratic model. Taken from E. J. Hall (2012) [92]. On the right, schematic representation of the RBE for two different levels of survival fraction.

hensive explanation of cell death mechanisms. It is the basis of the model most widely used to interpret and fit cell survival curves: the linear quadratic model. According to the model, the surviving fraction can be expressed as the product of two exponentials:

$$SF = e^{-\alpha D - \beta D^2} \tag{1.15}$$

The formula generates a "shouldered" curve on a logarithmic axis (Fig. 1.20) determined by the parameters α and β that quantify cell radiosensitivity. The hypothesis behind the model is that cell killing is the consequence of both single-track events proportional to the dose (first term of the exponential) and multiple-track events proportional to the square of the dose (second term of the exponential). Thus, at low doses, survival is mainly affected by the linear α term, while at high dose the curvature increases thanks to the contribution of the quadratic term β. Fig.1.20 also shows the difference in cell survival for high-LET and low-LET radiation. As LET increases, not only do cells become more sensitive to radiation (the red curve is well below the blue curve) but the curve shape also changes, becoming more linear [152]. The first phenomenon is due to the more severe DNA damage events generated by densely ionising radiation, as illustrated in section 1.4.1, whereas the linear shape is related to the higher probability of causing multiple and spatially dense DNA lesions in single track events. Conversely, low-LET radiation causes severe lesions primarily through the action of multiple independent track hits, which explains the increasing bending at higher doses.

1.4.4 Quantifying the radiation toxicity: the RBE

As discussed, cell survival can be easily related to the absorbed dose and to the radiation LET. Nevertheless, it depends on many other factors, including biological parameters such as oxygenation and cell type, and temporal aspects of dose delivery, such as dose rate and fractionation. For this reason, the toxicity of different radiation qualities, or different irradiation protocols, on a given cell line is usually evaluated using a relative toxicity index called Relative Biological Effectiveness (RBE). It is defined as the ratio between the dose of a reference radiation D_{rr} (normally Co^{60} or 250 kVp X-rays) and the dose of the examined radiation D_{er} producing the same biological effect or "end-point":

$$RBE_{er} = \frac{D_{rr}(\text{end-point X})}{D_{er}(\text{end-point X})} \tag{1.16}$$

The RBE quantifies the toxicity of a given radiation by comparing its biological effect to a reference. Its definition requires the choice of a biological end-point that can be rigorously quantified. The end-point usually used for *in vitro* assays is the surviving fraction. In this sense, RBE can be defined as the ratio between the dose of X-rays and the dose of the radiation under investigation inducing the same degree of cell survival. It is experimentally measured by tracing the survival curves obtained with both the reference and the examined radiation. A schematic draft of the RBE is drawn in Fig. 1.20. As shown, the value of RBE is affected by the SF level at which it is evaluated (typical values of SF are 0.1 and 0.5) and by all the aforementioned factors.

Relation between RBE and LET Fig.1.21 shows survival curves for two cell lines irradiated with protons having different LET values and with X-rays [45]. The proton LET was tuned by placing the *in vitro* sample at different depths along a 60 MeV SOBP. Two important general conclusions can be drawn from the figure. First, different cell lines exhibit a different cell survival for a given delivered dose and radiation. This formally translates into different values of α and β in the linear quadratic model. Secondly, cells are more sensitive to high-LET radiation, because of the severity of biological damage caused by the higher ionisation density.
In general, the RBE increases with the LET up to a peak at around 100 keV/µm (typical LET values of C^{12} ions and α-particles), which is the optimum level of LET causing the maximum cell killing for a given delivered dose, as shown in Fig. 1.22. Radiation having lower LET are less efficient because of the higher level of dose required to produce multi-track severe damage events such as DSBs. Above the optimum LET value, higher LET

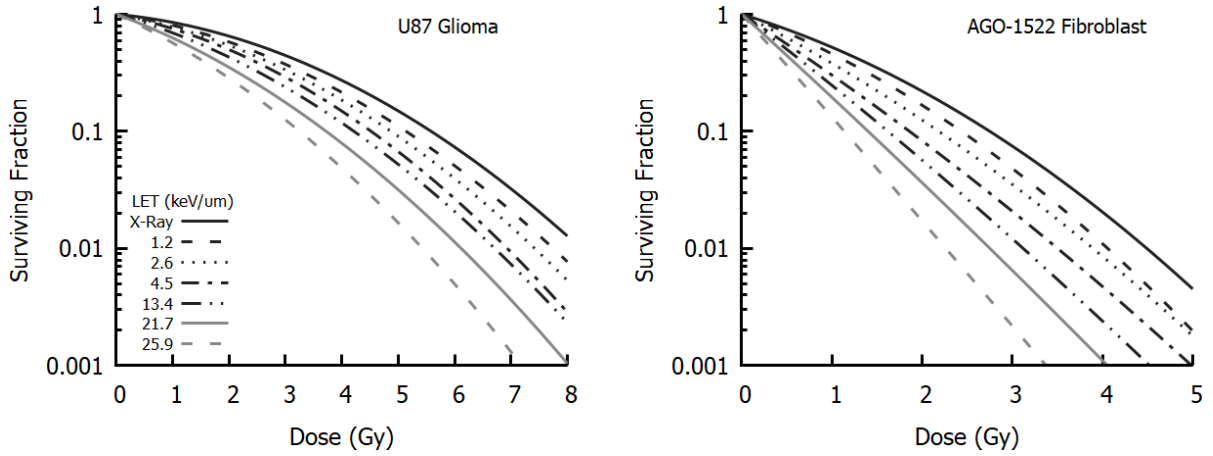

Figure 1.21: Surviving curves for two different cell lines: brain cancer cell U87 (left) and fibroblast (right). The figures show the effect of different proton LET and conventional X-rays on the survival curve. Taken from McMahon et al. (2019) [135].

radiations are also inefficient because of the "overkill effect", i.e. an excessive amount of energy is deposited in a given cell and, therefore, too many DSBs than those actually required for cell killing are produced in the same cell. As a consequence, it is less likely that other cells are killed for a given delivered dose.

Since it is a direct measurement of cell sensitivity, RBE is a key *in vitro* radiobiology parameter to evaluate the effect of new dose delivery approaches. Its assessment has been indeed the main concern of most radiobiology experiments with laser-plasma accelerated particles, with the aim of evaluating their suitability for radiation biology or medical applications, as it will be discussed in section 2.4.

1.5 Temporal aspects of dose delivery

The therapeutic benefit of radiotherapy has considerably improved over the last decades thanks to technological innovation, involving beam control techniques, imaging and dosimetry precision and simulation tools. All together, these advances have led to major improvements in dose conformity, allowing the reduction of the dose deposited in healthy tissues. In particular, target definition has become more and more accurate as a result of significant developments in high-resolution imaging techniques such as Positron Emission Tomography (PET), Magnetic Resonance Imaging (MRI) and Computed Tomography (CT-scan) [44, 158]. In addition, such techniques allowed the development of Image Guided Radiation Therapies (IGRT), widely used to treat tumours that are prone to movement during the irradiation (such as lung cancer) or to carefully monitor

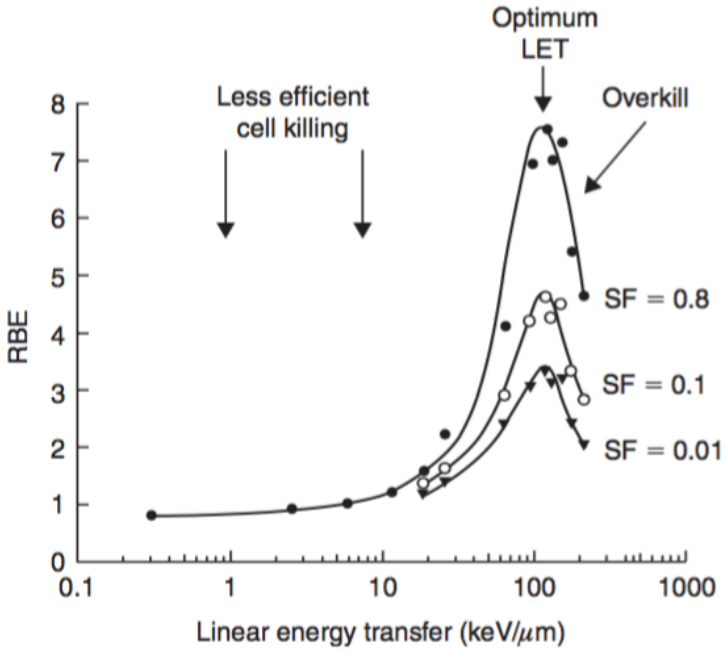

Figure 1.22: Dependence of RBE on LET for different values of SF, taken from G. W. Barendsen (1968) [15]. The reference radiation use to quantify the RBE is 250 kVp X-rays.

tumour shape during high precision radiotherapy techniques such as protontherapy. In addition, the use of protons has brought great benefits to the treatment of those tumours close to critical organs, such as brain, spinal cord and prostate, and might decrease secondary effects in pediatric tumour radiotherapy. In parallel with technological advances, medical and biological studies continuously bring to the clinics new strategies to reduce healthy tissue toxicity. Such strategies include, for example, drug administration to inhibit molecules involved in cell death mechanism (Inhibitors of pro-apoptotic molecules such as p53) and anti-oxidant therapies to restore redox equilibrium immediately after the treatment [140].

Despite these progresses, damage on healthy tissues still remain an important dose-limiting factor in treatments of highly radioresistant tumours. In this scenario, further increase of the therapeutic index may come from novel approaches in dose delivery modalities. In particular, the effects of dose rate modulation, irradiation time and fractionation have not been extensively explored outside typical time scales of clinical radiotherapy.

1.5.1 Fractionation and dose rate modulation in clinics

Clinical radiotherapy treatments employ continuous beams with typical dose rates of the order of 1 Gy/min. The effect of dose fractionation and dose rate modulation has been

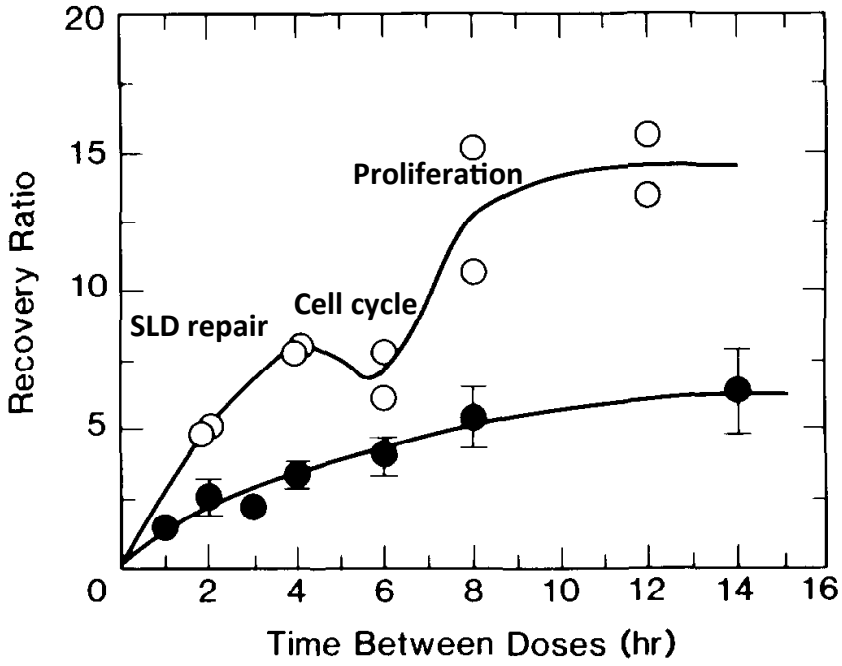

Figure 1.23: Increase of recovery ratio as a function of the interval between two dose fractions for A549 (black dots) MCF7 (white dots) human tumour cells, taken from Matthews (1989) [131]. The recovery ratio is defined as the ratio between cell survival after two dose fractions and after a unique fraction. For the MCF7 cells we can observe both the positive effect of SLD repair and proliferation processes and the counterproductive effect of cell-cycling.

extensively investigated in clinics for exposure times and intra-fraction intervals ranging from minutes to hours, a time scale comparable with the time required for cells to start repairing processes. Clinical approaches based on dose fractionation[15] take advantage of the greater ability of healthy tissues to recover from sub-lethal damage events[16] compared to cancerous tissues. For example, if the same dose is delivered in two fractions separated by few hours, the cell survival increases (see Fig. 1.23) because of recovery processes taking place during the intra-fraction interval. Such processes are due to different phenomena occurring at different time after the first fraction. Initially, the increase in cell survival in a split-dose irradiation results from the prompt repair of Sub-lethal Damages (SLDs). After many hours, the regeneration capacity of proliferating cells also contributes to the increase of cell survival. Many other phenomena such as cell cycling and reoxygenation play a role in the sensitivity to the intra-fraction interval[17]. A detailed discussion of all

[15]Standard fractionation protocols in clinics apply a dose per fraction of about 2 Gy with a delay between fractions of about 24 hours.

[16]Sub-lethal damage (SLD) is defined as cell damage that can be easily repaired unless an additional SLD is generated before the end of the repairing process.

[17]Cell cycle is a counterproductive effect for the recovery capability. The cells that die after the first fraction are principally those that are in a more sensitive phase of the cell cycle. There is then a temporary

phenomena related to fractionation techniques in clinics, which would be out of the scope of this introduction, can be found in E. J. Hall (2012) [92].
Reducing the dose rate is comparable to a fractionated dose delivery with an extremely high number of fractions. By the same token, the longer exposure time of a low dose-rate irradiation eases cell repair processes during the treatment. Therefore, cells are able to repair an SLD before an additional damage is produced in its vicinity. This is the rationale of low dose-rate brachytherapy, which consists in implanting a low dose-rate radioactive source inside or in the proximity of the tumour. Typical dose rates are around few cGy/h and the treatment normally lasts few days [127]. In general, beneficial effects are obtained for dose-rate below 1 Gy/min [91, 150, 59].
What is important to note is that all clinical approaches based on fractionation and dose-rate modulation rely on the different response of normal and tumour tissues at a biological time scale (minutes-hours). The effect of fast dose deposition, i.e. high dose-rate (> 100 Gy/s) and short exposure time ($<$ s), has been under-explored because of the challenges to reach such conditions with conventional accelerators available in clinics [69]. Research in this field is now in rapid evolution thanks to the recent discovery of the FLASH effect.

1.5.2 High dose-rate pulsed irradiation: FLASH effect and LPA beam perspectives

FLASH radiotherapy (FLASH-RT) consists in the ultrafast delivery of a therapeutic dose at a dose-rate several orders of magnitude higher than that typically employed in conventional radiotherapy (CONV-RT). The pioneering study of V. Favaudon et al. (2014) [64] demonstrated that the very short irradiation time ($<$ 500 ms) can remarkably decrease radiation induced toxicity on healthy tissues compared to conventional treatments[18]. In their study, they irradiated mice thorax with 4.5 MeV electrons at conventional dose-rate (0.03 Gy/s) and high dose-rate (40 Gy/s). The harmful effect on mice lungs (pulmonary fibrosis) was starkly reduced with FLASH irradiation. Only a small percentage of mice

radioresistance right after the first fraction, which is lost if the interval between fractions is longer than the time required for cells to cycle and repopulate the fraction of cells that was in the more radiosensitive phase of the cycle. The phenomenon, called "reassortment", is responsible for the slight decrease in the recovery ratio of Fig. 1.23.

[18]The first observations of biological effects of high dose-rate irradiation date back from the '70 [20, 101, 67]. The studies showed an impact of dose-rate on induced hypoxia (lack of oxygen) in normal and tumour tissues. However, this effect was found to be significant only for already slightly hypoxic cells (which would imply a detrimental effect on tumours) and machines delivering such high dose-rates were not available at the time [198]. For these reasons, research in this field did not evolve until the pioneering study of Favaudon et al. (2014) [64].

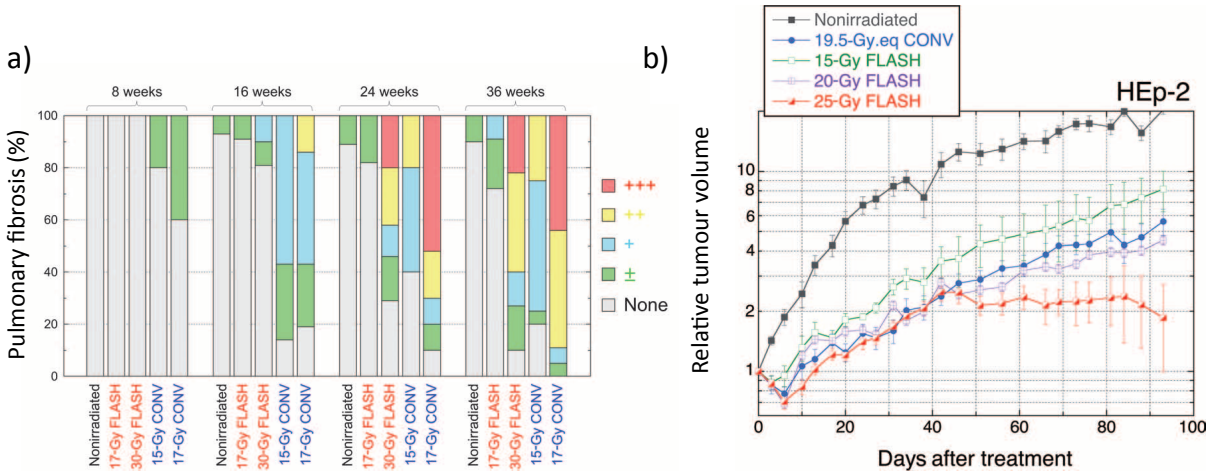

Figure 1.24: Images taken from the pioneering work of V. Favaudon et al. (2014) [64] demonstrating the FLASH effect in mice. a) Time and dose dependence of pulmonary fibrosis after FLASH and conventional irradiation of mice thorax. The colors indicate the severity of the induced fibrosis. b) Response of Hep-2 tumour xenografts (head and neck cancer) implanted in mice to FLASH and conventional irradiation. The graph reports the relative tumour growth as a function of the time after treatment. The tumour response to 19.5 Gy CONV is similar to the response to 20 Gy FLASH, indicating that the harmful effect on tumours is maintained with FLASH irradiation.

irradiated with FLASH-RT presented moderate pulmonary fibrosis 36 weeks after irradiation, while 100% of mice irradiated with CONV-RT presented moderate and severe lung fibrosis, as shown in Fig. 1.24.a. In the same study they also showed a comparable tumour-control efficacy of FLASH-RT and CONV-RT on breast and head and neck carcinoma established in mice (Fig. 1.24.b), demonstrating that high dose-rate irradiation can increase the differential response between normal and tumour tissues.

The potential benefits that FLASH-RT could bring to present days radiotherapy have motivated numerous studies in recent years to replicate the FLASH effect on other tumors and animals. To date, the beneficial effect of FLASH-like irradiation on healthy tissues have been proven on mice brain (neurocognitive functions) [142] and on pig and cat skin [199], leading to Dose Modifying factors (DMFs)[19] between 1.13 and 1.8 [198]. Notably, many studies reported the same tumour response compared to CONV-RT for different tumour types [215, 141, 121]. All studies demonstrating sparing of healthy tissues have been performed with low-energy electrons produced by dedicated LINAC prototypes.

[19]The Dose Modifying Factor (DMF) is defined as the relative dose required to produce a given effect. In this case, DMF is used to compare the harmful effect on healthy tissues of high dose-rate to clinical dose rates. A DMF > 1 would mean an increased therapeutic index, provided that the harmful effect on tumours is maintained.

However, a recent study demonstrated beneficial effects of FLASH-like irradiations with X-rays [143].
Although the number of studies on FLASH effect has grown exponentially over the last few years, the role of the pulsed beam parameters in triggering the FLASH effect still needs to be elucidated. The major limit of the existing preclinical studies is indeed the lack of consistency in the beam parameters used to trigger FLASH effect, as shown in Fig. 1.25.a. These parameters are schematically shown in Fig. 1.25.b and listed below [205]:

- Total irradiation time
- Mean dose rate, defined as the total delivered dose divided by the irradiation time
- Dose per pulse (DPP)
- Pulse duration
- Dose rate within the pulse, defined as the DPP divided by the pulse duration
- Pulse repetition rate

Although systematic studies addressing the relative importance of such parameters have not yet been reported in literature, it is widely agreed that the therapeutic dose (few Gy) must be delivered in less than hundreds of milliseconds, regardless of the number of applied pulses. As far as the dose rate is concerned, FLASH effect is evident at a mean dose-rate higher than 100 Gy/s, although it was also induced with 30 Gy/s in some studies.
The vast majority of the studies have been performed using microsecond pulses at dose-rates within the pulse in the order of 10^5-10^6 Gy/s. Recent experiments performed with protons at dose rates within the pulse of 10^3 Gy/s failed to produce a FLASH effect [22]. B. P. Venkatesulu et al. (2019) [196] showed an even worse effect of high-dose rate irradiation on the development of gastrointestinal syndrome in mice compared to CONV-RT, probably due to the mean dose-rate employed (35 Gy/s), not sufficiently high to observe healthy tissue sparing effect. All together, these studies attest the complexity of this phenomenon, which requires further investigation to precisely identify its triggering factors.

Hypothesis on mechanisms underlying the FLASH effect If the parameters triggering the FLASH effect still need to be precisely defined, the underpinning biological and chemical phenomena are not well understood either. Given the relevant role of oxygen

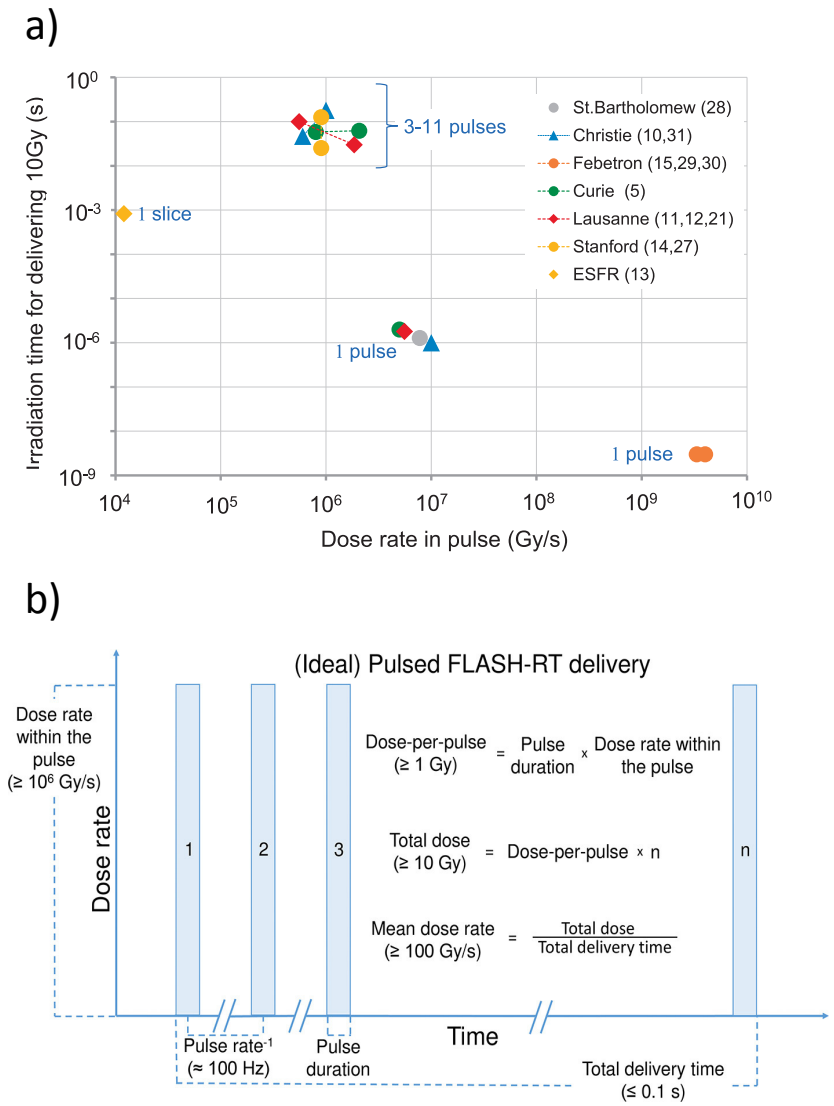

Figure 1.25: a) Conditions to obtain a reproducible FLASH effect. Taken from J. Bourhis et al. (2019) [32]. b) Schematic of the parameters of the dose delivery modality playing a role in triggering the FLASH-effect. Taken from J. D. Wilson et al. (2020) [205].

concentration in the regulation of tissue radiosensitivity (it is well known that oxygen radicals are crucial for indirect DNA damage), it has been suggested that the beneficial effect of FLASH-RT could be due to rapid oxygen depletion following high dose-rate irradiation. In clinical radiotherapy, the exposure time is longer than the oxygen diffusion time and, therefore, the physiological amount of oxygen is continuously restored during irradiation. On the contrary, if the irradiation time is shorter than the time required for oxygen to diffuse and replenish, then a temporary hypoxia and subsequent radioresistance are in-

duced [4]. The maintained toxicity on tumours, which are not completely anoxic[20], may be the result of different redox metabolisms[21] between normal and tumour tissues [187]. In other words, the detrimental effect of temporary induced hypoxia in tumours would be counterbalanced by a reduced ability to remove the high amount of free radicals produced in a short time. The crucial role of oxygen in inducing FLASH effect would also explain the difficulty of reproducing this phenomenon in *in vitro* studies.[22]

Another mechanism that may play a role in the onset of FLASH effect involves a modified immune response. While during a CONV-RT treatment a great portion of circulating T-lymphocytes[23] are irradiated, only a small portion of them is damaged during FLASH-RT. In other words, the short treatment duration of FLASH-RT would preserve the efficiency of the immune response. This hypothesis has also been strengthen by the absence of FLASH effect on immunocompromised animals reported in many studies [140, 215, 32]. It is worth noting that all the mentioned hypothesis are not mutually-exclusive and that the mechanisms behind the FLASH effect is probably a complex combination of all these phenomena.

Although the exact mechanism and parameters triggering the FLASH effect have not been precisely elucidated yet, in 2019 the first patient was successfully treated with FLASH-RT [33], paving the way for further clinical studies.

Laser-plasma accelerated particle perspectives These important results point out the importance of temporal aspects of dose delivery, asking for a deeper understanding of the physico-chemical and biological processes triggered by fast dose deposition. In this scenario, LPA beam's temporal regime might help to shed some light on the radiobiological response at a different time-scale. Altough it is still challenging to reach irradiation times shorter than hundreds of milliseconds (see section 2.2.1 for a detailed discussion), the ultra short pulse duration (fs-ns) and the typical peak dose-rate within the pulse exceeding 10^9 Gy/s allow irradiation conditions extremely different from conventional radiotherapy

[20] Tumours are usually less oxygenated than healthy tissues and therefore feature a higher radioresistance. However, they are not completely anoxic and, therefore, a detrimental effect of FLASH-RT should be expected.

[21] Redox metabolism indicates the oxidation/reduction activity involved in removal of oxidative radicals. Normal tissues have a lower production of oxidative species, thus a higher efficiency in removing the huge amount of free radicals generated in a short time in FLASH irradiation.

[22] Only the study conducted by M. Buonanno et al. (2019) managed to show evidences of FLASH effect on delayed biological effects in *in vitro* cell samples [39].

[23] Lymphocytes (T-cells) are cells of the immune system responsible for discrimination of self from non-self molecules [197] mounting an immune response against these latter. The role of T-cells in tumour response to radiotherapy has been the object of a strong research activity in recent years and it is now widely accepted that they play a key role in tumour control [52].

treatments and, to some extent, even harder than FLASH-RT conditions. Indeed, LPA beams can deliver meaningful doses (cGy-Gy) in a time that is shorter than the time required for radiation-produced radicals to react and diffuse, which may produce unknown effects such as different hydrolysis chemical paths and a modified biological response. In addition, LPA beams can also help identify the key parameters that cause FLASH effect, for example, whether it is the instantaneous dose-rate in the pulse or the average dose-rate of exposure that improves the differential response between healthy and tumour tissues. In conclusion, LPA particles represent a unique tool for fundamental and groundbreaking studies on fast dose deposition radiation biology.

Chapter 2

From laser-plasma accelerated beams to radiation biology

Contents

Overview

Following a brief introduction on the physics of laser-plasma acceleration, this chapter discusses the properties of these particle beams in view of their appplication to radiation biology and presents the techniques mostly used in recent years to control and shape such beams. Section 2.4 then provides an overview of the key results obtained in radiation biology with laser-plasma accelerated electron and proton beams. The chapter finally discusses the results obtained at the SAPHIR facility with laser-plasma accelerated protons.

2.1 Laser-plasma acceleration

Laser-plasma accelerated (LPA) particles are produced by focusing a high power (TW–PW), short (ps–fs) laser pulse onto a solid or gaseous target. Such laser systems have received great attention by the particle acceleration community after the application of the Chirped Pulsed Amplification (CPA) technique to laser pulse amplification by D. Strickland and G. Morou (1985) [188], which allowed a jump in peak power of several order of magnitudes. Before the introduction of the CPA, the peak power of femtosecond lasers was limited to $\sim 10^9$ W by non-linear effects and damages on the amplifier optical components. To avoid such effects, in the CPA the laser pulse leaving the oscillator is stretched in time through optical separation of its spectral components. The stretched pulse preserves its original spectrum and total energy but, thanks to the longer duration, can be safely amplified up to higher energies, pushing further the limits on the maximum allowed peak intensity by a factor of $\sim 10^6$. After amplification, the pulse is then compressed almost to its original duration. This technique paved the way towards commercially available table-top lasers capable of reaching a peak power of hundreds of terawatt in femtosecond pulses, marking the beginning of the laser-plasma acceleration era.

Laser interaction with matter The interaction of a high power laser pulse with matter can lead to ionisation if its intensity exceeds 10^{10}-10^{12} W/cm^2 (multiphoton ionisation threshold). Above such intensity, electrons can be freed from their atoms, thus turning the target into a plasma. When a plasma is traversed by an electromagnetic wave, electrons are accelerated by the electric field whereas heavier ions remains at rest because of their heavier mass. This lead to charge separation and consequent electron oscillation to restore the neutrality at a plasma frequency ω_{pe} that depends on the plasma electron density n_e, according to the following formula:

$$\omega_{pe} = \sqrt{\frac{n_e e^2}{m_e \varepsilon_0}} \tag{2.1}$$

It can be demonstrated that an electromagnetic wave can not propagate into a plasma if its frequency ω is lower than the plasma frequency, since electrons shield the oscillating electromagnetic field. In other words, an electromagnetic wave can propagate in a plasma only if its electron density is lower than the critical density n_c, given by:

$$n_c = \frac{m_e \varepsilon \omega^2}{e^2} \tag{2.2}$$

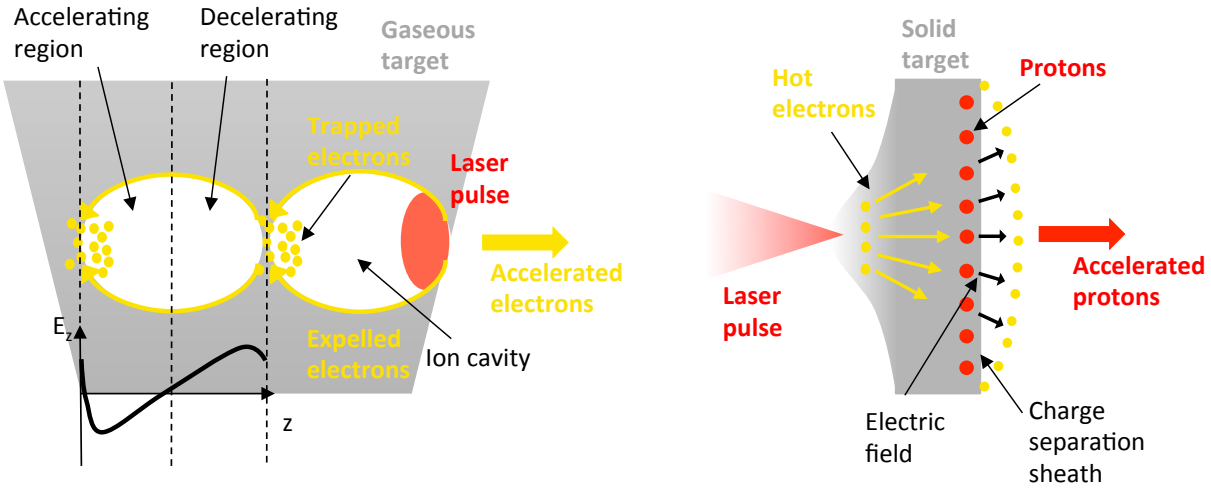

Figure 2.1: Laser-plasma acceleration of electron and proton beams. Left: schematic of electron acceleration through interaction of a relativistic laser pulse with an underdense plasma leading to the generation of a travelling electric field in the pulse wake. In the bubble regime, electrons are expelled from the laser path through the ponderomotive force and a travelling ion cavity is created. Electrons that are injected in the rear side of the bubble are accelerated as long as they reach the decelereting region. Right: schematic of TNSA proton acceleration. The laser interacts with the plasma created by the laser prepulse on the illuminated surface of a thin foil and accelerates electrons mainly in the forward direction. Some of the electrons escape in vacuum, generating a charge separation on the rear side of the target. The high electric field associated accelerates protons in the forward direction.

The plasma density is a key parameter in laser-plasma acceleration, since the different mechanisms of energy transfer from the laser to matter depend on whether the created plasma is under-dense ($n_e < n_c$) or over-dense ($n_e > n_c$).

Particle generation Electrons are accelerated by a travelling electric field generated by the laser pulse propagation in an underdense, gaseous target. When the laser pulse propagates through a gas, the ponderomotive force, proportional to the laser intensity gradient, can excite large amplitude plasma waves. This creates a longitudinal travelling electric field in the wake of the laser beam that moves forward with a phase velocity close to the speed of light. If the laser intensity is high enough to accelerate electrons up to relativistic energies, the ponderomotive force tends to expel all electrons from its wake, thus creating an ion cavity with no electrons (Fig. 2.1.a). In this "bubble structure", electrons can be accelerated if they are efficiently trapped in the accelerating region of the electric field created inside the travelling cavity. During past years, numerous injection techniques have been tested and are to date succesfully used to produce electron beams. They differ in the way electrons are injected and trapped into the accelerating field of the

plasma wave. Among them, ionisation-injection is an easy and efficient method to produce energetic electrons [153, 83, 78]. In this regime, electrons initially at rest in the bubble are ionised and gain enough energy in the accelerating field to remain trapped. Adding high-Z atoms in the gas jet enable tuning of the electron spectrum and charge [134] and, in particular, the use of purely high-Z gas have been shown to generate high-charge electron beams [86]. Other techniques make use a particular gas density profile to trap electrons for a longer distance inside the accelerating side of the bubble [72, 185, 37, 190] or a counter-propagating laser-pulse to inject electrons at a precise position with respect to the travelling wave and generate quasi-monenergetic electron bunches [62, 63]. A review of the electron acceleration techniques can be found in Malka et al. (2012) [125].
Contrary to electrons, protons are efficiently accelerated by a static or quasi-static electric field generated in a solid foil target. When the laser pulse is focused onto a thin foil (∼µm), a plasma slab is created by the laser prepulse (Fig. 2.1.b). The scenario is therefore a laser-pulse interacting with a pre-plasma density gradient generated on the target surface. The laser propagates until the density of the pre-plasma reaches the critical density n_c and then it is reflected back. Several acceleration mechanisms can take place depending on the interplay between laser and target parameters. In most of the experiments performed with TW-class lasers, the dominant regime is the Target Normal Sheath Acceleration (TNSA) [204]. In TNSA, proton acceleration is mediated by hot (MeV) electrons created at the illuminated surface, that absorb the laser energy and propagate through the target bulk, driving the plasma expansion [144, 145]. A fraction of these electrons reach the rear side of the target and escape in vacuum, forming a dense charge-separation sheath. The high electric field associated (∼TV/m) ionises atoms located at the rear surface and accelerates protons coming from hydrogen-rich impurities in a cone along the axis perpendicular to the foil surface [14]. A review of the mechanisms of proton acceleration by laser-plasma interaction can be found in Macchi et al. (2013) [124].

2.2 Overview of LPA beam properties

This section discusses the properties of Laser-Plasma Accelerated (LPA) particles, with a special emphasis on the aspects relevant to their use in radiation biology. Table 2.1 includes a list of typical beam properties (spectrum and charge) and dosimetry parameters (dose and dose-rate) obtained in radiobiology or dosimetric characterisation experiments with LPA beams reported in literature or presented in this thesis. It provides an overview of the capabilities of various laser systems in terms of the properties of the accelerated

particles and of the dosimetric conditions at the biological target. Two cases relevant for radiation biology applications are distinguished for both electrons and protons:

- Laser-plasma accelerated electrons

  I : $\sim$ 100 TW lasers running at 10 Hz and delivering few joules at the target.

  II : $\sim$ 1 TW lasers running at 1 kHz and delivering few millijoules at the target.

- Laser-plasma accelerated protons

  III : $\sim$ 100 TW lasers running at 10 Hz and delivering few joules at the target.

  IV : $\sim$ 100 TW lasers running at $\sim 10^{-3}$ Hz and delivering tens of joules at the target.

Proton and electron sources driven by terawatt lasers running at 10 Hz (I and III) have been the most widely used because of the large commercial availability of such laser systems. On the other hand, kHz electron sources (II) and low repetition rate, high-energy-laser-driven proton sources (IV) have been under-explored. These cases are briefly discussed in the following sections and are adressed in details in the following chapters of this manuscript.

2.2.1 Temporal properties

As mentioned in previous sections, the key asset of LPA beams is the extremely different temporal structure in comparison with conventional accelerators used in clinics. Clinical accelerators such as synchrotrons, cyclotrons and LINAC operate in a continuous or quasi-continuous regime[1], with an average dose rate of Gy/min and typical exposure times of few minutes. On the contrary, LPA beams are produced in separate bunches, whose duration after spatial stretch is typically around tens of femtoseconds for electrons and few nanoseconds for protons. Each bunch can deliver, depending on the acceleration conditions, between $\sim$ 1 mGy and $\sim$ 1 Gy on a biological sample[2] (see Fig. 2.2). They can therefore reach peak dose-rates within the pulse in the order of 10^9 Gy/s, whereas the mean dose rate and the total irradiation time depend on the interplay between repetition rate and dose-per-pulse (DPP).
Laser-plasma accelerated electron's (LPAE) repetition rate is limited by the frequency of

[1] The interval between bunches is negligible compared to the pulse-width (Synchrotrons and cyclotrons) or the dose delivered in a single bunch is a marginal fraction of the total prescribed dose (LINAC). They can therefore be considered continuous beams for the purpose of radiotherapy [181].

[2] Considering a $1 \times 1\,\mathrm{cm}^2$ irradiated surface.

Table 2.1: Table summarizing laser-plasma accelerators relevant to radiation biology applications.

		ELECTRONS	
		(I) 10 Hz, J lasers	**(II) kHz, mJ lasers**
Beam parameters	Spectrum	$1 - 10^2$ MeV tunable	few MeV
	Charge	$10^{-2} - 1$ nC	$1 - 10$ pC
Irradiation conditions	**Dose per pulse**	**$1 - 10^2$ mGy/pulse**	**$10^{-1} - 1$ mGy/pulse**
	Irradiated surface	$10^{-1} - 1$ cm^2	$10^{-1} - 1$ cm^2
	Peak dose-rate	**$10^9 - 10^{11}$ Gy/s**	**$\sim 10^7$ Gy/s**
	Repetition rate	$1 - 3$ Hz	1 kHz
	Mean dose-rate	**~ 1 Gy/min**	**~ 1 Gy/s**
References		[78, 10, 119, 150, 21, 147], section 5.5	[88], Chapter 6
		PROTONS	
		(III) 10 Hz, J lasers	**(IV) 10^{-3} Hz, $10^1 - 10^2$ J**
Beam parameters	Cut-off energy	< 20 MeV	< 20 MeV
	Charge	∼nC	$10 - 10^2$ nC
Irradiation conditions	**Dose per pulse**	**$10^{-1} - 1$ Gy/pulse**	**~ 10 Gy/pulse**
	Irradiated surface	$10^{-1} - 1$ cm^2	$10^{-1} - 1$ cm^2
	Peak dose-rate	**$\sim 10^8$ Gy/s**	**$> 10^9$ Gy/s**
	Repetition rate	~ 1 Hz	Single shot
	Mean dose-rate	**$10 - 30$ Gy/min**	**$> 10^9$ Gy/s**
References		[210, 211, 213, 116, 163], sections 3.1.3 and 4.1	[58, 68, 93], section 4.2

the laser itself. Different acceleration methods have been developed and succesfully used during past years with a wide range of laser systems, from low-energy, high frequency (mJ, kHz) to high-energy, low frequency (J, Hz) lasers. In particular, radiobiology experiments have been conducted with $\sim$ 100 TW class lasers delivering few joules at the target and running at 10 Hz, which are able to accelerate an electron charge per bunch between tens of pC to few nC [77, 147, 86, 78, 13]. With such conditions, doses in the order of tens of mGy over a $\sim$ 1 cm^2 surface have been obtained, leading to typical dose rates in the order of Gy/min (Section (I) of Table 2.1) [78, 10, 118, 150, 21, 147].
High repetition rate electron sources driven by low-energy (1-10 mJ/pulse), kHz lasers have been developed in last years [96, 178, 88]. Such lasers are able to accelerate few pC per bunch, thus allowing the reach of DPP around 1 mGy/pulse and mean dose-rates around Gy/s (Section (II) of Table 2.1). The high repetition rate is the key asset of these sources and an attractive feature for medical applications since it improves the beam stability between irradiations. In fact, a high number of shots ($\sim 10^3$-10^4) need to be

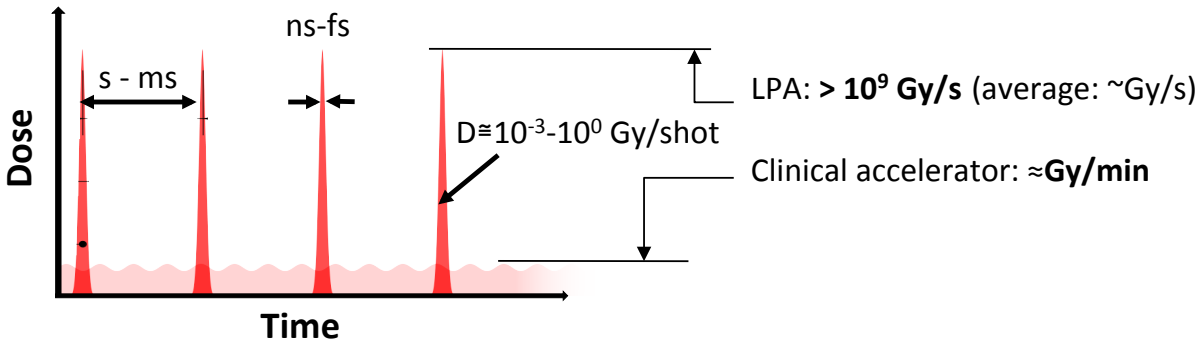

Figure 2.2: Temporal structure of laser-plasma accelerated beams compared to clinical beams.

integrated to reach the desired dose, which reduces the effect of shot-to-shot charge and pointing instabilities on the final dose distribution. Radiation biology experiments were performed during this thesis with the kHz Salle Noire laser system at the LOA and are described in Chapter 6.

Regarding laser-plasma accelerated protons (LPAP), the most limiting factor for the repetition rate is, besides the laser repetition rate itself, the replacement of the solid target that is physically destroyed after each shot. Typically, the thin foil target is inserted in a plate containing a set of holes. After a shot, the target holder moves and positions the next hole in the laser focus, which limits the current repetition rate at around $\sim$1 Hz[3]. Similarly to electrons, $\sim$ 100 TW lasers have been mostly employed in radiobiology experiments with LPAP. As shown in section (III) of Table 2.1, with 10 Hz class lasers delivering few joules at the target, DPP between 0.1 Gy and 1 Gy with field of few mm^2 up to 1 cm^2 have been obtained, leading to mean dose-rates around a few tens of Gy/min (section 2.5 and 4.1) [210, 211, 213, 116, 163]. An attractive option for radiation biology experiments is represented by high-energy lasers delivering tens of joules at the target, which are able to accelerate a proton charge per bunch in the order of tens of nC (section (IV) of Table 2.1). The high charge available at the source allow the delivery of a therapeutic dose in a single pulse, thus reaching irradiation conditions even harder than FLASH-RT, with a mean dose-rate (equal to the peak dose-rate) in the order of 10^9 Gy/s and an irradiation time in the order of few nanoseconds (see section 4.2).

[3]Various solutions to increase the LPAP repetition rate are under investigation and include the use of solid hydrogen, cryogenic targets or liquid jets [173].

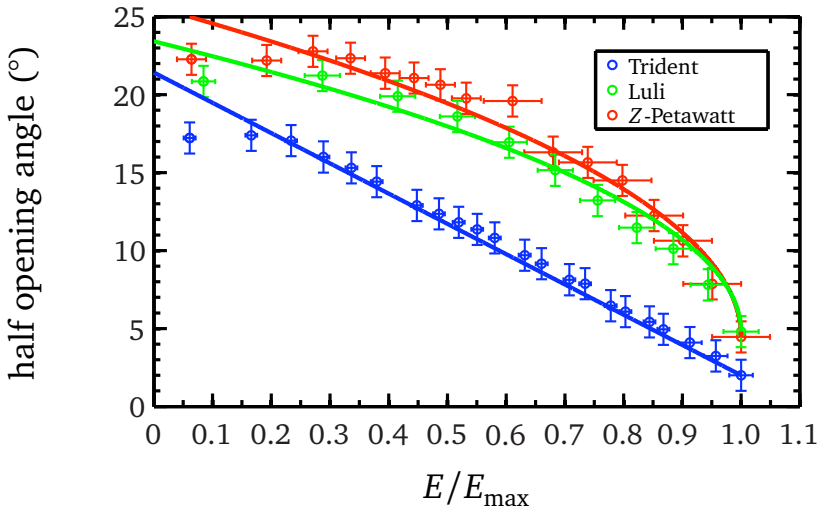

Figure 2.3: Typical energy-dependent divergence of laser-plasma accelerated protons. Taken from M. Roth (2016) [174].

2.2.2 Spectral and spatial properties

The spectral properties of LPA beams depend on numerous parameters such as laser intensity, target properties and type of acceleration mechanisms.

Regarding TNSA protons, the spectrum has an exponential shape whose characteristic slope and maximum energy (cut-off energy) depend on the interplay between laser intensity and target thickness and composition. The maximum proton energy achieved with the most advanced laser systems available to date does not exceed a few tens of MeV, which limits their radiobiology application to *in vitro* or *in vivo* studies on millimiter thick targets such as zebrafish embryos [176]. The divergence at the source is in the order of several degrees and decreases with the proton energy (Fig. 2.3). As a consequence, LPAP beams require the use of a transport system to maximise the transported charge at the irradiation site in air.

Regarding LPAE, low-charge, quasi-monoenergetic high-energy (hundreds of MeV) electrons [138, 63, 190] and high-charge, low-energy (few MeV) electrons with exponential spectrum [86] have been obtained with 100 TW class lasers (Fig. 2.4). Both type of sources already meet the requirement for *in vivo* irradiation in terms of available energy. Furthermore, they feature an extremely small divergence at the source (few milliradians) compared to protons, which allows direct irradiation of biological samples without the need of transport systems [150, 119]. The major limit of such beams is the pointing instability at the source in the order of the divergence, related to non-linear phenomena occurring during the interaction of the laser pulse with the under-dense gaseous target.

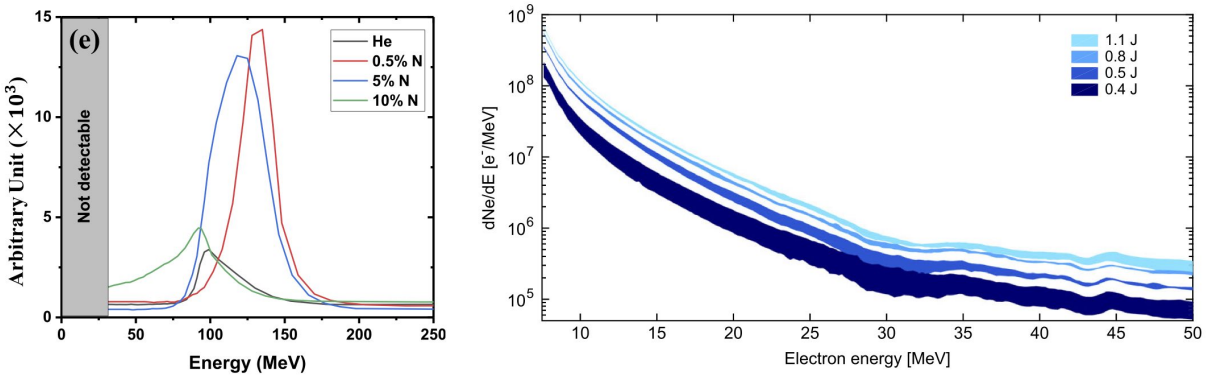

Figure 2.4: Typical spectra obtained with TW class lasers through high-Z ionisation injection. Left: typical low charge, quasi monoenergetic electrons obtained with different gas mixtures. The charge below the red and blue curves is respectively 18 pC and 21 pC. Taken from M. Mirzaie et al. (2018) [138]. Right: typical high-charge, low energy electrons obtained with a pure argon gas jet. The total charge above 7 MeV is 250 pC (1 nC considering also the spectrum below 7 MeV according to simulations). Taken from E. Guillame et al. (2015) [86].

This means that the beam spot on the biological target can move from one shot to another over a distance equal to or greater than its dimension. This aspect may be relevant in low repetition rate, high charge LPAE beams, since irradiation is performed by integrating a limited number (10-100) of shots and, therefore, the dose distribution at the target between irradiations may vary considerably. On the contrary, the effect of shot-to-shot pointing instability can be reduced with kHz electron beams, as previously discussed.

2.3 Transport and spectral tailoring

Since LPAE feature a small divergence at the source, they have been previously used for direct irradiation of biological samples without transport systems. In addition, thanks to their smooth depth-dose profile and higher penetration depth compared to protons, they do not necessarily require spectral shaping to perform irradiation of thin biological samples.

On the contrary, LPAP can not be directly used to irradiate biological samples for a number of reasons. Firstly, the large divergence at the source requires the use of a transport system to collect as much charge as possible and to transport it to the biological sample. Secondly, the transport system becomes crucial to perform spectral shaping required for volume irradiation. As explained in section 1.3, spectral tailoring is indeed necessary to modify the relative yield of the spectral components and generate a flat Spread-Out Bragg Peak (SOBP) by weighing the contribution of the individual

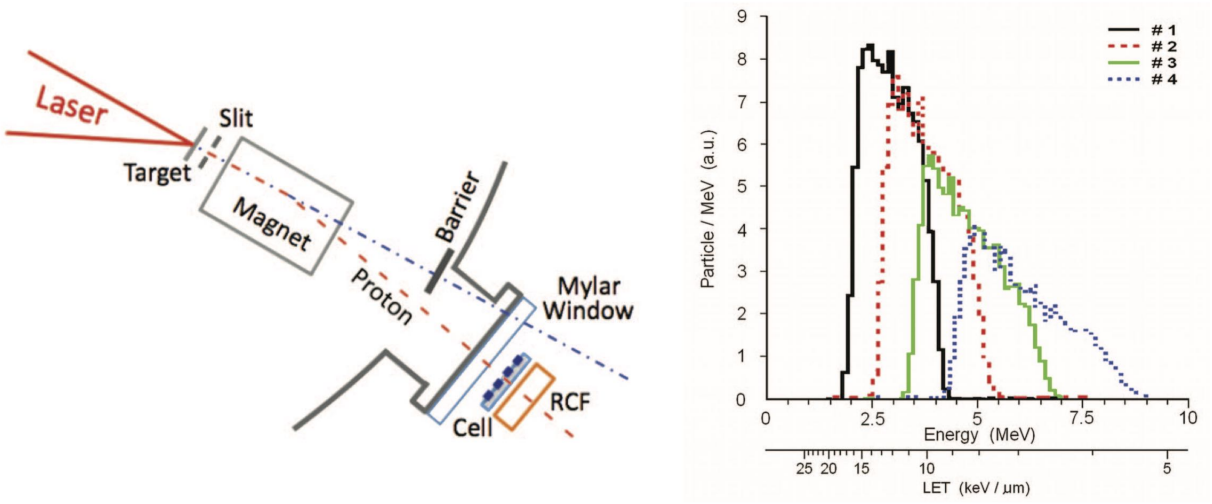

Figure 2.5: Left) set-up of biological sample irradiation with a dipole magnet for spectral selection. Right) spectra reaching the four biological sample and corresponding LET distribution. Taken from D. Doria et al. (2012) [58].

Bragg peaks on the depth-dose profile. Therefore, when used to irradiate thick biological targets, LPAP beams must be spectrally and spatially shaped before reaching the sample, similarly to what is done for clinical protons. In this case, the availability at the source of a polychromatic spectrum eases the realization of a uniform depth-dose deposition (see section 4.2).
In this section, we briefly review the transport techniques used in the last decade in applications of LPAP to radiation biology.

Depending on the application, many transport systems have been proposed and succesfully tested during the last years. Dipoles were largely employed for first irradiation experiments, both in single magnet configuration [210, 116, 68, 24, 58] and in the chicane configuration [211]. A typical set-up, employed by Doria et al. (2012) [58], is shown in Fig. 2.5. The main advantage of using a dipole is the spatial separation of energy components, which enable irradiation with small spectral windows and, in turn, reduction of the ΔLET at the biological sample. In addition, the use of bending magnets prevent electrons and x-rays (generated simutaneously with protons during laser-plasma interaction) from reaching the biological sample. Furthermore, thanks to the proton exponential spectrum, such approach enables dose escalation essay in a single irradiation by placing the biological samples at different positions after the dipole magnet (see Fig 2.5). However, each biological sample would be irradiated with a different LET distribution, which can have a non negligible effect on cell-survival for proton

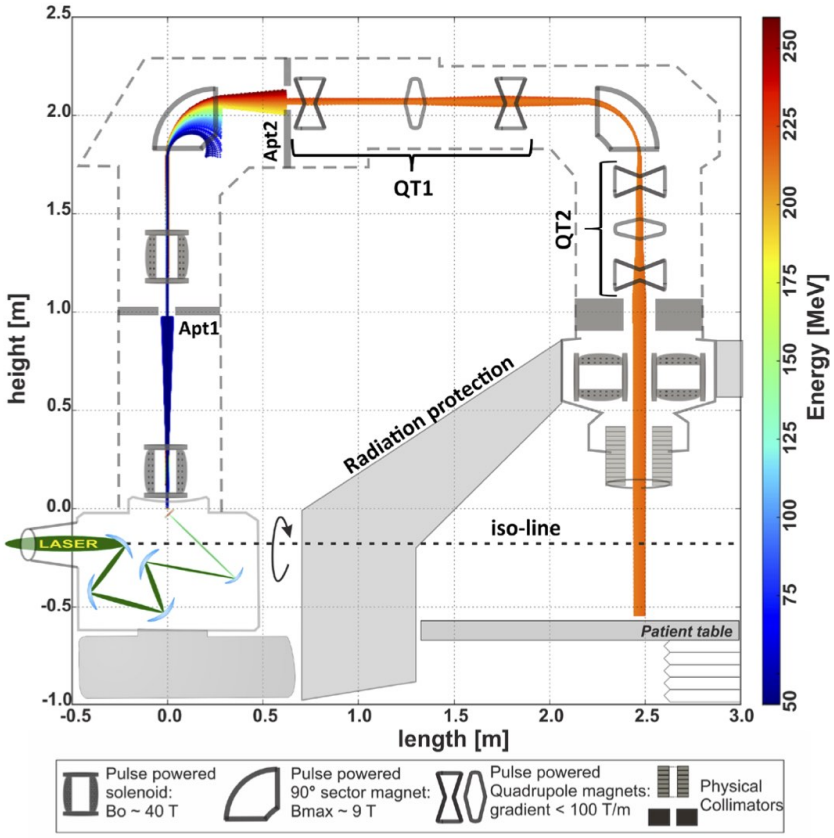

Figure 2.6: Schematic design of the 360° rotatable gantry designed by U. Masood (2017) [130]. The design includes the laser-target interaction chamber, the transport beamline composed of pulsed magnets and the patient treatment site.

energies close to the Bragg-peak. Since bending magnets do not reduce the initial beam divergence, the major disadvantage of such system is the low transport efficiency [162]. In addition, bending magnets alone can not be used for 3D irradiation, as a large, transversally homogeneous spectrum is required to generate a flat SOBP.

Focusing systems such as quadrupoles and solenoids have been recently used to overcome the limits of dipoles and conceive complex dose delivery strategies [100, 99] for clinical applications. A set of four PMQs has been recently tested at the LOA [183] and used for the radiation biology experiments described in section 2.5. Similar PMQs will be part of the ELIMED transport beamline [172], which will be the first European facility entirely dedicated to radiation biology applications of LPAP. Pulsed quadrupoles and solenoids have been also used for irradiation experiments [213] and theoretic studies on proton Gantry (see Fig 2.6) for future clinical applications [40, 129]. The key advantage of pulsed electro-magnetic focusing systems is the possibility of performing versatile shot-to-shot spectral tailoring by tuning the coil current and, consequently, the induced magnetic

field. This opens up the possibility of more advanced dose delivery methods, such as active beam scanning [130]. Compared to quadrupoles, solenoids have a slightly higher transmission efficiency [98], as they focus the beam on radial direction, whereas the beam defocusing introduced by the first quadrupole of a beamline results in significant particle losses. On the other hand, solenoids are more subject to space-charge effects produced by electrons accelerated together with protons. In fact, these electrons are forced to circulate around the solenoid axis at their smaller gyroradius by the strong magnetic field and interact with protons, focusing them more than what would be expected by single-track simulations [95].
Overall, permanent magnets represent a good solution to shape and adapt the proton beam to the biological target while avoiding the complexity of pulsed electro-magnetic systems. In fact, if on the one hand PMQs are less versatile than pulsed quadrupoles and solenoids, since they require mechanical movement to adjust the configuration of the beamline and obtain different beam parameters, on the other hand they provide a compact and simple solution to obtain high field strenght without the large superconducting systems needed by pulsed magnets to achieve comparable performances.

2.4 Radiobiology with laser-plasma accelerated beams: state of the art

The biological effect of LPA beams on living matter is still being debated. The open question is whether the ultra-high dose-rate can lead to a different biological response with potential benefits on clinical protocol optimisation strategies. It was suggested that the extremely high dose-rate may produce a spatio-temporal overlap of the tracks, which may produce, at a molecular scale, effects similar to those induced by high-LET radiations. Besides, the extremely high dose-rate may also yield different water hydrolysis chemical paths, thus modifying the relative impact of indirect DNA damage on cell killing [77, 167]. To date, the effect of high dose-rate irradiation on living cells has not yet been elucidated. A definitive answer requires systematic radiobiology studies providing a deeper understanding of the complex link between the physical aspects of early events following irradiation and the consequent evolution of biological processes and cell kiling. This section reviews the key results obtained in radiation biology experiments with LPA beams.

Laser-plasma accelerated protons The first preliminary studies conducted by different teams between 2009 and 2011 showed breaking of DNA in *in vitro* human cancerous

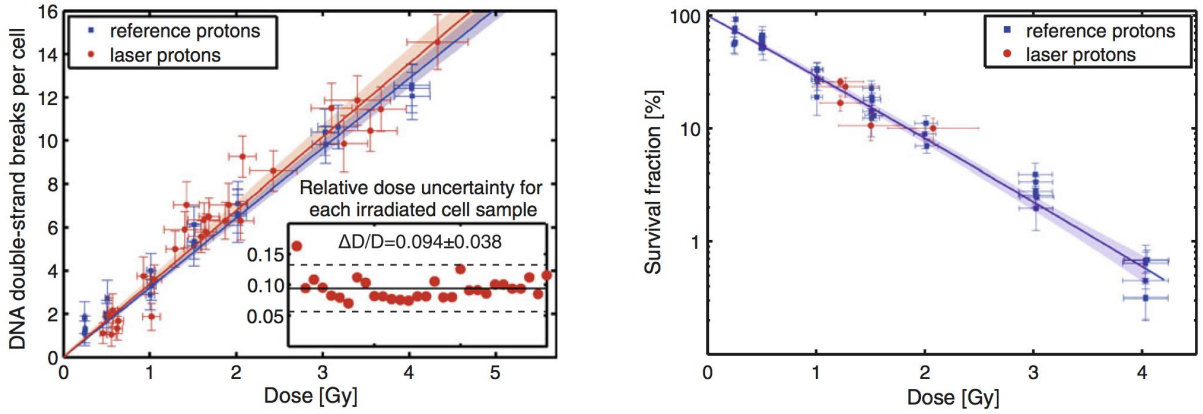

Figure 2.7: Example of DNA double strand breaks (left) and survival fraction (right) after irradiation with laser-accelerated protons compared to conventional protons for human squamous cell carcinoma cell line SKX. Taken from K. Zeil et al. (2013) [213].

cells after irradiation with LPAP beams [210, 116]. In successive studies, three different teams [211, 68, 213, 58] measured cell survival after LPAP irradiation and obtained values close to those of clinical proton beams with the same energies (Fig. 2.7). Thus, they concluded that there is no evidence of nonlinear high dose-rate effects leading to a drastic change in laser-accelerated proton RBE. The experiments conducted at the LOA between 2015 and 2018 with 7.5 MeV LPAP, described in detail in section 2.5, confirmed the results obtained so far. Precisely, no significant difference in DNA double strand breaks and cell survival was found compared to clinical protons. However, we showed that variation of the repetition rate of proton bunches produces cell survival oscillation, related to the presence of an active PARP1 protein. This pioneer result indicates that the temporal delivery modality of LPAP bunches can have a great impact on the biological response. Overall, no study showed any substantial difference between LPA and conventional proton radiobiological effectiveness. The legitimate question is why no FLASH-like effect has been detected so far, despite the typical extremely high dose rate in the pulse of 10^9 Gy/s. There could be numerous reasons for that. Firstly, the *in vitro* endpoints chosen to assess the impact of such peculiar irradiation conditions may not be sufficiently representative of the *in vivo* biological effect. Indeed, S. Raschke et al. (2016) [167] demonstrated that, although LPAP show the same RBE of conventional accelerated protons, they generate less nitroxidative stress[4]. They attributed this behaviour to the lower yield of short-lived radicals caused by the extremely high dose-rate. This finding suggests that RBE may not

[4]The formation of azote radicals following irradiation is a well establish cellular endopoint. The generation of reactive radicals contributes not only to indirect DNA damage formation but also to other complex non-targeted effects such as the bystander effect.

be a complete indication of the real outcome of *in vivo* irradiation with LPAP and that further *in vitro* endpoints should be analysed. Secondly, as we explained in section 1.5.2, the effect of high dose-rate irradiation is strongly correlated with physiological conditions and phenomena, such as the oxygen level and the induced temporary hypoxia, which are hard to reproduced in *in vitro* biological samples. Indeed, while first high dose-rate *in vitro* studies showed a sparing effect on healthy cells only at oxygen tension closer to physiological levels [20, 61], all LPAP studies were conducted on cancerous cells and under ambient oxygen concentration (21%), which is higher than the typical physiological concentration (2-9%) [106]. In addition, the role of the immune system in the onset of a FLASH effect is certainly not reproducible in *in vitro* assays and, finally, the irradiation conditions achieved in the aforementioned experiments, i.e. a dose per pulse equal to or less than 1 Gy and an average dose-rate comparable to clinical ones, may not have been sufficient to cause any difference in the radiobiological response[5]. In other words, experiments so far may not have reached the required irradiation conditions for a different biological response to emerge.

Laser-plasma accelerated electrons Contrary to protons, LPAE are already mature for pre-clinical applications in terms of spectrum at the source for *in vivo* studies. As discussed in section 1.3.2, typical electron energies required in clinics range from 4 to 20 MeV and the required dose rate usually ranges from 1 to 10 Gy/min. LPAE may fullfill all these performances. However, because of the higher attractiveness of LPAP related to their potential use as future alternative to protontherapy facilities [38, 126, 120], LPAE received little attention and very few radiation biology experiments have been reported in literature.

The first systematic radiobiology studies were conducted at the JETI laser system [21], where low energy electrons in the range 3-20 MeV were used for *in vitro* irradiation (Fig. 2.8) [119] and for the first and only *in vivo* [150] study. The results, confirmed by more recent *in vitro* studies [10], showed no significant difference between the biological effectiveness of LPAE and of clinical electron beams. As discussed in the previous section, however, these preliminary results may not be exhaustive of the complex phenomena that occur during *in vivo* irradiation and further studies need to be carried out. In addition, the irradiation conditions achieved in the experiments may not have been adequate to produce high dose-rate effects.

Besides the experiments with low-energy electrons, the ability to produce $\sim$ 100 MeV

[5] We remind that the FLASH effect has been observed for average dose-rates higher than 40 Gy/s and dose within the pulse higher than 1 Gy/s

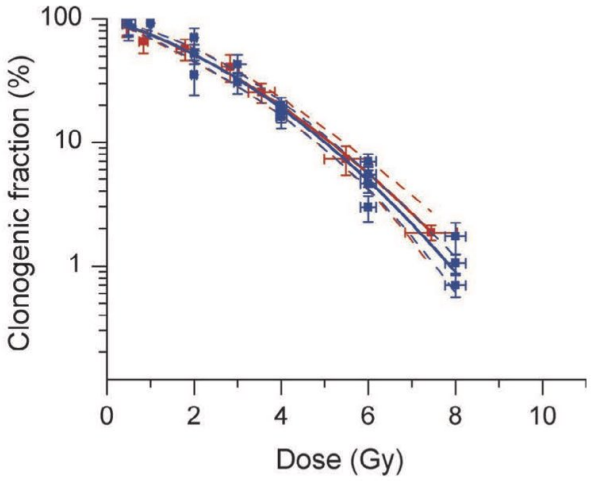

Figure 2.8: Example of survival fraction of tumour cell line FaDu after irradiation with laser-accelerated electrons (red curves) and continuous electron beam delivered by a therapeutic LINAC (blue curves). Taken from L. Laschinsky et al. (2012) [119].

electrons also prompted theoretical studies on the use of Very High Energy Electrons (VHEE) driven by lasers for treatment of deep-seated tumors. The results showed that an adequate dose can be delivered in deep seated tumours [123] with better dose uniformity and sparing of healthy tissues compared to photons [71], but no experimental study has been reported so far.

2.5 Fast dose fractionation experiment at the SAPHIR LPAP beamline

The SAPHIR project began in 2010 with the objective of demonstrating the feasability of employing LPAP beams for extensive radiation biology experiments. After a 4-year period dedicated to the development of the laser system, the optimisation of the proton source and transport beamline, the resulting beam conditions finally enabled a systematic radiobiology study [163, 17], carried out with numerous partnerships with the medical community (the Gustave-Roussy and Curie institutes, the Protontherapy centre of Orsay and the medical physics group of INFN-LNS of Catania). I participated to the last experimental campaign conducted before the end of the project, whose goal was to investigate the impact of proton bunch repetition rate on cell survival. Following a brief description of the beamline, this section presents the obtained results.

Figure 2.9: Pictures of the SAPHIR laser facility and radioprotected irradiation area.

SAPHIR beamline The SAPHIR 200 TW laser system, shown in Fig. 2.9, was a CPA laser-chain powered by a Ti:Sapphire oscillator having a central wavelength of 800 nm, designed to reach an energy per pulse of 6 J before compression at a frequency of 5 Hz. After compression, the laser-pulse featuring an energy of 4 J and a duration of 25 fs, was transported to the interaction chamber placed in the radioprotected area, where the biological samples were irradiated (Fig. 2.9). A detailed description of the CPA laser chain can be found in L. Pommarel (2017) [162]. A 7.5 MeV TNSA proton beam was produced by focusing the laser onto a 5 µm thick titanium foil and was guided towards an exit window by a system of four quadrupoles[6] [182, 183] arranged in a configuration (Fig. 2.10) designed to transport the spectral components around 6 MeV. A PTW Transmission Ionisation Chamber (TIC) model 786 [7], placed after the exit window (see Fig. 2.10), was used to evaluate the dose received by the cell sample and for online monitoring of the shot-to-shot dose fluctuation. The cells were inserted in a plastic holder and placed right after the ionisation chamber on a magnetic support that allowed quick replacement of the sample and reduced positioning errors, as shown in Fig. 2.10.

Irradiation conditions The delivered dose per shot was evaluated by correlating the dose absorbed by the TIC[8] to the dose delivered in the cell sample with Monte Carlo simulations, following the protocol detailed in L. Pommarel (2017) [163]. The 2D profile of the proton beam energy deposition on an image plate placed at the cell position is shown

[6]The two sets have a net bore aperture of 20 mm, a length of respectively 80 mm and 40 mm and an average magnetic field of about 100 T/m. The quadrupoles were designed by the INFN-LNS of Catania in collaboration with SIGMAPHI for the INFN-ELIMED beamline.

[7]The ionisation chamber has a diameter of 155 mm and two sensitive air gaps with 2.5 mm measuring depth. The chamber walls and the electrodes are made of 25 µm thick polyimide (https://www.ptwdosimetry.com/en/products/monitor-ionization-chambers-34014-786/)

[8]The TIC had been prviously calibrated with the proton beam generated by the isochronous cyclotron available at the Institut Curie's Proton Therapy Center in Orsay [163].

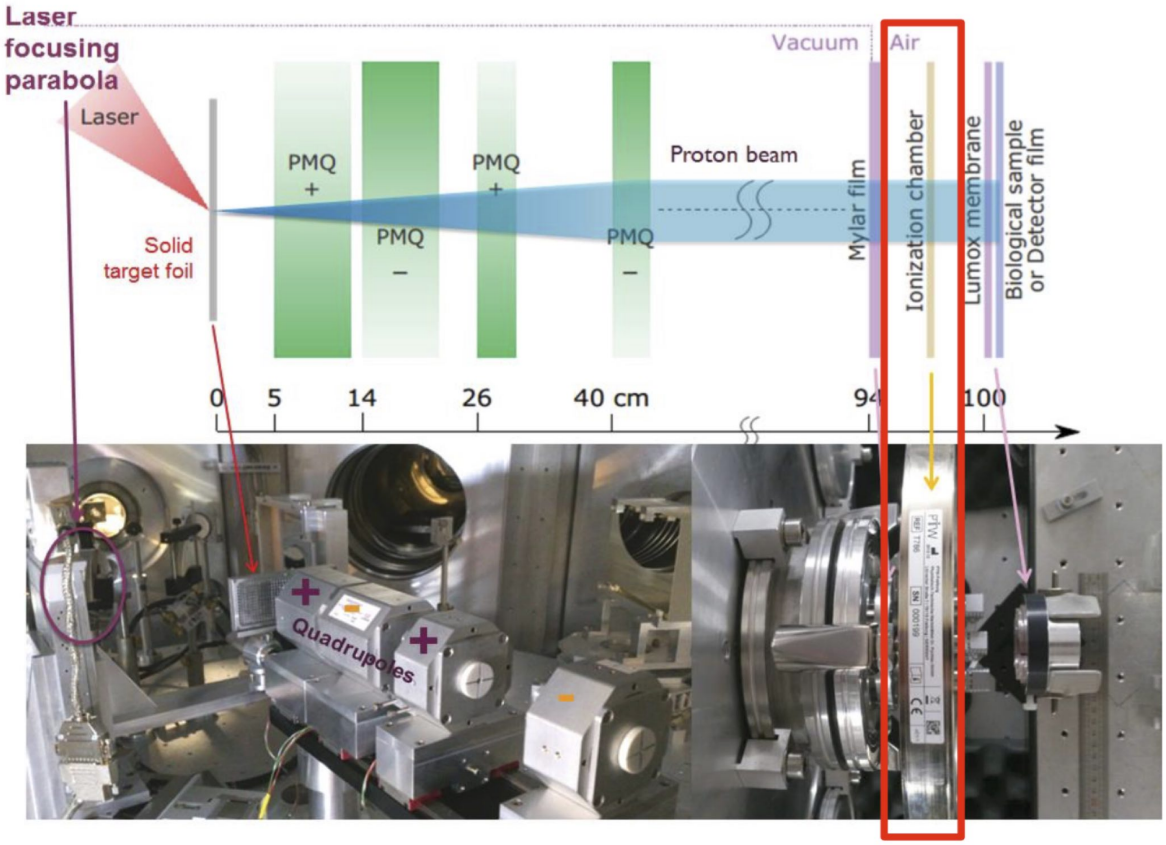

Figure 2.10: Top: schematic of the SAPHIR beamline. Bottom: Picture of the PMQ set-up mounted inside the interaction chamber (left) and lateral view of the transmission ionisation chamber and cell holder placed after the mylar exit window (right). Taken from L. Pommarell (2017) [162].

in Fig 2.11. Only the cells inside the 1.5 cm^2 area delimited by the white rectangle were considered for the biology analysis. The dose delivered over such surface was estimated to 0.72 ± 0.17 Gy/shot, where the 25% error is due to the inhomogeneity of the 2D dose distribution. Altough the error is larger than the acceptable inaccuracy in radiation biology (10%) [55], it is comparable to typical errors obtained in LPAP radiobiology experiments. For example, Hanton et al. (2019) [93] had a dose homogeneity of 15% over a $10 \times 1\,mm^2$ surface whereas Kraft et al. (2010) [116] had a 9% dose homogeneity over a $5 \times 5\,mm^2$. The dose homogeneity obtained at the SAPHIR facility is not the worst, considering that the irradiated surface is about one order of magnitude larger than in the aforementioned experiments. Indeed, one of the challenges in carrying out LPAP radiation biology experiments is to achieve both a high transverse dose homogeneity and

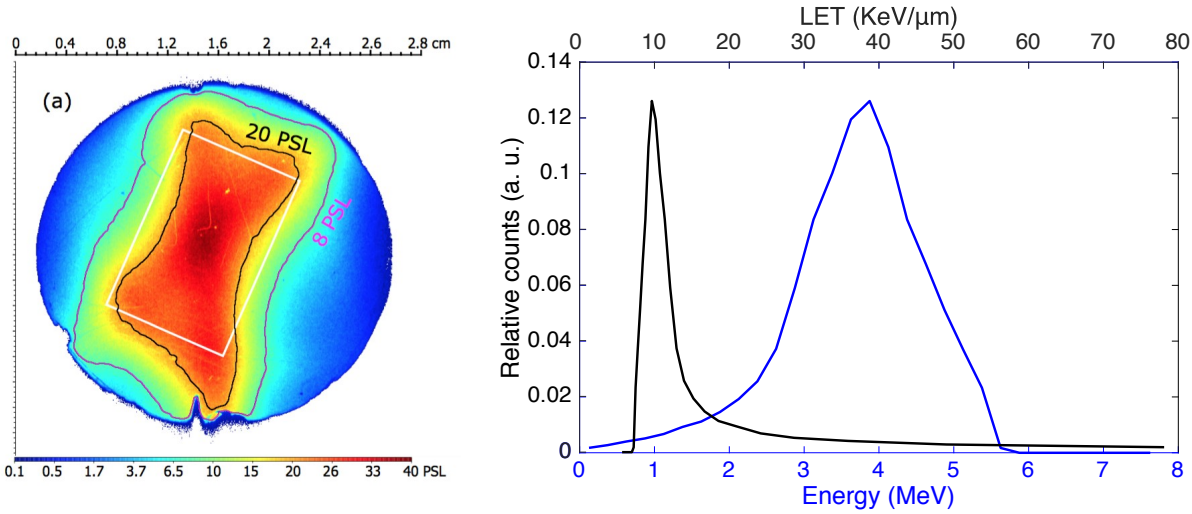

Figure 2.11: Left: 2D profile of the proton beam energy deposition at cells obtained with an image plate (taken from [163]). The black and purple lines represent respectively 50% and 20% of the maximum signal, while the white rectangle shows the area selected for cell analysis after irradiation. Right: spectrum of the proton beam reaching the sample area of 1.5 cm^2 (bottom X-axis, blue line) and corresponding LET distribution (top X-axis, black line)

a meaningful dose per shot with the typical ∼nC charge at the source[9].
The proton energy spectrum reaching the cells, after interaction with the mylar window, the air gap and the TIC, features a peak around 3.8 MeV. The spectrum is obtained by simulating the beam transport and interaction with matter with the Geant4 Monte Carlo tool, as described in Chapter 3. The corresponding LET spectrum has a peak at 9.6 keV/µm and a HWHM of the peak of 1.75 keV/µm. The long high-LET tail is due to the low-energy components that are not completely suppressed by the transport beamline. However the contribution of high-LET protons can be considered negligible, since the LET tail above 20 keV/µm is due to protons having energy below 1.4 MeV, which represent 3% of the total flux reaching the sample.

Irradiation results The proton beam was used to irradiate *in vitro* highly radioresistant glioblasoma U87-MG and SF-763 cell lines and colorectal cell line HCT116[10], both wild type (HCT116 WT) and its radioresistant counterpart (HCT116 $p53^{-/-}$) mutated for the tumour suppressor gene p53. The radiobiological response to LPAP irradiation was

[9]Reducing the irradiated surface would increase both the dose homogeneity and the total dose per shot, however the reduced number of irradiated cells would lead to higher statistical errors in radiobiology analysis. This issue is discussed in details in section 3.3 and in chapter 4, where various strategies to optimize the trade-off between these parameters are presented.

[10]The choice was motivated by the fact that protontherapy has proven to be effective especially for brain, skull and head and neck cancers.

compared with X-rays and conventional accelerated protons (CAP). X-ray irradiations were performed using a Varian NDI 226 X-ray tube with an applied tension of 200 kV and a dose rate of 1.23 Gy/min, as previously described in E. Bayart et al. (2017) [16]. CAP were generated by an IBA C230 isochronous cyclotron available at the Curie Institute Proton Therapy Center [42]. The cyclotron accelerates protons with initial energy of 235 MeV, which is lowered down to 201 MeV right at the cyclotron output and further reduced to 20 MeV by sequential polycarbonate and Plexiglas attenuators.

I: DNA foci and RBE As discussed in section 2.4, quantifying both the number of DNA double strand breaks (DSB) and the RBE is a key *in vitro* essay to assess the biological response of living cells to a given radiation quality. Formation of DNA DSBs after irradiation with the 7.5 MeV LPAP SAPHIR source was evaluated for U87-MG and SF-763 cell lines. Cells were fixed 1 or 24 hours after exposure to different applied doses (different number of proton bunches, separated by 30 s) and DSBs were detected by microscopy through immunodetection of the histone H2AX phosphorylation on Ser139 (γH2AX)[11]. The detailed discussion of the cell handling methods can be found in E. Bayart et al. (2019) [17]. As shown in Fig. 2.12.a, the number of DSBs increases with the applied dose, whereas it decreases between 1 hour and 24 hours after irradiation, reflecting the onset of DNA repair processes. The number of DSBs were also compared to those obtained with X-rays and CAP. The results, in line with recent findings (see section 2.4), showed no significant difference in DSB formation (Fig. 2.12.b and Fig. 2.12.c).
Cell survival was then evaluated to assess the radiobiological effectiveness (RBE) of LPAP compared to conventional sources. Different cell samples were irradiated with increasing number of pulses, separated by 30 s, corresponding to doses ranging from 0 to 10 Gy within the 1.5 cm^2 surface (Fig. 2.11). The resulting cell survival curves were compared to those obtained with CAP and X-rays, as shown in Fig. 2.13. The survival curves, obtained with the linear quadratic model fit, show no signficant difference in RBE_{10} $p > 0.3$). The large error bars of LPAP data represent the 25% error on the 2D dose distribution over the analysed 1.5 cm^2 surface.
All together, these results are in good agreement with previous findings and suggest that potential errors due to the ionisation chamber response at high-dose rate (see chapter 5) do not introduce significant errors on the absolute dose estimation.

[11] Phosphorylation of the histone H2AX protein, a component of the core nucleosome around which the DNA is packed, is one of the earliest event following DSBs formation. The resulting phosphorylated form γH2AX is necessary for the recruitment of other proteins involved in the DNA repair process following irradiation [107].

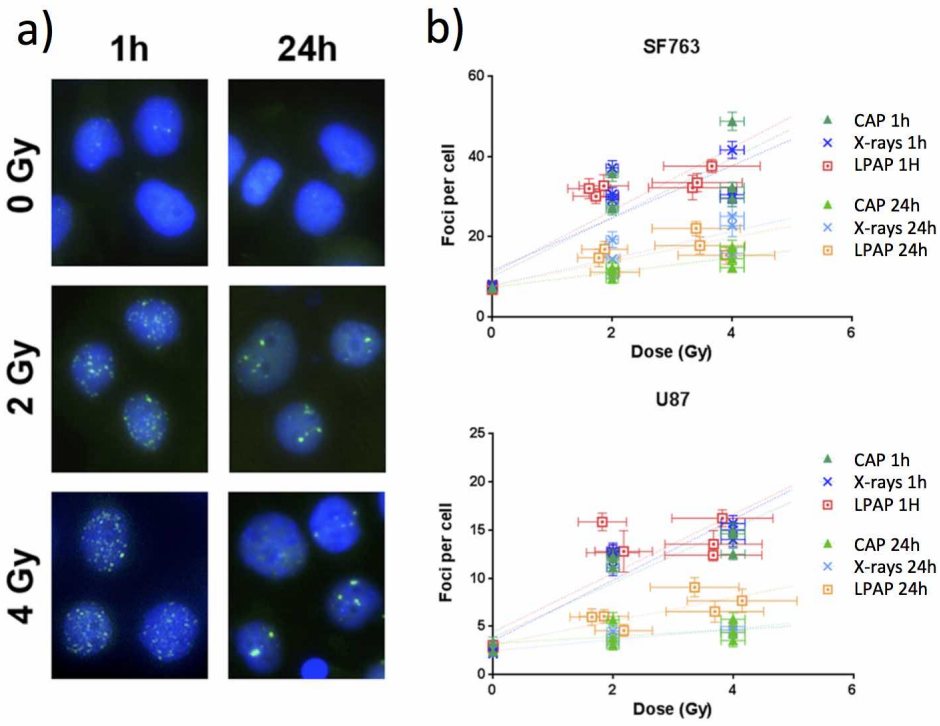

Figure 2.12: a) Representative immunefluorescent images of SF763 cells obtained 1 h and 24 h after exposure to the indicated doses of laser-accelerated protons. The green spots represent the phosphorylated histone H2AX foci. b) Number of phosphorylated H2AX foci induced by laser-plasma accelerated protons (LPAP, dotted square), conventional accelerated protons (CAP, triangles) and X-rays (x cross) respectively in SF763 and U87-MG cells.

II: Effect of LPAP bunch frequency on cell mortality All previous results were obtained by appliying a given number of proton bunches separated by a fixed time delay of 30 s. Given the arising interest towards temporal aspects of high dose-rate irradiation, we investigated for the very first time the effect of dose fractionation with LPAP on cell survival. Cell samples were irradiated with the same total delivered dose (same number of bunches) varying the time delay between the LPAP bunches from 2 s, which was the lower limit due to the mechanical refresh of the target, to 60 s, corresponding to an average dose-rate between 1.1 Gy/min and 33 Gy/min. Highly radioresistant HCT116 colorectal cell samples were irradiated with 9 consecutive shots while SF763 and U87-MG samples were irradiated with 6 consecutive shots, and cell survival was monitored as a function of the time delay. The results show that the bunch frequency does not affect neither the SF763 nor the U87-MG cell survival (Fig. 2.14.a Fig. 2.14.b). On the contrary, variation of the bunch frequency generates cell survival oscillation of both HCT116 WT ($p < 0.0038$) and its radioresistant counterpart HCT116 $p53^{-/-}$ ($p < 0.0001$). The two curves show a maximum for a time delay of about 25 s, where the cell survival difference

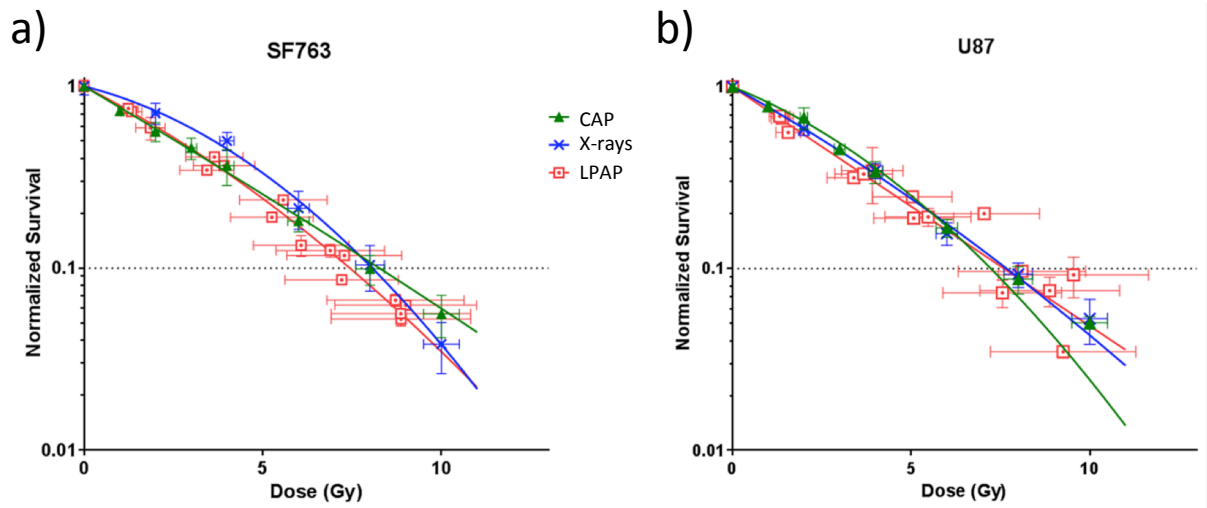

Figure 2.13: Normalized cell survival resulting from exposure to increasing doses of laser-accelerated protons (LPAP), conventional accelerated protons (CAP) and X-rays respectively in SF763 (a) and U87-MG cells (b). Each data point represents the mean and standard deviation (SD) of three replicates obtained at least with three independent experiments. Survival curves were generated following the linear quadratic model ($R > 0.96$ and $R > 0.97$ for SF763 and U87-MG cell lines respectively).

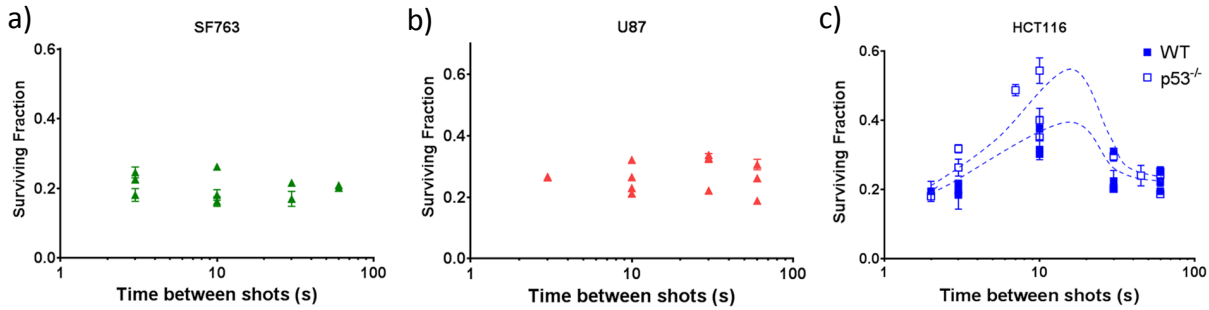

Figure 2.14: Surviving fraction as a function of the time delay between pulses. SF763 (a) and U87-MG (b) samples were exposed to 6 consecutive shots while HCT116 samples (c) were exposed to 9 consecutive shots. Each data represent the mean of three different replicates and the error bar represent the standard deviation of the three measures.

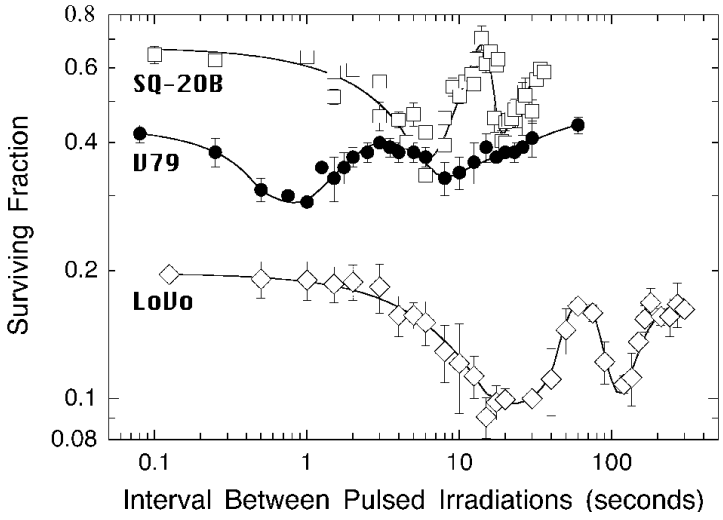

Figure 2.15: Time-dependent profile of the clonogenic survival of different cell lines following exposure to two dose fractions with 3.5 MeV electrons at a dose rate of 12 Gy/s and with dose per fraction higher than 1 Gy. Taken from Ponette et al. (2000) [164].

between the wild type and the $p53^{-/-}$ type is maximum (Fig. 2.14.c). The two curves converge together to their minimum value at the shortest time delay, where survival of the radioresistant HCT116 $p53^{-/-}$ cell line equals that of its radiosensitive counterpart HCT116 WT. Besides, the curve of the radioresistant HCT116 $p53^{-/-}$ lies well above the WT counterpart, which further confirms the reproducibility of LPAP irradiations for different samples.

It should be noted that while the survival oscillation may result from the variation of both the time delay between bunches and the average dose-rate, no apparent effect of the dose-rate has been observed with clinical beams above 1 Gy/min [91, 150, 59]. It is therefore more likely that the oscillation is due to the impact of the repetition rate on the DNA damage signaling and repair processes.

III: Cell survival oscillation is related to the presence of PARP1 functional protein A similar behaviour was previously observed by another group with low energy electrons [164, 65]. In their experiment only two dose fractions were applied and cell survival exhibited a W-like oscillation as a function of the interval between the two fractions (Fig. 2.15). The phenomenon, called W-effet, was proven to be sensitive to the presence of an active PARP1 protein. The PARP1 (poly(ADP-ribose) polymerase) enzyme is involved in many DNA repair processes. It catalizes the so-called PARylation (poly ADP-ribosylation) process, which is a post-translational protein modification appearing rapidly at DNA damage sites and is known to be crucial for the activation of

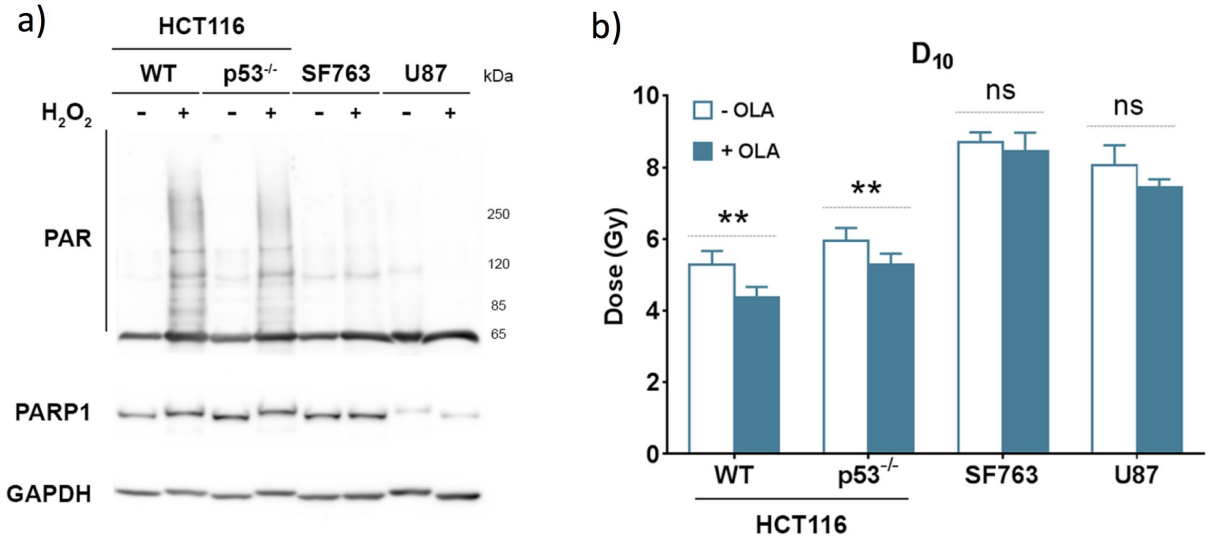

Figure 2.16: a) Western-Blot detection of the PARP1 protein and parylation in total protein extracts from HCT116 WT, HCT116 $p53^{-/-}$, SF763 and U87-MG cells. The minus (−) columns show the untreated cells while the plus (+) columns show cells treated 10 minutes with 1 mM hydrogen peroxide H_2O_2. b) D_{10} values (mean from at least three independent experiments) for the three cell lines, where white bars correspond to untreated cells and filled bars to cells treated with 200 nM Olaparib. The error bars represent the standard deviation of the mean. The star flags above the HCT116 columns indicate a high level of statistical significance (p-value < 0.01), whereas the ns label above the SF763 and U87-MG columns indicates that the cell survival variation is not significant ($p > 0.05$).

DNA repair pathways [202]. In particular, inhibition of the PARP1 protein leads to an accumulation of SSBs and consequent formation of more lethal DSBs [92].

The bell shape of cell survival observed with LPAP for HCT116 cell-lines may correspond to the central peak of the W-shape curves, whereas the behaviour of SF763 and U87-MG cell lines may be related to the absence of a functional PARP1 protein. To verify this hypothesis, PARP1 activation in all cell lines was stimulated by generating DNA damage through oxidative stress. After exposure of cells to hydrogen-peroxide H_2O_2, Western-Blot analysis was performed to detect the PARP1 protein and the related PARylation. As shown in Fig 2.16.a, the PARP1 protein and the induced PARylation was clearly observed for the two cell lines HCT116. In the SF763 cell line, although the PARP1 protein was detected, no increase of PARylation was induced by exposure to hydrogen-peroxide, suggesting that the PARP1 protein was not functional in this cell line. In the U87-MG cells, very low amount of PARP1 was detected and only extremely weak parylation was observed.

To further correlate the survival oscillation to the presence of a functional PARP1 protein, all cell lines were treated with Olaparib, a PARP1 inhibitor developed to

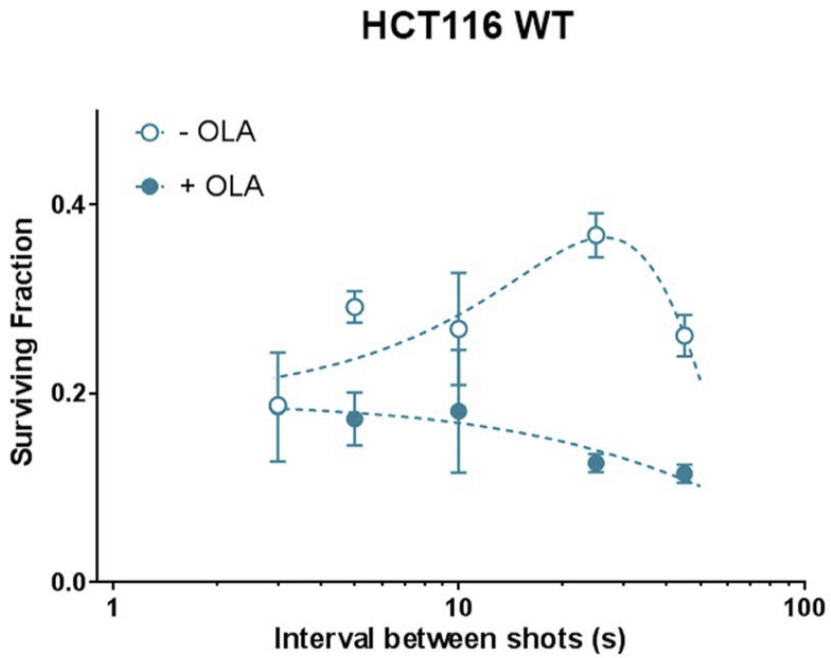

Figure 2.17: Surviving fraction of HCT116 cells, treated (filled dots) or untreated (white dots) with Olaparib irradiated with five consecutive laser-accelerated proton bunches. Each data point represents the mean and standard deviation of three replicates obtained in two independent experiments.

increase cancer sensitivity to ionising radiation [148], and then irradiated with increasing doses of X-rays. From the cell survival curve the D_{10} values (the amount of dose corresponding to 10% surviving fraction) were retrieved and compared with that of non-treated cells. As expected, no significant variation of cell survival was observed for SF763 and U87-MG cell lines (Fig. 2.16.b) whereas a significant increase of cell mortality was measured in HCT116 cell lines, where PARP1 was found to be functional, resulting in a decrease of D_{10} up to 17%. All together, these results suggest that cell survival variation with the time delay between LPAP bunches is related to the presence of a functional PARP1 protein. The phenomenon may be related to a stronger genomic instability promoted by interaction with radiation occuring at a critical time of the DNA damage signalling and repair process triggered by a previous fraction.

Since cell survival oscillation appeared to be correlated to the presence of a functional PARP1 protein, we verified the effect of the Olaparib PARP1 inhibitor on this behaviour. To this aim, HCT116 cells were exposed or not to Olaparib and, similarly to previous experiments, were exposed to 5 LPAP bunches with time delay ranging from 2 s to 45 s. As expected, while non-treated cells exhibited the same oscillatory behaviour

observed in previous experiments, cell samples treated with Olaparib showed no survival oscillation with the bunch frequency (Fig 2.17). Interestingly, the two curves reach the same surviving fraction at a time delay of 2 s. This latter result not only confirms that cell survival oscillation depends on the presence of a functional PARP1 protein, but also indicates that LPAP irradiation at a specific bunch repetition rate (in this case of 0.5 Hz) may bring the same clinical benefit as a drug combined radiotherapy with continuous beams.

To resume, this study points out the key role of the LPAP bunch frequency on cancer cell response. The survival peak at a time delay of around 25 s may also explain why the RBE obtained at the SAPHIR facility with a 30 s delay between bunches showed no significant difference with RBE of conventional proton beams. Besides, the results suggest that the discrepancies in the RBE of LPAP btained by different groups in the last decade may be also due to the different temporal structure of the proton bunches. Further study would also be needed to precise the parameters potentially playing a role in the fast fractionation effect, such as the total delivered dose, the number of pulses and the dose within the pulse.

2.6 Conclusions

The key feature of laser-plasma accelerated beams is the extremely high dose-rate in the pulse, which motivated a strong research activity in the last decade to asses their radiobiological effectiveness (RBE). Although classical survival assays showed no difference between the RBE of LPA and clinical beams, some studies showed potential therapeutic benefits and ask for further investigation. The activities carried out at the LOA with the SAPHIR laser-accelerated proton beam showed for the first time an oscillation of cell mortality with the bunch repetition rate, pointing out that the temporal modality of dose delivery with LPA might affect the biological response of living cells.

Chapter 3

Tools and techniques for LPAP spectroscopy and beam shaping

Contents

Overview

This chapter describes the approaches used to takle some of the issues related to the application of Laser-Plasma Accelerated Protons (LPAP) to radiation biology mentioned in the introduction of this manuscript. In particular, it presents the techniques to characterise the source and to shape the proton beam. The measurements performed at the SAPHIR facility prior to the beginning of this thesis by L. Pommarel (2017) [162] enabled a robust validation of the tools and strategies developed. For this reason, the chapter also

presents the application of such techniques to the SAPHIR beamline.

3.1 Source characterisation

Precise characterisation of the proton source is essential to perform the design of a beamline and establish the irradiation conditions at the biological target. In the following, we describe two of the most common spectroscopy diagnostics: the Thomson Parabola (TP) and the radiochromic film stack. In particular, a deconvolution technique developed to infer the proton spectrum from the film stack is presented. A review of all techinques employed to characterise LPAP sources can be found in P. R. Bolton et al. (2014) [29].

3.1.1 Thomson Parabola

The Thomson Parabola (TP) is widely used as real time spectroscopy diagnostic for laser-plasma accelerated ion beams [146, 29, 51, 81, 161]. It is a type of electro-magnetic energy and mass spectrometer, whose invention dates back to 1911 [191]. By combining electric and magnetic fields, TP allows the distinction of both particle energy and charge-to-mass ratio. Particle tracks are revealed with a detector (CR-39, imaging plate or micro channel plate coupled with a phosphor screen and a CDD camera) placed after the electro-magnetic field, providing spatial resolution over a plane perpendicular to the beam-axis. Fig. 3.1 shows a typical TP configuration, consisting of two superposed magnetic and electric fields coupled with a Micro Channel Plate (MCP) for particle-track detection. The pinhole placed at the TP entrance cuts-out all particles with a given deflection from the propagation-axis. It sets the acceptance angle of the device and the trace width on the detector, i.e. the system resolution.
Particle trajectories can be determined analytically if we assume constant, no-fringe fields and small deflections. In the following analysis, we consider the set-up shown in Fig. 3.1 with superposed electro-magentic fields oriented towards the positive $\hat{x}$ direction over a length l. Particles propagating in the $\hat{z}$ direction are deflected by the Lorentz Force:

$$\vec{F} = q \cdot \left(\vec{E} + \vec{v} \times \vec{B} \right) \tag{3.1}$$

By decomposing the vector equation into its components, the particle acceleration along the two axis $\hat{x}$ and $\hat{y}$ can be expressed as a function of respectively the electric and magnetic field:

$$a_x = \frac{F_x}{m} = \frac{q}{m} E_x \tag{3.2}$$

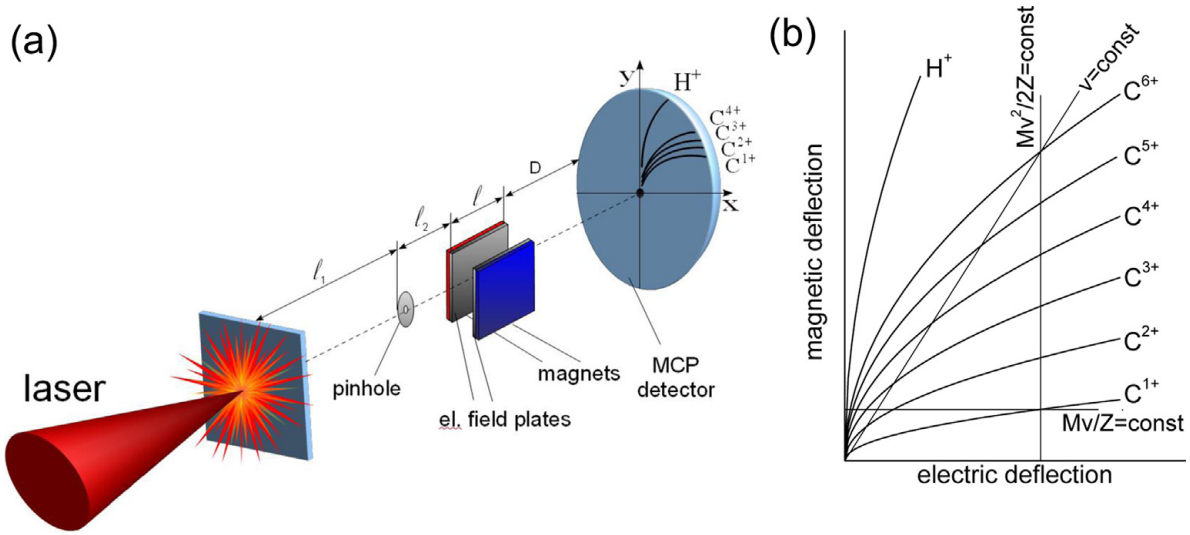

Figure 3.1: a) Schematic set-up of a typical Thomson Parabola (TP) spectrometer. b) Particles having a different charge-to-mass ratio draw different parabolas on the detection plane. The particle energy determines its position along a trace, higher energy particles impinging closer to the centre of the detection plane. Taken from P. R. Bolton et al. (2014) [29].

$$a_y = \frac{F_y}{m} = \frac{q}{m} v_z B_x \tag{3.3}$$

In the case of small deflections, the time spent by the particle in the electro-magnetic field and the kinetic energy can be expressed as, respectively, $t_{em} = l/v_z$ and $k = \frac{1}{2}mv_z^2$. The deflections at the end of the electro-magnetic section are therefore given by:

$$\theta_x = \frac{v_x}{v_z} = \frac{a_x t_{em}}{v_z} = \frac{1}{2}\frac{qE_x l}{K} \tag{3.4}$$

$$\theta_y = \frac{v_y}{v_z} = \frac{a_y t_{em}}{v_z} = \frac{qB_x l}{\sqrt{2mK}} \tag{3.5}$$

The final deviations Δx and Δy at the detection plane after a drift distance D are expressed by:

$$\Delta x = D \cdot \tan\theta_x = D \cdot \theta_x = \frac{1}{2}\frac{qE_x l}{K} \cdot D \tag{3.6}$$

$$\Delta y = D \cdot \tan\theta_y = D \cdot \theta_y = \frac{qB_x l}{\sqrt{2mK}} \cdot D \tag{3.7}$$

The combination of the two formulas (3.6, 3.7) provides the particle trajectory equation over the detection plane [94]:

$$y^2 = \frac{q}{m} \cdot \frac{B_x^2 l D}{E_x} x \tag{3.8}$$

As mentioned above, for a given TP configuration, particles with a different charge-to-mass ratio trace parabolas with different slopes. Moreover, formulas (3.6) and (3.7) show that the position along each parabola depends on the particle energy (higher energy particles imping closer to the centre of the detection plane) and that the resolution decreases as the energy increases.

TPs allow for real time, single shot, spectral characterisation of LPAP beams. However, since the measured spectrum is restricted to the narrow solid angle set by the pinhole dimension, the information on the proton divergence is lost. Moreover, since LPAP features a divergence that is a function of the energy, the characteristic slope of the spectrum obtained with a TP does not represent the slope of the total spectrum at the source. For this reason, TPs are primarly employed to characterise such beams in terms of their cut-off energy, whereas a detailed measurement of the source spectrum and total accelerated charge can be performed through film-stack spectroscopy technique.

3.1.2 Film stack spectroscopy

Radiochromic films (RCFs) are largely used as dosimetry instrument in many medical and radiation physics applications. A radiochromic film consists in a micrometer thick sensitive layer, coated by plastic substrates. When irradiated, the active layer undergoes polymerisation and the change in its optical density (OD) can be calibrated against the absorbed dose[1]. To perform LPAP spectroscopy, RCFs are used in a stack placed perpendicular to the beam axis in front of the proton source. The stack is then irradiated with a given number of shots depending on the film's dose sensitivity[2] and the accelerated charge per bunch. Each layer acts as a filter for the following films, blocking all protons having an energy $E < E_{co}$, where E_{co} is the minimum energy of protons that reach the following film. The in-depth energy deposition profile in the stack is then used to reconstruct the impinging proton spectrum. Moreover, the 2D resolution of RCFs allows for the determination of the energy-dependent divergence of LPAP beams, which is crucial to perform a precise design of transport beamlines dedicated to radiobiology studies.

To a first approximation, for a typical TNSA exponential spectrum, the dose deposited

[1] For a detailed description of radiochromic films see section 5.1

[2] Usually, HDV2 films are preferred because their thinner, sensitive layer allows a higher energy resolution.

in a film can be taken as proportional to the number of protons having their Bragg-peak in its sensitive layer [124]. This assumption, which allows for a rough and easy spectral characterisation of the beam, was used to obtain the spectrum of the SAPHIR proton source [17]. However, this approach can lead to large errors on the characteristic slope of the TNSA spectrum, as it will be shown in section 3.1.3 and does not allow absolute charge measurement. Therefore, a more precise deconvolution technique has been developed.

Similarly to other approaches reported in literature by few research groups [111, 149, 207, 35, 186], the method selects the entire observed beam area on the irradiated films to obtain the total spectrum at the source (otherwise, the analysis can also be performed for specific portions of the beam envelope to obtain a spatially resolved spectrum). The 2D dose maps measured in each film are converted into 2D energy maps by multiplying the dose deposited in a pixel by the sensitive layer pixel mass, considered as composed by water[3]. The total energy deposited in the film is simply obtained by summing up the energy released in the pixels within the selected beam area. Thus, for a number of irradiated films N, we obtain a vector containing N values of total released energy, which is used to infer the spectrum impinging on the stack. The challenge is to reconstruct a spectrum containing a number of energy bins, and therefore a number of variables, higher than the number of available data points N. The developed spectroscopy technique makes use of two different and subsequent approaches. Both repose on a 2D library containing the energy released by a proton of a given initial energy as a function of the active layer number [111, 149]. In the following we refer to such library as "RCF - Energy Coefficient Library" (RCF-ECL).

Energy deposited in the film stack The RCF-ECL is obtained using the Monte Carlo Geant4 tool. Rather than making separate simulations for each initial proton energy, a single simulation generates spatially separated, monoenergetic, collimated beams impinging on a HD-V2 stack. To cover a spectrum from 0.1 MeV to 25 MeV[4], a total number of 250 proton beams is simulated, which leads to an energy resolution of 100 keV. A Geant4 sensitive scoring divided in pixels is associated to each sensitive layer of the stack. Each pixel of the scoring corresponds to a beam position, so as to separately retrieve the energy released in the active layers for each monoenergetic beam. The output of the simulation consists in a 2D library containing the energy deposited in each active layer by protons of a given initial energy, as shown in Fig. 3.2. If we move horizontally

[3]This assumption does not introduce any error since RCFs are usually calibrated in dose to water.
[4]Typical maximum proton energy obtained with TW lasers.

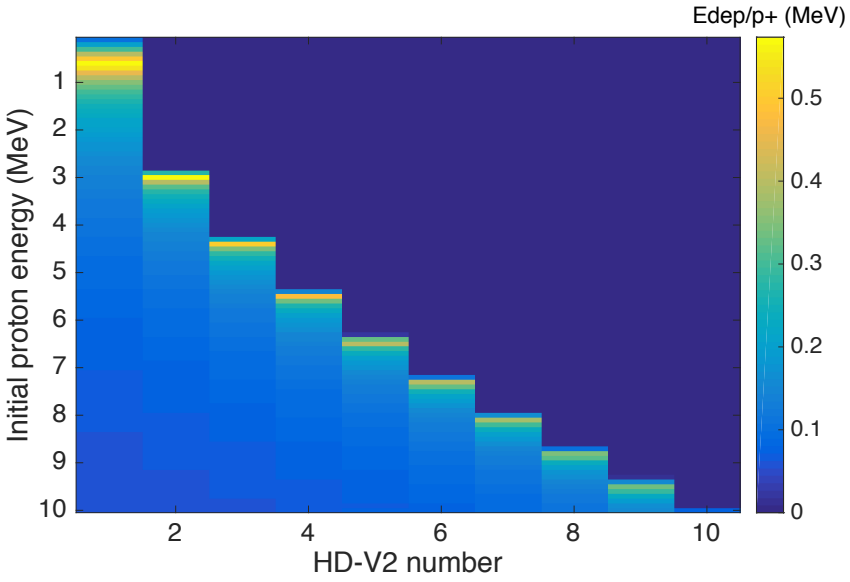

Figure 3.2: RCF energy coefficient library for the first ten films of the stack. It contains the energy delivered in each sensitive layer of the stack by a proton of a given initial energy.

through the matrix, we observe the typical in-depth energy profile of a monochromatic proton beam, releasing an increasing amount of energy until it stops. If we move vertically through the matrix, we can observe the relative amount of energy deposited in a sensitive layer by protons of a given initial energy. The higher amount of energy is released by those protons having their Bragg-peak in the senstive layer.

Backward approach This first approach is employed to reconstruct a spectrum composed by a number of energy bins equal to the number of irradiated films. To explain the technique, let us first express the energy measured in the last irradiated film N of the stack:

$$E_m(N) = \int_{E_{co}^{N}}^{E_{co}^{N+1}} \frac{dN}{dE}(E') \cdot EC_N(E')dE' \tag{3.9}$$

where dN/dE is the proton spectral density expressed in MeV^{-1}, EC_N is the energy coefficient of the N^{th} film as a function of the initial proton energy obtained from the Geant4 RCF-ECL library (expressed in energy deposited per proton) and E' is the initial proton energy. The expression is integrated between the energy cut-off (E_{co}) limits of the $(N+1)^{th}$ and N films, where the energy cut-off is defined as the lower proton energy component reaching a film. For example, if the 8^{th} film is the last irradiated film, then

such integral would be solved between $E_{co}^{9} = 9.3MeV$ and $E_{co}^{8} = 8.7MeV$.
In this approach we assume a constant spectral density within the cut-off limits of each film. We can therefore pull dN/dE out of the integral and write:

$$E_m(N) = \frac{dN}{dE}(N) \int_{E_{co}^{N}}^{E_{co}^{N+1}} EC_N(E')dE' \tag{3.10}$$

Then, by expressing the integral of the energy coefficient as the mean value times the ΔE_{co} interval, according to

$$\int_{E_{co}^{N}}^{E_{co}^{N+1}} EC_N(E')dE' = \overline{EC}_{N}^{E_{co}^{N},E_{co}^{N+1}} \cdot \left(E_{co}^{N+1} - E_{co}^{N}\right) \tag{3.11}$$

we obtain the equation:

$$\frac{dN}{dE}(N) = \frac{E_m(N)}{\overline{EC}_{N}^{E_{co}^{N},E_{co}^{N+1}} \cdot (E_{co}^{N+1} - E_{co}^{N})} \tag{3.12}$$

We have therefore obtained the average proton spectral density (protons/MeV) within the energy bin associated to the last film N, delimited by the cut-off energy limits (E_{co}) of the $(N+1)^{th}$ and N films. Once such spectral density is determined, the algorithm computes the spectral density associated to the $(N-1)^{th}$ film. The energy measured in such film is the sum of two contributions:

$$\begin{aligned} E_m(N-1) =& \frac{dN}{dE}(N) \cdot \overline{EC}_{N-1}^{E_{co}^{N},E_{co}^{N+1}} \cdot (E_{co}^{N+1} - E_{co}^{N}) \\ &+ \frac{dN}{dE}(N-1) \cdot \overline{EC}_{N-1}^{E_{co}^{N-1},E_{co}^{N}} \cdot (E_{co}^{N} - E_{co}^{N-1}) \end{aligned} \tag{3.13}$$

Since the spectral density $dN/dE(N)$ is known, the equation can be solved for $dN/dE(N-1)$. By the same token, the algorithm continues until the first film of the stack is reached, the average spectral density associated to the generic n^{th} film being:

$$\frac{dN}{dE}(n) = \frac{E_m(n) - \sum_{i=n+1}^{N} \frac{dN}{dE}(i) \cdot EC_{n}^{E_{co}^{i},E_{co}^{i+1}} \cdot \left(E_{co}^{i+1} - E_{co}^{i}\right)}{\overline{EC}_{n}^{E_{co}^{n},E_{co}^{n+1}} \cdot (E_{co}^{n+1} - E_{co}^{n})} \tag{3.14}$$

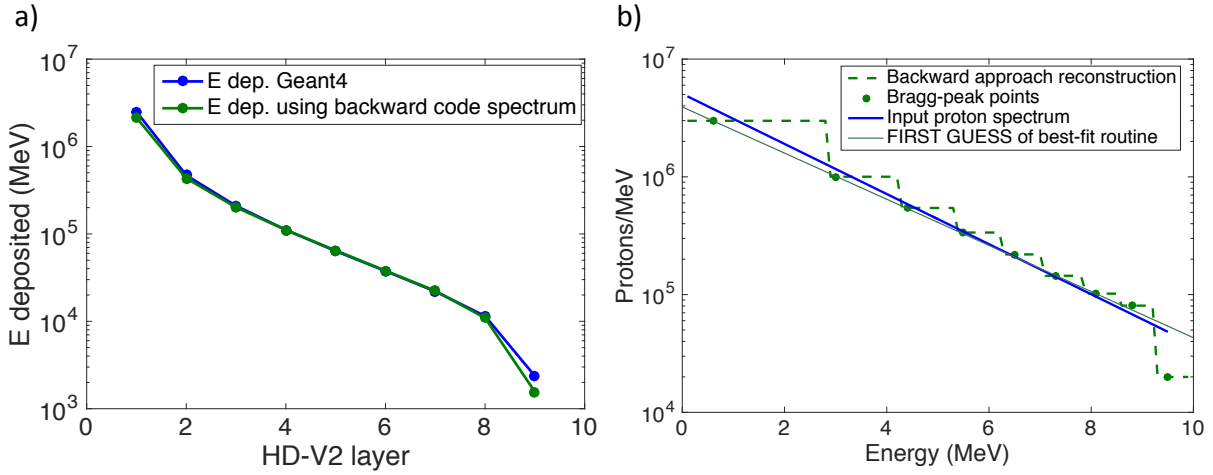

Figure 3.3: Left: Energy deposited by the input exponential spectrum with a cut-off energy of 9.5 MeV (blue line) and by the spectrum reconstructed using the backward approach.

The final output of the routine is a stepped spectrum composed by a number of energy bins N equal to the number of irradiated films. The value of each bin is an average spectral density expressed in protons/MeV. Similar approaches have been used by E. Breschi et al. (2004), M. Schollmeier et al. (2014) and D. Kirby et al. (2011) [35, 186, 111]. To be valid, the approach requires the proton beam to be completely stopped within the film stack.

Before further discussing the limits and advantages of such approach, let us test the algorithm by simulating with the Geant4 Monte Carlo tool a collimated proton beam with an exponential spectrum between 0.1 MeV and 9.5 MeV impinging on a HD-V2 stack. Fig. 3.3.a (blu line) shows the energy released in the sensitive layers. The simulation was performed using 10^7 protons at the source. The proton beam penetrates until the 9^{th} layer of the stack, in agreement with the film energy cut-off shown in Fig. 3.2. The vector containing the 9 values of delivered energy is used as input to reconstruct the well known incident spectrum using the backward approach. The spectrum reconstructed with the backward routine is shown in Fig. 3.3.b (green dashed line) together with the input spectrum (blu line). It is a stepped spectrum divided into 9 energy bins, delimited by the cut-off energy of each film, whose resolution increases with the energy. The corresponding in-depth energy profile in the stack, shown in Fig. 3.3.a (green curve), matches closely the profile generated by the input specturm. The total charge, computed by integrating the obtained stepped curve, is 1.1×10^7 protons, a good estimation of the incident charge with an error of 10%.

The major limitation of this approach is the poor energy resolution, which leads to two

main drawbacks. Firstly, it is not possible to precisely determine the cut-off energy of the proton spectrum, which can only be estimated within the energy bandwidth delimited by the cut-off energies of the $(N+1)^{th}$ and N sensitive layers of the stack, whose width decreases with the energy. While the error on the spectrum cut-off would be negligible for beam energies of tens of MeV, it may be significant for typical LPAP beams. Indeed, their maximum energy is often in the range of few MeV, and a precise determination of the cut-off proton energy may be crucial for the design of radiobiology experiments.
The other issue related to the low energy resolution is to what energy coordinates assign the N average spectral density to obtain a continuous and smooth spectrum. For example, E. Breschi et al. (2004) [35] employed the "medium energy point of each RC foil". The choice made in the following is to assign the average spectral density to the Bragg-peak energy of the corresponding film, since protons having the Bragg-peak in the film deliver the highest energy fraction, as shows in Fig. 3.2. The Bragg-peak points of each layer are indicated in Fig.3.3.b with the green dots. By comparing the input spectrum with an exponential fit of the Bragg-peak points (represented by the green line in Fig.3.3.b) we can estimate the precision of such approach. The input spectrum (blu line) has the form:

$$\frac{dN}{dE} = N_0 \cdot \exp\left(-\frac{E}{E_0}\right) = 5.06 \times 10^6 \cdot \exp\left(-\frac{E}{2.04}\right) \tag{3.15}$$

where N_0 [protons/MeV] is the initial charge at $E = 0$ while E_0 [MeV] is the characteristic slope of the exponential. The exponential fit of the reconstructed spectrum using the Bragg-peak points has $N_0 = 3.92 \times 10^6$ and $E_0 = 2.21$, leading to errors from 7% to 22% on the exponential parameters.
Despite the limitations of this approach, the absence of any assumption on the spectral shape may represent an advantage in some situations. For example, the backward approach could prove to be useful to characterise the spectrum after a transport beamline, where the spectral shape is not known.
In the case of TNSA protons, the precision of the reconstructed spectrum may be further improved by employing unfolding techniques with an assumed exponential spectral shape.

Exponential deconvolution method The backward approach can be considered as an inverse solving technique: starting from the energy deposited in the stack, the Geant4 RCF-ECL is employed to obtain the spectral density. The alternative direct approach is to assume a spectral function, defined by certain parameters, and to find the set of parameters that minimise the error between the energy measured in the stack and the energy profile corresponding to the assumed spectrum, calculated using the RCF-ECL [149, 207].

In the case of TNSA protons, the spectrum can be characterised by a Boltzmann exponential of the form:

$$\frac{dN}{dE} = N_0 \cdot \exp\left(-\frac{E}{k_b \cdot T}\right) = N_0 \cdot \exp\left(-\frac{E}{E_0}\right) \tag{3.16}$$

Where $E = E_{cut-off}$ defines the maximum value of E in the formula.
The goal of the deconvolution process is to find the fittest set of parameters $[N_0, E_0, E_{cut-off}]$ minimising the error between the experimental energy profile in the stack and the simulated energy profile corresponding to exponential spectra defined by the given set of parameters. To this aim, the routine needs the definition of a first-guess set of parameters around which it can search the fittest set. The result of the backward approach is used to define the first guess. Precisely, the exponential fit obtained using the Bragg-peak points (green line in Fig. 3.3) defines the first-guess parameters $N_{fg} = N_0$ and $E_{fg} = E_0$. The best-fit routine then defines a 2D domain of parameters around the first-guess set, with a given resolution. To illustrate the technique and test its precision, we use the Geant4 simulation test mentioned in the previous section as a guideline example. The solution of the backward approach was:

$$\frac{dN}{dE} = 5.06 \times 10^6 \cdot \exp\left(-\frac{E}{2.04}\right) \tag{3.17}$$

where the cut-off energy may range from 9.3 MeV and 10 MeV. The routine then defines all possible sets of parameters N_0 and E_0 in a given range around the first-guess set ($N_{fg} = 5.06 \times 10^6$ protons/MeV and $E_{fg} = 2.04$ MeV) for each possible cut-off energy value, with a resolution on $E_{cut-off}$ of 100 KeV.
For a fixed value of $E_{cut-off}$, the best-fit routine works as follow:

1. For each set of parameters N_0 and E_0, the routine creates the corresponding exponential spectra, as in formula (3.16), with an energy resolution of 100 keV.

2. For each spectrum, the energy deposited in the active layers of the stack is computed using the Geant4 RCF-ECL (Fig. 3.2).

3. The error between the computed and the experimental energy profile for each set of parameters is used to find the fittest set of parameters. It is defined as the average percentage error between the measured energy in the sensitive layers E_m and the

simulated energy E_s:

$$f = \frac{\sum_{i=1}^{N} \left| \frac{E_m(i) - E_s(i)}{E_m(i)} \right|}{N} \cdot 100 \tag{3.18}$$

where N is the number of irradiated films.

4. Thus, the routine evaluates f for each set of N_0 and E_0 and creates a 2D f-matrix containing the average error corresponding to each set of parameters. Fig. 3.4 shows the f-matrix for a domain of parameters around the first-guess set [N_{fg}, E_{fg}]. The minimum value of f defines the fittest set of N_0 and E_0 for a given $E_{cut-off}$.

5. At the end of the loop, the fittest set of N_0 and E_0 is stored, together with the corresponding f value and the vector containing the energy deposited in the active layers.

6. The procedure from point 1 to point 5 is repeated for each possible cut-off energy value.

7. The overall lower value of f defines the set (N_0, E_0, $E_{cut-off}$) of the fittest spectrum.

In the present example, the procedure from point 1 to 5 is therefore repeated 8 times for all the possible cut-off energies ranging from 9.3 MeV and 10 MeV. The obtained fittest spectrum is shown in Fig. 3.5.a (red line), together with the input spectrum and the previous reconstruction obtained with the backward approach. The fittest spectrum obtained with the best-fit routine remarkably improves the precision of the spectrum reconstruction compared to the backward approach and perfectly matches the input proton spectrum, with errors on the parameters N_0 and E_0 of 1%. Moreover, among all possible spectrum cut-off energies, the best-fit routine finds the lower fitting parameter f for $E_{cut-off} = 9.5$ MeV, in perfect agreement with the cut-off energy of the input spectrum. The perfect match between the fittest spectrum obtained with the best-fit routine and the input spectrum used in the Geant4 simulation test confirms the accuracy of the approach. In addition, it indicates that the energy resolution of 100 keV used to generate the Geant4 RCF-ECL, which is employed to compute the energy delivered in the active layers, does not introduce significant errors. Figure 3.5.b shows energy profile corresponding to the spectra obtained with the best-fit routine (red line), which is compared to the profile corresponding to the backward approach spectrum (green line) and to the input spectrum used in the Geant4 test simulation (blue line). The stepped spectrum obtained with the backward approach generates an energy profile in the active layers with an average error

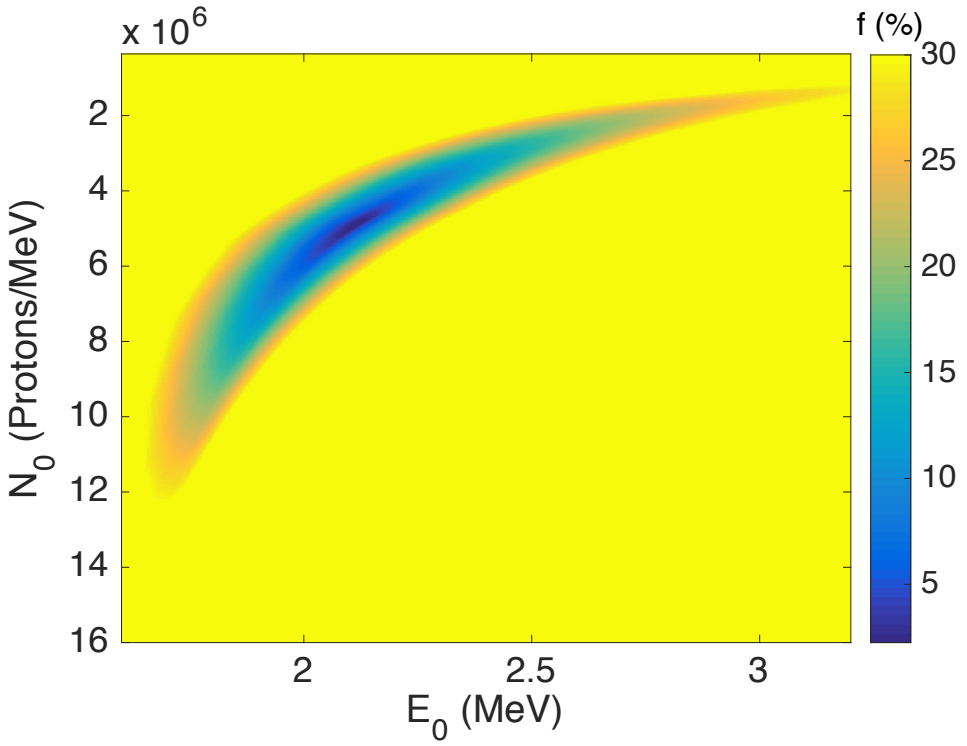

Figure 3.4: Matrix containing the fitting parameter for each set of N_0 and E_0

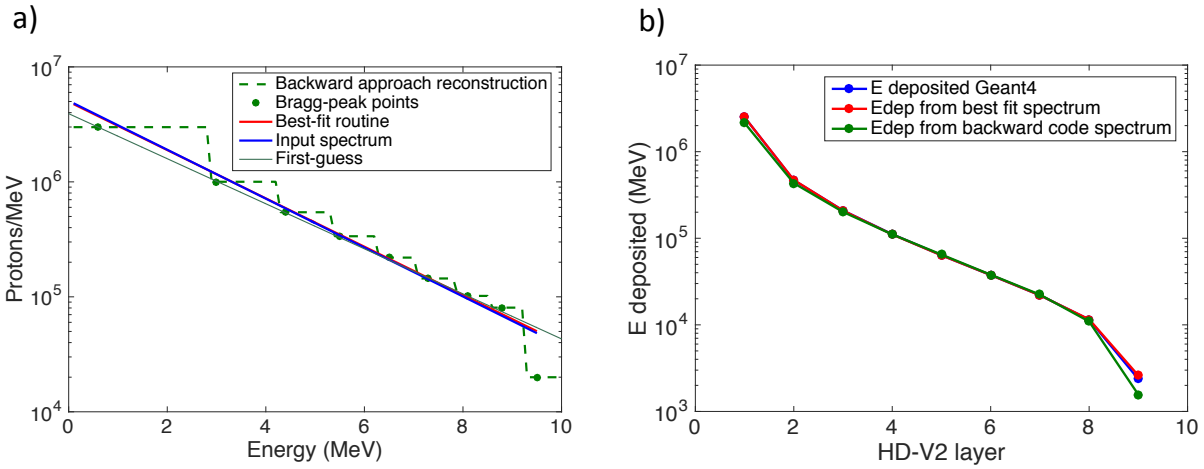

Figure 3.5: a) Comparison of the spectra obtained through both the backward approach and the best-fit routine with the original spectrum simulated in Geant4 (blue line). b) Energy profiles in the stack corresponding to the spectra obtained with both the best-fit routine (red line) and the backward approach (green line), compared with the energy released in the stack in the Geant4 test simulation (blue line), generated by the input spectrum.

of 7.7%. The discrepancy with the energy deposited by the input spectrum (blu line) is evident for the last foil because of the overestimation of the energy cut-off. The energy profile generated by the best-fit spectrum perfectly matches the energy deposited by the input spectrum, with an error of 1%.
This procedure is employed in the next section to reconstruct the spectrum of the TNSA source of the SAPHIR facility described in section 2.5.

3.1.3 SAPHIR source characterisation

The SAPHIR accelerator produced, as described in section 2.5, a 7.5 MeV TNSA proton source. It had been characterised during the experimental campaign using a Thomson Parabola (TP) and a radiochromic film stack[5] [162]. In this section, the spectroscopy technique described in section 3.1.2 is used to reconstruct the SAPHIR spectrum compare the results with previous data.

The scanned images of the irradiated films (Fig. 3.6, left column) are used to obtain the dose deposited in each film and the in-depth energy profile. Since no calibration curve was available for the batch of HD-V2 that had been used for the stack measurement, conversion of the optical density into dose was performed with a calibration curve obtained by the INFN-LNS group with another batch using 60 MeV protons[6]. The obtained dose maps are shown in Fig. 3.6 (right column).
The energy delivered in the films is employed, as explained in section 5.1, as input and fitting parameter of the spectroscopy technique. Since the dose absorbed by the first film is above the upper limit of the dynamic dose range of HD-V2 films, only the energy released from the second to the last film is used as input to the best-fit spectroscopy technique. Also, a more accurate Geant4 Energy-Coefficient Library (RCF-ECL) was generated by simulating the 13 µm thick aluminum layer used to cover the stack, resulting in the ECL shown in Fig. 3.7. Fig. 3.8 shows the comparison between the in-depth energy profile measured in the stack and the in-depth energy profile generated by the spectrum resulting from the best-fit technique, computed using the Geant4 RCF-ECL.

[5]The stack was positioned 4 cm behind the target and covered with an aluminium layer of 13 µm to protect it from laser light and debris. The films were irradiated with 25 consecutive shots and then scanned with a resolution of 600 DPI.

[6]A correct use of radiochromic films requires calibration of each film batch with the same scanner used for film reading. Employing a calibration curve obtained for a different film batch and with a different scanner typically entails error in the dose conversion around 15-20% [60, 206].

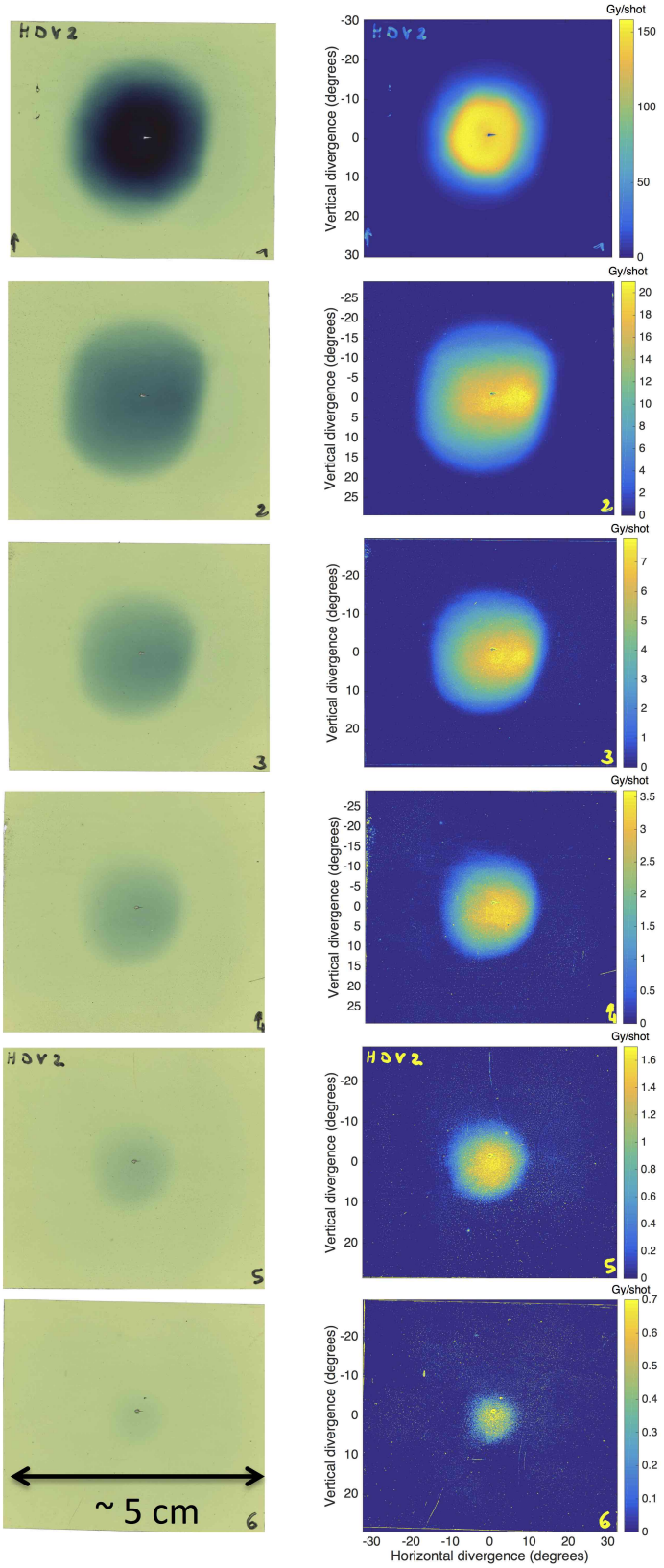

Figure 3.6: Left column: scan of the HDV2 film stack. Right: dose maps as a function of the divergence angle. No signal was measured on the 7th layer.

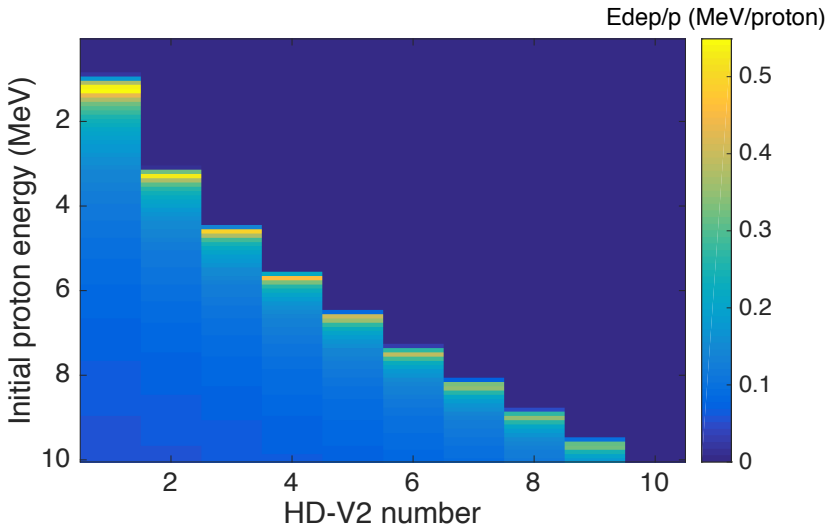

Figure 3.7: Energy released per proton in the active layers of the stack as a function of the initial proton energy. The Aluminium layer in front of the stack stops all protons with energies lower than 0.9 MeV.

The agreement between the two curves is remarkably good, with an average error of 11%[7], largely due to the error on the last film. Such error can be ascribed to the resolution employed for the cut-off energy in the spectroscopy routine limited to 100 keV and to the imprecision of the OD to dose conversion in the last film[8]. The proton spectrum is shown in Fig. 3.9.a. It's analytical exponential shape is:

$$\frac{dN}{dE} = 1.79 \times 10^{10} \cdot \exp\left(-\frac{E}{1.24}\right) \tag{3.19}$$

It features a cut-off energy of 7.4 MeV and a total integrated charge of 1.8 nC/shot. The cut-off energy determined by the best-fit technique is in good agreement with the spectrum measurements obtained with a Thomson parabola, as shown in Fig. 3.9.b.The energy-dependent divergence (Fig. 3.9.c) was obtained by analysing the film 2D dose profile and assigning the obtained average divergence to the corresponding initial proton energy having the Bragg-peak in the film[9].

[7]The error does not take into account the first-film of the stack, which was not used for the best-fit procedure. However, we observe that the energy released in the first film by the best-fit spectrum closely matches the energy obtained experimentally through OD conversion, although the dose received by such film is outside the dynamic range. This is not surprising since the films do not abruptly saturate, as shown in few works reported in literature [57, 128].

[8]The last film received a dose of around $\sim$ 12 Gy, which is very close to the lower dose range limit of the HD-V2 films of 10 Gy).

[9]This approach could be further improved by implementing a spatially-resolved spectroscopy technique employing the 3D dose distribution in the stack as fitting parameter instead of the in-depth energy profile.

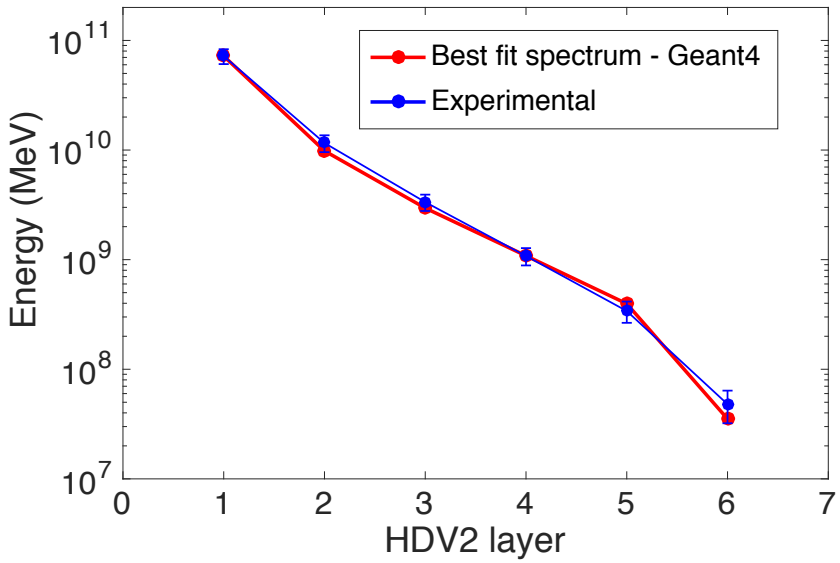

Figure 3.8: In-depth energy profile in the film stack. The blue line represents the measured profile while the red line represents the profile obtained by computing the energy released by the best-fit spectrum using the Geant4 energy coefficient library.

As it was previously mentioned, a rough estimation of the spectrum can be obtained by simply assuming that the energy delivered in each film is due to protons having their Bragg-peak in the sensitive layer. This was the method initially used to reconstruct the SAPHIR proton source [162]. Figure 3.10 shows a comparison between the SAPHIR proton spectrum obtained using the best-fit deconvolution technique and the spectrum obtained using the aforementioned assumption. Since the energy released in a film of the stack is due to all energy components with $E > E_{co}$, the "rough" spectral reconstruction (black line) overestimates the yield of lower energy components with respect to the higher energy components, which can lead to non negligible errors in the spectral shape. Moreover, this simple method does not allow to quantify the total charge but only to determine the relative yield of the spectrum. For this reason, a deconvolution technique is necessary to obtain the spectrum at the source with a high accuracy prior to the design of a transport beamline.

Source reconstruction in Geant4 The SAPHIR source parameters, i.e. spectrum and energy-dependent divergence (Fig. 3.9), were reproduced in Geant4 using multiple

Such technique would also need a precise modelisation of the beam divergence analytical shape, which is a complex issue. In the following, the divergence of the beam is simply modeled as a gaussian profile on the transversal axis. As it will be shown, this modelisation does not introduce significant errors in the beam transport simulation.

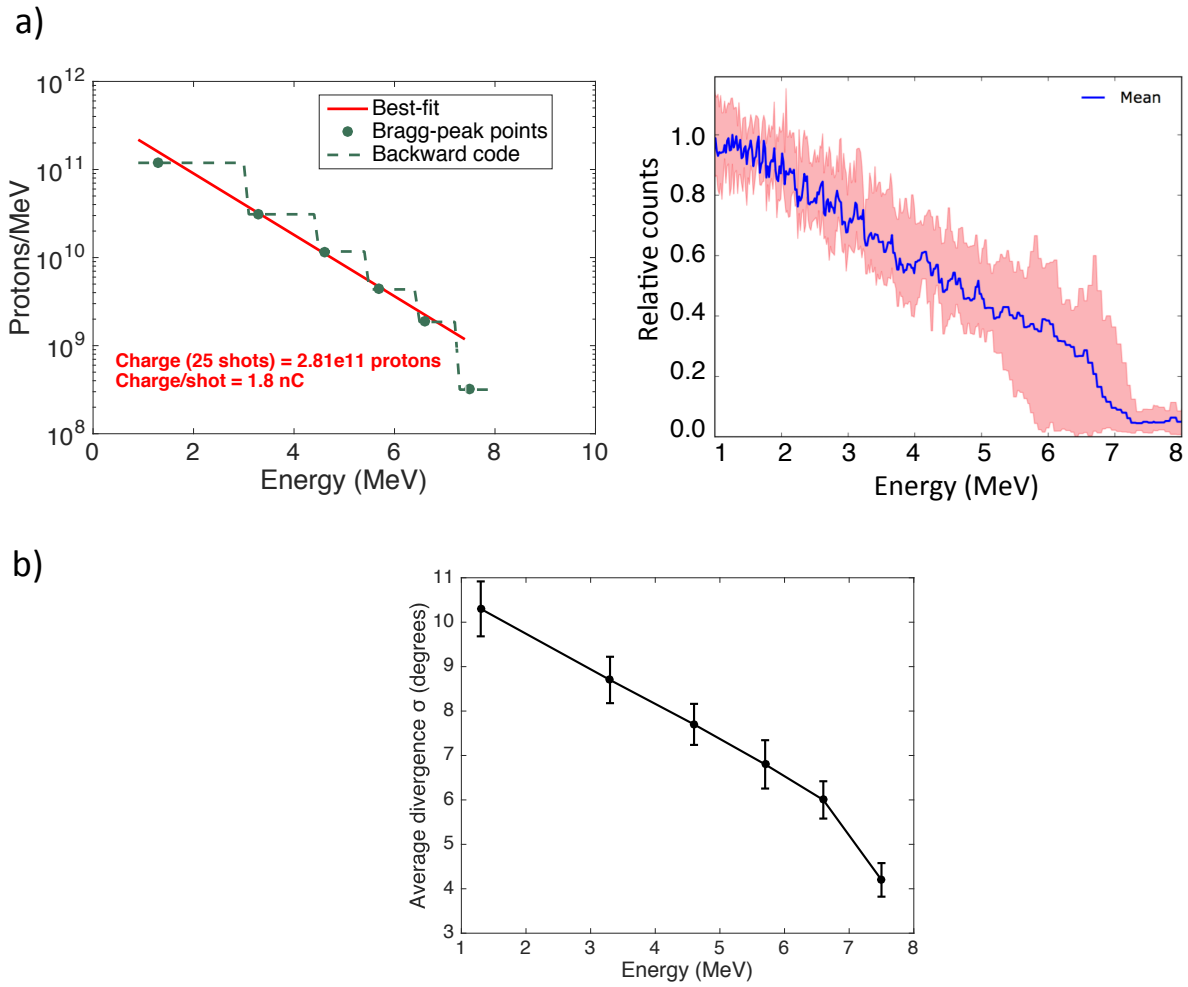

Figure 3.9: a) Left: source spectrum obtained through film spectroscopy techniques. The green dashed line indicates the spectrum obtained through the backward approach, used as input to the best-fit routine to obtained the best-fit spectrum (red line). Right spectrum on the target normal axis obtained with a Thomson parabola spectrometer integrating 8 shots. Taken from Pommarel et al. (2017) [163]. b) Energy resolved divergence.

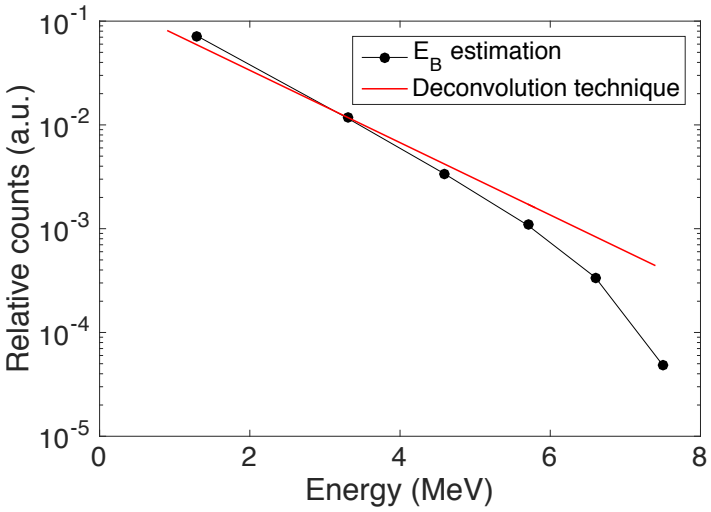

Figure 3.10: Comparison between the spectrum estimated using the assumption that the energy deposited in the film is due to protons having their Bragg-peak in the sensitive layer (black points) and the spectrum obtained using the deconvolution technique.

divergent sources. The exponential spectrum was divided into energy bins of 100 keV and each spectral bandwidth was simulated with the corresponding energy-resolved divergence. The energy deposited in an HD-V2 film stack positioned in front of the beam (as in the experiments) was simulated to further validate the spectrum obtained with the best-fit spectroscopy routine, which employs the RCF-ECL library to generate the in-depth energy profile in the stack. Fig. 3.11 shows the in-depth energy deposition profile in the stack produced by the divergent source simulated in Geant4 (black line), compared with the measured profile (blue line). The two profiles perfectly agree except for the last film. The energy delivered in such film by the divergent beam simulated in Geant4 is 77% lower than the measured energy and even lower than the energy associated to the best-fit spectrum obtained with the Geant4 RCF-ECL (red-line). The seemingly remarkable difference is actually due to a negligible underestimation of the cut-off energy obtained with the spectroscopy technique. It can be explained by considering that the best-fit spectrum is obtained through the use of Geant4 energy-coefficients computed by simulating a collimated beam impinging on the stack (see section 3.1.2). Divergent protons need to travel for a longer distance to reach the last active layer compared to protons impinging perpendicularly to the stack. As a consequence, the energy of protons reaching the last film is higher if they feature a given divergence compared to the collimated beam scenario. Therefore, since the Geant4 RCF-ECL is obtained with collimated beams, the best-fit procedure may slightly underestimate the cut-off energy of a divergent beam. To give an estimation of the inaccuracy on the cut-off energy, let us consider the distance traveled

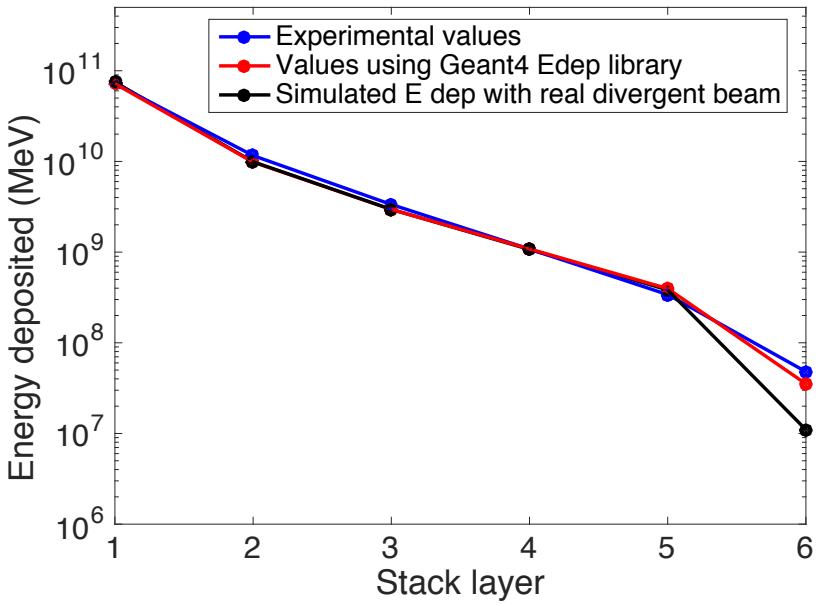

Figure 3.11: In-depth energy profiles in the HD-V2 film stack. The blue line represents the measured profile, the red line represents the profile generated by the best-fit spectrum obtained with the Geant4 energy coefficient library (collimated beam) and the black line represents the energy profile obtained by simulating the divergent beam with Geant4.

to reach the last sensitive layer by protons with an initial divergence of 5°, corresponding to the typical divergence of the energy components reaching the last film (see Fig. 3.9.c), and by protons with initial momentum along the propagation axis. The initial divergence of 5° results in a difference of travelled distance (or proton range) at the 6^{th} film of 2.3 µm and, as a consequence, in an underestimation of the cut-off energy in the order of several tens of keV. Since only the higher energetic components of the spectrum deposit their energy in the last film (the portion of spectrum above 7.3 MeV according to Fig. 3.7) an underestimation of tens of keV may explain the large difference in the energy released in the last layer. This estimation has been verified by simulating the energy deposited in the last film with an initial spectrum extrapolated to 7.5 MeV. As expected, with this correction the energy deposited in the last sensitive layer resulted to be perfectly in line with the experimental value, with an error of only 2%.

In conclusion, the remarkable error on the energy deposited in the last film is the result of a sufficiently small error of 0.1 MeV (1.3%) on the cut-off energy. Moreover, LPAP transport systems are typically designed to transport a spectral bandwidth that is significantly lower than the cut-off energy in order to reduce the impact of shot-to-shot fluctuations. Therefore, the inaccuracy on the cut-off energy is definitely negligible for the definition of irradiation conditions at the biological sample.

3.2 Transport

As discussed in section 2.3, various transport systems have been used in the last years to both shape the proton beam and select the desired spectral bandwidth. The approach used in this thesis to shape LPAP beams consists in the use of quadrupoles coupled with scattering systems. The design of the beamlines is performed with an in-house algorithm that computes the particle trajectories and with the Geant4 tool. Before entering into details, this section briefly presents the theoretical aspects of quadrupoles.

3.2.1 Quadrupole theory

Charged particle beams are transported and shaped through the use of electric and magnetic fields, that can modify the beam trajectory (bending magnets) and keep particles close to the beam axis (focusing magnets). The electromagnetic force acting on a charged particle is described by the well-kwown Lorentz formula:

$$\vec{F} = q \cdot \left(\vec{E} + \vec{v} \times \vec{B} \right) \tag{3.20}$$

where $\vec{E}$ and $\vec{B}$ are respectively the external electric and magnetic fields, q is the particle charge and $\vec{v}$ its velocity. Since the magnetic force is proportional to the particle velocity, magnetic devices are more efficient than electrical ones for high-energy and particularly relativistic particles, and are preferably used for beam guidance. Among magnetic devices, dipoles are typically used to deflect the beam path while quadrupoles act as a focusing-defocusing system without affecting the beam direction. In this section we will briefly discuss the properties of such devices with particular attention to quadrupoles, as they are largely employed in this thesis for LPAP beam transport and shaping.

Beam deflection When a charged particle enters a magnetic field, according to formula (3.20), it is accelerated in a direction that is orthogonal to both the velocity and the magnetic field vectors. Its trajectory is determined by the equilibrium between centrifugal force and Lorentz force:

$$\vec{F_c} = m \cdot a_c^2 = q \cdot (\vec{v} \times \vec{B}) \tag{3.21}$$

We introduce, for simplicity, a Cartesian axis oriented in such a way that the initial particle velocity vector has only the z component, i.e. $\vec{v} = v_z$. Assuming a transversal magnetic field oriented towards the vertical direction y, a positive charged particle is deflected on

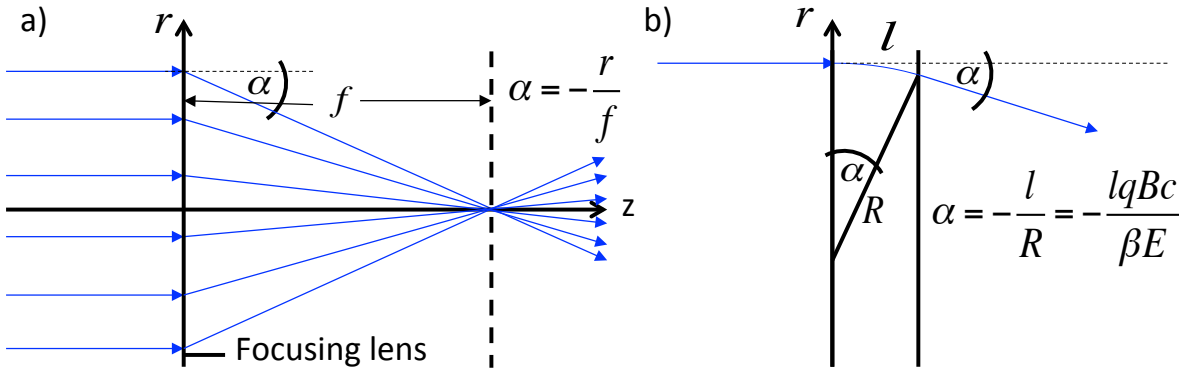

Figure 3.12: a) Schematic of a focusig lens. b) Property of a magnetic focusing device

the z-x plane towards the negative x direction, with a bending radius R given by:

$$m\gamma \cdot \frac{v^2}{R} = qvB \tag{3.22}$$

$$R = \frac{\beta E}{qBc} \tag{3.23}$$

Where $\gamma = 1/\sqrt{1-\beta^2}$ is the Lorentz factor to correct for relativitic energies, $\beta = v/c$ and E is the particle energy. Therefore, particles follow a circular trajectory on a plane perpendicular to the magnetic field with a bending radius proportional to the particle energy and inversely proportional to the magnetic field.

Beam focusing In beam dynamics, focusing systems are required to keep particles together. Charged particle beams often feature an inherent divergence, due to the mutual repulsion between particles, or an initial divergence at the source, as it is the case for LPAP. In addition, focusing elements can be used to shape the beam and obtain requested properties at the end of a transport beamline, such as given beam shape and emittance. The properties of a magnetic focusing device are similar to those of optical lens. Optical lens can deflect the incoming parallel light rays by an angle α proportional to the distance from the lens axis r (see Fig. 3.12.a) and focus them to the so-called focal point at a distance f. For small angles, we can assume $\tan\alpha = \alpha$ and write:

$$\alpha = -\frac{r}{f} \tag{3.24}$$

According to its definition, the existence of a focal point requires the bending angle to increase linearly with the distance r. We can therefore employ this definition to derive the

properties required for a magnetic field to obtain the same focusing effect. To this aim, we assume that the length l of the magnetic field traversed by the particle is negligible compared to the focal length $l \ll f$ (thin lens approximation). With this assumption, and recalling that a particle entering a magnetic field is deflected along a circular trajectory having a radius R given by equation 3.23, the deflection angle α can be simply expressed as:

$$\alpha = -\frac{l}{R} = -\frac{lqBc}{\beta E} \tag{3.25}$$

The expression indicates that focusing properties can be achieved by a magnetic device with an azimuthal magnetic field increasing linearly with the distance r:

$$B = g \cdot r \tag{3.26}$$

Such field can be produced with a so-called quadrupole magnet.

Quadrupole system In a quadrupole transverse section, the vertical field component increases linearly along the horizontal axis and the horizontal field component increases linearly along the vertical axis, as shown in Fig. 3.13, according to:

$$B_x = g \cdot y \tag{3.27}$$

$$B_y = g \cdot x \tag{3.28}$$

Where g is the quadrupole gradient. By inserting this expression in equation 3.25, we obtain the formula of the quadrupole focal length as a function of its length l and its field gradient g [203]:

$$f = \frac{\beta E}{lqcg} = \frac{1}{kl} \tag{3.29}$$

where k is called "quadrupole strength" and is used to characterize the magnetic properties of the quadrupole. It is a function of both the quadrupole field gradient g and the particle energy E. Therefore, quadrupoles are chromatic elements, and a given quadrupole beamline configuration is optimised for a specific energy component of the beam. In their simplest structure, quadrupoles consist in four permanent magnets[10] arranged with alternating polarity, genereting hyperbolic magnetic equipotiential surfaces and a magnetic

[10]The quadrupole field can be also generated with electric currents flowing in coils wrapped around the poles (electromagnet quadrupoles). To reach the required field of ∼100 T/m, large superconducting systems are needed.

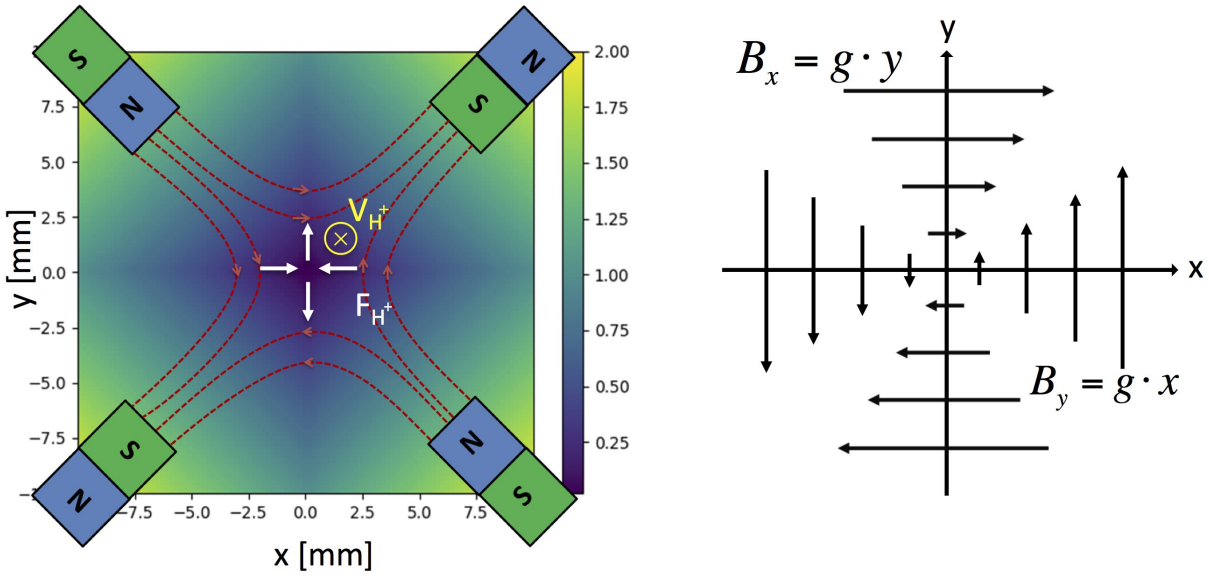

Figure 3.13: Quadrupole field structure. Left: magnetic field intensity of quadrupole transverse section with a gradient of 100 T/m, adapted from A. Ghaith (2019) [75]. The red arrows indicate the magnetic field lines while the white arrows indicate the direction of the force exerted on a positively charged particles along the axis. A proton beam would be focused on the horizotanl axis and defocused on the vertical axis. Therefore, at least another quadrupole with a 90° rotation is needed to focus the beam on both directions. Right: schematic of the magnetic field pattern on the axis.

field that increases with the radial distance (see Fig. 3.13). Thus, particles that are farther from the centre experience a larger force. Due to geometrical properties of a permanent quadrupole magnet (PMQ) structure, the magnetic field of a real quadrupole features a slightly non-constant gradient and other magnetic impurities leading to higher order multipoles. Therefore complex PMQ structures are usualy employed to eliminate higher order magnetic components [75]. However, real quadruopoles are often modelled as ideal quadrupole with an average field gradient. This approximation is often appropriate and allows the use of analytic solutions and methods to determine particle motion.

As shown in Fig. 3.13, a quadrupole acts as a focusing system along one axis and as defocusing system along the other axis. Therefore, in order to focus a beam in both transverse directions, a beamline composed of two or more quadrupoles rotated of 90° is nedeed.

The interesting property of quadrupoles (supposing an ideal field), is that the horizontal and vertical motions are decoupled, as the force exerted on one axis depends only on the particle position along such axis. For the x axis, for example:

$$F(x) = qvB_y(x, y) = qvgx \tag{3.30}$$

The force exerted along the x axis does not depend on the particle position on the y axis and, therefore, the equation of motion along the independent variable z can be written and solved separately for the two axis.

Matrix formalism For a non-perturbated beam and considering only dipoles and quadrupoles (linear optics), the equation of a particle motion in a magnetic field can be written separately for each coordinate, as follows [203]:

$$u''(z) + Ku(z) = 0 \tag{3.31}$$

where u is the coordinate x or y and K contains the two terms:

$$K = k + k_0^2 \tag{3.32}$$

The first coefficient k is the focusing strength of a quadrupole field (see eq. 3.29) and the coefficient k_0 is the deflection angle of the beam axis path introduced by a bending dipole field (see eq. 3.23). Therefore:

$$\begin{cases} k = 1/fl = qcg/\beta E \\ k_0 = 1/R = qcB/\beta E \end{cases} \tag{3.33}$$

A beam transport line is normally composed by many magnet lattices, each of which has a different value of k or k_0. In general, these coefficients are therefore not constant along the independent coordinate z. However, if we consider ideal quadrupoles, they can be assumed to be constant within individual magnets and null in drift spaces between the magnets. With this assumption, the equation of motion can be solved analitically and the value of $u'(z)$ and $u(z)$ can be obtained at each position along the beamline using a simple "transformation matrix", as follows:

$$\begin{bmatrix} u(z) \\ u'(z) \end{bmatrix} = \begin{bmatrix} C_u(z) & S_u(z) \\ C'_u(z) & S'_u(z) \end{bmatrix} \begin{bmatrix} u_0 \\ u'_0 \end{bmatrix} \tag{3.34}$$

For a quadrupole beamline, the transformation matrix is expressed by:

$$\begin{cases} \begin{bmatrix} \cos(\Psi) & \frac{1}{\sqrt{k}}\sin(\Psi) \\ -\sqrt{k}\sin\Psi & \cos\Psi \end{bmatrix} & \text{Focusing quadrupole } k<0 \\ \begin{bmatrix} \cosh(\Psi) & \frac{1}{\sqrt{|k|}}\sinh(\Psi) \\ \sqrt{|k|}\sinh\Psi & \cosh\Psi \end{bmatrix} & \text{Defocusing quadrupole } k>0 \\ \begin{bmatrix} 1 & l \\ 0 & 1 \end{bmatrix} & \text{Drift space } k=0 \end{cases} \tag{3.35}$$

In the expression, $\Psi = \sqrt{k} \cdot l$, where l is the length of the quadrupole or the length of the drift space for $k = 0$. The matrixes are valid for any quadrupole section of length $l = z - z_0$. Therefore, the value of $u^{'}$ and u at a generic position z along a beamline composed by a given number of quadrupoles and drift spaces can be obtained by simply multiplying the initial vector $[u_0^{'}, u_0]$ by the total transformation matrix:

$$\begin{bmatrix} u(z) \\ u^{'}(z) \end{bmatrix} = M_{tot} \begin{bmatrix} u_0 \\ u_0^{'} \end{bmatrix} \tag{3.36}$$

For example, for the PMQ beamline shown in Fig. 3.14, the total transformation matrix at the position z is given by:

$$M_{tot} = M_{d/0-l_1} \cdot M_{Q/l_1-l_2} \cdot M_{d/l_2-l_3} \cdot M_{Q/l_3-z} \tag{3.37}$$

3.2.2 PMQ beamline design and simulation tools

The design of PMQ-based transport lines for LPAP required the development and validation of specific tools, described herafter.

Development of an algorithm to compute the particle envelopes The matrix approach previously presented allows the study of particle trajectories in a quadrupole beamline without the need of solving the equation of motion through complex finite difference methods. The matrix approach has been implemented in a Matlab code to determine particle trajectories in a given quadrupole beamline configuration. The code requires to specify the quadrupole parameters such as field gradient, length and bore aperture, the

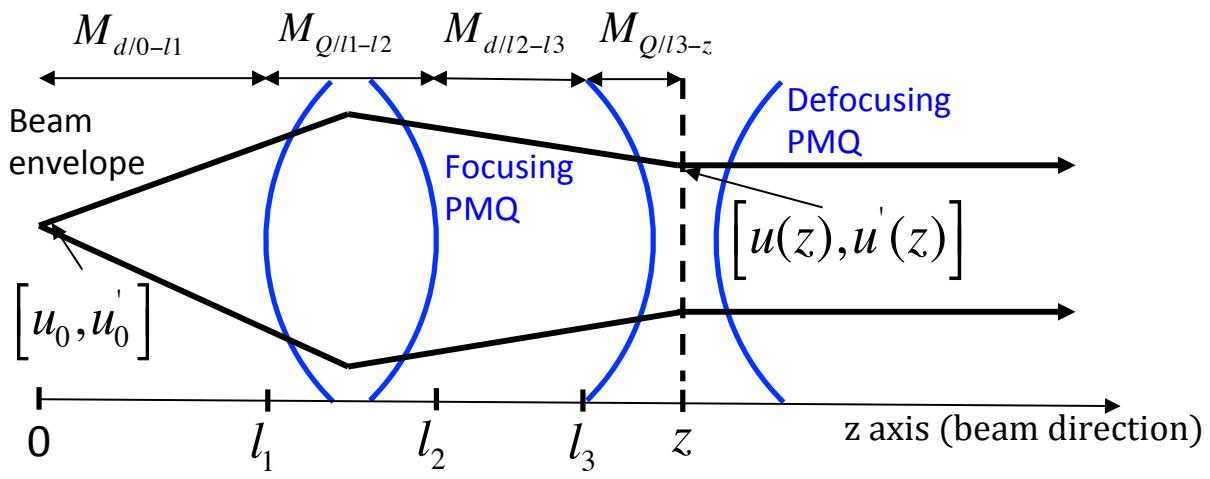

Figure 3.14: Schematic of the matrix approach for a simple beamline composed by two quadrupoles and two drift spaces.

beamline configuration (relative position of the quadrupoles and their polarity), as well as particle parameters, such as the type and the initial energy and direction. Through the matrix approach, the code determines the trajectory of a given particle along the independendent propagation axis z for a system of (ideal) quadrupoles. In addition, the algorithm can also solve the equation of motion through the finite difference Tajima's implicit method (https://www.particleincell.com/2011/vxb-rotation/). This approach can be used to determine the particle trajectories in a real quadrupole beamline, if the field maps inside the magnets are known. However, for the precision required in LPA particle transport, the assumption of ideal fields and the use of the matrix approach is an acceptable approximation. Fig 3.15 shows an example of the algorithm output for 6 MeV and 8 MeV protons entering an ideal quadrupole doublet system with a different initial divergence (as it is the case for laser-plasma accelerated protons). The trajectories are determined with both the matrix approach (Fig 3.15.a) and the Tajima's method (Fig 3.15.b). The finite difference solution perfectly agrees with the analytic one, with an error of the order of 1 mm on the focus position.

The code is used for preliminary design of quadrupole beamlines[11] (see section 4.1 and 4.2 devoted to the design of LPAP beamlines for radiation biology experiments), since it allows for the rapid visualisation of the divergence and size of the envelopes of different energetic components along the beamline. The design of the beamline is then refined and further optimised with a Geant4-based code.

[11]The quadrupole configuration is optimised to adjust the output beam dimension and focus the desired energy components. The parameters to be optimised are the relative position between quadrupoles, their order and polarity (90° rotation).

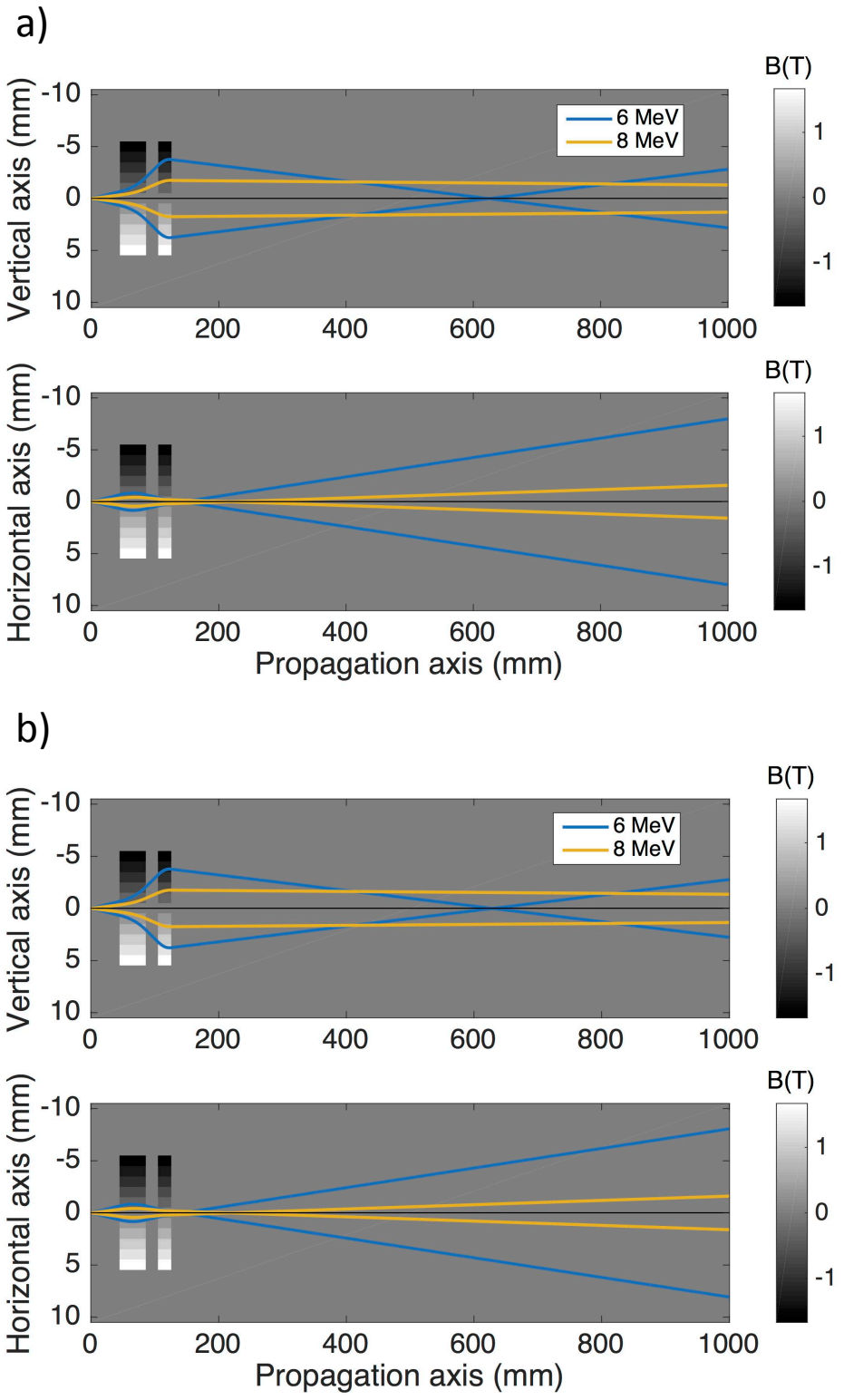

Figure 3.15: Envelopes of protons along a doublet quadrupole system. The quadrupoles have a length of 40 mm and 20 mm, an ideal field of 333 T/m and a bore aperture of 10 mm. The envelopes have been calculated using the analytic matrix approach (a) and the finite difference Tajima's method with a time step of 0.5 ps (b).

Geant4 for transport simulation The Geant4 tool[5] (Geant4.10.04 version)[12] is used in this thesis to simulate both particle transport and interaction with matter. In recent years, the use of Geant4 for LPA beam transport simulation has increased rapidly [171, 193, 172, 137, 49]. The benefit of using a Monte Carlo (MC) code lies in the ability to simulate both the beam transport and radiation-matter interaction with a single tool. This means that the desired dose distribution at the biological sample can be used as fitting parameter to directly optimise different beamline aspects, such as the transport system configuration and the position and design of scattering systems. Furthermore, simulation of the beamline with a Monte Carlo code opens up the possibility of studying complex shaping techniques that combine the chromatic properties of the transport system with the energy losses induced by interaction of the beam with matter (see section 3.3).
A modified version of the "Hadrontherapy" Geant4-based application [47, 50] is employed to simulate the SAPHIR beamline. The application, released by INFN-LNS of Catania, was specifically developed to address typical needs related to the proton and ion therapy and was recently used to simulate the ELIMED beamline. It is used for the simulation of the SAPHIR beamline since the INFN-LNS quadrupole field-maps had already been implemented. The source code has been further modified to reproduce other geometries and to allow for a 90° rotation of the quadrupoles.

3.2.3 Validation of Geant4 transport simulation

The SAPHIR beamline (2.5) was reconstructed in Geant4 to validate the transport simulation through comparison with measurements and simulations performed with transport codes prior to the beginning of this thesis [183]. The 7.5 MeV TNSA source was generated as described in section 3.1.3 and the beam was tracked along the four quadrupoles arranged in the configuration used for radiobiology experiments showed in Fig. 3.16. The quadrupole field was simulated using measured field maps [182] and the QGSP_BIC physics list was used to model transport and radiation-matter interaction, as it has been extensively validated in the energy domain of medical applications [46, 90]. A side view of the beamline simulated in Geant4 is shown in Fig. 3.16.
The simulated transverse beam profile along the beamline was compared to the measured profile in order to assess the accuracy of the transport simulation. The measurements were previously carried out [183] with EBT3 radiochromic film stacks consisting of two films shielded by 26 µm of aluminium foil. The stacks were placed at different positions along the beamline, as shown in Fig. 3.16. The dose delivered in the two layers of the

[12] https://geant4.web.cern.ch/support/user_documentation

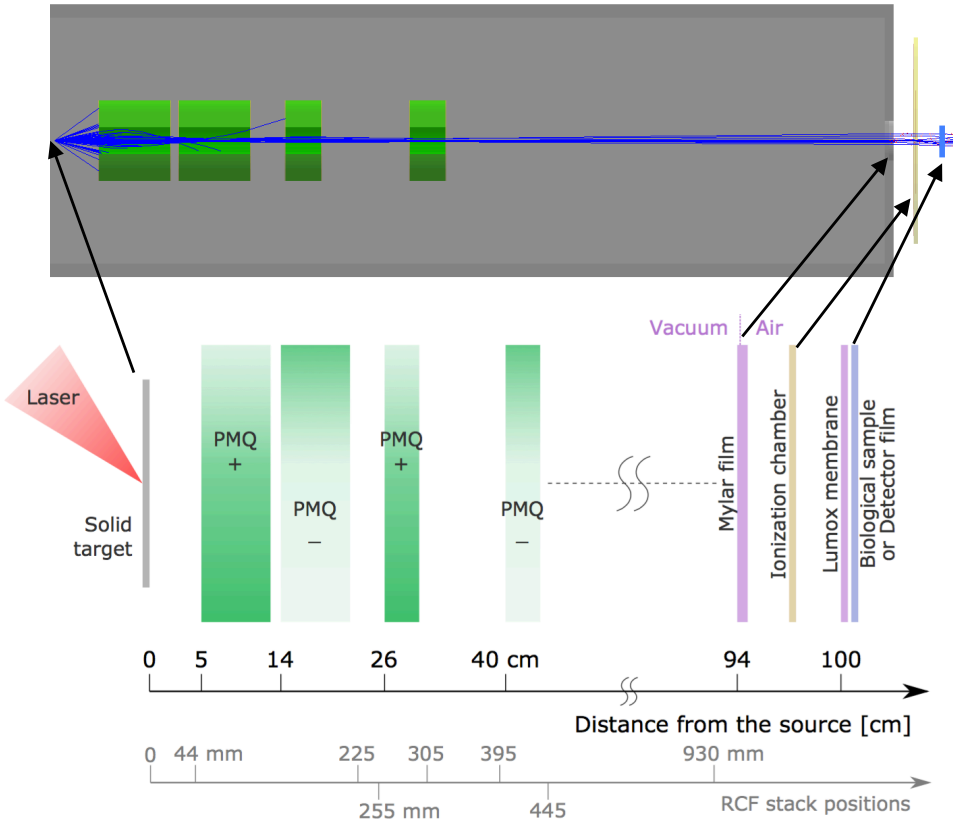

Figure 3.16: Top: side view of the SAPHIR beamline simulated in Geant4. Bottom: Schematic of the beamline containing the relative position of the elements and of the EBT3 stacks along the beamline used to measure the beam trasnverse profile.

stack is due to different energetic components, similarly to what was previously described regarding the HD-V2 film stack spectroscopy technique (see section 3.1.2). Precisely, the first sensitive layer is reached by the energetic components above 3.66 MeV, since lower energies are blocked by the aluminium foil and by the first protective layer, and the second sensitive layer is reached by the energetic components above 6.48 MeV. Therefore, separate Geant4 simulations have been performed for each stack position to reproduce the experimental dose transverse profiles obtained with the EBT3 stacks. In each simulation, the simulated EBT3 stack was placed at one of the specified positions along the beamline and the dose delivered in the two film sensitive layers were retrieved with a Geant4 sensitive scoring.

Fig. 3.17 and Fig. 3.18 show the simulated 2D dose transverse profiles along the beamline respectively in the first and second film of the stack. They are compared with the experimental dose profiles obtained with the EBT3 films[13] and with the results previously

[13]The experimental dose profiles are obtained using a generic EBT3 calibration for 5 MeV protons [195].

obtained [183] by simulating the beamline with a transport code called Simion[14], which takes into account beam collective effects such as space-charge, but it does not enable simulation of the particle interaction with matter. The beam dose profile simulated with Geant4 matches remarkably well the experimental profiles and seems to be as accurate as a transport code as Simion[15].

To further validate the beamline modeling, the total energy released in the second film of the stack[16] has been compared with the total energy registered in simulations. The released energy is obtained by converting the 2D dose maps into deposited energy maps, considering the sensitive layer as composed by water, and then integrating the deposited energy over the beam shape. The energy retrieved with Geant4 simulations (the number of primary particles shoot in the simulations is 10^8 protons) is normalised for a charge at the source of 1.8 nC, as estimated in section 3.1.3, with an error bar of 20% due to the estimated error in the HD-V2 calibration. Likewise, the error on the EBT3 measurements due to calibration inaccuracy is estimated around 20%. The results of the comparison are shown in Fig. 3.19. As it is shown, the absolute values of the energy simulated in the second layer of the stack, considering the total charge at the source of 1.8 nC obtained with HD-V2 film stack spectroscopy, matches, within the error bars, the energy measured with EBT3 stacks. This result further validates both the estimation of the total charge at the source obtained with film stack spectroscopy and the reconstruction of the transport system with Geant4. In addition, the result suggests that modelling the proton source divergence with a gaussian distribution does not introduce significant errors in the transport efficiency.

Space-charge effect The external forces exerted on a single particle by the PMQ's magnetic field do not depend on the particle density. However, the beam itself could produce additional electro-magnetic fields, called "self-fields", that depend on the charge density and its distribution. Such self-fields can generate space-charge effects, often undesired in beam dynamics, such as spectral spreading and change in the transversal and longitudinal charge distribution [66].

Single-particle tracking codes as Geant4 can not natively simulate space-charge effects, which may affect the accuracy of the beam transport simulation. Altough the results obtained in the previous section suggest that space-charge along the beamline is negligible,

[14] https://simion.com/.

[15] It is worth noting that Simion's output is the 2D flux profile, since the code does not simulate radiation matter interaction.

[16] The dose received by the first film of the stack slightly exceeds the upper limit of the EBT3 dynamic dose range. For this reason only the second film was used for the purpose.

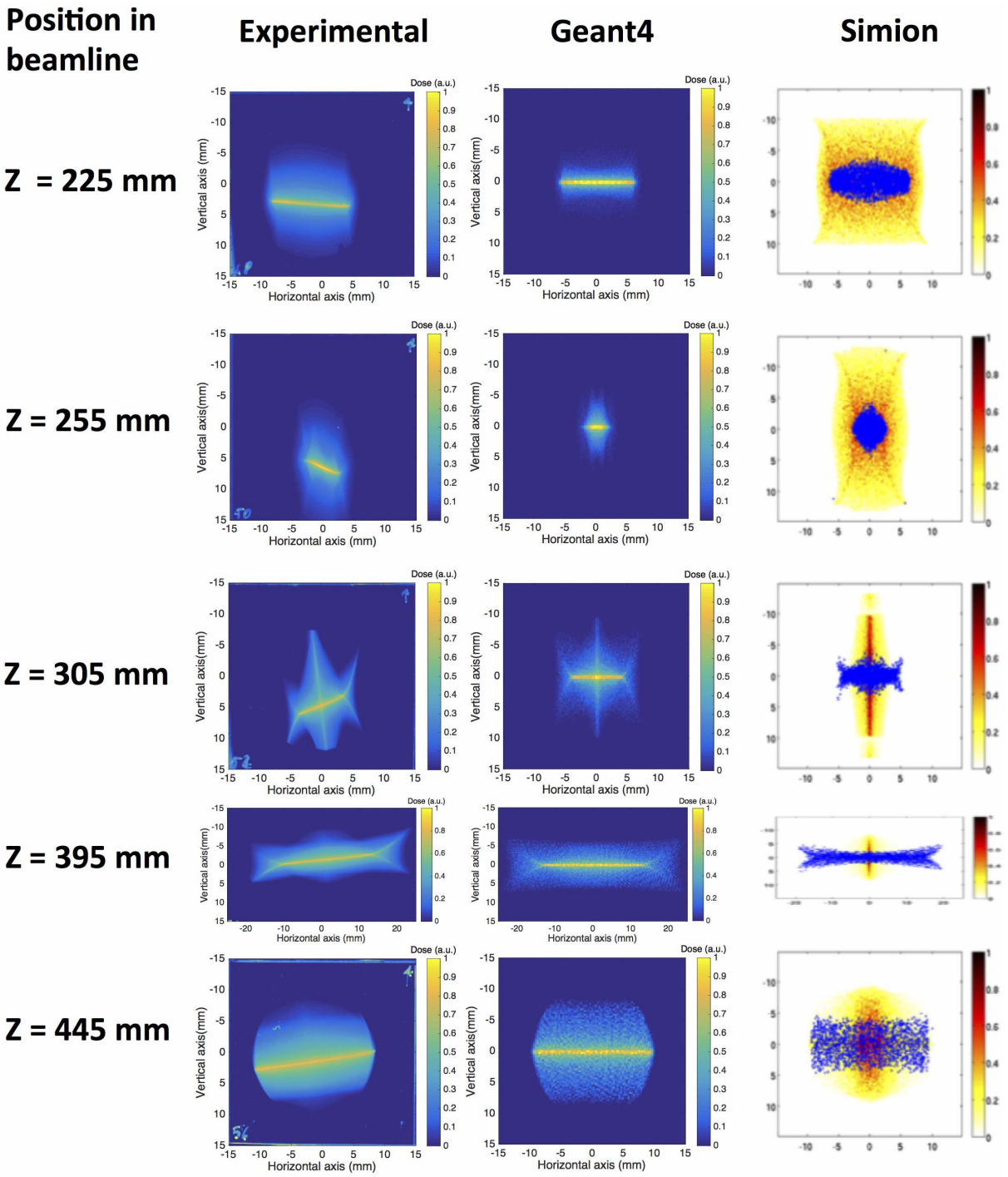

Figure 3.17: Dose profiles on the first film of the EBT3 stack along the transport system. The first column contains the experimental profiles, the second column contains the profiles obtained with Geant4 and the third column contains the results obtained by L. Pommarel (2017) [162] with Simion.

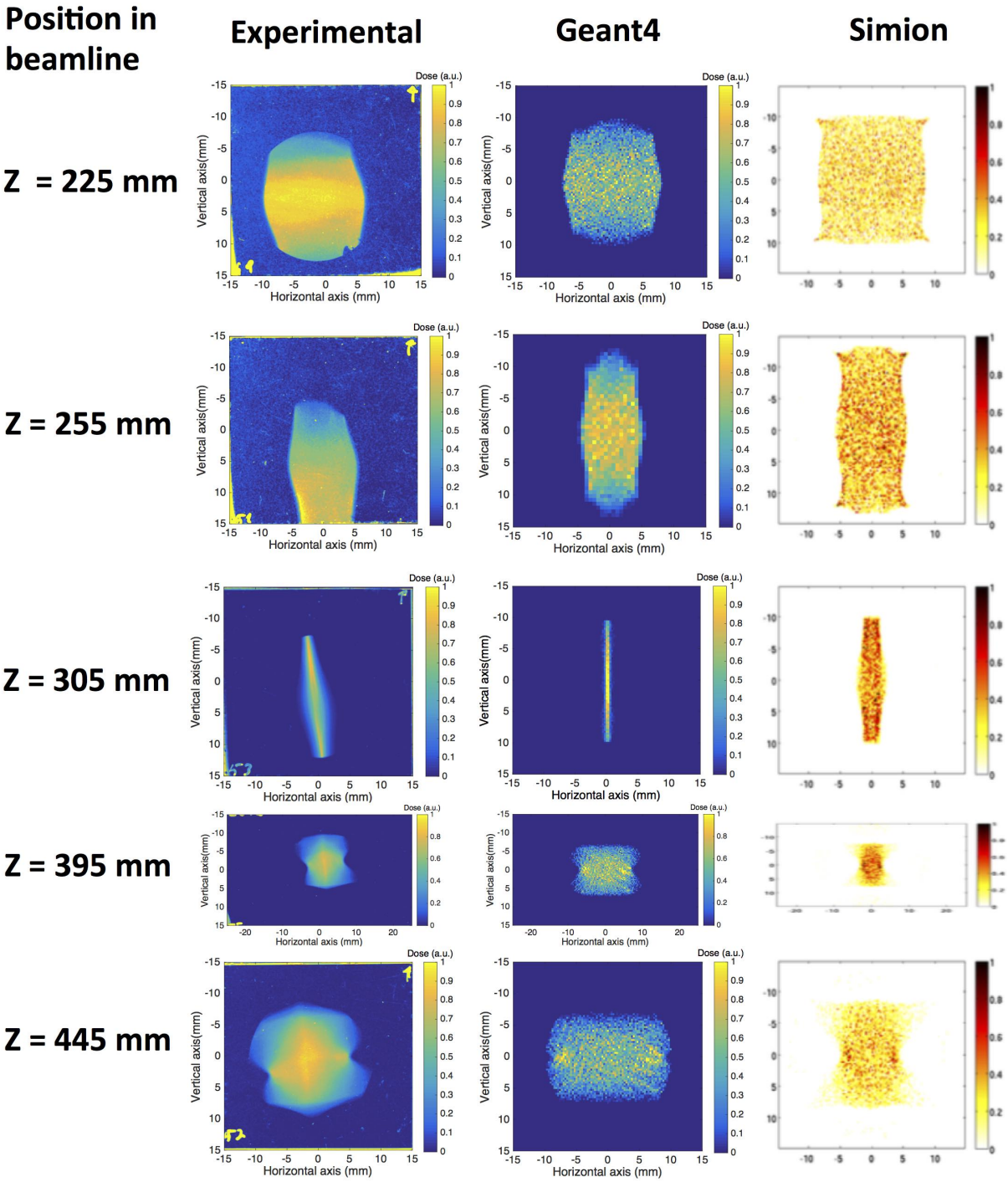

Figure 3.18: Dose profiles on the second film of the EBT3 stack along the transport system. The first column contains the experimental profiles, the second column contains the profiles obtained with Geant4 and the third column contains the results obtained by L. Pommarel (2017) [162] with Simion.

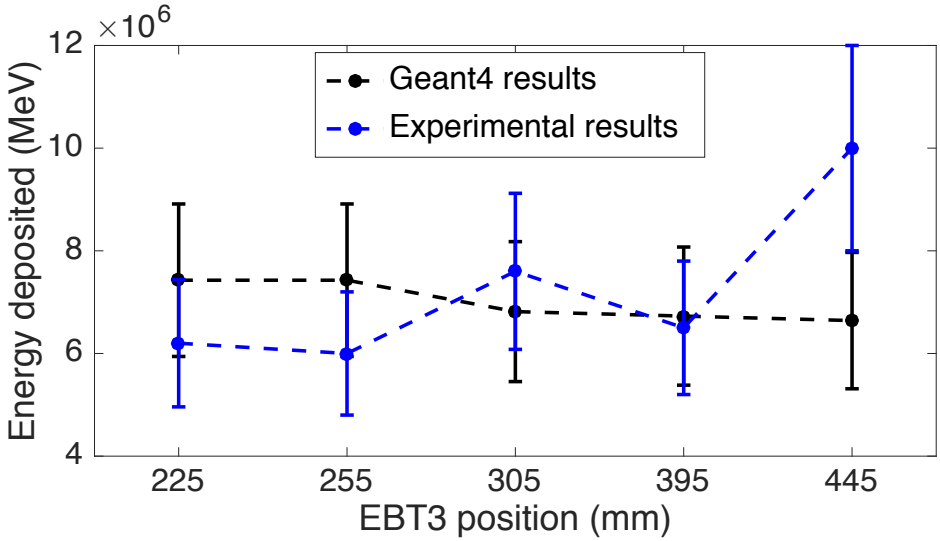

Figure 3.19: Energy released in the second film of the stack at the five different positions along the beamline. The 20% error bars are due to inaccuracy of film calibration.

we verified its impact with the G4beamline package (release 3.04) [170], a Monte Carlo particle-tracking program based on Geant4 [5, 8] specifically developed to simulate beamlines and transport systems[17]. With respect to classical Geant4-based user-constructed applications, G4beamline has features that mangle on a deeper level on the particle tracking, allowing additional collective computations such as space-charge effect. To simulate self-fields, it uses a grid in the beam frame to solve Poisson's equation via a Green's function and macro-particles to enable simulation of larger bunches that could not be feasibly simulated as individual particles. Each macro-particle contains a charge given by the total bunch charge divided by the number of macro-particles. The way macro-particles' identifiers are mangled to track them all together through finite time steps limits to 10^6 the maximum number of macro-particles handled by a single simulation[18].

The G4beamline tool was used to investigate the space-charge effect in the SAPHIR beamline[19]. The proton source was simulated using typical values of initial transversal size and duration [70], precisely 500 µm diameter and 26 µm length corresponding to an initial pulse duration of 10 ps for a monochromatic beam of 3.5 MeV. The impact of

[17]The G4beamline tool relies on a rather usable input deck, which in turns communicates with the standard Messenger classes of Geant4. Such input deck eases creation of typical geometries used by the particle-acceleration community. The particle tracking takes advantage of Geant4 libraries and of an accessible physics list, like any user-constructed Geant4 application.

[18]A complete guide and explanation of the G4beamline features and structure is available at http://g4beamline.muonsinc.com.

[19]Simulation of the SAPHIR beamline with G4beamline without space-charge features showed perfect agreement with the Geant4 Hadrontherapy tool.

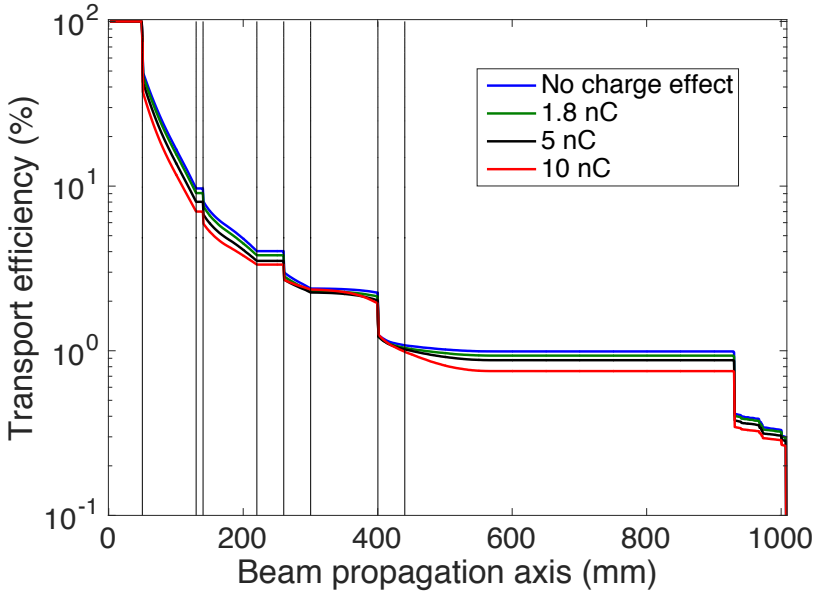

Figure 3.20: Effect of space-charge on the beamline transport efficiency for different value of total charge at the source. Simulations were performed with 10^6 macro-particles at the source. The black vertical line indicates the four quadrupoles.

space-charge effect is evaluated for a total charge at the source ranging from the estimated value of 1.8 nC to 10 nC by comparing the transport efficiency and the transported spectrum to the results obtained when no space-charge feature is activated. As expected, the transport efficiency along the beamline decreases with the total charge at the source (Fig. 3.20). Interestingly, such decrease is entirely due to the losses introduced by the first quadrupole bore aperture. This result indicates that the space-charge effect is negligible along the beamline and exclusively affects the beam tracking in the very first instants of propagation.

The absence of space-charge effect along the beamline is further supported by the analysis of the beam spectrum before the first quadrupole entrance and at the exit window. Fig. 3.21.b shows the proton spectrum over a $3 \times 3\,\mathrm{cm}^2$ surface placed before the exit window for increasing values of the beam charge. As it is shown, the effect of space-charge on the transported spectrum is negligible for a total charge at the source of 1.8 nC and becomes significant at around 10 nC. However, the decrease of the proton counts at the window compared to the case with no space-charge effect depends entirely on the spectral losses at the first quadrupole entrance (Fig. 3.21.a). For example, the reduction of 17% of the 5 MeV proton counts at the window for an initial charge of 10 nC corresponds exactly to the decrease of counts at the first quadrupole entrance. All together the results show that the space-charge effect along the beamline is negligible.

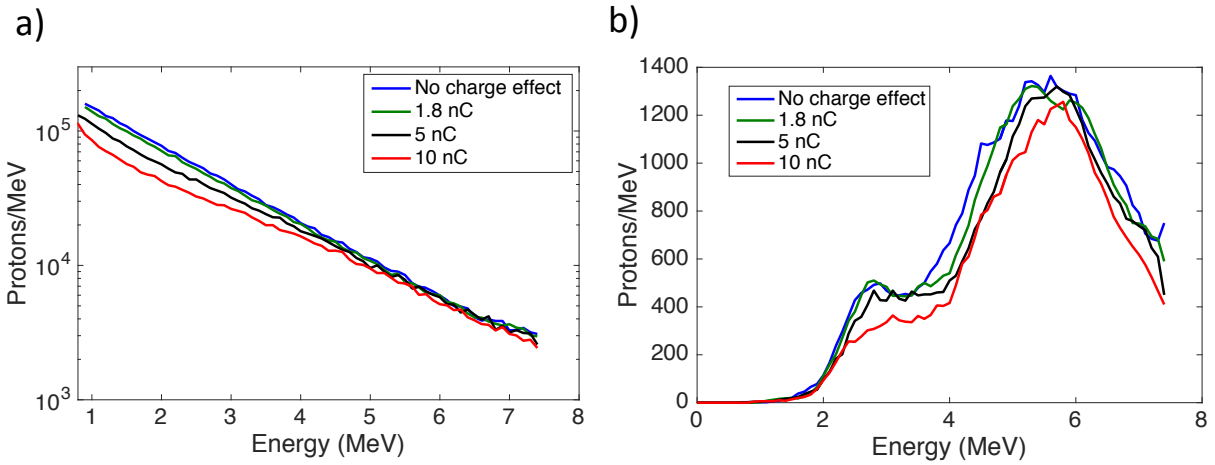

Figure 3.21: Effect of space-charge on proton spectrum. a) Spectra over a $3 \times 3\,\mathrm{cm}^2$ surface at the first quadrupole entrance. As expected, the effect of the self-field is stronger for the lower energy components and generates both an increase of the envolpe transverse size, which causa a decrease of proton counts, and a small energy loss. b) Spectra over a $1 \times 1\,\mathrm{cm}^2$ surface at the exit window

3.3 Beam shaping with MC codes and GA algorithm

In LPAP applications to radiobiology studies, the beamline configuration must be adapted to meet the requirements of dose homogeneity in the biological sample, which implies optimisation of both the spatial and spectral shape of the beam. Handling both aspects by means of a quadrupole transport system alone is challenging, since it requires the system to be configured not only to focus the desired spectral components at the biological target but also to provide a field of a suitable size, so as to generate a uniform transverse dose distribution. Coupling a scattering flat foil, or flat Scattering System (SS), with the magnetic transport beamline eases the spectral and spatial shaping of the beam, since optimisation of the two aspects are performed separately: the transport system can be primarily designed to focus the desired spectral components while the SS can be used to spread the beam and adapt its transverse dimension to the biological sample. As it was mentioned in section 1.3.2, flat SSs are widely adopted in conventional protontherapy to spread the beam before its spectral shaping and their application to LPAP beams has also been recently investigated [137]. Indeed, the use of flat SS is a practical and effective solution, since it does not require particular technological efforts but only a proper choice of the foil thickness. Flat SSs, however, improve the beam uniformity at the target at the high cost of a loss of charge focused on its surface.

Given the limited charge available in LPAP bunches produced with Hz, TW lasers and the inevitable losses in transport, increasing the total charge transported to the biological

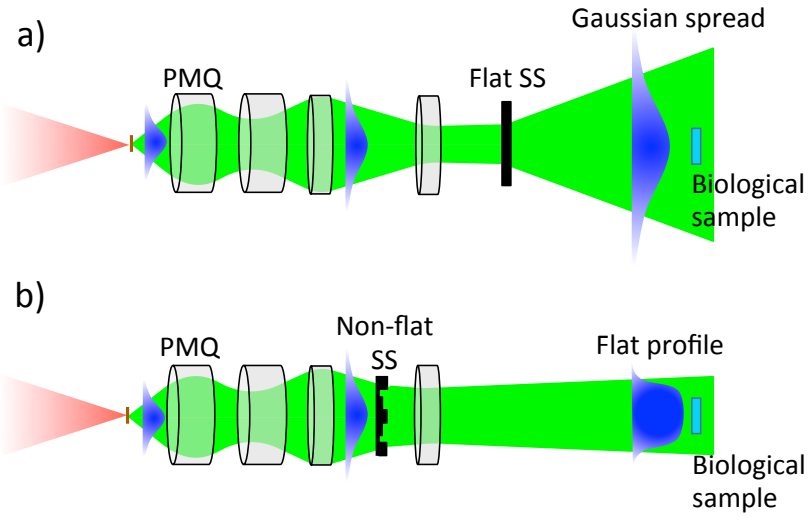

Figure 3.22: a) After the quadrupole system, a flat Scattering System (SS) can be used to further spread the beam and deliver a homogeneous transverse dose to the sample. b) Inserting a non-flat SS properly optimised inside the transport system can flatten the beam profile more efficiently. It not only optimises the scattering effect over the transverse section of the beam, but it also intermingles the particle trajectories in the following quadrupole.

sample is another key aspects of LPAP applications to radiation biology. More precisely, the challenge is to concentrate as many protons as possible on the biological sample maintaining an acceptable level of dose homogeneity over a surface sufficiently large for radiobiology statistics. This section presents a solution to optimise these aspects through the use of an SS composed by tiles of variable thicknesses inserted in the transport beamline. The concept is illustrated in the schematic of Fig. 3.22, which shows a monochromatic divergent beam with a gaussian profile entering the transport system. The quadrupole beamline collects the initially divergent beam and guides it towards the sample without changing the initial beam profile (assuming ideal quadrupole fields). The beam exiting the transport system can then be scattered through a flat SS in order to irradiate a biological sample with a homogeneous transverse dose profile (Fig. 3.22.a). Inserting a non-flat SS along the transport beamline (Fig. 3.22.b) can flatten the beam profile more efficiently, since not only it optimises the scattering effect over the transverse section of the beam, but it takes also advantage of the quadrupole chromaticity to improve the beam shaping. In other words, by properly introducing different energy losses over the transverse section of the beam, the particle trajectories can be intermingled to optimise the beam profile at a given position along the beamline, as illustrated in the schematic in Fig. 3.23.

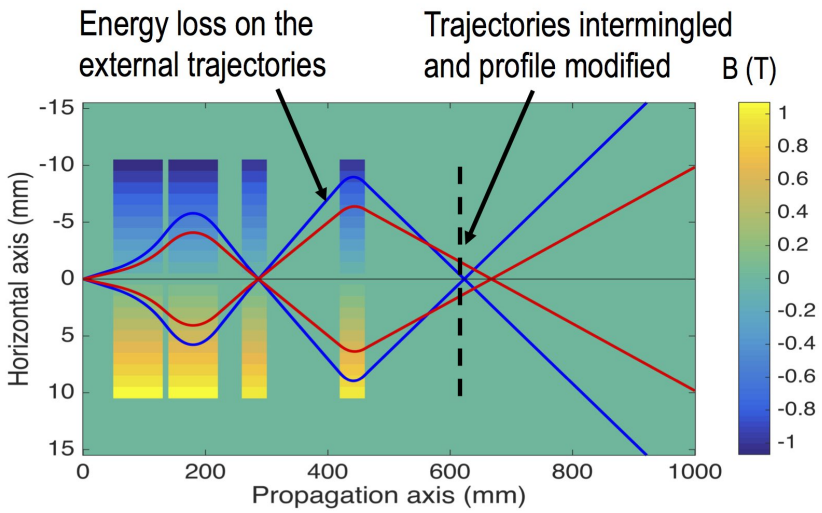

Figure 3.23: Effect of energy losses along the transport system on the beam profile. The figure shows the trajectories of 5.5 MeV protons entering a quadrupole transport system (SAPHIR beamline, section 2.5) with a different divergence at the source. The beam profile is not modified, i.e. the internal trajectories do not intercept the external trajectories, unless an energy loss is induced. In the exemple, an energy loss of 1 MeV is induced on the external trajectories (blue lines) before the last quadrupoles. At a distance to the source of around 60 cm, the trajectories are mixed and the profile is modified.

The design of such SS is not straightforward, since the energy losses (i.e. the SS shape) must be optimised to properly modulate a polychromatic beam, whose spectrum varies over its transverse section, to obtain the desired beam parameters at a precise position after the transport system. An analytical approach, therefore, is not a viable option. The approach presented in this section combines Monte Carlo simulations and a Genetic Algorithm (GA) to optimise the shape of the SS in order to meet given constraints at the biological target, such as maximising both the beam homogeneity and the total charge reaching its surface.

GAs are heuristic computing techniques that have been developed to find the best or near-best solution to optimisation problems where the parameters are numerous and a theoretical approach is not suitable. Their application area is wide and includes engineering [23], traffic problems [102], medical applications such as radiology, radiotherapy, oncology and surgery [74]. This type of algorithm makes use of an abstract version of the Darwinian laws of genetics: a population of possible solutions, which are called chromosomes, is recombined randomly and evolves from a generation to the next through an iterative process. A selection of the fittest solutions is operated at every iteration with the use of a fitness function that tunes the parameters to be optimized. The selected solutions are then randomly recombined to give rise to a new generation of chromosomes,

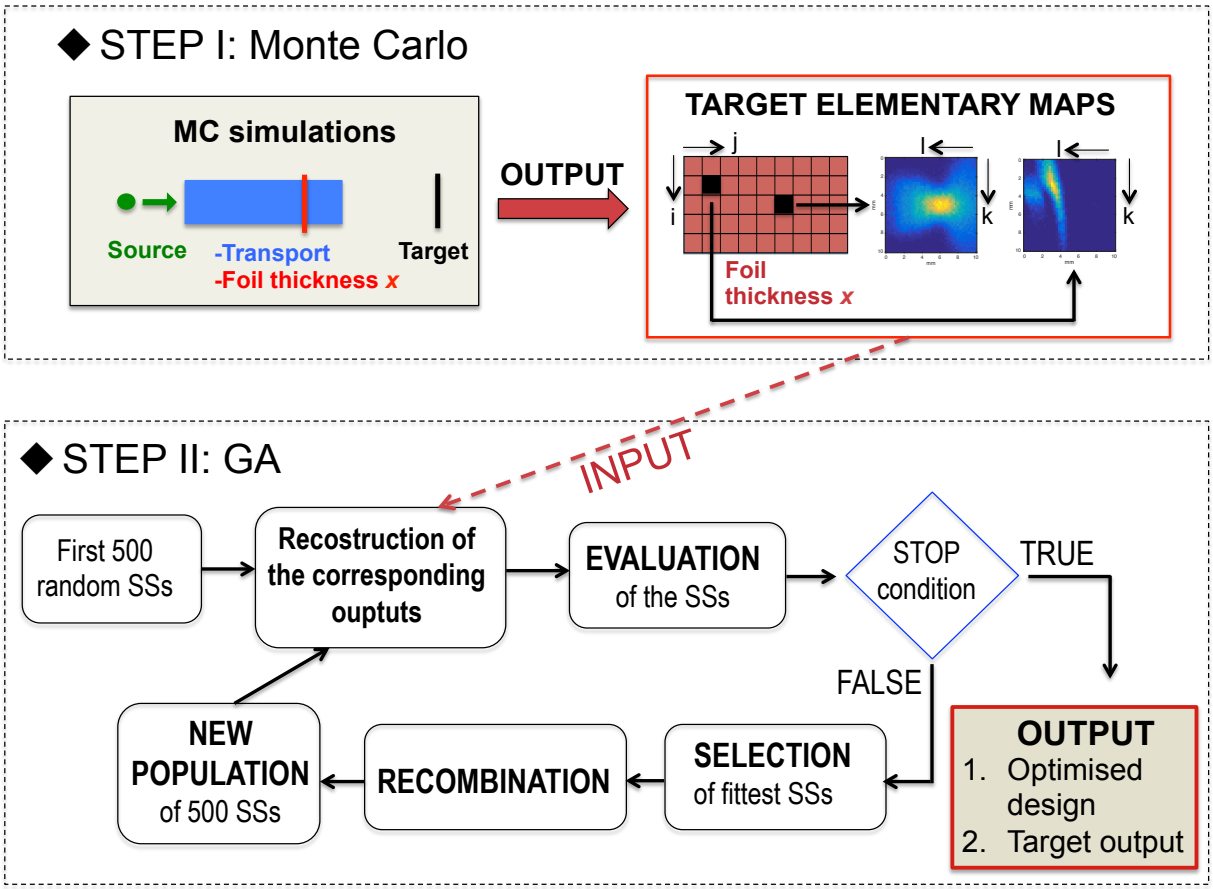

Figure 3.24: Scheme of the scattering system design process. Monte Carlo simulations (STEP I) are first performed to produce flux and dose elementary maps that are used as input in the Genetic Algorithm (GA) (STEP II) to optimise the Scattering System (SS) design. The elementary maps at the target are retrieved separately for each portion of the beam crossing a different tile of the SS. The final output obtained with the GA includes the optimised SS design and the corresponding optimised output maps at the target.

which go again through a selection and recombination process. The loop is repeated until a certain stop criteria is met, for example when a "good-enough" solution is found or when a maximum number of iteration is reached. A detailed description of GAs can be found in J. McCall (2015) [133].

3.3.1 Optimisation process

Optimisation of the SS design involves two steps, as shown in the schematic drawing of Fig. 3.24. In the first step, Monte Carlo (MC) simulations are performed to reproduce both the propagation of the beam through the transport system and the interaction with an SS. The SS is a grid of tiles of variable discrete thicknesses, whose effect on the beam

parameters at the biological target is determined through the MC simulations. Before starting the design process, the values and number of discrete thicknesses that will be used for the design need to be determined. The choice depends on many factors, such as the energy spectrum of the beam and the computational burden. In fact, a number of MC simulations equal to the number of available thicknesses needs to be performed. The aim is to correlate the effect of every tile, for each possible thickness placed in every position of the scattering system grid, on the 2D flux and dose profiles at the target. Therefore, in each MC simulation a scattering foil of a different thickness and a target are placed at a well-defined position. During the simulation, the propagation of each primary particle, crossing the scattering system at the tile (i,j) and arriving to the target plane at the quantized coordinates (k,l), is recorded (Fig. 3.24). The dose deposited in the target is then added to the cell (i,j,k,l) of a 4-dimensional matrix. In other words, elementary flux and dose maps at the target are created separately for each tile of the SS crossed by a different portion of the beam, as shown in the schematic drawing of Fig. 3.24. Once all the MC simulations are performed, the output at the target can be reconstructed for any scattering system design made up of different discrete values of thickness in each tile.
In the second step, a GA is used to find the optimal configuration of the scattering system (i.e. the optimal configuration of the available thicknesses) generating a proton beam that meet the required specifications at the target. The schematic of the GA algorithm is shown in Fig. 3.24. The GA is initialised with the creation of the first generation of $N = 500$ random scattering systems, i.e. 500 random combinations of the tiles' thicknesses. The resulting maps at the target associated to each design are reconstructed using the data set of elementary maps previously obtained with MC simulations. Such 2D maps are then evaluated through the use of a fitness function, which associates a scalar value to each of the analysed SS solutions, depending on how good a scattering system performs with respect to the pre-defined criteria for the desired output. After the evaluation phase, the SSs under analysis undergo the recombination phase. In the recombination phase, $\mathrm{N}-1$ parent couples of SSs are randomly selected among the $\mathrm{N}/2$ fittest ones. From each parent couple a new child SS is created by randomly mixing the parent tiles' thicknesses. At the end of this phase, a new population of SS is composed by the $\mathrm{N}-1$ issued by recombination plus the fittest one promoted from the previous population. This ensures the fitness function to remain monotonic non-decreasing over GA iterations. The new population is then fed to the GA algorithm for the next iteration of the loop, which is repeated until the algorithm converges to a solution.

3.3.2 Application to the SAPHIR transport system

The described approach is applied to the SAPHIR trasnport system, already presented in section 2.5. The beam transport and the interaction with matter are simulated using the Geant4-based G4beamline package [170] (section 3.2.3)[20], modified to make the output data format (elementary maps described above) compatible with the GA code. The 7.5 MeV proton beam[21] is tracked along the quadrupoles, simulated simulated using measured field maps [182].

Beam shape optimisation in vacuum The GA approach is first tested to shape the beam flux profile over a 1 cm^2 target surface placed 10 cm after the last quadrupole in vacuum (T1 in Fig. 3.25), so as to avoid any scattering effect in air and on the Mylar exit window. Three configurations have been analysed:

1. Scattering system placed before the third quadrupole
2. Scattering system placed before the fourth quadrupole
3. Scattering system placed after the fourth quadrupole

The results are also compared with the case of a simple flat scattering foil placed after the fourth quadrupole. The three configurations and the beam shapes at the scattering system positions are shown in Fig. 3.25. The SS is a $10 \times 18\,mm^2$ rectangle composed by 5×9 square Mylar tiles. The choice of Mylar is motivated by its low density, which allows to use tiles of manageable thicknesses in view of experimental implementation. The dimensions and orientation of the SS are chosen so as to cover the beam profile at the SS position, as shown in Fig. 3.25. The choice of the number of tiles is motivated by considerations on the number of particles that need to be simulated in MC simulations to retrieve input elementary maps for the GA with accuracy. For each geometry shown in Fig. 3.25, G4beamline simulations using 5×10^7 particles have been performed to simulate the effect of 11 foil thicknesses going from 1 to 100 µm on the flux distribution at the target (T1) surface.
As discussed, the goal of the approach is to efficiently shape the beam to maximise both the homogeneity and the total charge reaching a surface of a fixed dimension. The GA is therefore used to obtain the best trade-off between flux homogeneity and total flux at the

[20] No special feature such as space-charge was used.
[21] The proton spectrum is simulated using the results reported by L. Pommarel [163, 17], obtained with the film stack spectroscopy assuming that the energy delivered in the film is due to protons having the Bragg peak in the sensitive layer.

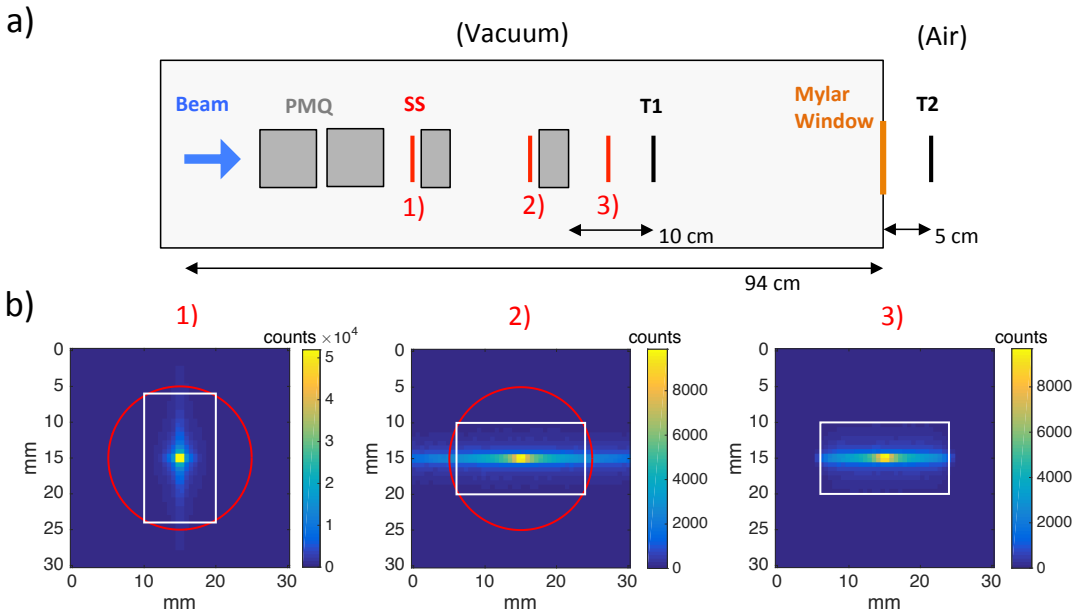

Figure 3.25: a) Schematic drawing of the three scattering system configurations. b) beam shape at the scattering system position in the three configurations. The white rectangles represent the contour of the scattering system and the red circles represent the aperture of the quadrupole placed after it.

target T1. The parameter employed to quantify the beam homogeneity is the standard deviation (σ) of the 2D profile. In this case, the fitness function that is minimised and used to select the SS during the iterations was the following:

$$F = a \cdot \left(\frac{\sigma_{ss} - \sigma_{no-ss}}{\sigma_{no-ss}}\right) - b \cdot \left(\frac{\Phi_{ss} - \Phi_{no-ss}}{\Phi_{no-ss}}\right) \tag{3.38}$$

The first term in brackets represents the difference between the standard deviation of the flux at the target with and without scattering system and the second term in brackets represents the difference between the total flux at the target with and without scattering system. The two coefficients a and b are used to set different relative weights to the parameters. In other words, the higher is the a/b ratio, the more the final SS design maximises the beam homogeneity instead of the total charge. To compare the four configurations, the coefficients were adjusted in each case so as to obtain the same total flux at the target surface. Fig. 3.26 shows the optimised SS designs obtained with the GA for the three configurations and the corresponding flux at the target surface, as well as the flux obtained with a flat foil of 60 µm.

As expected, the GA-SS placed after the transport system (3) allows a better trade-off between the two parameters compared to a flat foil placed in the same position (4). This

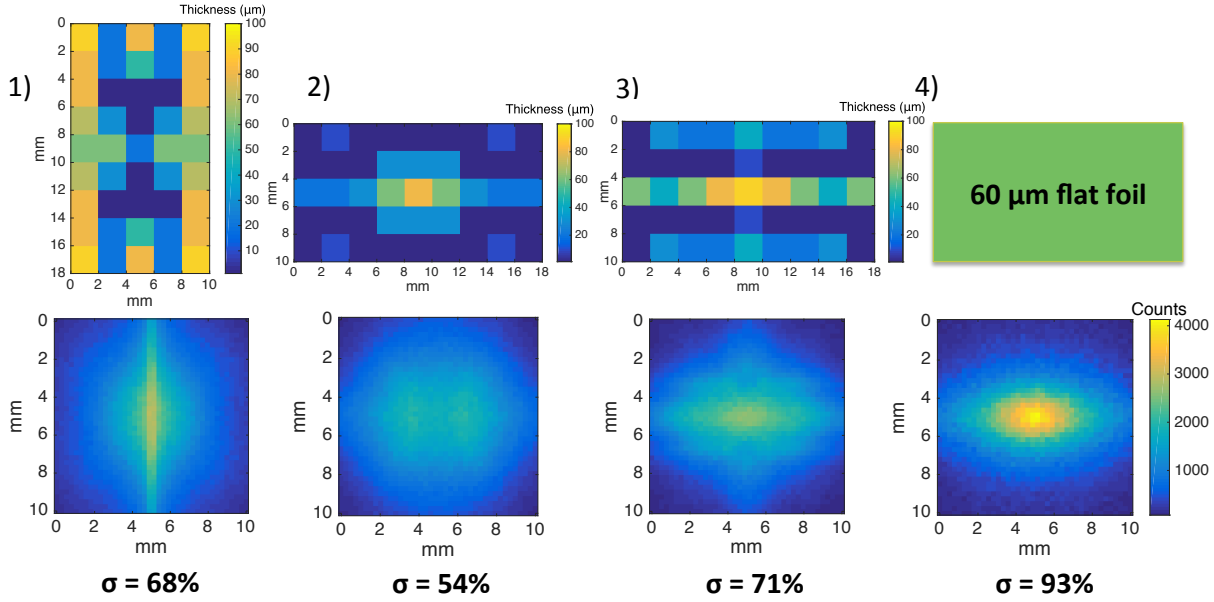

Figure 3.26: Top: scattering system designs in the four configurations. Bottom: corresponding flux at the target surface (represented by T1 in Fig. 3.25). The total flux at the surface is the same for all configurations.

is due to the optimisation of the scattering effect over the transverse section of the beam obtained with the GA design: the beam is spread mainly at the centre and at the edges so as to flatten the beam profile in a more efficient way compared to a flat foil. A major improvement in homogeneity is obtained in the two first configurations, in which the SS is placed along the quadrupole system. In particular, the SS placed before the fourth quadrupole (2) allows a decrease of 42% in standard deviation compared to the flat foil configuration. As previously discussed, this is explained by the fact that such a scattering system allows the shaping of the beam in two ways: it spreads the beam through scattering effect and it intermingles the trajectories in the following quadrupole by introducing different energy losses on the transversal section of the beam.

2D dose optimisation This paragraph shows the application of the GA to the optimisation of transverse dose distribution on an *in vitro* biological sample, simulated as a 10 µm thick water target with a $10 \times 10\,\mathrm{mm}^2$ square surface placed 5 cm after the Mylar window in air (represented by T2 in Fig. 3.25). The standard deviation (expressed as a percentage of the mean value) is the parameter employed to quantify the flatness of the transverse dose distribution and compare the effect of GA-SS with flat foils. The GA is used to optimise the scattering system design in the 3 configurations already discussed.

a)

Maximum dose	σ flat foil (thickness)	σ GA-SS
0.48 Gy/nC	9.6% (40 μm)	8%
0.37 Gy/nC	7.9% (60 μm)	5.8%
0.31 Gy/nC	7.2% (80 μm)	4.5%

b)

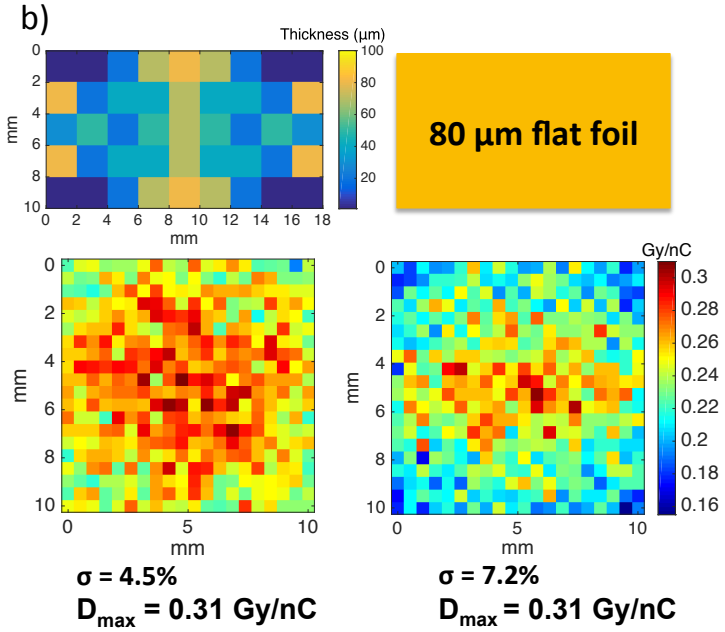

Figure 3.27: a) Doses and standard deviations obtained at the target T2 with flat foils of increasing thickness compared with the standard deviation obtained using a GA-designed scattering system placed before the fourth quadrupole allowing the same delivered dose. b) Design of the non-flat scattering system and comparison between the dose distributions for the third case listed in the table.

The fitness function used in this case is the following:

$$F = a \cdot \left(\frac{\sigma_{ss} - \sigma_{no-ss}}{\sigma_{no-ss}}\right) - b \cdot \left(\frac{D_{ss} - D_{no-ss}}{D_{no-ss}}\right) \tag{3.39}$$

The first term in brackets represents the difference between the standard deviation of the 2D dose distribution in the sample with and without scattering system and the second term in brackets represents the difference between the mean value of the 2D dose distribution in the sample with and without scattering system. Also in this case, it turns out that a GA-SS placed before the fourth quadrupole flattens the transverse dose profile in the most efficient way. In Fig. 3.27.a the standard deviation obtained using flat foils of increasing thicknesses placed after the fourth quadrupole is compared with

the standard deviation obtained using GA-designed scattering systems placed before the fourth quadrupole allowing the delivery of the same maximum dose. A 20-40 % decrease in standard deviation is obtained with a genetic approach. Fig. 3.27b shows the scattering system design for the third case listed in the table and a comparison between the corresponding dose distribution and the dose distribution obtained with the 80 µm flat foil. As it is shown, the GA-SS generate a more uniform dose transverse profile at the biological target for the same maximum value of the dose in comparison with a flat foil.

To summarise, the use of a GA assisted approach to design non-flat SSs is shown to efficiently shape an LPAP beam and improve the irradiation conditions at the biological target. The method has been theoretically tested in this section with a 2D biological target and is applied in section 4.2.4 to optimise the 3D dose distribution in thicker targets. In this case, not only should the beam be spatially shaped to deliver a transverse homogeneous dose, but it would also require a proper spectral tailoring to produce a flat depth-dose profile in the target.
To be experimentally implemented, the method requires a robust characterisation of the source as well as a precise simulation of the beam along the transport system, as described in previous sections. The approach may be used, toghether with other shaping techniques, in LPAP facilities entirely dedicated to radiation biology studies to further improve the irradiation conditions. The SSs can be realized by superposition of 10 µm layers, which are easily handled, or by laser ablation. Also, the realization of such systems to shape higher energy proton beams would be easier thanks to the thicker tiles necessary to introduce the required energy loss and scattering effect. On the other hand, flat SSs can be easily optimised during experiments and offer, therefore, a viable and more suitable solution for short-run radiation biology experimental campaigns.

3.4 Conclusions

The tools and techniques developed to characterise laser-plasma accelerated protons (LPAP) sources and to design LPAP beamlines were presented in this chapter. A deconvolution technique for film stack spectroscopy of LPAP has been developed and validated with the SAPHIR proton source. The results show that the technique can reconstruct the impinging proton spectrum with a high accuracy (few percent error). Further improvements of the technique should aim at retrieving the energy-dependent divergence with a higher energy resolution. This would require the use of the dose distribution in the films

as fitting parameter and the study of appropriate functions to model the proton angular divergence, assumed as gaussian in the presented study.
The simulation of LPAP beam transport with the Geant4 Monte Carlo tool has been validated with the SAPHIR beamline. The simulation of both beam transport and interaction with matter with a single software allows optimisation of the beamline parameters according to the desired irradiation conditions at the biological target as well as the development of complex shaping techniques. In particular, a genetic approach was succesfully used to optimise the coupling between non-flat scattering systems and the transport system to shape the dose distribution in 2D biological samples.

Chapter 4

Design of LPAP beamlines for radiation biology experiments

Contents

Overview

This chapter presents the beamline designs for two types of laser-plasma proton accelerators. The first section presents the beamline design for the 8-10 MeV Laser-Plasma Accelerated Proton (LPAP) beam of the ∼150 TW, Hz ILIL laser system of Pisa (Italy) for 2D *in vitro* irradiation experiments. The second section presents the beamline design for a high-charge, ∼13-15 MeV LPAP generated at the pico2000 high energy (80 J/shot) laser system of the LULI laboratory of Palaiseau (France) in view of a single-shot, *in vivo* irradiation experiment with zebrafish embryos in FLASH-like conditions.

4.1 LPAP at the ILIL-PW facility at Hz repetition rate

The group of CNR-INO of Pisa, together with the INFN of Milan, carried out a significant research activity in the last years to establish an operational beamline for laser-driven TNSA ion beams with the ILIL sub-PW class laser [79, 80, 81]. Much effort has been devoted to the optimisation of the laser-pulse temporal profile, the study of laser-target interaction, targetry design and proton beam characterisation. A parallel upgrade of the laser system enabled the reach of a peak power of 150 TW, which will be increased up to 200 TW before the end of 2020, and the generation of a 8-10 MeV LPAP beam. A specific research activity will be dedicated in the next three years to radiation biology applications, including the development of dosimetry, source and beam diagnostics, and beam transport techniques. The goal is to carry out a systematic study on the toxicity of different LPAP irradiation protocols on living cells. In this framework, the CNR-INO and INFN groups have started a collaboration with our research team at the LOA, which conducted similar experiments during the SAPHIR project [163, 17]. I was involved in the characterisation of the ILIL proton source and carried out preliminary transport studies in view of the incoming radiobiology applications. The proton beam had been previously characterised in terms of its cut-off energy using a Thomson Parabola (TP) and a Time-Of-Flight (TOF) diagnostics [81]. It was therefore necessary to measure the source divergence and total available charge per shot prior to the study of potential transport beamlines and irradiation conditions. A 2 weeks experimental campaign was therefore dedicated to the characterisation of the proton source with both online diagnostics (TP and TOF) and film stacks. The results allowed preliminary studies on the transport beamline and the assessment of the irradiation conditions that can be achieved.

4.1.1 Experimental characterisation of the TNSA source

The experimental set-up, similar to the one used in previous experimental campaigns [81], is shown in Fig. 4.1. The laser was focused with an off-axis parabola having a focal length of 240 mm and delivered 4 J at the target. TP and TOF diagnostics were employed as on-line monitor of the proton cut-off energy and relative charge (over a limited solid angle) while a remotely controlled RCF stack, shielded with a 1 cm thick lead plate, was positioned in front of the source once optmimal and stable beam conditions were achieved to retrieve the absolute source spectrum.

The first part of the experiment was dedicated to the characterisation of various target

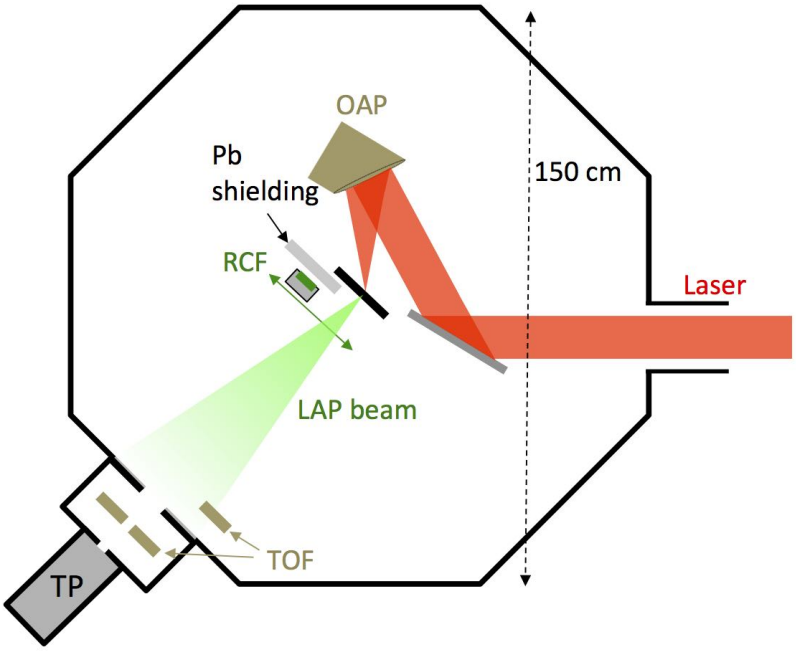

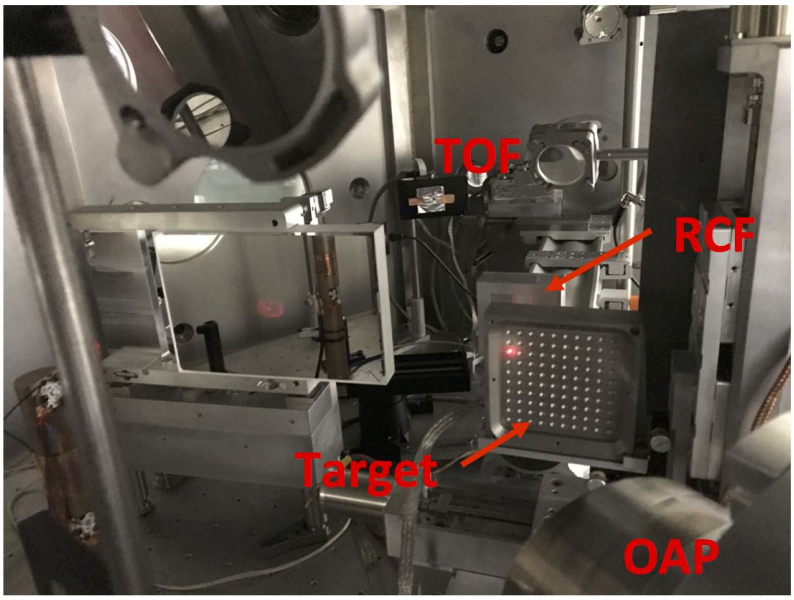

Figure 4.1: Top: schematic of the experimental set-up. Bottom: picture of the set-up inside the interaction chamber.

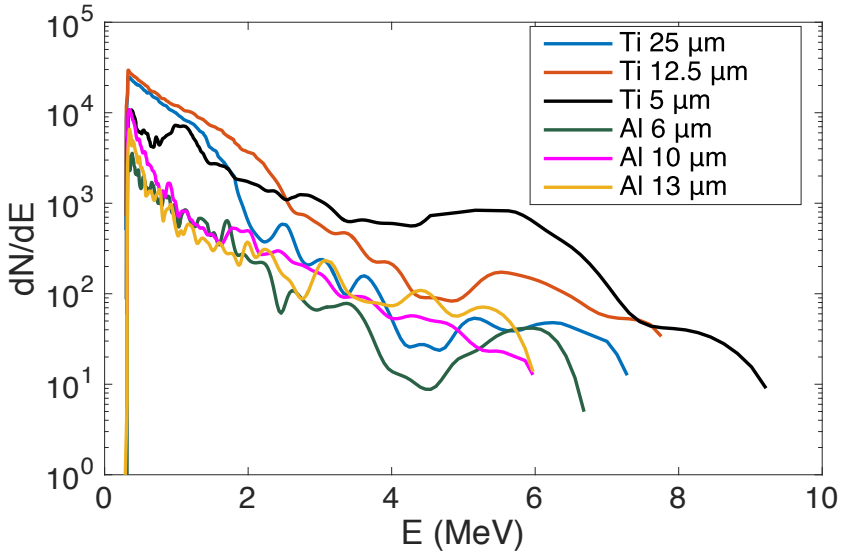

Figure 4.2: Spectra obtained with a Thomson Parabola spectrometer (see section 3.1.1). A detailed description of the TP is given in S. Tudisco et al. (2016) [194]

foils (materials and thickenesses) in terms of the maximum proton beam energy and charge using the online diagnostics. Fig. 4.2 shows typical spectra obtained with the TP for different target materials and thicknesses. The highest cut-off energies of ∼8 MeV and ∼9 MeV were reached with titanium foils of respectively 12.5 µm and 5 µm thickness. The two targets also produced proton beams with the highest charge, which makes them the best candidates to reach meaningful doses in radiobiology applications. They were therefore selected to perform film stack spectroscopy characterisation of the source during the last days of the experiment.

The films (HD-V2 type), covered with a 13 µm thick aluminium layer to protect them from light and debris, were inserted at a distance to the source of 6 cm to record the entire beam transverse profile. The irradiated stacks corresponding to the two target foils (Fig. 4.3) show a cut-off energy around 5 MeV [1]. An overall decrease in the cut-off energy of around 3 MeV was indeed observed during the last days. Further investigation would have been required to explain such degradation of the maximum beam energy but more experimental tests were blocked by the COVID-19 crisis. The decrease in energy measured with the film stack is also confirmed by the measurements performed with the TP and TOF diagnostics. Fig. 4.4 shows 10 consecutive TP measurements of the proton spectrum produced with the 12.5 µm thick foil prior to the film stack measurement to evaluate the shot-to-shot spectral stability. The measures indicate an average cut-off energy of 5 MeV,

[1] A weak signal was detected on the fourth film with the 5 µm thick titanium foil, which indicates a cut-off energy around 5.7 MeV.

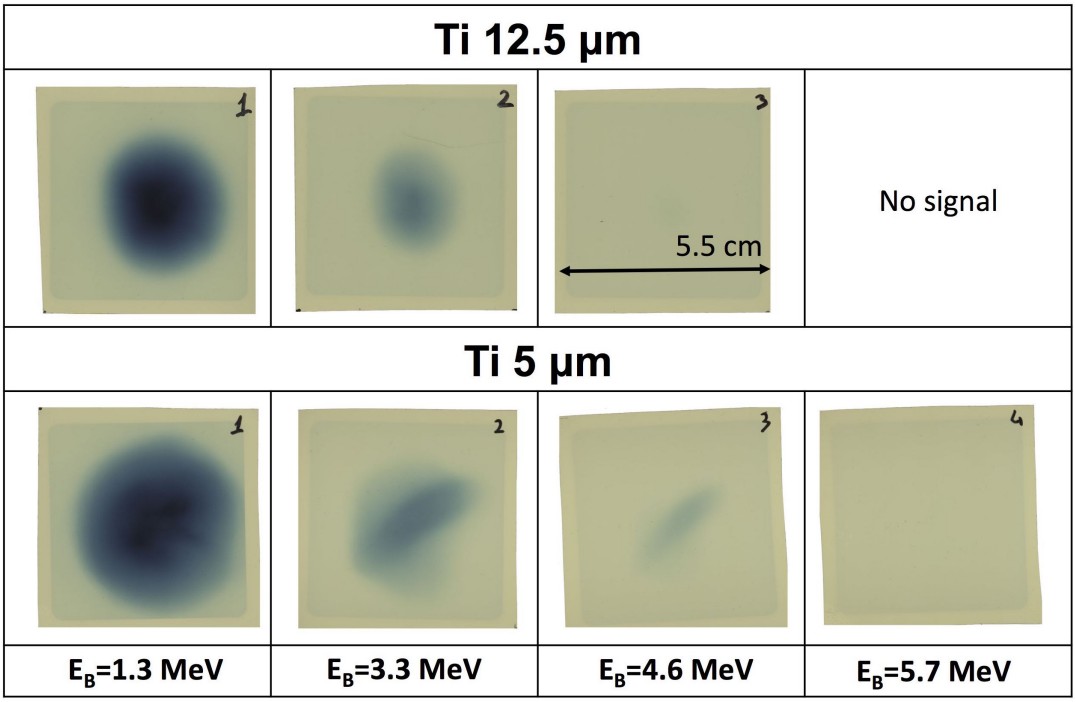

Figure 4.3: HD-V2 stack measurements with 12.5 µm thick titanium foil (21 shots) and 5 µm thick foil (16 shots).

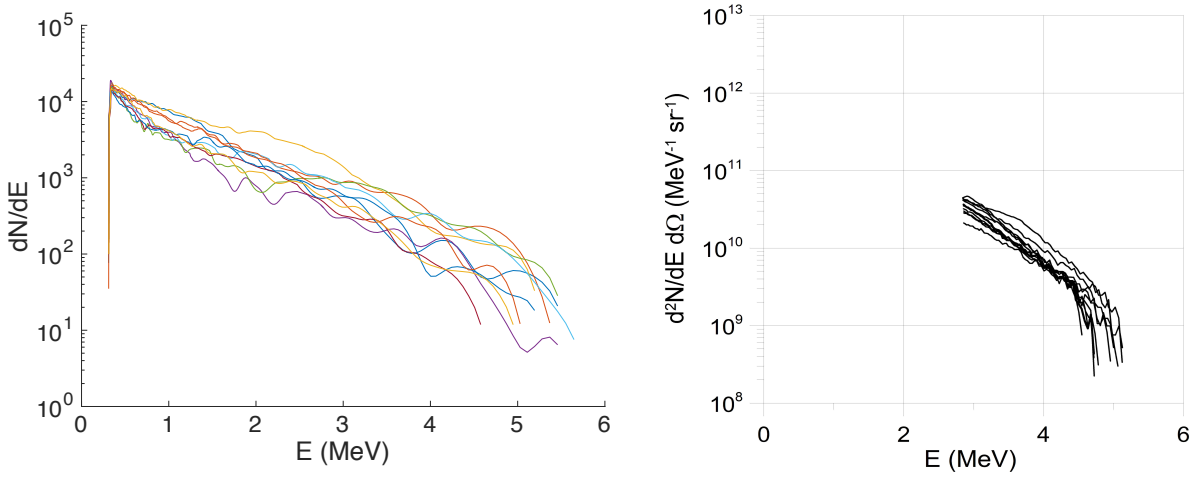

Figure 4.4: Degradation of the cut-off proton energy (generated with the 12.5 µm thick foil) during the last days of the experiment measured with the TP (left) and the TOF (right) detectors over 10 shots. The spectra are measured over a solid angle of 6×10^{-9} sr and 3×10^{-7} sr for the TP and TOF, respectively.

with a good shot-to-shot stability of 6% (standard deviation).
Altough the acceleration conditions were degradated during the film measurements, the results allowed the determination of the beam transverse profile and total accelerated charge, which are crucial parameters to design the transport beamline and define the irradiation conditions. The LPAP beam generated with the 5 µm foil shows an asymmetric beam angular distribution that depends on the proton energy, as indicated by the different beam shape recorded on the three films of the stack (Fig. 4.3). On the contrary, the proton beam generated with the 12.5 µm foil shows a symmetric round shape with a remarkably small divergence (Fig. 4.5.c), compared to the typical divergence of LPAP (see section 2.2.2) and to the divergence of the SAPHIR source (section 3.1.3). The beam generated with the 12.5 µm titanium foil is therefore a suitable candidate for application to radiation biology. The results of the film stack measurements were thus used to retrieve the proton spectrum and the total accelerated charge with the film stack spectroscopy technique described in section 3.1.2[2]. The energy measured in the films is in perfect agreement with the energy simulated using the reconstructed spectrum (Fig. 4.5.a, blue line and red line respectively), whose spectral intensity is shown in Fig. 4.5.b (red line). The beam features a total charge of around 1.7 nC/shot, in line with the charge accelerated at the SAPHIR facility with similar laser and target conditions (see section 3.1.3), with a cut-off energy of 4.6 MeV, in good agreement with the TP and TOF measurement (Fig. 4.4). These parameters have been used as source term for an extensive transport analysis carried out in collaboration with the INFN of Milan, which is presented in the following sections.

4.1.2 Transport study

The proton source and various transport beamlines have been simulated in Geant4 to investigate possible transport schemes and define achievable irradiation conditions. Since at the time of the film measurements the beam cut-off energy was degradated, the spectrum obtained with the film stack spectroscopy technique has been extrapolated up to 7.5 MeV (Fig. 4.5.b, light blue line) and 10 MeV (Fig. 4.5.b, black line) to study transport systems focusing respectively the spectral bandwidths around 6 MeV and 8 MeV to a biological sample. The extrapolation is performed by assuming the same total charge at the source and multiplying the characteristic slope of the exponential for a factor of respectively 4.5/7.5 and 4.5/10, as in U. Masood et al. (2014) [129]. Two different PMQ transport

[2]The dose absorbed by the film was evaluated using an HD-V2 calibration performed at INFN-LNS with 60 MeV protons, also employed for the SAPHIR source analysis presented in section 3.1.3

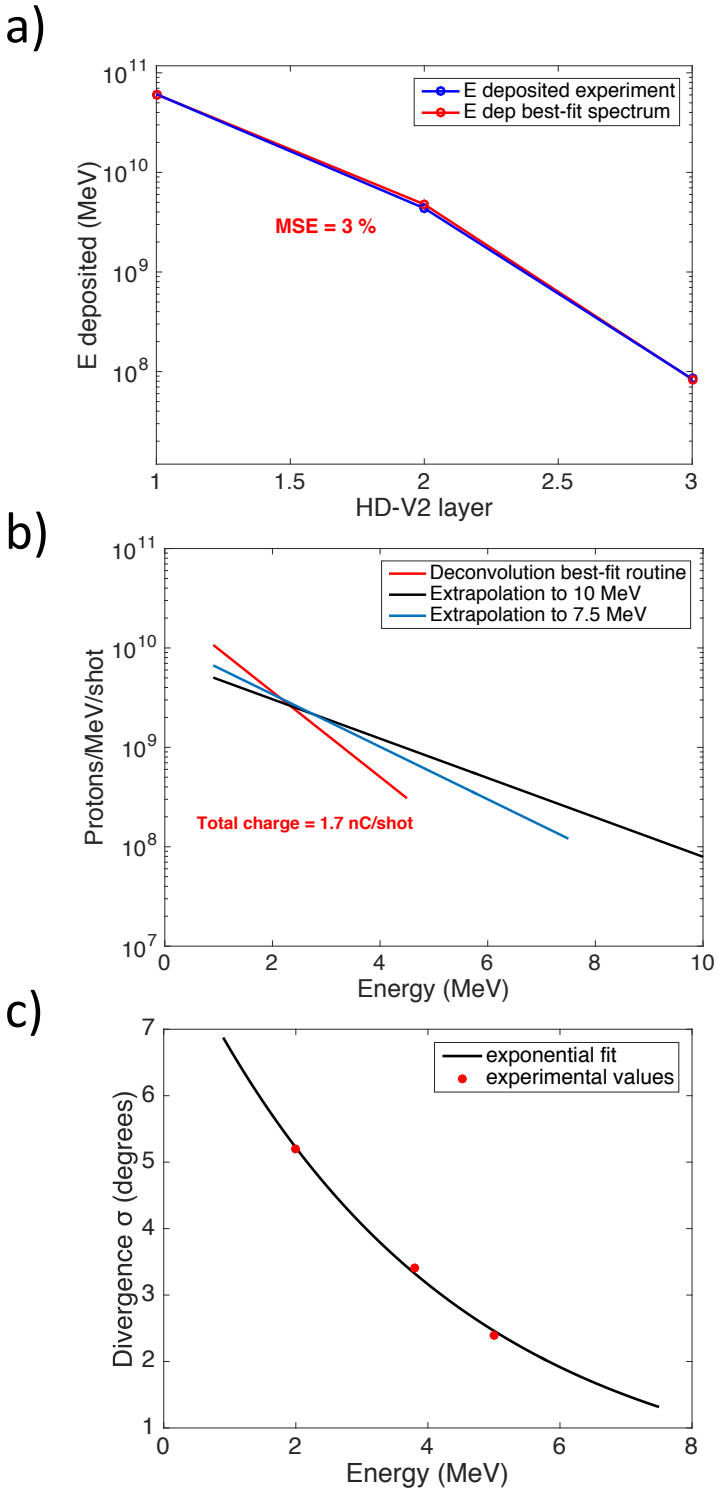

Figure 4.5: Source characteristics for the 12.5 µm titanium foil obtained with the film stack. a) comparison between the energy measured in the films of the stack and the energy simulated using the best-fit spectrum (figure b, red line) obtained with the film stack spectroscopy technique. b) beam spectrum reconstructed using the best-fit deconvolution technique described in section 3.1.2 (red line), together with the extrapolation to a cut-off energy of 7.5 MeV (light blue line) and 10 MeV (black line) for preliminary transport studies. a) beam divergence.

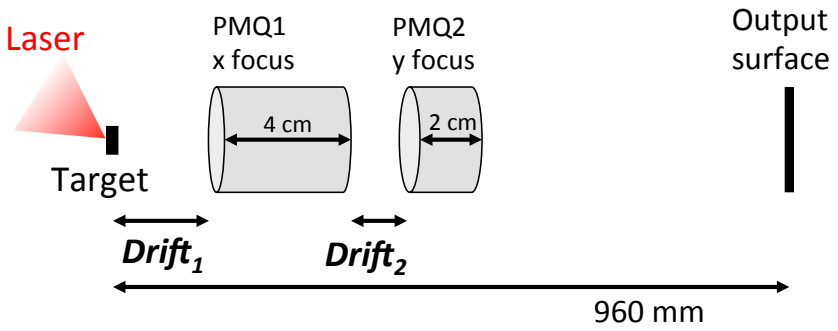

Figure 4.6: Schematic of the doublet parametric study geometry.

systems have been investigated to focus the aforementioned spectral bandwidths: one based on the 4 PMQs of the INFN-LNS (∼100 T/m field gradient, 20 mm bore diameter, 80 mm and 40 mm length) used during the SAPHIR experiments (see section 2.5) and a second one based on a doublet composed by smaller PMQs (∼334 T/m field gradient, 10 mm bore diameter, 40 mm and 20 mm length) designed at the Ludwig-Maximilians University (LMU) of Munich [175]. While configurations of the INFN-LNS quadruplet system to focus both 6 MeV and 8 MeV had already been investigated [162, 183], no indications of the doublet performances with typical LPAP source parameters were available. We have therefore carried out a preliminary characterisation of the doublet transport system in order to identify the best configurations for the two operating points.

Doublet parametric study Prior to the experiments carried out at the ILIL-PW facility, we characterised several doublet configurations in terms of transport efficiency on a $1 \times 1\,\mathrm{cm}^2$ surface placed at a distance of 960 mm from the source, compatible with the geometry of the ILIL interaction chamber. An LPAP-like beam was reproduced in Geant4 assuming an exponential spectrum from 1 MeV to 14 MeV and a divergence of 6°, based on the values of the SAPHIR proton source divergence at energies around 6 MeV (see section 3.1.3). The doublet consists in two quadrupoles with a net bore aperture of 10 mm, a length of 40 mm and 20 mm and a field gradient of respectively 334 T/m and 333 T/m. The only parameters to vary in order to focus the beam are the relative positions of the two magnets (Fig. 4.6), i.e. the distance between the source and the first quadrupole ($Drift_1$) and the distance between the first quadrupole and the second quadrupole ($Drift_2$)[3]. The geometry shown in Fig. 4.6 was simulated in Geant4 and different combinations of the two parameters $Drift_1$ and $Drift_2$ were investigated. Precisely, $Drift_1$ was varied between

[3]We observed that the configuration with the shorter quadrupole placed before the longer quadrupole is not suitable to focus the beam.

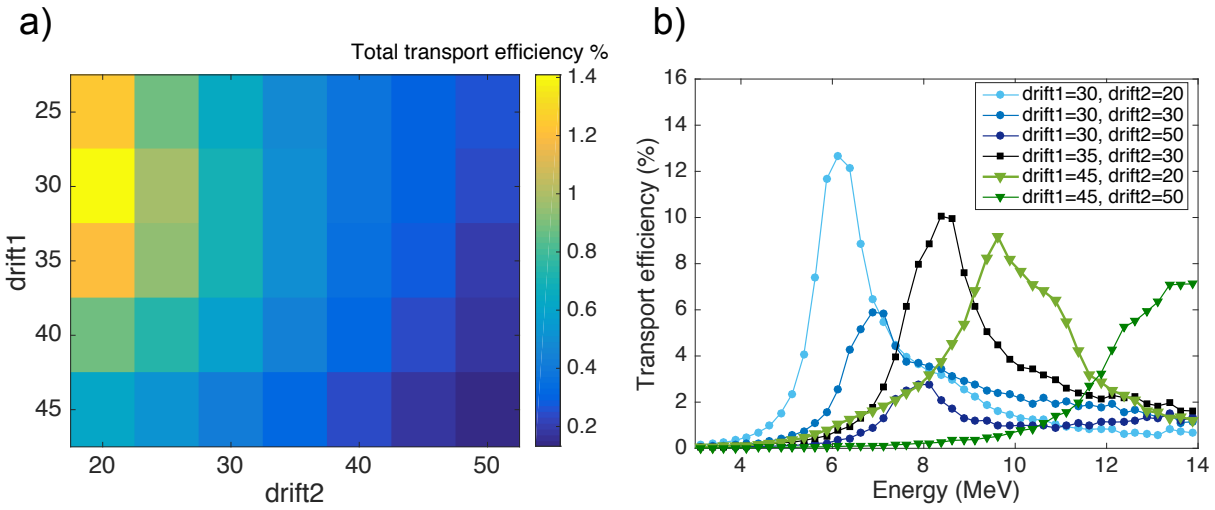

Figure 4.7: Results of the parametric study obtained using the Geant4 tool (10^7 particles were used in each simulation). a) Total transport efficiency at the output surface. b) Transport efficiency at the output surface as a function of the proton energy.

25 mm and 45 mm whereas $Drift_2$ was varied between 20 mm and 50 mm, which leads to a total number of 35 configurations. The limits on the two parameters were chosen so as to cover a range of focused spectral bandwidth between 6 MeV and 14 MeV and were determined by observation of the proton envelopes simulated with the Matlab code described in section 3.2.2.

For each of the 35 combinations of $Drift_1$ and $Drift_2$, the spectrum over the $1 \times 1\,cm^2$ surface was retrieved in the Geant4 simulations using a sensitive scoring. Fig. 4.7.a shows the total transport efficiency[4] as a function of the parameters $Drift_1$ and $Drift_2$. The total transport efficiency reaches a maximum for $Drift_1 = 30$ mm and $Drift_2 = 20$ mm and decreases with an increase of both parameters, which is due to the higher losses along the drift sections. The transport efficiency as a function of the proton energy varies according to the combination of the drift parameters, as shown in Fig. 4.7.b. For $Drift_1 = 30$ mm, an increase of $Drift_2$ leads to a shift of the focused spectral bandwidth from 6 MeV to 8 MeV, together with a decrease of the total transport efficiency. To focus higher energy components, the first quadrupole must be positioned further from the proton source.

Overall, the results show that a doublet with such a quadrupole strength can be used to focus typical LPAP energies required in radiation biology applications. The results of this study were used to identify two doublet configurations to transport 6 MeV and 8 MeV.

[4]Total number of particles reaching the $1 \times 1\,cm^2$ surface divided by the total number of particles at the source.

Comparison of doublet and quadruplet configurations As previously mentioned, two different configurations of both the doublet and quadruplet systems were studied in order to transport the spectral bandwidths around 6 MeV and 8 MeV. This leads to the definition of four configurations:

- *Configuration 1*: 100 T/m quadruplet to focus the spectral bandwidth around 8 MeV, using a spectrum at the source with a cut-off energy at 10 MeV.
- *Configuration 2*: 100 T/m quadruplet to focus the spectral bandwidth around 6 MeV, using a spectrum at the source with a cut-off energy at 7.5 MeV.
- *Configuration 3*: 330 T/m doublet to focus the spectral bandwidth around 8 MeV, using a spectrum at the source with a cut-off energy at 10 MeV.
- *Configuration 4*: 330 T/m doublet to focus the spectral bandwidth around 6 MeV, using a spectrum at the source with a cut-off energy at 7.5 MeV.

Concerning the LNS quadruplet configurations, the arrangement employed for the SAPHIR beamline (section 2.5) is used to focus 6 MeV protons (*configuration 2*). To focus the spectral bandwidth around 8 MeV (*configuration 1*), the distance between the second quadrupole and the third quadrupole of *configuration 2* is increased from 40 mm to 80 mm. The two quadruplet configurations and the proton envelopes along the transport system are shown in Fig. 4.8.
The choice of the doublet configurations was based on the results of the parameteric study (Fig. 4.7.a). The configuration with $Drift_1 = 35$ mm and $Drift_2 = 30$ mm is adopted to focus 8 MeV (*configuration 3*), whereas the configuration with $Drift_1 = 30$ mm and $Drift_2 = 20$ mm is adopted to focus 6 MeV (*configuration 4*). The two configurations and the proton envelopes along the transport system are shown in Fig. 4.9. For each of the aforementioned configurations, the spectrum focused over a$1 \times 1\,cm^2$ surface placed at a distance from the source of 900 mm are obtained in Geant4 to compare the four systems. As shown in Fig. 4.10 the performances of the quadruplet and doublet are comparable in terms of both the number of protons transported to the window and the width of the selected spectral bandwidth. The total transport efficiency in the four cases ranges between 3.5% and 5%, which is rather high compared to the transport efficiency of a comparable LPAP beamline (the transport efficiency with the SAPHIR proton beam using the *configuration 1* was around 1%). The high transport efficiency obtained with the ILIL proton beam is due to the extremely small divergence at the source, which reduces the impact of the losses in the first quadrupole of the beamline. The *configuration 4* was then used to

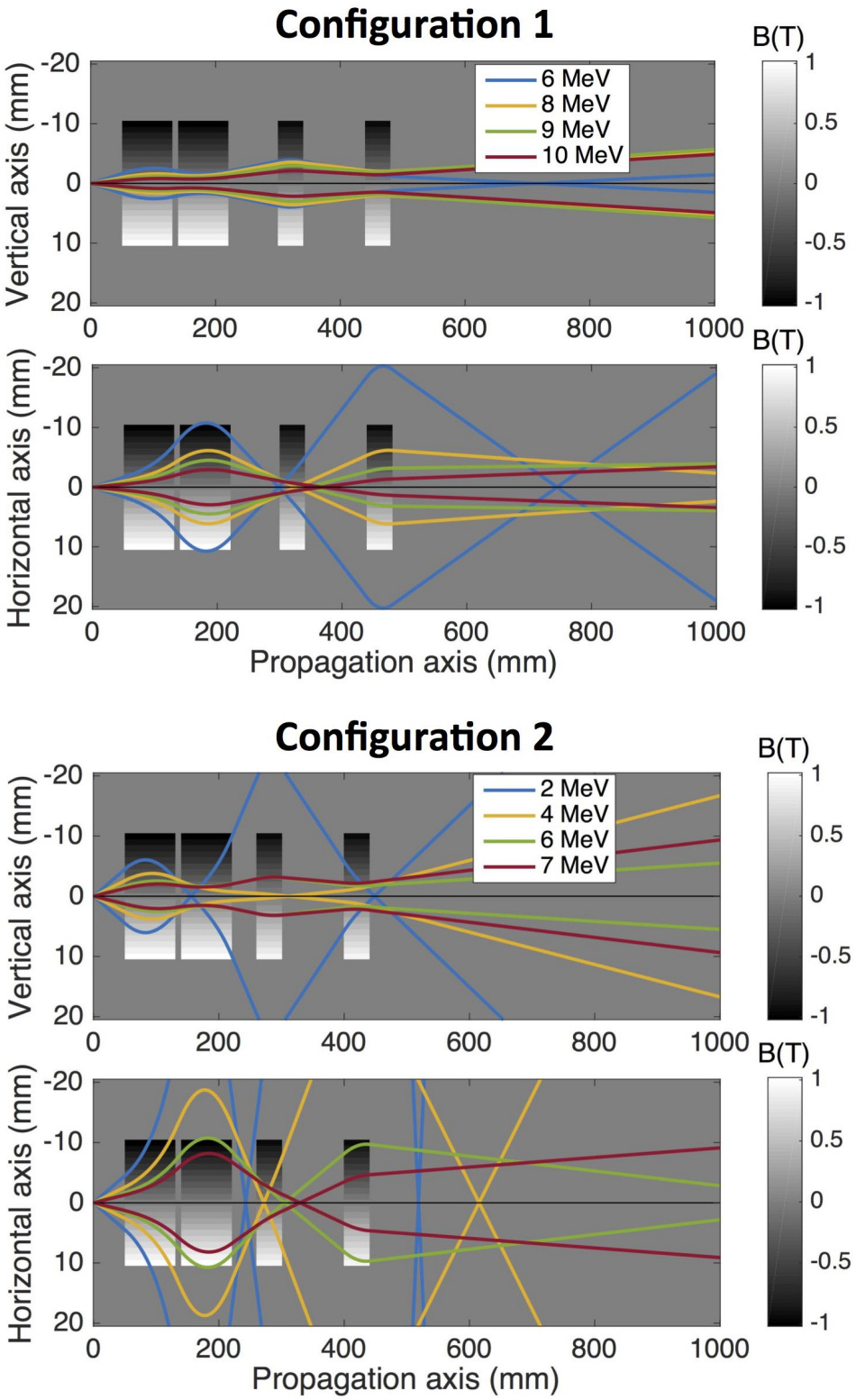

Figure 4.8: Envelopes ($\pm\sigma$ isoflux lines) of different energetic components along the quadrupole transport system in the configuration to focus the 8 MeV spectral bandwidth (configuration 1) and in the configuration to focus the 6 MeV spectral bandwidth (configuration 2).

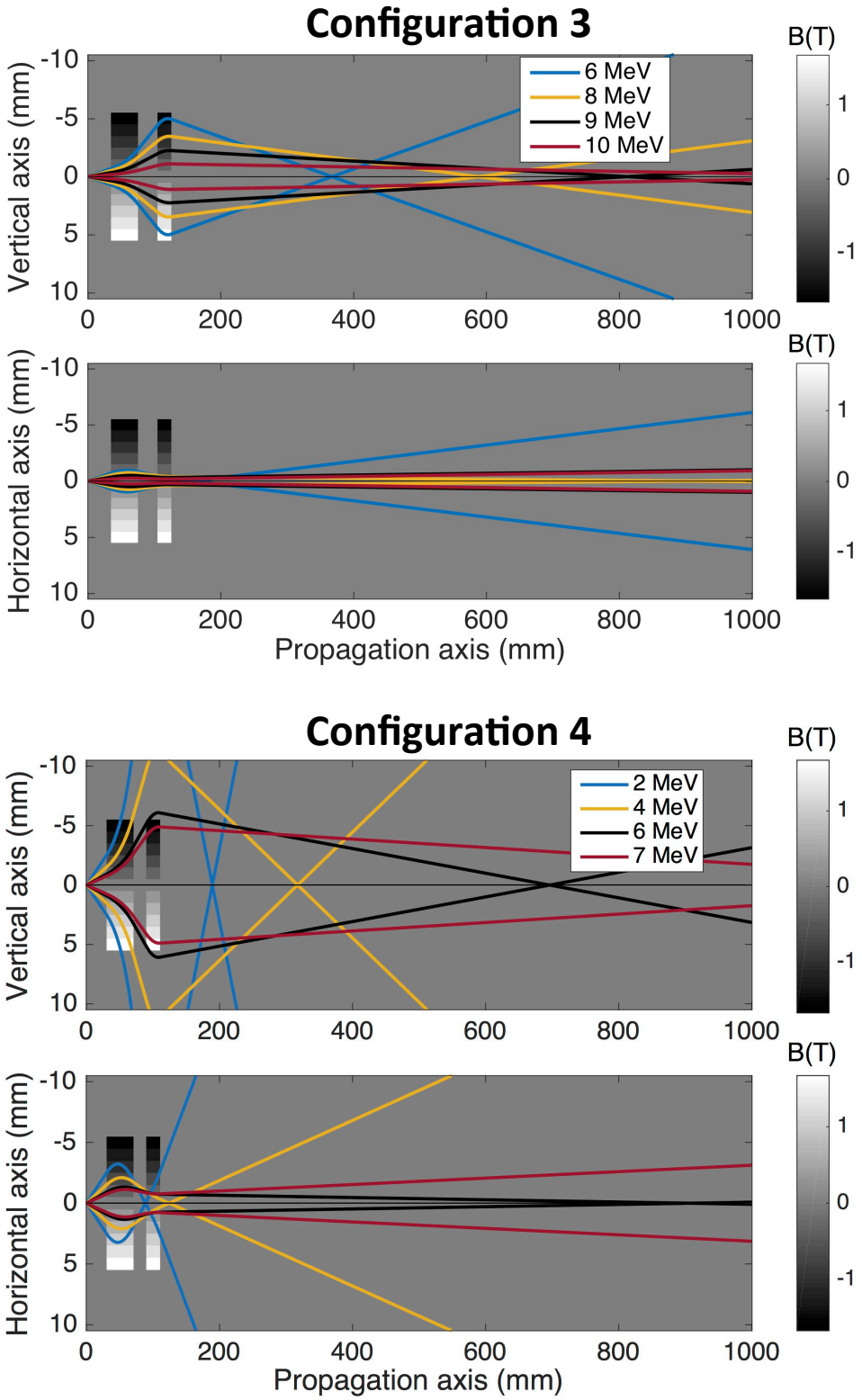

Figure 4.9: Envelopes ($\pm\sigma$ isoflux lines) of different energetic components along the doublet transport system in the configuration to focus the 8 MeV spectral bandwidth (configuration 1) and in the configuration to focus the 6 MeV spectral bandwidth (configuration 2).

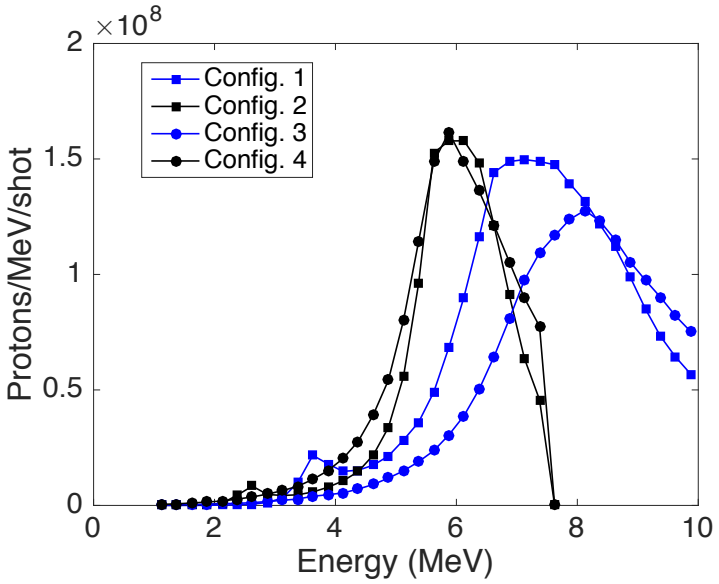

Figure 4.10: Spectra obtained with Geant4 over a $1 \times 1\,\mathrm{cm}^2$ surface placed at a distance from the source of 900 mm with the quadruplet configurations (square dots) and the doublet configurations (round dots). The simulations were run with 5×10^7 particles at the source and the vertical scale is normalised for the estimated charge at the source of 1.7 nC/shot.

evaluate the irradiation conditions achievable on an *in vitro* biological sample simulated as water.

4.1.3 Irradiation conditions

In the simulations, the ILIL proton beam is transported to a 50 µm mylar window placed at a distance from the source of 900 mm (Fig. 4.11). A transmission monitor chamber as the one used during the SAPHIR experiments (see section 2.5) is placed after the window to account for energy losses caused by on-line dosimetry instruments. A 20 µm water

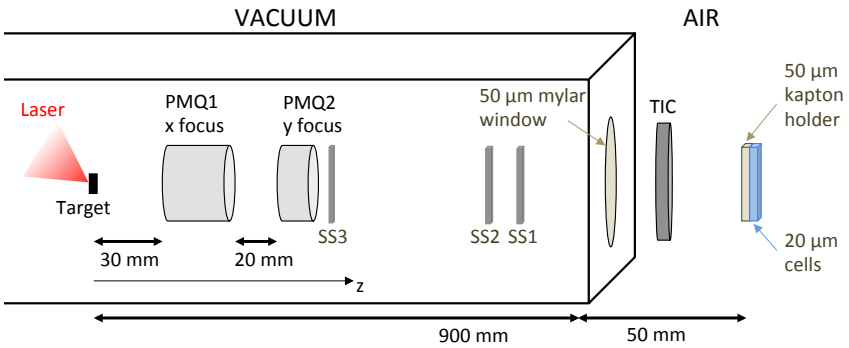

Figure 4.11: Schematic draft of the set-up used in the simulations.

Table 4.1: Table summarizing the irradiation conditions achievable on a 2D *in vitro* target, simulated as water, with different aluminium flat scattering system configurations.

	SS1	SS2	SS3
Position (z)	800 mm	720 mm	120 mm
Foil thickness	100 µm	100 µm	10 µm
Dose delivered in isodose 80%	3.7 Gy/shot	1.5 Gy/shot	1.95 Gy/shot
Area of isodose 80%	0.34 cm^2	0.8 cm^2	0.95 cm^2

target having a $1 \times 1\,cm^2$ surface is placed at 50 mm from the mylar window, covered by 25 µm of plastic.

Three configurations of flat Scattering Systems (SS) have been simulated to spread the beam and deliver a homogeneous dose over a surface of around $1\,cm^2$, as shown in the schematic draft of Fig. 4.11. The three configurations and the parameters of the resulting dose distributions are summarised in Table 4.1, where the dose values are normalised to a total charge available at the source of 1.7 nC/shot. In the SS1 configuration, a 100 µm thick aluminium (Al) foil is placed at $z = 800$ mm, producing an homogeneous dose ($\pm 10\%$) of 3.7 Gy/shot over a $0.34\,cm^2$. The high dose leaves margin for further optimisation of the dose over a larger surface. Positioning the same filter further from the sample, at $z = 720$ mm (SS2 configuration), increases the beam dimension at the target and, as a consequence, entails a decrease in the total dose. The best option consists in placing the flat foil as far as possible to the biological sample (SS3). In such configuration, the longer drift distance after the SS enables the use of a thinner foil to produce the same beam dimension at the target. With a 10 µm Al foil, a dose of 1.95 Gy/shot ($\pm 10\%$) is delivered over a surface of $0.95\,cm^2$. Compared to the SS2 configuration, a thinner foil placed closer to the last quadrupole allows a higher dose to be delivered at the target for a comparable given isodose surface, as shown in Fig. 4.12.b. This is due to the fact that the thinner foil reduces the energy losses and, as a consequence, more protons reach the sample in comparison with the thicker foil, as shown by the proton beam spectra at the sample position in the SS2 and SS3 configurations (Fig. 4.12.a). The benefit of the thinner foil is not only the higher dose delivered to the target but also the lower spread of the LET spectrum (Fig. 4.13). As it is shown, the thinner foil reduces the ΔLET, quantified as the FWHM of the LET peak, from 19.2 KeV/µm to 9.3 KeV/µm. Furthermore, the contribution of the high-LET tail above 30 KeV/µm due to the low-energy part of the spectrum is reduced from 50% to 35%.

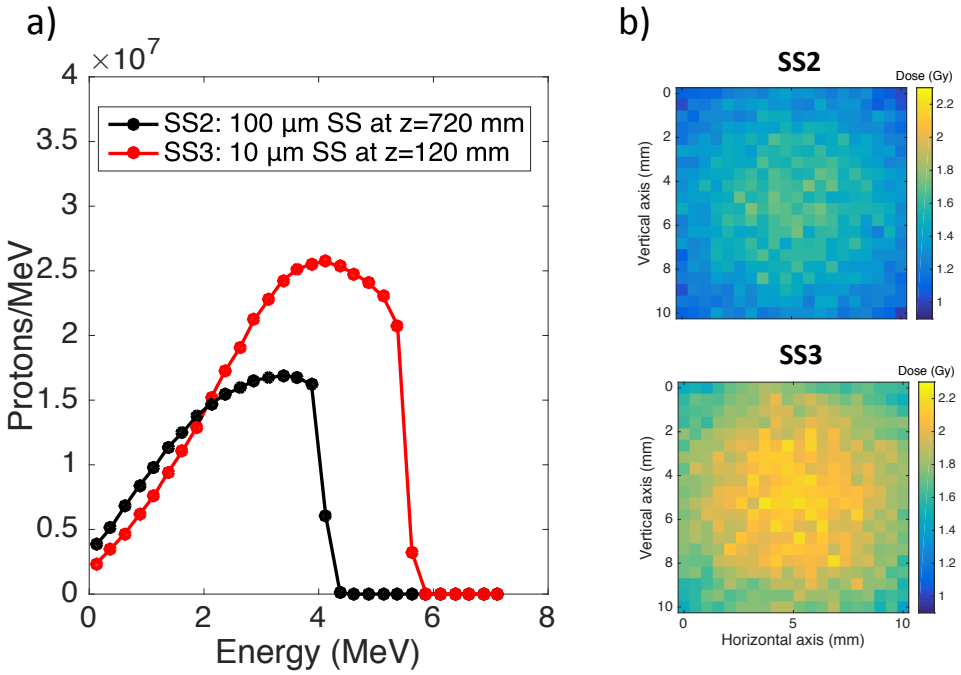

Figure 4.12: Irradiation conditions at the sample for the SS2 and SS3 configurations of the scattering system. Geant4 simulations were runned with 5×10^7 particles but all values are normalised to a charge at the source of 1.7 nC. Left: spectra over the 1 cm^2 surface of the sample. Right: 2D dose distributions.

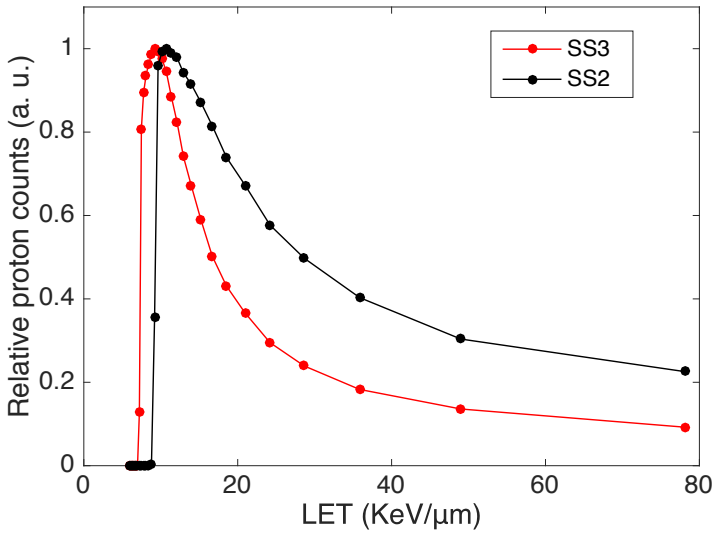

Figure 4.13: LET spectrum at the biological sample in the SS2 and SS3 configurations.

In general, we observe that the small beam divergence, probably due to the advanced target support developed for the ILIL-PW facility [81] ensuring a high planarity of the foil, has a strong impact on the amount of charge that is collected and transported to the sample. Indeed, whereas the use of different transport systems (doublet or quadruplet) does not affect significantly the transport efficiency (Fig. 4.10), the small divergence strongly reduces the charge losses along the quadrupole system and allows to transport a higher charge to the sample in comparison with similar LPAP facilities. An homogeneous dose of around $\sim$2 Gy/shot can be delivered with the source conditions achieved at the ILIL-PW facility and the analysed transport systems. Considering the temporal stretch due to the different velocity of the spectral components between 5 MeV and 7 MeV, the bunch duration at the sample position can be estimated to 4.7 ns, leading to a dose-rate in the pulse of the order of 4.3×10^8 Gy/s. Assuming an automatic target alignement operating at 0.5 Hz, a mean dose rate of 1 Gy/s can be reached.

4.2 LPAP source of the high-energy laser facility pico2000 for single-shot ultra high dose-rate irradiation

Recent observations on FLASH-RT (see section 1.5.2) have shown that delivering the therapeutic dose ($>$ 10 Gy) in a very short time ($<$ 500 ms) and at a higher dose-rate ($>$ 40 Gy/s) than conventional treatments selectively spares healthy tissues while maintaining a comparable therapeutic effect on tumors. As discussed in the previous sections, 10 Hz lasers delivering few joules at the target are able to accelerate $\sim$nC proton bunches at a repetition rate of about 1 Hz, limited by the mechanical replacement (or displacement) of the solid target. Such beams can deliver doses around 1 Gy/shot over a sufficiently large surface ($\sim$1 cm^2), thus reaching a mean dose rate in the order of $\sim$Gy/s and a peak dose-rate in the pulse higher than 10^8 Gy/s. The unique temporal structure has been shown to produce unknown biological phenomena in irradiated cells, such as a different nitroxidative stress and a sensitivity of cell mortality to the pulse repetition rate. However, reaching FLASH-like conditions with such beams is not straightforward, since it would require to displace the target at 10 Hz or an increase of the total charge at the source of a factor of 10. In this context, high-energy lasers delivering tens of joules at the target (see Table 2.1 in section 2.2) and running at 10^{-3} Hz may be a perfect candidate to reach FLASH conditions with LPAP. Such lasers can accelerate several tens of nanocoulombs in

a single proton bunch, thus enabling the delivery of a therapeutic dose in a single pulse, i.e. in less than few nanoseconds, and the reach of irradiation conditions that are even more severe than those used in FLASH-RT. Furthermore, FLASH effect has been observed only with electrons and photons. Indeed, reaching the mean dose-rate required for FLASH-RT with commercially available proton accelerators requires challenging technological developments[5] that hindered extensive studies on proton FLASH effect with conventional accelerators.

This section presents the design of an LPAP beamline to perform *in vivo* zebrafish embryo irradiation in FLASH conditions at the 80 J LULI2000 laser facility of the Laboratoire pour l'Utilisation des Lasers Intenses (LULI). The study was conducted in the framework of an experimental campaign scheduled for December 2020 in collaboration with the LULI, the INFN-LNS of Catania (Italy), the CPO of Orsay and the Laboiratoire d'Optique et Bioscience (LOB) in Palaiseau. In particular, the section shows how an homogeneous 3D dose may be delivered in a 500 µm thick biological target by coupling the transport system with flat SSs and further optimised with non-flat SSs designed with the genetic approach described in section 3.3.

4.2.1 Experimental set-up and LPAP source

The experiment will be carried out at the LULI2000 facility employing the pico2000 beamline. The laser (∼80 J, ∼1 ps) will be focused on a thin (∼ 50 µm) gold foil target to accelerate a TNSA proton beam at a repetition rate of one shot every ∼1 hour.

According to available film stack measures carried out with a 50 µm gold target, an exponential spectrum with a cut-off energy at around 13 MeV is expected. The source spectrum and divergence, shown in Fig. 4.14, have been obtained with the film stack spectroscopy technique described in section 3.1.2. A total integrated charge of 58 nC per shot was measured, with a divergence between 10° and 4°. The cut-off energy exceeding 10 MeV will enable irradiation of 500 µm thick targets, compatible with the typical thickness of zembrafish embryos [176].

A schematic draft of the experimental set-up is shown in Fig. 4.15. The proton beam will

[5]Both passive scattering and active scanning techniques suffer from a considerable reduction of the dose-rate. Active scanning techniques may enable high peak dose-rates within each spot but the time required to scan typical tumour volumes may be too long to trigger a FLASH effect [32]. On the other hand, in passive beamlines (see section 1.3.2) the beam needs to be scattered to cover the tumour volume, which also strongly reduces the mean dose-rate achievable. A scattered proton beamline (scattering system coupled with a ridge filter) designed to reach FLASH conditions with a clinical proton accelerator over a 12×12 mm^2 was succesfully implemented at the Centre de Protonthérapie d'Orsay (CPO - Institut Curie) in 2019 [157].

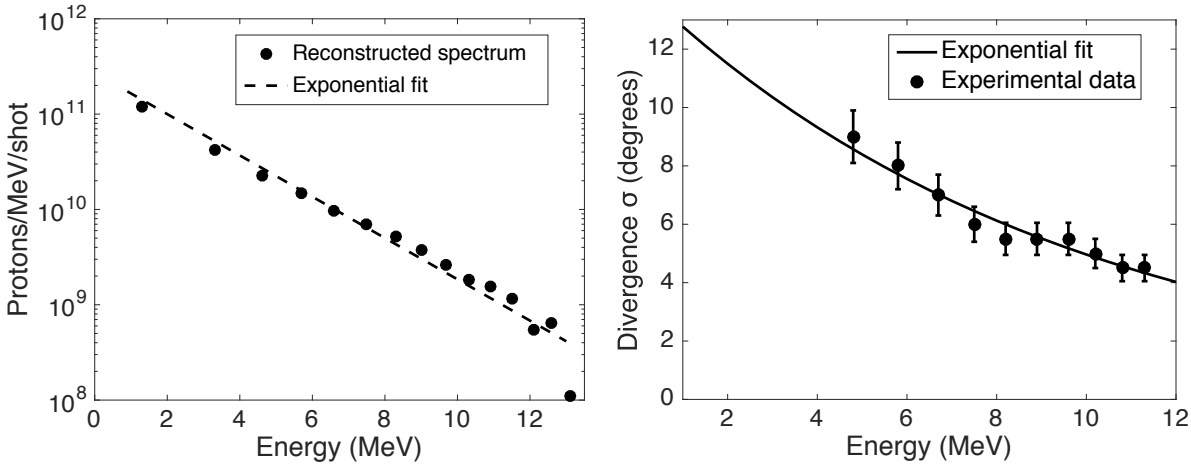

Figure 4.14: Left: proton spectrum of the LULI2000 obtained with a 50 µm gold target. The spectrum was reconstructed using film stack spectroscopy (backward approach described in section 3.1.2). Right: energy dependent divergence of the proton source.

be collected and transported with the four INFN-LNS quadrupoles [182, 183] described in previous sections. Spectral and spatial shaping will be achieved by coupling the chromatic transport system with a scattering system of a proper thickness. The beam will exit the chamber through a 70 µm kapton window to irradiate the biological target placed in air. The targeted biological volume considered for the design of the beamline has a $5 \times 5\,\mathrm{mm}^2$ surface and a thickness 500 µm. Such surface dimension will allow the reach of meaningful doses (> 10 Gy) with a high uniformity ($\pm 5\%$). The spectrum focused at the biological target will be measured before irradiation with an HD-V2 film stack and retrieved using the backward spectroscopy technique described in section 3.1.2. Dosimetry will be performed with a radiochromic film placed at front and at the back[6] of the biological target at each irradiation.

4.2.2 Transport beamline

As discussed in section 4.1, the configuration of a beamline for *in vitro* irradiation must take into account the constraint on the transverse homogeneity of the dose distribution on the target. In *in vivo* experiments a more demanding configuration is searched, since not only the transverse but also the depth-dose uniformity must be optimised. As it was mentioned in section 1.3.2, a proton beam needs to be spectrally tailored to deliver an

[6]The front radiochromic film will provide information on the transverse beam shape and on the dose delivered at the entrance of the biological target. The back radiochromic film will provide information on the beam shape after traversing the biological target and on the dose delivered in the last micrometers of the target.

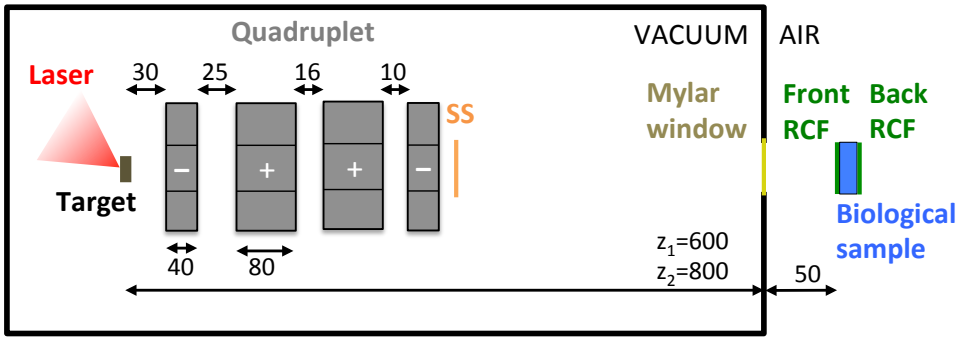

Figure 4.15: Schematic draft of the beamline. The distances are in millimiters. The plus and minus signs in the quadrupoles indicates the polarity (vertical or horizontal focus).

homogeneous depth-dose in a thick target. Conventional proton accelerators employed for protontherapy produce mono-energetic beams that require complex range-modulators (rotating weels or ridge filters) to spread the spectrum and obtain a flat Spread-Out Bragg-Peak (SOBP). The large spectrum available at the source represents therefore an

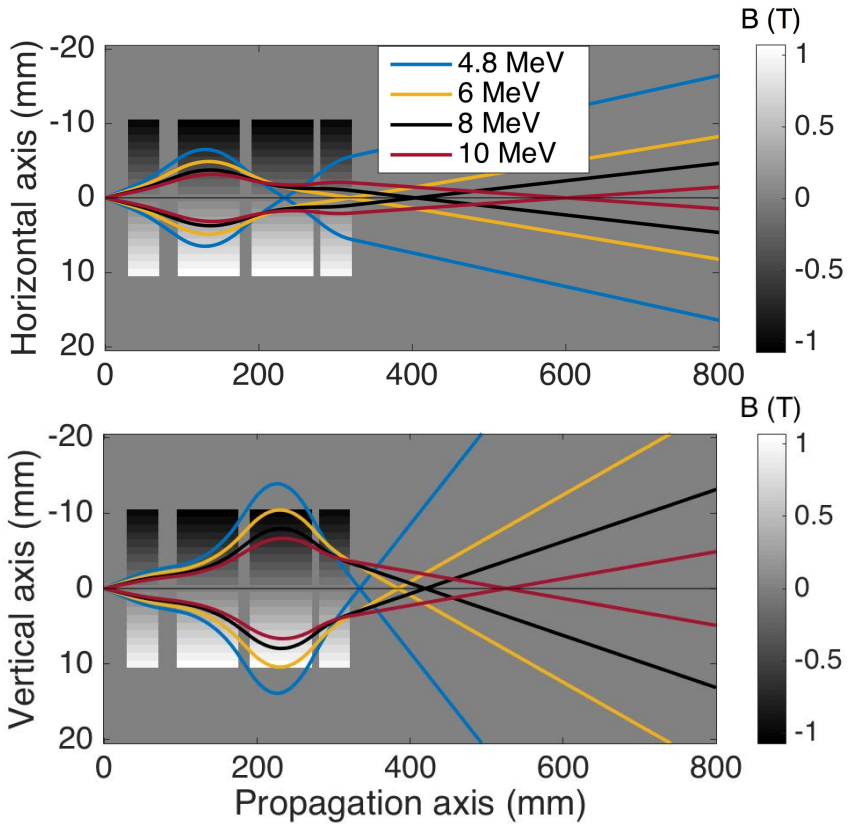

Figure 4.16: Envelopes ($\pm\sigma$ isoflux lines) of different energetic components along the transport system.

asset of LPAP, since it ease creation of a SOBP in case of 3D irradiation. Precisely, the chromatic transport beamline can be used to both transport the beam to the irradiation area and properly select the desired spectral bandwidth, which can be then shifted with the use of scattering systems acting as range-shifters (see section 1.3.2).
The configuration of the INFN-LNS quadruplet designed for the experiment (Fig. 4.15), is optimised to focus the spectral bandwidth around 10 MeV at the exit window placed between 60 cm and 80 cm far from the source. The envelopes of different energetic components along the transport system are shown in Fig. 4.16.

4.2.3 3D dose optimisation with flat SS

A theoretical study has been performed with the Geant4 tool, validated with the same quadrupole system in section 3.2.3, to evaluate the irradiation conditions and define the strategy to optimise the 3D dose distribution at the biological target[7]. Two set-up with a different position of the mylar exit window have been investigated and are described in this section.

Configuration 1 In the first set-up, the mylar window is placed at a distance of 60 cm from the source, where the energy components around 10 MeV are focused. After the energy losses in the mylar window and in the RCF (simulated as an EBT3 type), the proton beam features a peaked spectrum around 9 MeV over the targeted $5 \times 5\,\mathrm{mm}^2$ surface (Fig. 4.17.a, black line). The resulting dose distribution at the target features a maximum transverse and in-depth error of respectively 70% and 13.4%, which indicates that the beam must be further spread before reaching the target. To this aim, the configuration of the transport system was specifically designed to produce a monotically-increasing depth-dose profile at the target (Fig. 4.17.b, black bars). This condition, together with the high dose delivered (55 Gy/shot), leaves margin for optimisation of both the transverse and in-depth dose uniformity through the use of a flat SS. As it was mentioned in section 4.1, optimising both the spectral selection and the transverse uniformity of the beam with the transport system alone is not a viable and easy solution. Coupling an SS with the transport system allows a greater flexibility in dose distribution optmisation. However, when dealing with a 3D dose distribution, an SS not only increases the beam transverse uniformity at the biological target but also acts as a range-shifter introducing energy losses in the proton beam. Therefore, placing an SS in the beamline affects

[7]The dose distribution in the target is retrieved using a Geant4 sensitive scoring divided in voxels of $250 \times 250 \times 50\,\mu\mathrm{m}^3$.

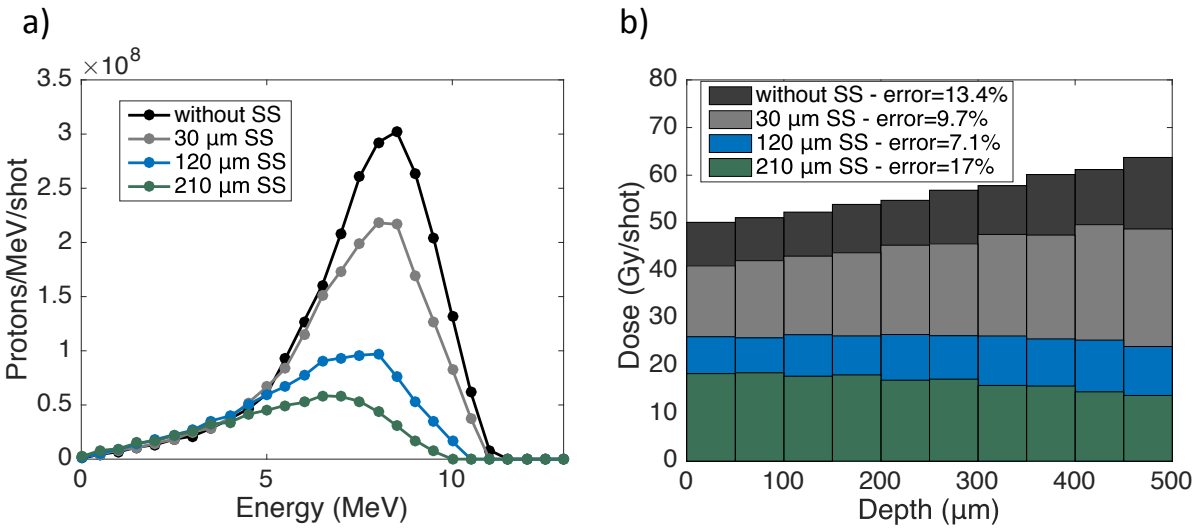

Figure 4.17: Irradiation conditions at the biological target for different thicknesses of the Scattering System (SS). Left: spectrum focused over the $5 \times 5\,\mathrm{mm}^2$ surface of the biological target. Right: corresponding depth-dose profile in the biological target (for each thickness, the legend displays the depth-error, i.e. the ratio between the maximum and the minimum values of the depth-dose profile). As the SS increases, the spectrum focused at the target shifts towards lower energies, thus flattening the monotonically increasing depth-dose profile obtained without the use of SSs.

both the transverse and in-depth dose uniformity. If the depth-dose profile in the biological target obtained with the transport system alone is monotonically increasing, an SS has a positive impact on both the transverse and depth-dose profile, since it increases the transverse homogeneity by spreading the beam and flattens the depth-dose profile by shifting the spectrum towards the lower energy components, as shown in Fig. 4.17. The figure shows the effect of Mylar flat SSs of various thicknesses, placed right after the fourth quadrupole, on both the spectrum reaching the biological sample, simulated as water, and the corresponding depth-dose distribution. As the SS thickness increases, the spectrum is shifted towards the lower energies, thus increasing the relative contribution of low-energy protons on the depth-dose profile. As a consequence, the monotonically-increasing depth-dose profile obtained with the transport system alone is flattened, until the profile becomes monotonically-decreasing and a further increase of the SS thickness worsens the in-depth uniformity. At the same time, the beam spread introduced by the SS results in a decrease of both the transverse dose error and total dose delivered, as shown in Table 4.2. Optimisation of the SS thickness depends, therefore, on the interplay between these three parameters. As shown, when the best condition on the depth error

Table 4.2: Table summarizing the irradiation conditions obtained at the target in the configuration 1 (mylar window placed at 60 cm from the source) for different thicknesses of the scattering system.

SS thickness (µm)	Dose (Gy/shot)	Maximum transverse error	Maximum depth error
30	45.4	47.4%	9.7%
120	25.9	23%	7.1%
150	22.2	20%	9%
180	19.2	18%	16%
210	16.7	16.6%	17%
240	14.5	16.6%	18%

is reached (SS thickness of 120 µm), the transverse error is still high[8]. The best trade-off is reached with an SS thickness of 210 µm, which corresponds to the decrease of both the transverse and depth errors below 17% and to a total delivered dose of 16.7 Gy/shot.

Configuration 2 Further optimisation of the dose errors requires modifications of the beamline or of the set-up to generate, without SS, a larger beam with a similar spectrum at the biological target. An easy and viable solution is to move the Mylar window further away from the source, so as to propagate the beam along a greater distance in vacuum. This would produce a larger beam field at the sample without introducing additional energy losses. In this second configuration, the Mylar window is placed at a distance of 80 cm from the source whereas the 5 cm distance between the biological sample and the window is kept fixed. In this configuration, the spectrum focused at the window by the transport system is slighlty shifted towards higher energies (Fig. 4.18), as the low energy components feature a higher divergence after the transport system (Fig. 4.16). The condition is equally suitable to optimise the dose distribution with flat SSs, as shown in Table. 4.3. The trend is the same as the one observed in the previous configuration: the transverse error decreases as the SS thickness increases whereas the depth error reaches a minimum value and then increases. However, in comparison with the previous set-up, the larger beam at the biological target position enables the reach of a lower transverse error for a comparable depth error. For example, a transverse maximum error of around 11% and a depth error below 3% can be reached with a 90 µm thick SS. The corresponding dose

[8]The depth error is defined as the ratio between the maximum and minimum values of the depth-dose profile. The transverse error is defined as the ratio between the maximum and minimum values of the transverse dose map. Since the beam shape changes as the beam goes through the target, 10 values of tranverse errors are obtained separately for each of the 50 µm thick slices in which the biological target is divided, and the maximum value of the transverse error is considered for the study.

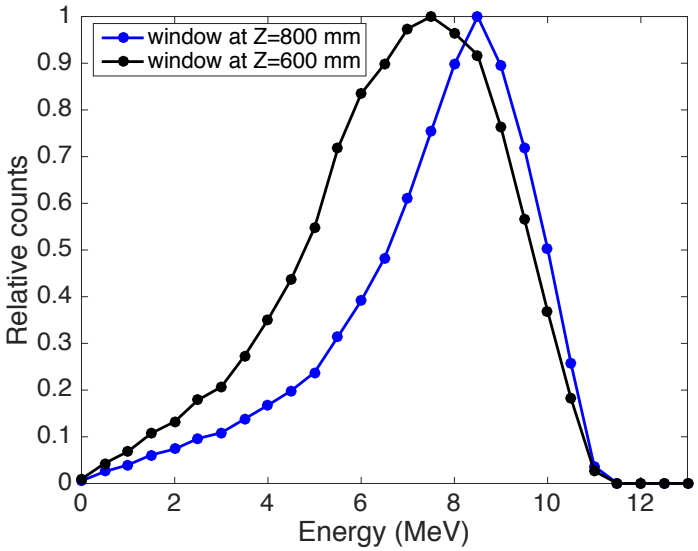

Figure 4.18: Spectra focused at the exit window in configuration 1 (window at $z = 600$ mm) and configuratio 2 (window at $z = 800$ mm).

Table 4.3: Table summarizing the irradiation conditions obtained at the target in the configuration 2 (mylar window placed at 80 cm from the source) for different thicknesses of the scattering system.

SS thickness (µm)	Dose (Gy/shot)	Maximum transverse error	Maximum depth error
30	14.9	18.6%	7%
90	10	11%	2.8%
120	8.5	10.8%	5.1%
180	6.5	10.8%	13.4%

of 10 Gy would be sufficiently high to trigger a FLASH-like effect on Zebra-fish embryo.

4.2.4 3D dose optimisation with GA-designed SS

In the previous sections we showed that the 3D dose distribution can be shaped and optimised through the use of a flat SS. This approach will be used during the short-run LULI experiment, since the SS thickness can be easily re-optimised if the proton source is considerably different (different characteristic slope of the spectrum or cut-off energy) than the one used for the study. Film stack spectroscopy of the source will allow a first optimisation of the scattering system thickness through Geant4 simulations, as discussed. An experimental verification of the SS impact on the dose distribution at the biological target can then be performed with a film stack placed at the target position.
The use of flat SS, as shown, has a limited flexibility since it does not allow for a sepa-

rate control of the in-depth and transverse dose homogeneity. For example, in the first analysed configuration (exit window placed at 60 cm from the source), it was not possible to decrease both the transverse and depth errors below a 10% threshold. A higher flexibility could be reached by employing non-flat SSs placed along the transport system, provided that a fine characterisation of the proton source and beam transport is previously performed (as it was the case in the SAPHIR facility, section 3.1.3). In section 3.3 we presented this approach together with the strategy adopted to optimise the SS design with a Genetic Algorithm (GA). In particular, we showed that a non-flat SS inserted in the transport beamline and properly designed can shape the dose distribution over a 2D *in vitro* biological target more efficiently than a flat SS. The most interesting application of this approach is, however, the optimisation of 3D dose distributions, where not only the transverse beam shape but also the in-depth dose profile (i.e. the beam spectrum) need to be optimised. The GA approach is therefore tested with the LULI beamline to further optimise the dose distribution in the biological sample in the first configuration (configuration 1).

A Mylar GA-SS is placed before the third quadrupole and has a surface of $18 \times 18\,\mathrm{mm}^2$ that covers the entire beam profile. It is divided in tiles of $2 \times 2\,\mathrm{mm}^2$, whose thickness can be varied between 20 µm and 300 µm with a resolution of 20 µm. Geant4 simulations[9] with 5×10^8 particles at the source have been performed to generate the GA elementary dose maps (see section 3.3) for each of the 2D 50 µm thick slices (10 slices) in which the 500 µm thick target is divided. The 3D dose distribution at the target is then optimised with the GA by minimising the following fitness function:

$$F = a \cdot \left(\frac{\sigma^t_{Mss} - \sigma^t_{Mno-ss}}{\sigma^t_{Mno-ss}}\right) - b \cdot \left(\frac{D_{ss} - D_{no-ss}}{D_{no-ss}}\right) + c \cdot \left(\frac{\sigma^d_{ss} - \sigma^d_{no-ss}}{\sigma^d_{no-ss}}\right) \tag{4.1}$$

The first two terms are similar to those used for the optimisation of the 2D dose profile presented in section 3.3. The first term is used to minimise the maximum value of the standard deviation of the transverse dose distribution in the 10 slices of the target whereas the second term is used to maximise the total delivered dose. In addition, a third term is used to minimise the standard deviation of the in-depth dose profile. The three coefficients a, b and c are used to set different relative weights to the parameters and to adjust the SS design and the corresponding dose distribution according to the specific goal.

In the analysed case, the aim is to verify wether it is possible, with such approach, to reach an error lower than 10% in the first configuration of the LULI set-up. The GA-SS

[9]The G4beamline Geant4-based application was used.

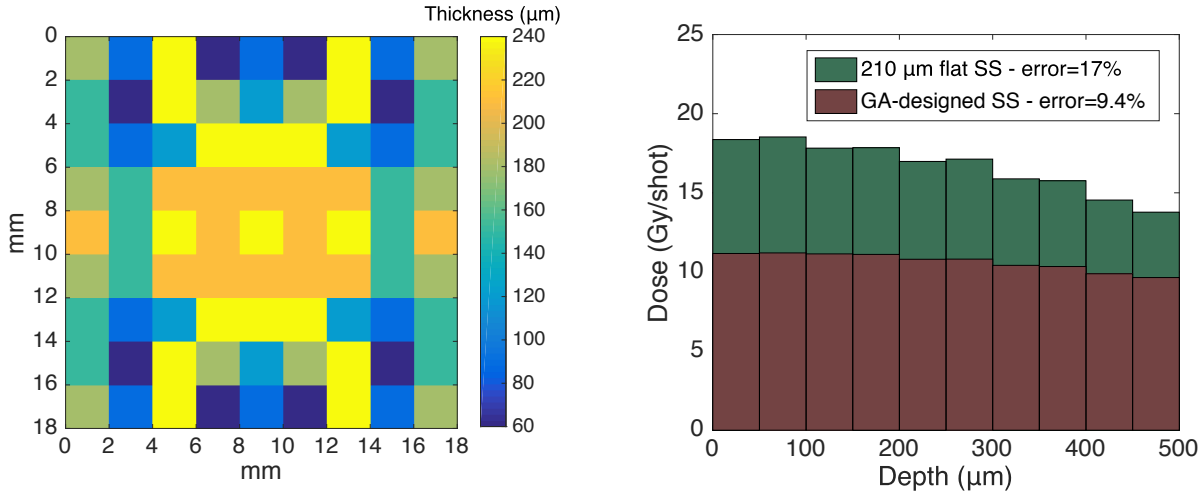

Figure 4.19: Left: design of the Scattering System (SS) designed with the Genetic Algorithm (GA). Right: depth-dose profile obtained with the GA-SS compared with the profile obtained using a 210 µm Mylar flat foil.

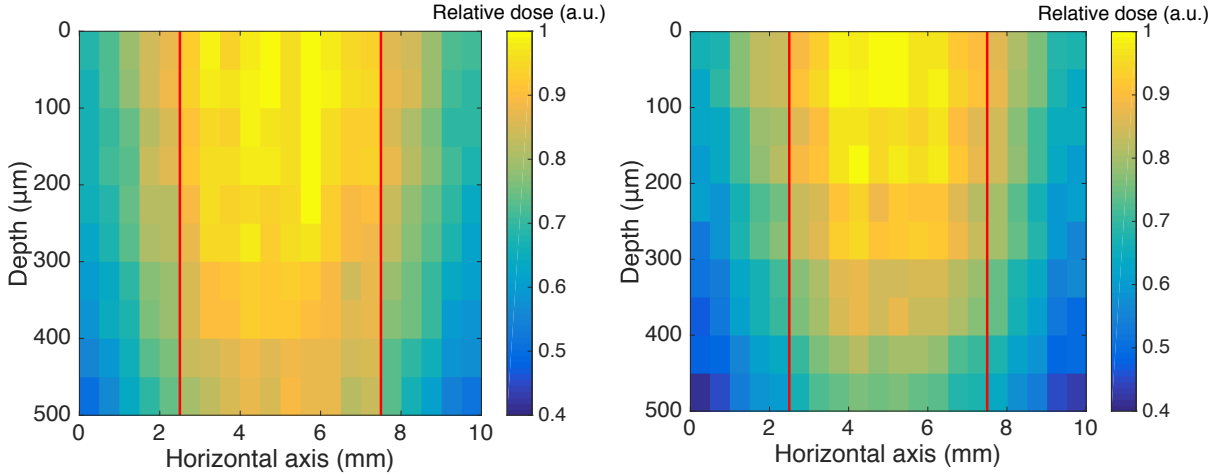

Figure 4.20: Horizontal cut of the dose distribution at the biological target on the central axis, obtained with the Mylar scattering system designed with the genetic algorithm (left) and with a 210 µm Mylar flat foil.

enables the reach of transverse and depth errors of respectively 9.8% and 9.4% for a total delivered dose of 10.7 Gy. The SS design obtained with the GA is shown in Fig. 4.19, together with the comparison between the depth-dose profile obtained with the 210 µm flat SS, which allowed the best trade-off between transverse and depth error (see previous section), and the GA-SS. A top-view of the relative dose distribution in the biological target in the two cases in shown in Fig. 4.20. As shown, the GA-SS can reduce the transverse error below 10% without entailing an increase of the depth dose error, as it was the case with flat SSs. This is due to the fact that the non-flat SS introduces variable energy losses on the transverse plane of the proton beam. As a result, it can separate to some extent the optimisation of the beam scattering and of the spectral shaping, thus improving the trade-off between transverse and depth dose errors.

4.3 Conclusions

The chapter presented theoretical and experimental studies carried out with laser-plasma accelerated protons (LPAP) generated by two types of lasers: the J-class laser of the ILIL-PW facility running at 10 Hz and the multi-J laser of the pico2000 facility firing a shot every hour.

A precise characterisation of the ILIL-PW proton source allowed to study different PMQ transport systems and to evaluate the irradiation conditions on *in-vitro* biological samples. The extremely small divergence compared to similar LPAP sources enables the reach of a high transport efficiency and, in turn, the delivery of a dose up to 2 Gy/pulse over a surface of 1 cm^2. Further optimisation of the spectrum focused on the sample may be obtained by adding an energy selection system after the quadrupole system. Mean dose-rates in the order of 1 Gy/s can be reached by implementing an automatic target alignment at a frequency in the order of 1 Hz. Such conditions will allow to study the biological effect of very high peak dose-rate ($\sim 4.3 \times 10^8$ Gy/s) and of the temporal modality of dose delivery with LPAP bunches.

The second section presented the design of an LPAP beamline for the high energy laser of the pico2000 facility to perform *in-vivo* FLASH irriadiation of zebrafish embryos. The results show that 3D dose optimisation can be succesfully performed by coupling a PMQ transport system with flat scattering systems and that a therapeutic dose ($>$ 10 Gy) can be delivered in a single ns bunch, thus reaching irradiation conditions even harder than FLASH-RT. In addition, the genetic approach presented in chapter 3 was shown to further improve the dose homogeneity in 3D biological targets.

Chapter 5

Ionisation chambers for high dose-rate, pulsed beam dosimetry

Contents

Overview

Ionisation chambers (ICs) are the recommended system for clinical reference dosimetry together with calorimeters [2]. At High Dose-Rate (HDR) and Ultra High Dose-Rate (UHDR) regimes, such as those of FLASH-RT and LPA beams, ICs suffer from incomplete charge collection due to recombination between positive and negative charges generated by ionisation. Characterization of ICs in these conditions is therefore one of the chal-

lenges to be addressed prior to the transfer of such dosimetry systems to high dose-rate irradiation protocols. Reliable alternatives for UHDR dosimetry are radiochromic films (RCF) and alanine detectors [108, 84], which however require post-irradiation processing and are therefore not convenient for practical use in clinics. RCFs have been largely used in this thesis for both laser-plasma accelerated beam spectroscopy (see section 3.1.2) and high dose-rate reference dosimetry in the following sections. They are described in the following section together with a discussion on their use for high dose-rate dosimetry. Then, following the discussion of ICs working principle, this section presents the recombination theory for pulsed beam and the calibration of a Razor Nano Chamber (IBA, Belgium) with high dose-rate, pulsed electron beams.

5.1 Radiochromic films

Radiochromic films (RCFs) are widely used as dosimetry system in most medical and radiation physics applications. They consist in a micrometric thick sensistive layer protected on one or both sides by a polyester coating. They exist in a variety of models, which have a different sensitivity depending on the active material thickness. A review of the most employed film structures and standard film dosimetry procedures can be found in S. Devic et al. (2016) [56].
Interaction with ionizing radiation causes polymerization of a dye molecule of the film sensitive layer, resulting in a blackening at macroscoping level. After exposure[1], the film is scanned with a standard flatbed scanner that measures the red, green and blue color components of light transmitted by the film. The film response is quantified using the change in optical density, defined as [48]:

$$OD = -log_{10}(\frac{I}{I_0}) \tag{5.1}$$

where I represents the pixel value read with the scanner for a given color channel, or an average value within a Region Of Interest (ROI) and I_0 represents the background value for the same channel, as shown in Fig. 5.1. The optical density can be converted into deposited dose after establishing the RCF calibration curve, which depends on several factors, including beam parameters, such as particle type and energy, film batch and the model of the scanner employed [60, 206]. An exemple of RCF calibration curve[2] obtained

[1]The blackening process is stabilised a few hours after irradiation.
[2]The calibration has been performed at the Oriatron eRT6 LINAC prototype and used for the film dose measurement during the ionisation chamber calibration experiments presented in section 5.4.

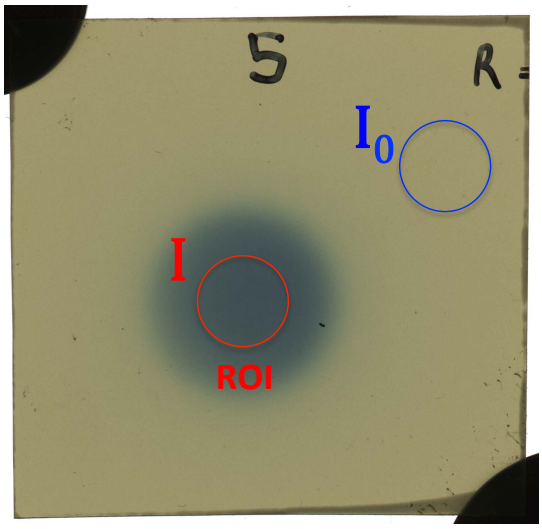

Figure 5.1: Example of a radiochromic film irradiated with 6 MeV electron beam.

with EBT3 film type and 6 MeV electrons is showed in Fig. 5.2.

Radiochromic films for high dose-rate dosimetry In recent years RCFs received great attention and many studies have been conducted to investigate their behaviour at high dose-rate. The dose-rate independence of radiochromic film is accepted by the medical community for typical clinical dose-rate, and some works demonstrated their dose-rate independence at higher dose-rates. M. Jaccard et al. (2017) demonstrated the EBT3 film dose rate independence in FLASH conditions, precisely in a range between 7×10^3 Gy/s and 8×10^6 Gy/s [104]. Regarding the behaviour of radiochromic films at the extreme conditions attained with LPA beams, L. Karsh et al. (2012) [110] found no significant dose-rate dependence of EBT film irradiated with 20 MeV pulsed electron beams for peak dose-rate whitin the pulse ranging from 3×10^8 Gy/s to 15×10^9 Gy/s. Similar results were found by M. Bazalova-Carter et al. (2016) [18] with 60 MeV pulsed electrons at even higher dose-rates, ranging from 3×10^{12} Gy/s to 9×10^{12} Gy/s. All together, these findings indicate that RCFs can be used as dosimetry system over a wide range of dose-rate levels and suggest that they are not sensitive to the dose-rate, although a systematic study of the film response over the entire dose-rate spectrum, from clinical to HDR and UHDR conditions, have not yet been conducted.

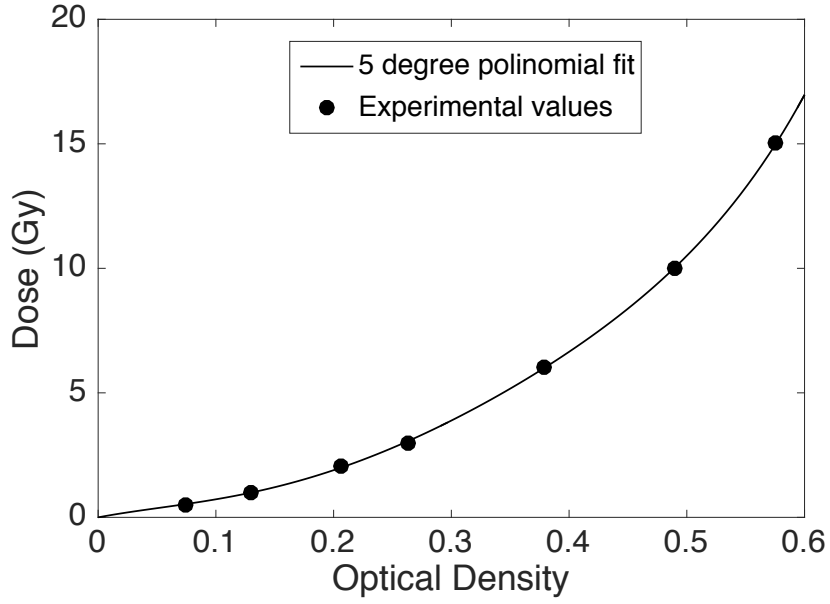

Figure 5.2: EBT3 calibration curve (red channel) obtained with 6 MeV electrons.

5.2 Ionisation chamber working principle

Ionisation Chambers (IC) are primarily employed for ionising radiation dosimetry in medical applications. They are based on the ionisation process generated by a radiation passing through the gas sensitive volume. In the most general version, ICs consist in an air-filled chamber at atmospheric pressure to which an electric field is applied by two electrodes. As radiation passes through the air, it elicits excitation and ionisation of the gas molecules, as described in section 1.2. If a voltage is applied, the resulting positive and negative charges, called ion-pairs, are collected by the electrodes (Fig. 5.3.a).

The chamber voltage is optimised to operate between two regions: the recombination and the proportional regions (Fig. 5.3.b). At low voltage (recombination region), ion pairs can recombine soon after they are formed and only a small fraction is collected by the electrodes. As the voltage is increased, fewer ion pairs recombine until the operating "ionisation region" is reached. In such region, all charges are collected and the chamber response does not depend on the applied voltage, since recombination becomes negligible. With a further increase of the voltage, ion pairs gain enough kinetic energy to generate further ionisation events. This is the typical region where other detectors such as proportional and Geiger-Muller detectors work.

The chamber response in terms of integrated charge (or ionisation current) is measured with an electrometer and related to the dose deposited in the IC sensitive volume. The relationship between the absorbed dose and the collected charge is expressed with the

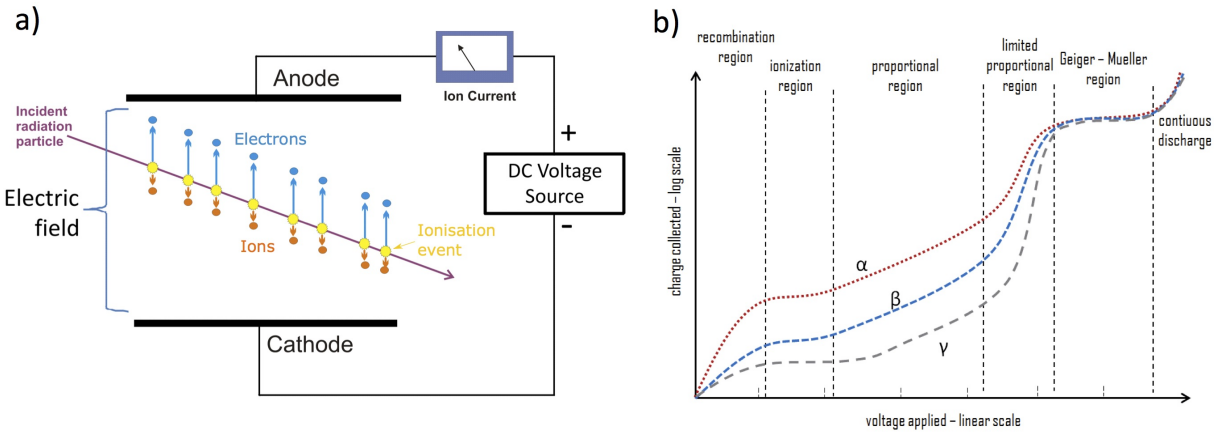

Figure 5.3: a) Schematic draft of an Ionisation Chamber (IC) operating principle: as radiation traverses the IC sensitive volume, ion-pairs are produced and collected at the electrodes. The ion current (or the total collected charge) is proportional to the radiation dose absorbed by the gas medium. Taken from L. Pommarel (2017) [162]. b) Typical operating voltage regions of gas-filled detectors for three different radiations. ICs operate in the ionisation region, where all ion-pairs are collected by the electrodes and the chamber response as a function of the applied voltage reaches a plateau. At higher voltages, secondary ionisation events are generated by the ion-pairs (taken from https://www.radiation-dosimetry.org/what-is-recombination-region-ionization-detector-definition/).

following formula [2, 159]:

$$D = M \cdot N_{W,Q_0} \cdot k \tag{5.2}$$

In the expression, M is the collected charge displayed by the electrometer in nC, N_{W,Q_0} is the calibration coefficient in Gy/nC, where W refers to the gas type and Q_0 indicates the reference beam quality[3] used in clinics for absolute calibration. The coefficient k is called "correction factor" and includes all factors leading to a different chamber response compared to the reference condition. Precisely, it is expressed as the multiplication of the following factors:

$$k = k_Q \cdot k_{T,P,h} \cdot k_{elect} \cdot k_{pol} \cdot k_{rec} \tag{5.3}$$

where:

- k_Q is used to correct for the different beam quality.
- $k_{T,P,h}$ is used to correct for the different atmospheric conditions such as temperature, pressure and humidity.
- k_{elect} is used to correct for a different electrometer response.

[3]The beam quality factors takes into account beam parameters such as particle type and geometry. In clinics, the reference beam quality usually used for chamber calibration is a CO^{60} beam of a 10×10 cm^2 transverse section.

- k_{pol} is used to correct for the the dependence on electrode polarizing voltage of opposite polarity.
- k_{rec} is used to correct for incomplete charge collection due to ion recombination.

All these factors can be computed theoretically or with standard protocols that can be found in the IAEA technical report of 2001 [2].
ICs are calibrated with clinical accelerators or in standards laboratories, using previously calibrated ICs or calorimeters as reference dosimetry. For typical clinical beams, the relationship between the absorbed dose and the measured charge does not depend on the dose-rate. However, ion recombination might become significant at high dose-rates because of the higher instantaneous ionisation density. In particular, recombination in pulsed beam regimes is an extremely complex phenomenon, since it depends on both the dose-rate and total dose within the pulse. Its characterisation is indeed a crucial issue when it comes to transfer the standard dosimetry protocols used in clinics to FLASH irradiation or even more severe conditions such as those available with LPA beams.

5.3 IC recombination correction with high dose-rate, pulsed beam

The collected charge for a given chamber voltage is generally smaller than the saturation charge Q_{sat}[4], since opposite charges recombine during their diffusion towards the electrodes. The ion collection efficiency is used to quantify the incomplete charge collection and is defined as the ratio between the charge collected by the chamber Q and the saturation charge Q_{sat}:

$$f = \frac{Q}{Q_{sat}} \tag{5.4}$$

The inverse of the ion collection efficiency $k_{rec} = 1/f$ is called recombination factor and is used to correct the chamber calibration (equation 5.2) for ion recombination.
As previously discussed, the charge collected by an IC depends, for a given deposited dose, on the applied voltage: it increases almost linearly with the chamber voltage from zero to some value (the "recombination region") and then reaches a plateau (the "ionisation region"), where all charges are collected and recombination can be considered negligible (see Fig. 5.3.b). At dose-rates higher than those typically employed in clinics, a complete

[4]The saturation charge is defined as the charge of secondary electrons produced by radiation in the sensitive volume, which would be equal to the charge collected by the electrodes if no recombination occurs (charge collected in the ionisation region in Fig. 5.3).

charge collection can not be achieved without increasing the chamber voltage to a level in which ions gain enough energy to produce secondary ionisations (proportional region in Fig. 5.3.b). In other words, ionisation chambers can only operate in a recombination region if the dose-rate exceeds some critical level. In such conditions, the recombination process needs to be carefully characterised.
Recombination can be divided into two types of processes, called initial and general recombination. Initial (or columnar) recombination occurs between ion-pairs produced within the track of a single ionising particle and, therefore, does not depend on the dose or the dose-rate. It can be predominant in the tracks of high-LET radiation such as protons and alpha particles. General (or volume) recombination occurs between ion-pairs generated from different tracks that encounter each other on their way to the electrodes. In high dose-rate, pulsed beams it is an extremely complex phenomenon since it depends on both the dose-rate and the total dose within the pulse. From a practical point of view, distinguishing between both recombination contributions is too cumbersome and not necessary if the combination of the two effects can be accurately quantified. Moreover, a comprehensive theoretical model enabling a precise description of recombination for all chamber types and dimensions and in a wide range of dose-per-pulse (DPP) and dose-rate has not been formulated yet. Recombination has therefore to be evaluated experimentally for each chamber and beam quality. Nonetheless, theoretical models have been proposed and, although they are not valid for the entire range of dose-rates and DPP, they are currently used to interprete and fit the experimental measurements.

Boag theory The models employed to describe ion recombination for pulsed beams in most dosimetry recommendations are based on the Boag theory. It describes ion recombination for pulsed beams meeting the following conditions [25, 109]:

- Independent pulses: the interval between pulses is longer than the ion collection time (i.e. the time required by the slowest ion to be collected at the electrodes) plus the time required by the electrometer to elaborate the signal. If this conditions are met, the pulses can be treated separately and recombination can be described as a function of the dose-rate and total dose within the pulse.

- Instantaneous pulses: the pulse duration is short compared to the ion collection time. As a consequence, the production of secondary charges within the chamber sensitive volume can be considered instantaneous and, as discussed in the following, recombination can be described as a function of the total dose delivered in the pulse rather than the dose-rate.

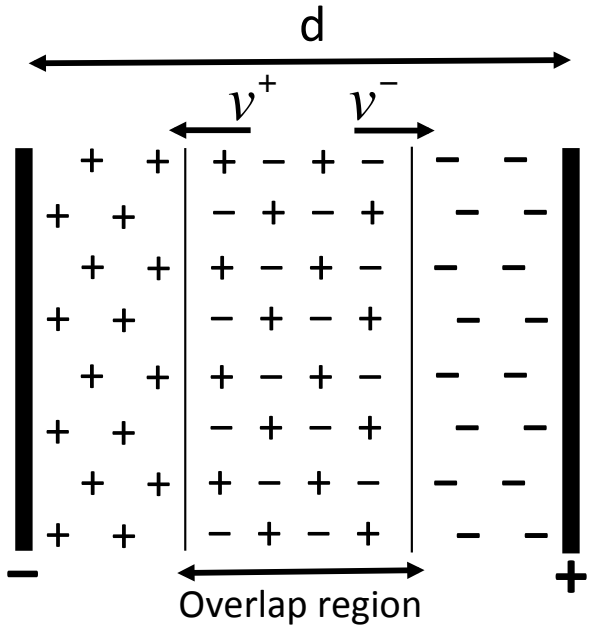

Figure 5.4: Schematic draft of the ion distribution in a parallel plate ionisation chamber after an instantaneous pulsed dose deposition according to the Boag model.

- Electronegative gas: electrons immediately attach to molecules forming negative ions. Therefore, recombination occurs primarily between positive and negative ions and no free-electrons reach the electrodes.

- No space-charge effect: the presence of charged ions in the chamber volume affects the electric field to a negligible extent.

For the formulation of his theory, Boag considers a parallel plate ionisation chamber, whose electrodes are separated by a distance d and apply a voltage V. After the instantaneous deposition of a dose D = DPP, the chamber's sensitive volume can be divided in three sections, as shown in Fig. 5.4: two sheaths composed of negative and positive ions directed towards respectively the positive and negative electrodes and a central region containing ions of both signs where volume recombination occurs. Since dose deposition is considered instantaneous, no further charges are created in the sensitive volume and ion recombination is exclusively affected by the diffusion process and the characteristic ionic recombination coefficient α of the gas. All these assumptions lead to the Boag's expression for the ion collection efficiency:

$$f = \frac{1}{u}\ln(1+u) \tag{5.5}$$

The parameter u depends on both the chamber characteristics (dimension and voltage) and the initial charge generated by the pulse, according to:

$$u = \frac{\mu d^2 Q_{sat}}{V} \tag{5.6}$$

where μ is a constant that depends on both the ionic recombination coefficient and the drift velocity of negative and positive ions ($\mu = \alpha/(v^+ v^- e)$). Therefore, since Q_{sat} is proportional to the total absorbed dose, the ion collection efficiency can be expressed as a function of the DPP and the chamber voltage [159]:

$$f = \frac{V}{\varepsilon \cdot DPP} \ln\left(1 + \frac{\varepsilon \cdot DPP}{V}\right) \tag{5.7}$$

where ε is a constant. Altough the Boag theory was formulated for parallel plate IC it can be also applied to cylindrical and spherical chambers by multiplying the electrode distance d by a geometrical correction factor [26].

Two voltage analysis For small values of $u \to 0$, i.e. small values of DPP, a first order approximation of equation (5.5) leads to the so called Two Voltage Analysis (TVA) method:

$$k_{rec} = a_0 + a_1 \cdot \left(\frac{Q_1}{Q_2}\right) + a_2 \cdot \left(\frac{Q_1}{Q_2}\right)^2 \tag{5.8}$$

The method assumes a linear dependence of $1/Q$ on $1/V$ and expresses the recombination factor k_{rec} as a function of the charge Q_1 and Q_2 collected by the chamber with a polarizing voltage of respectively V_1 and V_2. The coefficients a_0, a_1 and a_2 are constants that depend on the polarizing voltage ratio V_1/V_2 used for the method. Their values are tabulated in the IAEA code of practice (Technical Reports Series No. 398) [2], which recommends the use of a voltage ratio V_1/V_2 equal or higher than three for the TVA method.
The TVA should only be used to compute ion recombination for small DPP (tens of mGy) [76, 159, 136]. For higher values of DPP, TVA generally overestimates k_{rec} and recombination is described more precisely by the updated versions of the first Boag model, which are presented in the following.

Boag correction for free electrons The initial version of the Boag model (eq. 5.5) assumes that secondary electrons produced by radiation rapidly attach to molecules and that charge carriers are positive and negative ions alone. Therefore, it does not take into account the fraction of electrons that do not attach to oxygen molecules and rapidly reach

the electrodes. These free electrons cause a deficit of negative ions and, as a consequence, a reduction of ion recombination compared to the model estimation. Detailed theoretical and experimental studies on electron attachment were conducted in the '80-'90 by Hochausser and Balk [97], who found a considerable amount of free electrons (typical values of the free electron fraction range from 0.1 and 0.5).
Later, J. W. Boag et al. (1996) [27] proposed three revised versions of the first model accounting for the presence of free electrons. The concentration of negative ions n^- along the drift distance z towards the electrodes can be written as:

$$n^-(z) = n^+ \cdot (1 - e^{az}) \tag{5.9}$$

where n^+ is the initial concentration of positive ions following the instantaneous dose deposition (i.e. the concentration of negative ions without electron attachment) and a is a coefficient representing the probability of electron attachment per unit drift length. The fraction of free electrons p crossing the electrode gap without attaching to molecules can be expressed as a function of the attachment probability and the gap distance d, according to:

$$p = \frac{1 - e^{-ad}}{ad} \tag{5.10}$$

The three Boag's versions differ in the way they approximate the theoretical negative ion fraction (solid line in Fig. 5.5) between the electrodes:

- The first model assumes a constant negative ion density reduced by a factor of $(1 - p)$ (Fig. 5.5.a). The corresponding collection efficiency formula derived from this model is:
$$f = \frac{1}{u} \ln\left(1 + \frac{e^{pu} - 1}{p}\right) \tag{5.11}$$

- The second model assumes a concentration of negative ions equal to that of positive ions along a distance $d(1 - p)$ and a layer of thickness pd close to the negative electrode devoid of negative ions (Fig. 5.5.b). The corresponding collection efficiency formula is:
$$f = p + \frac{1}{u} \ln[1 + (1 - p)u] \tag{5.12}$$

- The third model fits more closely the concentration of negative ions (eq. 5.9) by combining the first two models. It assumes a constant negative ion density reduced by a factor $1-\lambda$ for a distance $d(1-\lambda)$ and a layer of thickness λd devoid of negative ions. The λ coefficient is expressed as a function of the free electron fraction as

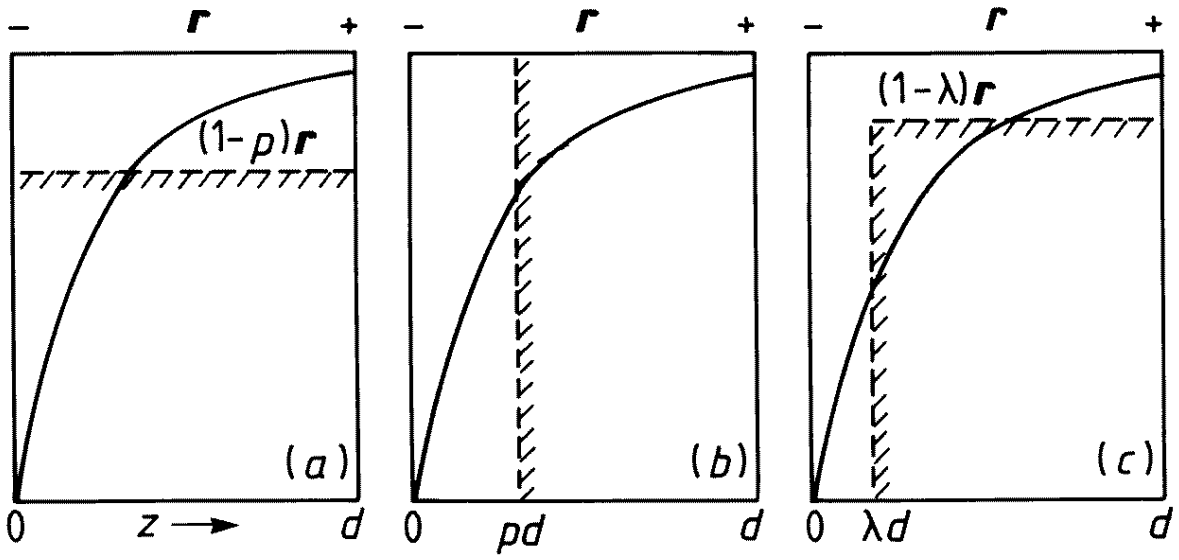

Figure 5.5: Schematic of the ion distribution following dose deposition in the three Boag models correcting for the free electron fraction. The charge of positive ions r is constant between the electrodes whereas the charge of negative ions is assumed to follow different distributions in the three models (dotted line) approximating in different ways the theoretical exponential curve of equation (5.9) (solid line). Taken from J. W. Boag et al. (1996) [27].

$\lambda = 1 - \sqrt{1-p}$. The corresponding collection efficiency formula is:

$$f = \lambda + \frac{1}{u}\ln[1 + \frac{e^{u\lambda(1-\lambda)}}{\lambda}] \tag{5.13}$$

As it can be verified, the three models may significantly diverge from equation (5.9) for high values of DPP. J. W. Boag et. al (1996) [27] did not give recommendations regarding the use of one of the three methods in particular. They only observed that the third formula, which approximates the real negative ion distribution more closely, provides intermediate values of f when the first two models start to diverge. R. F. Laitano et al. (2006) [117] tried to evaluate the recombination coefficient for parallel plate chambers starting from Boag's expressions[5]. They compared k_{rec} computed with the four Boag formulas to the results obtained with ferrous sulphate chemical dosimetry, which is independent on the dose-rate, in the range from 20 mGy/pulse to 120 mGy/pulse. They found that the first Boag method, which does not account for free electrons, may estimate k_{rec} with significant errors up to 40% [6]. Moreover, they found that among the

[5]The difficulty of calculating the recombination coefficient with theoretical approaches lies in the inaccuracy on the parameters affecting the free electron fractions, such as the drift velocity and the attachement coefficient, and on the approximations of the model itself.

[6]The importance of free electrons has been also recently confirmed by numerical transport models [85].

three models proposed by Boag, the third one provides the most accurate estimation of k_{rec}. This finding was further confirmed by Petersson et al. (2017) [159], who found the third model to be the most accurate to fit their experimental measurements of k_{rec}.
However, at higher DPP values ($\sim$ 1 Gy/pulse), these models may reach their limit since the space charge effect might significantly alter the electric field, as postulated by Boag et al. in 1996. For this reason, ICs need to be experimentally characterized at high dose-rate, pulsed beams.

5.4 Razor Nano Chamber calibration with microsecond electron bunches

Micro ionisation chambers present great advantages for small-field dosimetry[7], since they enable good spatial resolution and their response is less sensitive to beam quality [168]. Furthermore, in the context of HDR dosimetry, they may withstand higher values of DPP, since their smaller active volume reduces the ion collection time and, as a consequence, the ratio of recombined charges. They represent therefore a promising option for high dose-rate, pulsed beam dosimetry.
This section presents the calibration of a Razor Nano Chamber prototype (Fig. 5.6) with 5 MeV, $\sim$µs electron bunches. The Razor Nano Chamber (RNC) prototype, recently developed by IBA, is an air-filled IC with an extremely small spherical active volume[8] of 0.003 cm^3. This work was performed in collaboration with the IMNC-IN2P3 laboratory (Orsay, France) and the *Centre Hospitalier Universitaire Vaudois* (CHUV, Lausanne). The main goal was to characterize the chamber response in a microsecond pulsed regime and to compare it with standard chambers employed in clinics, in view of its transfer to LPA beam dosimetry. Section 5.5 presents some preliminary results on the chamber response under femtosecond laser-plasma accelerated electron bunches.

[7]Small fields are usually defined between $4 \times 4\,cm^2$ and $0.3 \times 0.3\,cm^2$ [156]. The use of ionisations chambers typically employed for conventional fields (around $10 \times 10\,cm^2$) can lead to large dose errors due to the similar or larger surface of the dosimeter compared to the radiation field, which prevent the signal to be accurately related to the absorbed dose in a given point of the field [3].

[8]The inner and outer electrodes of the Razor Nano Chamber have a diameter of respectively 1 mm and 2 mm and are made of Shonka (C-552) and graphite-EDM3 (https://www.iba-dosimetry.com/product/razor-nano-chamber/).

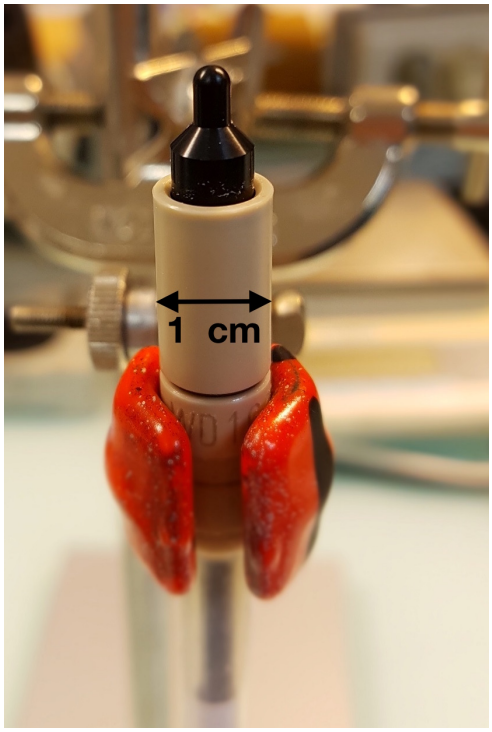

Figure 5.6: Picture of the Razor Nano Chamber.

5.4.1 Experimental set-up and methods

The chamber was characterized at the eRT6 Oriatron accelerator available at the CHUV. The Oriatron is a modified LINAC prototype capable of delivering 0.5 to 3 µs electron bunches with DPP ranging from 10^{-4} Gy to 10 Gy. It has been recently commissioned [105] and, after numerous experimental activities dedicated to characterisation and validation of the dosimetry [104, 159, 108], it was used for the first human FLASH-RT treatment in 2019 [33].

The generated horizontal electron beam presents a circular transverse section of 20 cm diameter (FWHM) at a Source-to-Surface Distance (SSD) of 100 cm. The output beam parameters are tuned by setting independently the LINAC parameters, i.e. number of electron pulses, repetition rate, pulse duration, and grid tension. This latter regulates both the accelerated charge and the beam energy. Different combinations of such parameters allow variation of the mean dose-rate between 10^{-2} Gy/s (Conventional mode) and 10^{3} Gy/s (FLASH mode).

The experimental set-up is shown in Fig. 5.7. The Razor Nano Chamber was inserted in an RW3 (water equivalent) phantom at 1.5 cm depth. Measurements were taken at three different SSDs, i.e. 0.3 m, 0.5 m and 2 m, in order to cover a dose range from about 10 mGy/pulse to 10 Gy/pulse. The DPP was varied by tuning the grid tension between

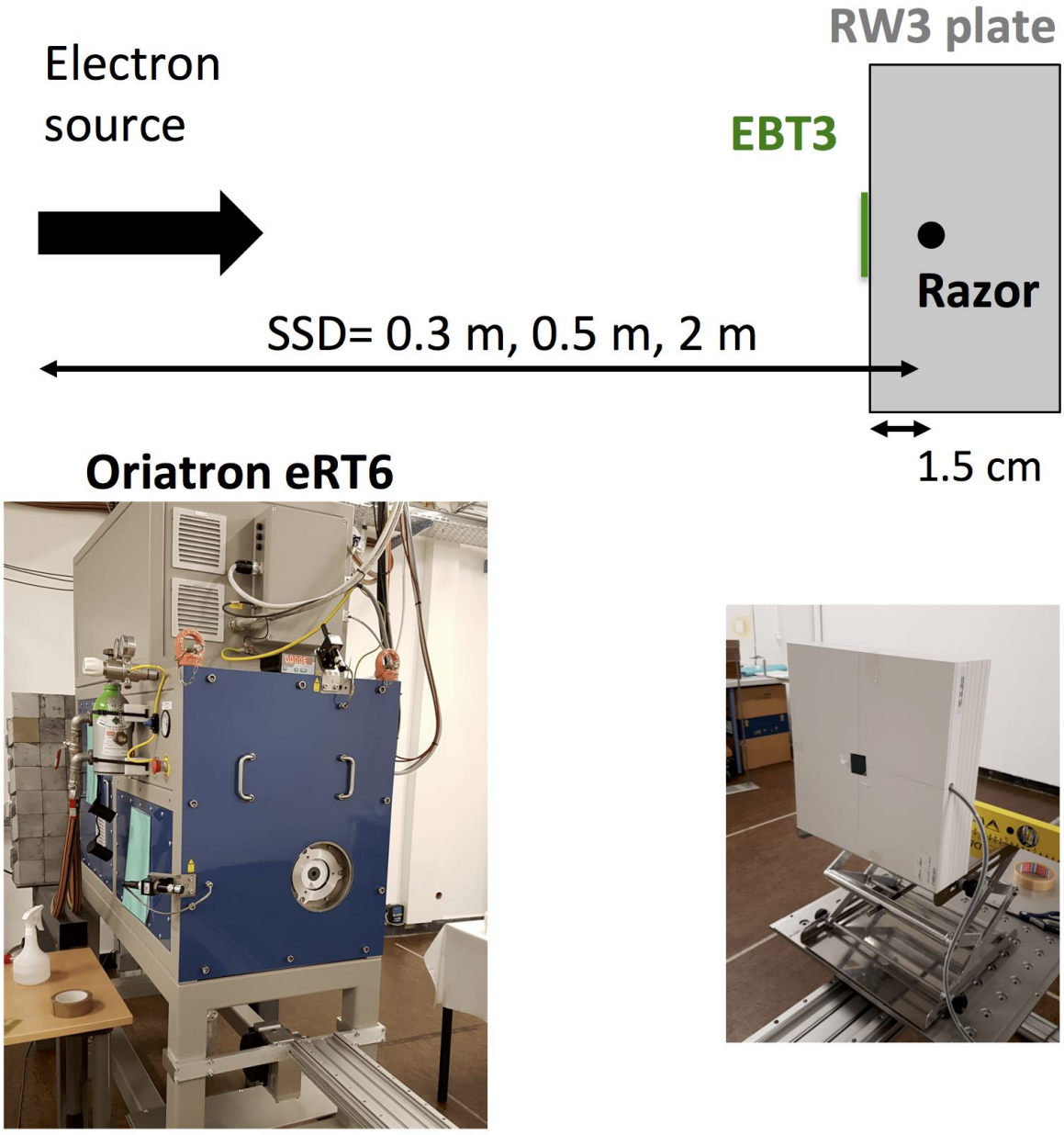

Figure 5.7: Top: schematic draft of the experimental set-up. Bottom: picture of the Oriatron Linac and of the RW3 phantom containing the Razor Nano Chamber chamber. The picture also shows the EBT3 radiochromic film placed on the surface.

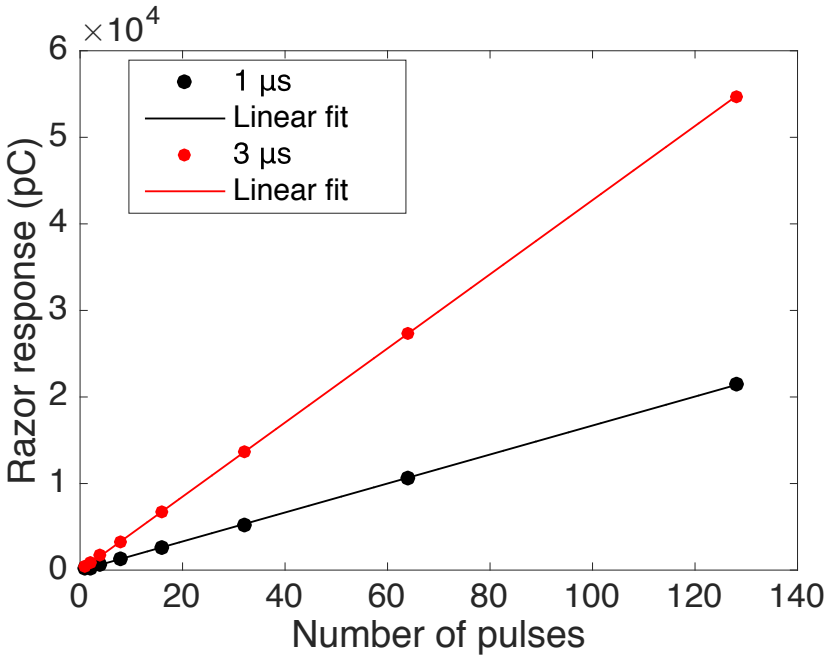

Figure 5.8: Razor Nano Chamber response as a function of the number of delivered pulses. The curves have been obtained with a grid voltage of 200 V, SSD of 0.5 m and a frequency of 10 Hz. The linearity of the collected charge with the number of pulses confirms that the interval between pulses is larger than the time required for the produced charge to be collected and, therefore, that the pulses can be treated separately.

100 V and 300 V. Two series of measurements with increasing grid tensions were performed at each SSD using pulse durations of 1 µs and 3 µs. At each measurement point, i.e. one combination of grid tension and pulse duration, two or three chamber measurements at the nominal chamber voltage of 300 V were taken. The dose was measured with a radiochromic film (EBT3) that was placed at the surface of the RW3 phantom (see Fig. 5.7) during one of the two measurements (see next section). The number of delivered pulses were varied from 1 at the shortest SSD to 100 at the largest SSD to keep the total dose within the dynamic range of the EBT3 films (100 mGy-15 Gy). The pulse frequency was fixed at 10 Hz. At such frequency the pulses can be considered independent (see section 5.3), as confirmed by the linear dependence of the chamber response with the number of pulses (Fig. 5.8), and the chamber can be characterised in terms of the DPP.

5.4.2 Dose computation through radiochromic film analysis

The dose was evaluated with an EBT3 film placed at the RW3 plate's surface for each irradiation condition (SSD, pulse duration and grid tension). The EBT3 film batch was

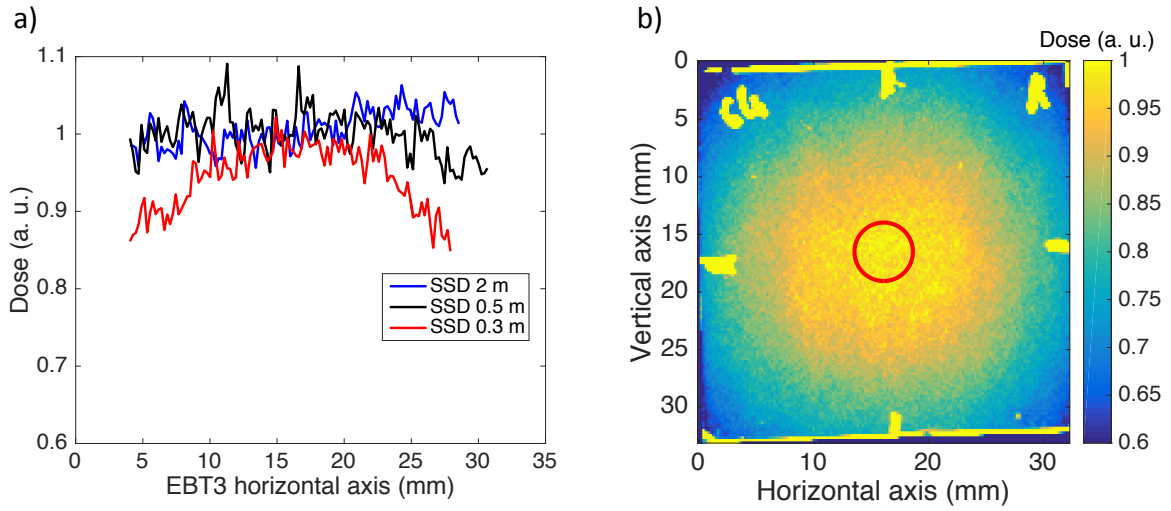

Figure 5.9: Dose profiles on the EBT3 films placed on the RW3 surface. a) Horizontal profiles at the three SSDs chosen for the measurements. b) 2D dose profile for the shortest SSD of 0.3 m. The red circle indicates the 5 mm ROI used for the dose measurement.

calibrated at the Oriatron[9] with the reference Advanced Markus ionisation chamber, calibrated in absorbed-dose-to-water and already corrected for recombination [159]. The films were scanned with a flatbed scanner (EPSON Perfection V750-M Pro scanner) and a resolution of 1200 DPI. The dose was measured within a 5 mm diameter ROI (red circle in Fig. 5.9.b) aligned with the beam axis and the RNC position. The dose was homogenous within the ROI for all the SSDs, as shown in Fig. 5.9. The uncertainty on film dose measurement associated to film uniformity and a $\sim$ 1 mm ROI positioning error[10] was estimated around 2%. The dose at the RNC depth (1.5 cm) was obtained by applying two correction factors accounting for the electron depth-dose profile and for the different beam quality at each SSD and grid voltage.

Geometrical correction The ratio $R_{1.5/surf}$ between the dose at 1.5 cm depth and the dose at the phantom entrance is used to correct for the non-flat depth dose profile (see section 1.3) and obtain the absorbed-dose-to-water at 1.5 cm depth. $R_{1.5/surf}$ was obtained by performing simultaneous measurements with two EBT3 films placed respectively at the RW3 surface and at the RNC position inside the plate. Since the electron spectrum is degradated due to the energy losses along the beam path in air, the $R_{1.5/surf}$ factor

[9]The calibration was performed in a dose range between 0.5 Gy and 15 Gy and the experimental points obtained for the red channel were fit with a five degree polynome. The calibration curve is shown in Fig. 5.2 (section 5.1).

[10]The positioning error was measured by quantifying the dose error within the ROI using pixels of $1 \times 1\,\text{mm}^2$.

depends on the SSD and must be measured for each of the three set-up. Furthermore, the different beam dimension at the three SSDs also affects the depth-dose profile on the beam axis, as it was shown in section 1.3. The double film measurements were therefore performed for each SSD. The films were irradiated with a fixed grid tension of 100 V and the measurements were repeated twice. The results provided the following ratios:

- SSD = 2 m: $R_{1.5/surf} = 1.35$
- SSD = 0.5 m: $R_{1.5/surf} = 1.22$
- SSD = 0.3 m: $R_{1.5/surf} = 1.13$

The error on these correction factors due to ROI positioning error and film uniformity is around 2%[11].

Spectral correction As the Oriatron grid tension increases, the electron energy slightly decreases from 6 MeV at 100 V to 4.9 MeV at 300 V. These values had been previously extrapolated by M. Jaccard et al. (2018)[105] from the depth-dose curve in water obtained at the lowest and highest grid voltages, as shown in Fig. 5.10. The $R_{1.5/surf}$ ratio at 300 V is 13% higher than the value at 100 V. Since the aformentioned $R_{1.5/surf}$ ratios were obtained with a fixed grid tension of 100 V, they must be further corrected to account for the decrease in beam energy with the grid tension. Therefore, an additional linear correction R_E ranging from 1 (100 V) to 1.13 (300 V) was applied to integrate this effect and correct the entrance film dose. This correction introduces an unknown error on the dose evaluation since the decrease in beam energy is likely to be non-linear with the grid tension[12]. The overrall error on the computed dose at 1.5 cm depth has been therefore increased to 5% to take into account the uncertainty associated to the linear extrapolation of R_E.
Therefore, the absorbed-dose-to-water at the RNC depth for each set of SSD and grid voltage was finally obtained as:

$$D_{1.5} = D_{film-surf} \cdot R_{1.5/surf}(SSD) \cdot R_E(V_{grid}) \tag{5.14}$$

5.4.3 Calibration results

Calibration curves The chamber response as a function of the DPP and for the two pulse durations is shown in Fig. 5.11.a. The data points include the measurements at

[11] Considering the dose error within the ROI using pixels of $1 \times 1\,mm^2$.
[12] The behaviour of R_E with the grid tension will be precisely characterized in future measurements in order to reduce dose uncertainty.

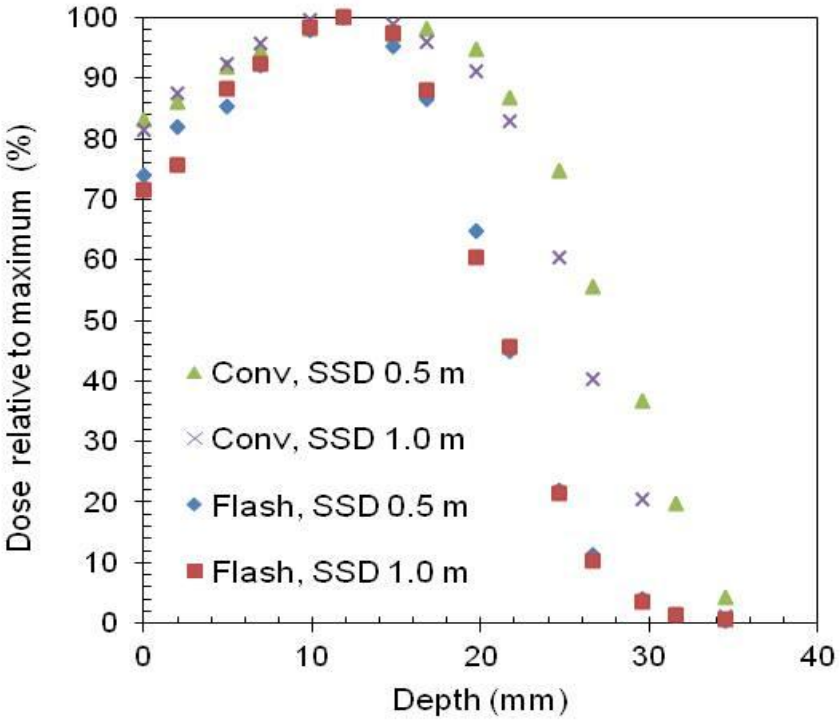

Figure 5.10: Percentage depth-dose profiles in water for two operating modes of the eRT6 Oriatron obtained with EBT3 films. The Conv and Flash modes correspond to a grid tension of 100 V and 300 V, respectively. Taken from M. Jaccard et al. (2017) [105].

the three distances[13] and the dose (x-axis) is obtained, as previously explained, by correcting the dose measured on the film placed at the RW3 surface at each data point (equation 5.14). The results show that the RNC response is linear with the DPP up to ~ 0.1 Gy and then gradually saturates, reflecting the increase of recombination with the DPP. Moreover, the 1 µs curve lies slighlty below the 3 µs curve, indicating that the ion collection efficiency decreases with the dose-rate and that the impact of the pulse duration on the chamber response is therefore not negligible.

At the greater SSD (2 m) and for the longer pulse (3 µs), recombination can be considered negligible, as shown by the initial linear behaviour of the RNC response and as already demonstrated by K. Petersson et al. (2017) [159]. Therefore, the RNC response at SSD = 2 m was fitted with a linear equation to compute Q_{sat}, i. e. the charge collected by the chamber without recombination (blue dashed curve in Fig. 5.11). The fit provided

[13] Only the measures at grid tension of 100 V and 110 V were not considered, since the accelerator variability was often larger in these conditions [105]. Moreover, at an SSD of 0.3 m we observed an abrupt saturation of the electrometer signal for the 3 µs pulse durations, which will be further investigated in upcoming experimental campaigns. Therefore, the data at the SSD of 0.3 m are for the 1 µs pulses only.

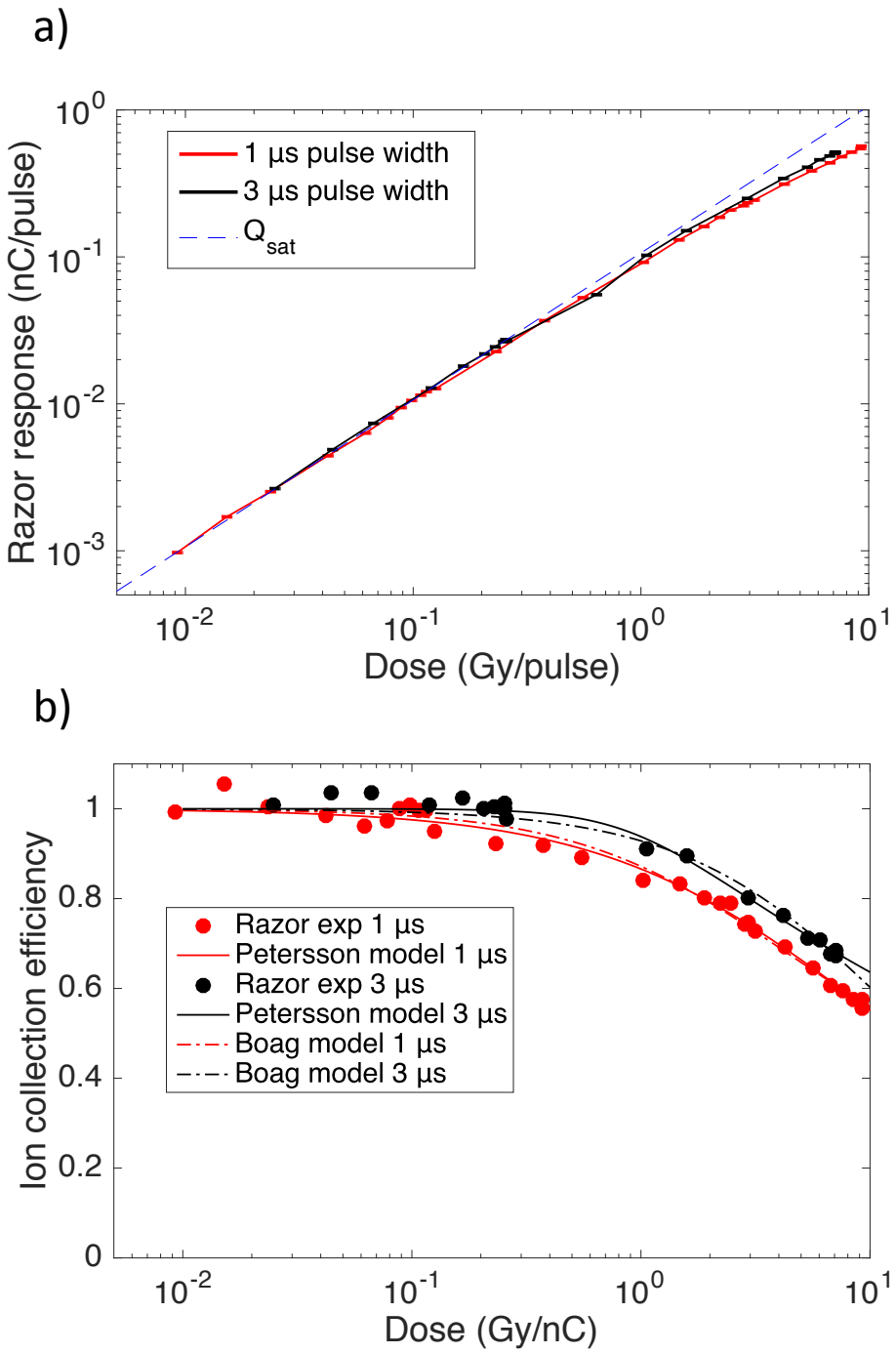

Figure 5.11: Razor Nano Chamber (RNC) calibration results. a) RNC response (collected charge) as a function of the dose-per-pulse for the two pulse durations. The horizontal length of the marker indicates the 5% error on the dose evaluation. b) Ion collection efficiency for the two pulse durations, fitted with the Petersson model (eq. 5.16) and the Boag model (eq. 5.13).

the following equation for Q_{sat}:

$$Q_{sat} = (0.106 \pm 0.001) \cdot D = \frac{1}{N} \cdot D \tag{5.15}$$

where $N = 9.43 \pm 0.09$ Gy/nC is the measured calibration coefficent for the Oriatron electron radiation quality[14]. The calibration coefficient is close to the value provided by the IBA technical calibration performed with Co^{60} photon radiation, i.e. $N_{Co^{60}} = 9.25 \pm 0.18$ Gy/nC. The good agreement between the two values further validates the quality of dose evaluation.

Ion collection efficiency The ion collection efficiency was computed separately for the two pulse durations as $f(DPP) = Q/Q_{sat}$. The results are shown in Fig. 5.11.b (circles). The 1% error on the Q_{sat} linear slope (equation 5.15) and the 5% uncertainty on the dose estimation generate an error on f of about 2% (the uncertainty on both f and the dose, i.e. the vertical and horizontal error-bars are not visible in the figure). The data points were fitted with a model proposed by K. Petersson et al. (2017) for the Advanced Markus chamber, whose equation is[15]:

$$f = \left(1 + \left(\frac{DPP}{\gamma}\right)^{\alpha}\right)^{\beta} \tag{5.16}$$

where α, β and γ are three fitting parameters with no explicit physical meaning. The three Boag models (equations 5.11, 5.12 and 5.13) were also used to fit the ion collection efficiency curves. As previously mentioned, the collection efficiency was expressed as a function of the DPP by writing the parameter u in the three models as:

$$u = \varepsilon \cdot \frac{DPP[mGy]}{V} \tag{5.17}$$

The lowest R^2-values were obtained when fitting the experimental measurements with the third model (equation 5.13), which matches more closely the theoretical distribution of negative ions in the electrode gap. The fitting curves are shown in Fig 5.11.b (dot-dashed line) and the fitting parameters are reported in Table 5.1. The precision of the Petersson fits is slightly higher, as it was found by the author, compared to the Boag fit. Regarding the Boag model, the 1 µs fit provides a meaningful value of the free electron fraction p of 0.37, in line with typical values obtained in literature. On the contrary, the p value for 3 µs

[14] Assuming that the other correction factors in formula (5.3.) are equal to 1

[15] In their model the best fit was obtained for γ equal to the polarizing voltage, whereas here γ is left as fitting parameter.

Table 5.1: Parameters of the ion recombination models used to fit the data. The Boag model refers to equation (5.13) (model 3).

		1 µs pulse duration	3 µs pulse duration
Petersson function	α	0.808	2.17
	β	0.566	0.089
	γ	4636	981
	R^2-value	0.9852	0.9884
Boag model	p	0.3716	0.0193
	ε	0.2022	0.0488
	R^2-value	0.9831	0.9805

is remarkably different and does not reflect realistics values of the free electron fraction. This may be explained by observing that the Boag's assumption of instantaneous pulse might not be valid for the extremely small RNC volume and such pulse durations (see next section).

Discussion According to the Boag model, ion recombination decreases with the chamber electrode gap, which is simply explained by considering the shortest time the ions spend to reach the electrodes. Consequently, the extremely small electrode spacing (0.5 mm) of the Razor Nano Chamber is expected to ensure a higher ion collection efficiency compared to typical chambers used in clinics. For considerations regarding possible applications of smaller chambers in high dose-rate, pulsed beam dosimetry it is therefore relevant to compare the RNC with the larger Advanced Markus chamber, characterized by K. Petersson et. al (2017) [159] with the same beam conditions. The Advanced Markus has circular plate electrodes of 5 mm diameter and 1 mm gap [89]. Its electrode spacing is therefore twice the RNC spacing. As shown in Fig. 5.12, the Advanced Markus has a lower ion collection efficiency, which decreases more rapidly with the DPP and reaches values around 0.25 at 10 Gy/pulse, whereas the RNC ion collection efficiency remains above 0.5 at 10 Gy/pulse. Ion recombination in the RNC is therefore reduced and the behaviour suggests that it could be successfully used at higher DPP compared to the Advanced Markus chamber, although further measurements would be needed to characterize the chamber response above 10 Gy/pulse.
On the other hand, the RNC is more sensitive to a change of dose-rate within the pulse. In fact, the two curves are well separated and, as it would be expected, the ion collection efficiency decreases as the pulse duration is reduced. On the contrary, the Advanced Markus chamber curves for different pulse durations are only slightly separated, which indicates that ion recombination is less sensitive to the dose-rate within the pulse.

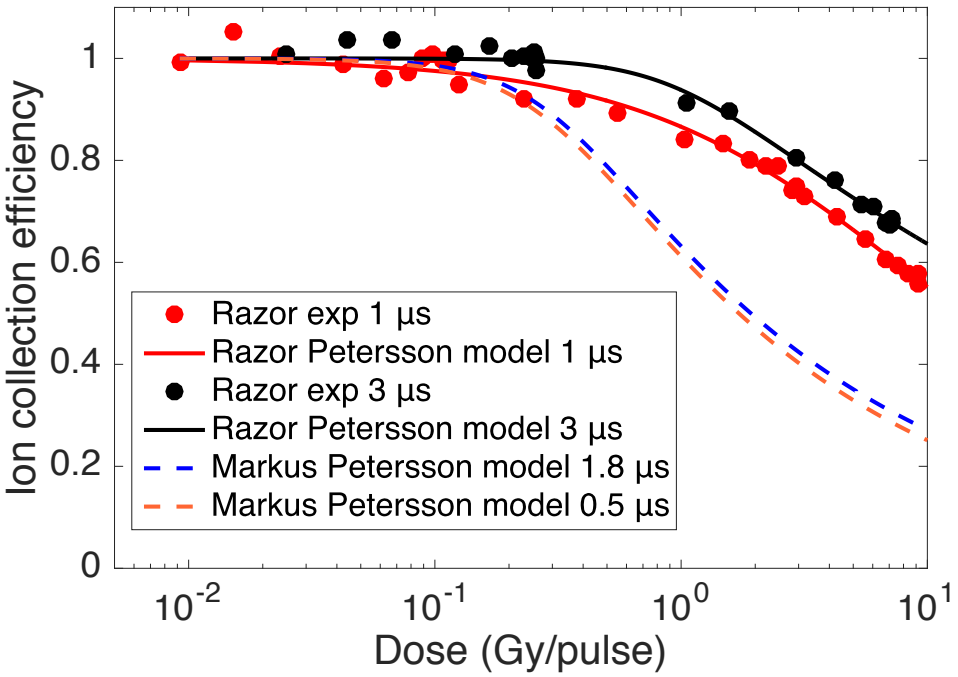

Figure 5.12: Comparison of the ion collection efficiency of the Razor Nano Chamber with the Advanced Markus chamber. The ion collection efficiency of the Advanced Markus is obtained using the coefficients of the Petersson function available in K. Petersson et al. (2017) [159].

This behaviour may be explained by considering the Boag's assumptions. The theory describes recombination as a function of the DPP assuming that the pulse duration is much shorter than the ion collection time. When this condition is met, the pulse can be considered instantaneous regardless of its duration, and recombination depends exclusively on the total amount of secondary charge created by the pulse (i.e. the DPP). As a consequence, the smaller the chamber volume the shorter is the pulse duration at which the Boag's condition of instantaneous pulses is met. In other words, smaller chambers becomes insensitive to the dose-rate with shorter pulses. It is therefore worth estimating the collection time of the two chambers and comparing it to the pulse durations used for the characterization. The ion mobility coefficients have been recently measured for air-filled ionisation chambers by G. Boissonnat (2015) [28]. In the range of electric field strengths relevant for ionisation chambers, the mobility of negative and positive ions is similar and can be taken as $1.9 \times 10^4\,\mathrm{m^2V^{-1}s^{-1}}$ for a rough calculation. Considering the RNC and Advanced Markus electrode gaps of respectively 0.5 mm and 1 mm, the corresponding drift velocity for a chamber voltage of 300 V[16] are respectively 120 m/s and 60 m/s. As a

[16]An error on the estimation of the Razor Nano Chamber collection time is made by assuming a constant electric field. For a more precise estimation the variable electric field in the spherical geometry

result, the Markus collection time is around 20 µs whereas the RNC collection time is four times lower (around 5 µs). As expected, a microsecond pulse can be therefore considered almost instantaneous compared to the markus collection time[17] whereas it is comparable to the RNC collection time. This can explain the higher sensitivity of this chamber to pulse durations in the order of microseconds.
Therefore, if on the one hand the small RNC volume reduces the ion recombination, on the other hand the chamber response is more sensitive to the dose-rate within the pulse over a larger range of pulse duration values. Characterization of the recombination process covering a pulse duration range from picoseconds to microseconds is indeed one of the issues to be adressed before transferring IC dosimetry to laser-plasma accelerated beams. Precisely, the question to be asked is: what is the pulse duration ensuring that the obtained calibration curve is valid for much shorter pulses?

5.5 Razor Nano Chamber response to laser-plasma accelerated femtosecond electron bunches

In order to perform precise dosimetry of LPA beams with ionisation chambers, it is crucial to investigate whether ion recombination correction for µs pulsed beams is affected by a further reduction of the pulse duration to typical LPA bunch time scales (ns-fs). This verification is particularly important for small ionisation chambers, whose ion collection time is around few microseconds. If an ionisation chamber was found to be dose-rate insensitive in such wide range of pulse durations (from µs to fs), the chamber calibration obtained with ∼µs pulses could be directly used for LPA beams. This finding would be particularly relevant for IC application to laser-plasma accelerated electrons, since the ionisation chamber could be calibrated on a modified Linac such as the Oriatron able to deliver high DPP (> 1 Gy) in µs pulses.
This section presents a preliminary investigation of the RNC response conducted with ~ 120 MeV, fs LPAE at the Salle Jaune (LOA).

5.5.1 Experimental set-up and method

A schematic of the irradiation set-up is shown in Fig. 5.13. A 60 TW, 30 fs laser was

should be used.

[17] This result is in line with the finding of M. Gotz et al. (2017) [85]. They found that the Advanced Markus chamber becomes independent on the dose-rate below pulse durations of few microsecond depending on the DPP and the chamber voltage.

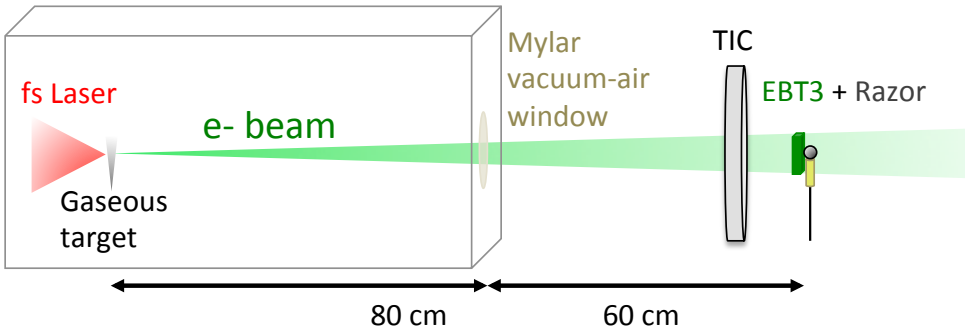

Figure 5.13: Schematic of the set-up used for the Razor Nano Chamber measurements in Salle Jaune (LOA) with fs laser-plasma accelerated electrons.

focused with a f/16 parabola onto an He gas jet (∼1.5 J on the target) containing 1% of N_2, The electron beam, generated through ionisation-injection acceleration mechanisms, was extracted through a 70 µm thick mylar vacuum window and used to irradiate the experimental set-up in air. The RNC was placed 60 cm after the vacuum window to let the beam diffuse and obtain a transverse section larger than few millimiters at the chamber plane. An EBT3 radiochromic film was placed in front of the RNC to measure the dose delivered at each irradiation and a Transmission Ionisation Chamber (TIC) was employed as on-line monitor.

The electron beam featured a continuous spectrum below 200 MeV, peaked at around 120 MeV (Fig. 5.14), and a divergence of $\sigma = 2.5$ mrad. The shot-to-shot instability of the energy corresponding to the spectral peak was 9%. The beam charge was estimated to 15 pC based on EBT3 measurements and Geant4 Monte Carlo simulations. The duration of the beam envelope at the RNC position after the spatial stretch due to the different velocity of the spectral components is estimated to be around several tens of femtoseconds[18].

To integrate a sufficient amount of dose on the EBT3, 50 separate bunches with a repetition rate of 0.2 Hz were delivered at each irradiation. This introduces an uncertainty on the DPP associated to the shot-to-shot instability. The films were marked to indicate the relative position of the RNC during the scan, performed with the flatbed scanner used for the Oriatron experiment (see previous section). An X-ray calibration (performed at the SARRP irradiator of the Experimental Radiotherapy Platform of Curie Institute in

[18]If we consider the spectral bandwidth from 100 to 150 MeV, the propagation along 140 cm causes a beam stretch in time of 38 fs, to which we should add an initial pulse duration at the source of few tens of fs.

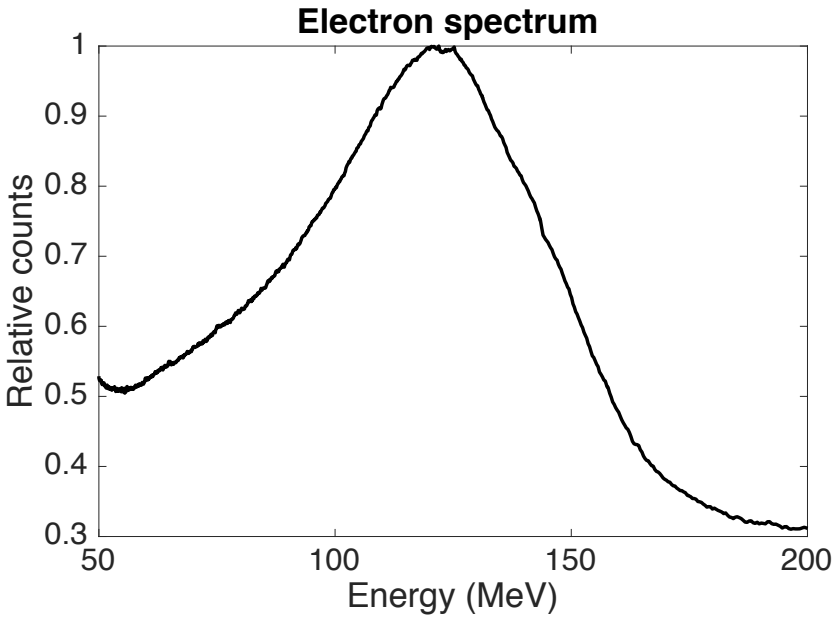

Figure 5.14: Spectrum of the laser-plasma accelerated electron beam obtained with an electron spectrometer composed of a permanent magnet dipole and a Lanex screen. The cut-off energy of the spectrometer was 50 MeV.

Orsay), with an effective X-ray beam energy of 69 keV was used[19] to obtain the dose. After few measurements dedicated to the alignement of the RNC sensitive volume to the electron beam axis, five consecutive irradiations were performed.

5.5.2 Results and discussion

Examples of the dose profiles on the EBT3 films for three irradiations are shown in Fig. 5.15. The black circle indicates the 2 mm diameter ROI where the absorbed dose was measured. As it is shown, although 50 shots were integrated, the beam was rather instable and both the transverse shape and the position of the centre of the beam varied from one series to another. The charge collected by the RNC and the dose measured with the film over the five series are reported in Fig. 5.16. A dose of roughly 0.8 Gy was measured with the films and the RNC collected charge follows closely the film response over the five series. The variability of the chamber and film responses were respectively 7.7% and 8.5% (standard deviation) over the five series.
Both the film dose and the total charge collected by the RNC were divided by the number

[19]The difference between the Oriatron e- calibration and the X-ray calibration, verified on another film batch, was in the order of 1% for an absorbed dose of 0.8 Gy (the dose absorbed by the EBT3 film in the LOA experiment). Therefore, the error associated to the X-ray calibration can be considered negligible compared to other errors due to beam instability.

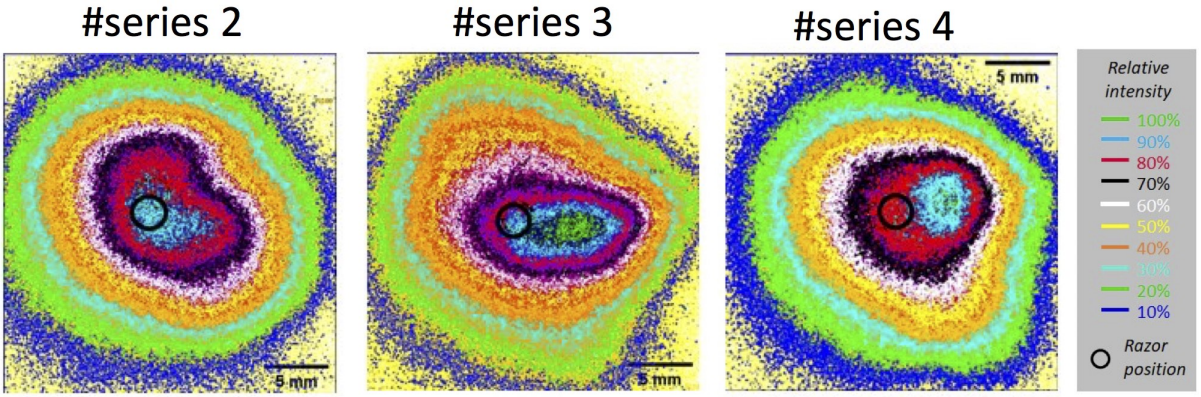

Figure 5.15: Examples of transverse dose distribution on the EBT3 film after 50 shots for three consecutive series. The 2 mm diameter black ROI indicates the Razor Nano Chamber position.

of shots to obtain the chamber response as a function of the DPP and compare it with the Oriatron measurements. The results of the five measurements (Fig. 5.16) were averaged to reduce the observed variability between series, resulting in a response of 2.46 pC/pulse for an absorbed dose of 16.3 mGy/pulse. This data point is compared with the response obtained at the Oriatron with 5 MeV, µs electron pulses in Fig. 5.17. The large error bars are associated to the shot-to-shot instability. An uncertainty of 15% on the dose-per-pulse was estimated based on the observed pointing instability of the order of the beam divergence. This value was increased to 20% to take into account the uncertanity on ROI positioning.

Results show that the RNC overresponds by 15% with the 120 MeV laser-plasma accelerated electron beam compared to the Oriatron calibration. This results can not be interpreted as an effect of the recombination process, since the shorter pulse should reduce the charge collected by the chamber for the same film dose[20]. This is most likely due to the uncertainty associated to beam instability and to the different beam energy. The different collisional stopping power S of electrons in air and water for the two beam energies may have a non-negligible impact on the chamber response. The chamber, filled with air, is indeed calibrated in dose-to-water against the dose absorbed by EBT3 film, whose sensitive layer has an effective Z close to that of water. The ratio between the collisional stopping power in air and water S_{air}/S_{water} increases of 8% from 5 MeV to 125 MeV[21]. Therefore, the film dose being equal, the chamber air-filled volume absorbs approximately a 8% higher dose when irradiated with 120 MeV electrons. This may in part explains, together with the mentioned uncertainties, the overresponse of the RNC

[20] We assume that the film response is not sensitive to a change of dose-rate (see section 5.1).
[21] Data taken from the NIST tables: https://physics.nist.gov/PhysRefData/Star/Text/ESTAR.html.

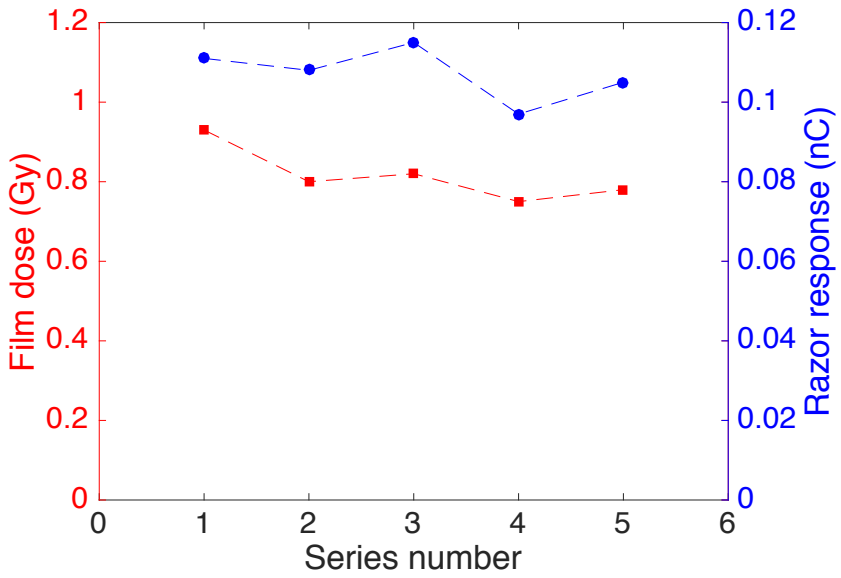

Figure 5.16: Dose absorbed by the film in the 2 mm ROI (left axis, red square dots) and charge collected by the Razor Nano Chamber (right axis, blue circular dots), integrated over 50 shots, for the five consecutive series.

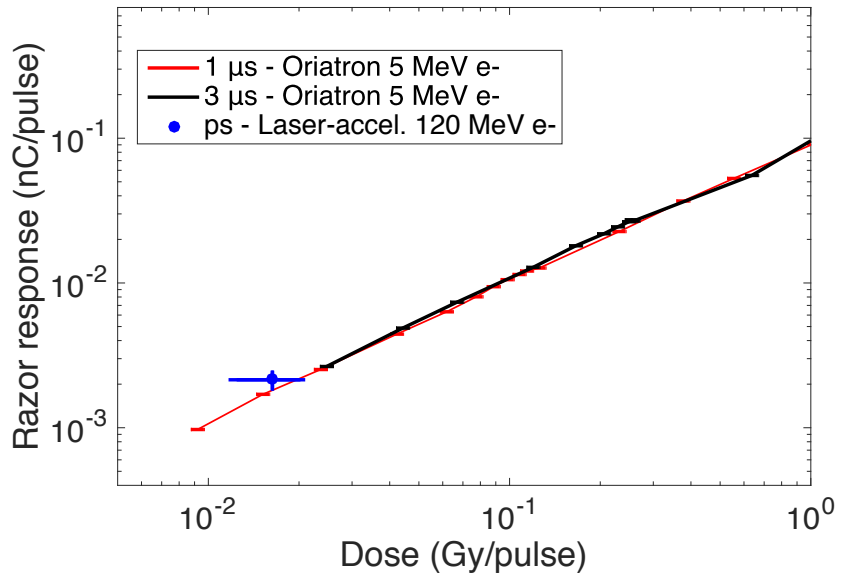

Figure 5.17: Razor Nano Chamber response with 120 MeV, fs laser-plasma accelerated electron bunches (blue point) compared to the response obtained at the Oriatron with 5 MeV, µs electron bunches.

for the same absorbed-dose-to-water measured with the film for the two beam qualities. Altough the uncertainty of the measurements is notable and the difference in stopping power associated to the different electron beam energy at the LOA and at the Oriatron is not negligible[22], the results are encouraging and suggest that, at least for low values of DPP, the chamber response remains insensitive to the dose-rate within the pulse even for a decrease of the pulse duration of several order of magnitudes (from 1 µs to tens of fs). Further measurements would be required to characterize the behaviour of the RNC with laser-plasma accelerated electrons over a wider range of DPP.

5.6 Conclusions

This chapter discussed the main issue related to the use of Ionisation Chambers (ICs) for high dose-rate dosimetry: ion recombination. After presenting the theoretical aspects, recombination was characterised in an IBA Razor Nano Chamber (RNC) with 6 MeV electron bunches at the eRT6 Oriatron LINAC, as a function of the dose-per-pulse ($0.01\,\mathrm{Gy} < \mathrm{DPP} < 10\,\mathrm{Gy}$) and for two pulse durations (1 µs and 3 µs). The results show that the extremely small active volume of the RNC ensures a high collection efficiency compared to larger ICs and suggest that this chamber can be efficiently used to measure high DPP, such as those typically applied in FLASH-RT. On the other hand, the small active volume seems to entail a higher sensitivity to the pulse duration. Further experiments are planned to measure recombination up to $\sim$30 Gy/pulse and for shorter pulses (fraction of µs).
Preliminary results on the chamber response to fs Laser-Plasma Accelerated Electrons (LPAE) suggest that the chamber response obtained with the Oriatron electron beam is not significantly affected by a reduction of the pulse duration to typical LPAE time-scales (tens of fs) for low DPP (tens of mGy).

[22]The collisional stopping power varies by 20%.

Chapter 6

Radiation biology with a kHz laser-plasma accelerated electron beam

Contents

Overview

Very low energy-per-pulse lasers running at 1 kHz repetition rate have been developed in recent years [96, 41, 178]. At present, such lasers feature an energy per pulse below ∼10 mJ, limited by thermal effects on crystal, and use advanced pulse compression techniques to achieve very short pulses (down to almost a single optical cycle, i.e few femtoseconds) and reach the relativistic intensity needed to accelerate electrons. Such

systems can be used to accelerate electrons to energies of few MeV with a charge per bunch of few pC. The key asset of these Laser-Plasma Accelerated Electrons (LPAE) lies in the much higher repetition rate in comparison with the LPAE employed for the radiation biology studies already reported in literature, which are produced by J-class lasers running at 10 Hz. In fact, besides the possibility of active feedback control and beam optimization, the high repetition rate boosts the mean beam current and allows averaging of the shot-to-shot fluctuations by rapid integration of a large number of shots. From a dosimetric point of view, this translates into higher mean dose-rates (Gy/s), compared to those obtained with J-class lasers (Gy/min), and into a higher stability of the delivered dose between irradiations. As already discussed, the main limiting factor of LPAE beam is the shot-to-shot pointing instability in the order of the beam divergence, which hinders the reach of a high stability of the delivered dose between irradiations (see the experiment performed with a J-class laser system described in section 5.5). High repetition rate LPAE may therefore represent a perfect candidate to approach the stability standards required in clinics. To our knowledge, no radiobiology study in these conditions is reported in literature at the time of writing.

The kHz *Salle Noire* laser system at the LOA is able to generate in a reproducible way few pC electron bunches in an energy range from sub-MeV to few MeV [88]. A two week radiobiology experimental campaign was carried out in collaboration with the Gustave Roussy institute (Villejuif, France) and the Laboratory of Subatomic Physics and Cosmology (LPSC) of Grenoble (France). The goal of the experiment was to perform a first dosimetric characterisation of the source, quantify its stability and validate a dosimetry protocol in order to asses the potentiality of this source and lay the foundation for future systematic radiobiology studies.

The chapter describes the dosimetry arrangement and protocol used in the experiment, the irradiation conditions achieved and the first preliminary results on *in vitro* irradiation of cancer cells.

6.1 Set-up and source parameters

A draft of the experimental set-up is shown in Fig. 6.1. The 3.5 fs laser pulse, carrying 3 mJ, was focused with a parabola (50 mm focal length) onto an N_2 gas-jet, producing a low-energy electron beam with a divergence of 70 mrad. A detailed description of the laser system, the acceleration mechanism and the installed beam diagnostics can be found in the thesis of D. Gustas (2019) [87]. A tube was inserted in the vacuum chamber to place

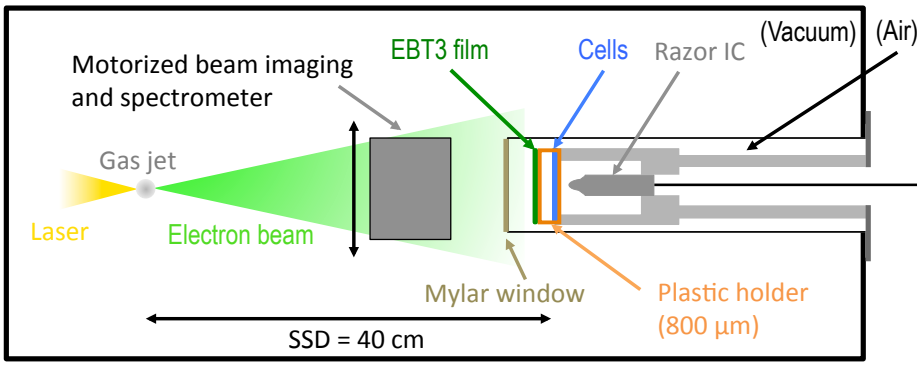

Figure 6.1: Schematic draft (horizontal cut, top view) of the experimental set-up.

the irradiation site (in air) closer to the electron source, compatibly with the installed beam diagnostics. A 100 µm thick vacuum-air Mylar window was placed 38 cm far from the source. At this location, the transverse dimension of the beam was 3 cm (FWHM), which allowed to irradiate a circular spot of 1 cm diameter with a good homogeneity (see section 6.3). The cell sample was positioned vertically in air, 2 cm after the Mylar window, in a 800 µm thick plastic holder aligned to the beam-axis. A customized metallic support allowed to hold in place the cell plastic support (see Fig. 6.2.c) and to place it at the same depth in the tube at each irradiation. The metallic support was also designed to house a Razor Nano Chamber (RNC) (described in section 5.4), which was inserted behind the cell sample (see Fig. 6.2.b) and used as on-line dose monitor during irradiations and as day-to-day dose reference during the optimisation of the interaction conditions between the laser and the gas-jet performed before each experimental run. A radiochromic EBT3 film was placed on the front side (in beam's view) of the plastic holder at each irradiation for dosimetry. A motorised set-up, located in the vacuum chamber between the source and the Mylar window, was used for beam imaging and spectroscopy and was removed during irradiations. It contains a removable dipole (0.058 T) and a phosphor screen coupled with a CCD camera[1]. Imaging of the beam transverse section, performed by removing the dipole magnet from the beam axis, allowed to align the electron beam to the cell sample and to measure the total accelerated charge per bunch. Since the position of the irradiation site inserted in the tube was fixed, the electron beam pointing needed to be carefully aligned by adjusting the incidence angle of the laser on the gas-jet before the beginning of the irradiations.

[1]The details of these beam diagnostics can be found in D. Gustas (2019) [87].

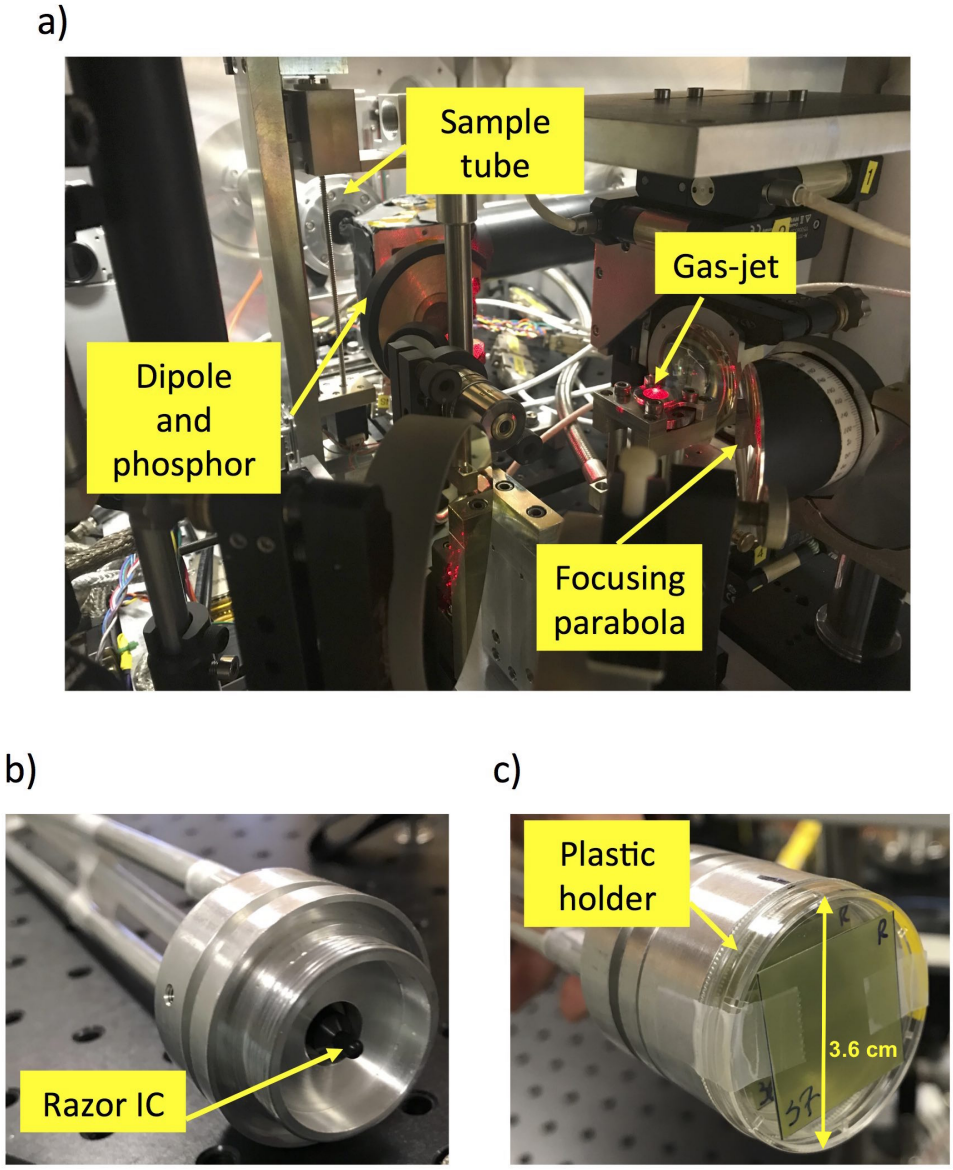

Figure 6.2: a) Set-up inside the vacuum chamber showing the motorised beam diagnostics (dipole and phosphor) positioned in front of the laser-plasma source and the tube inserted in the vacuum chamber to place the irradiation site in air closer to the source. b) Picture of the metallic holder, housing the Razor Nano Chamber, that was inserted in the tube. The plastic holder containing the cells was screwed in front of the Razor. c) Picture of the plastic holder, containing the cells during irradiations, inserted into the metallic holder that was screwed in front of the Razor chamber. The picture shows the two EBT3 film set-up used for the evaluation of the dose absorbed by the cells (see section 6.2.3).

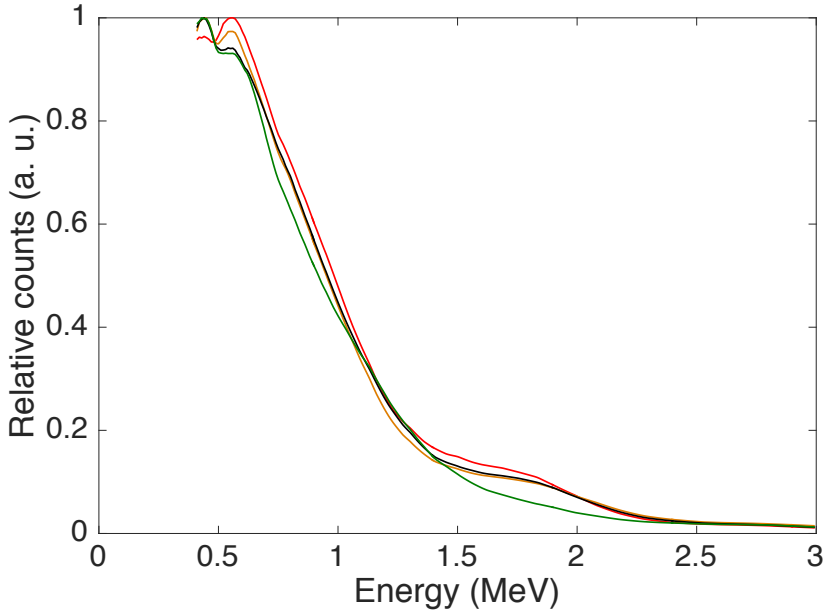

Figure 6.3: Spectrum of the electron beam taken in four different days, obtained by integrating 15 shots. The lower limit of the spectrometer is 400 keV.

Source parameters The *Salle Noire* laser facility can generate low energy electrons in a reproducible way in a range from sub-MeV up to few MeV with charges of ∼10 pC and few pC respectively, according to the interplay between the laser and gas-jet parameters. For the experiment, the source was optimised to obtain the highest charge per bunch[2], which corresponds to the production of a low-energy quasi-thermal spectrum up to ∼2 MeV. Fig. 6.3 shows the optimised electron spectrum taken in four different days. As it is shown, the electron spectrum can be reproduced from one day to another with a good precision. The measured charge for the four spectra (total charge at the source) was 9.8 pC/shot with an instability of ±0.7 pC/shot.

6.2 Methods

6.2.1 Radiation biology assays

We performed the first irradiation of *in-vitro* cancer cells with the *Salle Noire* electron source both to investigate the biological response to kHz laser-plasma accelerated electrons and to validate the dosimetry. To this aim, we irradiated colorectal cancer cells HCT116, both the wild type (HCT116 WT) and its radioresistant counterpart (HCT116

[2]By tuning the gas pressure it is possible to produce either a low-charge, peaked spectrum (lower gas pressure) or a high-charge, quasi-thermal specturm (higher gas pressure).

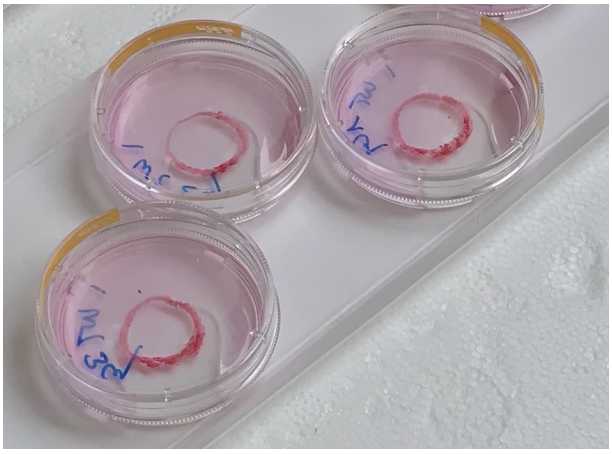

Figure 6.4: Picture of the cell dishes hosting the monolayer samples and filled with culture medium.

$p53^{-/-}$) mutated for the tumour suppressor gene p53. Besides evaluation of the cell surviving curves, we also investigated the effect of different dose fractionation schemes on cell mortality by varying the electron beam temporal structure (see section 6.2.4), similarly to what was done during the SAPHIR project (see section 2.5). The use of both the wild type and the radioresistant counterpart allowed to verify the quality of the dosimetry protocol and of the radiobiology analysis. For both the WT and the $p53^{-/-}$ cell types, we irradiated cell monolayers and 3D spheroid samples of ∼300 µm thickness. Each assay was repetead three times, which leads to a total of 12 irradiation series, performed in different days.

6.2.2 Cell handling

Cell lineage culture The colorectal cancer cells HCT116, wild type (WT) or mutated for the tumour suppressor gene p53 ($p53^{-/-}$), were cultured and grown as monolayers in plastic tissue culture disposable flasks (TPP) in McCoy's 5A (Modified) Medium with GlutaMAXTM (ThermoFisher Scientific), supplemented with 10% fetal calf serum (PAA) and 1% penicillin and streptomycin (ThermoFisher Scientific).
To produce spheroids, HCT116 WT and $p53^{-/-}$ cells were grown in AgrewellTM400 (3.106 per well in 2 ml; 2 wells per cell line) for 2 days.
All cell lineages were grown at 37° C in a humidified atmosphere of 5% CO_2 in air.

Cell survival assay Based on the beam transverse dimension deducted from radiochromic films (see section 6.3), a 1 cm diameter circular region was delimited on the inside face of the culture dishes (Fig. 6.4) with Creamy Color long lasting lip pencil (Kiko)

in which 4×10^4 cells were seeded in 100 µL of medium. The culture dish was positioned vertically behind the exit window, as discussed in section 6.1 After exposure to the laser-plasma accelerated electron beam, 1 ml of medium was added and the cell monolayers were incubated for 4 hours in standard conditions. Cells were harvested with Accutase (Merck), dispatched into 3 different wells of 12-well plate (TPP) in 2.5 mL of medium and grown for five generations corresponding to five days (replication time below 20 h)[3].
After this period, cells were harvested with 250 µL of Accutase inactivated with 250 µL of 1X PBS (ThermoFisher Scientific) supplemented with 10% fetal calf serum. The final volume was adjusted to 1 mL with 1X PBS and 200 µL of each well were dispatched into a non-sterile Ubottom 96-well plate (TPP). In each well, 2 µL of a propidium iodide solution (Sigma, 100 µg/mL in 1X PBS) were added just before counting by flow cytometry technology. Cell acquisition was performed using Guava® and the data analysis carried out with GuavaSoft (Merck Millipore).
Concerning spheroids, after a wash in 1X PBS, they were dissociated in 200 µL of Acctutase (Merck, solution for gentle and effective cell detachment and tissue dissociation of adherent cells) for 30 min at 37° C under agitation (950 rpm). Cells (2×10^4) were then seeded in 12 well plates, grown for 5 days and analysed as cells grown as monolayer.

6.2.3 Dosimetry

EBT3 The dose absorbed by the cells was evaluated with an EBT3 film placed on the sample plastic support (Fig. 6.2.c) at each irradiation. The films were scanned after 24 hours, as recommended by Devic et al. (2016) [56], with an EPSON V800 flatbed scanner with a resolution of 300 DPI. The dose was measured within a circular ROI of 10 mm diameter aligned with the cell sample.
The EBT3 film batch was calibrated at the Elekta Synergy linear accelerator[4] of the University Hospital of Lausanne (CHUV, Switzerland). The LINAC was set to generate an electron beam of 4 MeV at a dose-rate of 6 Gy/min. The EBT3 films were placed at 7 mm depth in a solid water phantom (reference condition for the LINAC dosimetry) and were exposed to doses in the range 0.1-10 Gy. The calibration curve of the red channel is shown in Fig. 6.5, together with the five degree polynomial expression used to fit the experimental points.

[3]Appropriate control samples were treated under the same conditions, including bringing the cell culture dish in a vertical position as for irradiation.
[4]https://www.elekta.com/radiotherapy/treatment-delivery-systems/elekta-synergy/.

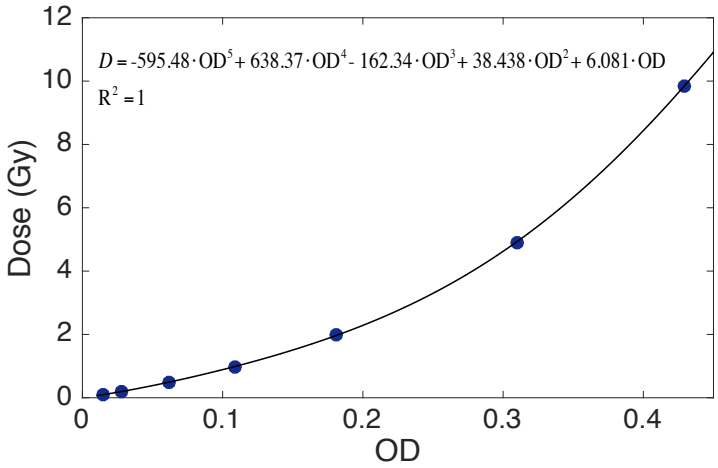

Figure 6.5: Calibration of the EBT3 film batch with the 4 MeV electron beam generated by the Synergy Elekta LINAC available at the University Hospital of Lausanne (CHUV, Switzerland). The experimental values (blue points) are fitted with a five degree polynomial (black curve), whose expression is reported in the image.

Dose at cell Because of the low energy of the electron beam, the attenuation caused by the 800 µm cell plastic holder and the air gap is not negligible. Therefore, the dose measured with the EBT3 film needs to be corrected to obtain the dose delivered in the cells placed inside the plastic holder. The ratio $R_{cells/EBT3}$ between the dose absorbed by the cells and by the EBT3 was measured with a double film arrangement, as shown in Fig. 6.2.c. A film was placed on the plastic holder surface, as during irradiations, and a second film was placed inside the plastic holder at the cell position. The ratio was used to correct the dose measured with the EBT3 film during each irradiation and obtain the dose delivered to the cell sample, according to:

$$D_{cells} = D_{EBT3} \cdot R_{cells/EBT3} \tag{6.1}$$

Since the ratio depends on the spectral shape of the beam, which varied slightly during the day and between days (see Fig. 6.3), the double film measurement was carried out before each irradiation series. The $R_{cells/EBT3}$ values taken before the 12 irradiation series (Fig. 6.6) exhibit good reproducibility (5.8% standard deviation), which reflects the stability of the electron spectrum. This procedure allowed not only to obtain the dose delivered to the cell in the post-processing analysis, but also to verify the beam alignment and the dose-per-pulse delivered in the sample prior to an irradiation series. However,

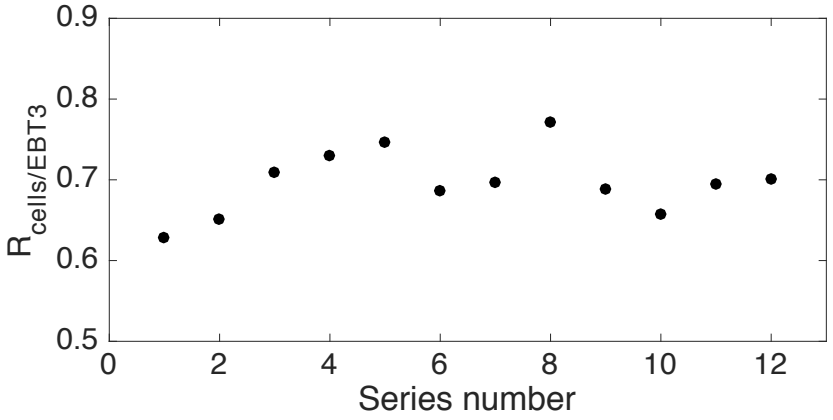

Figure 6.6: Value of the $R_{cells/EBT3}$ ratio for all irradiation series.

the film batch had not yet been calibrated at the moment of the experiment[5]. Therefore, we used the calibration obtained for another EBT3 batch and another scanner (EPSON Perfection V750-M Pro scanner) to estimate the dose-rate before each irradiation. After calibrating the film batch with the scanner employed for the experiment, it turned out that the calibration used during the experiment underestimated the dose of ∼25%, leading to a delivered dose higher than the dose targeted during the experiment.

6.2.4 Temporal modality of dose delivery

In the irradiations performed for the survival assay, the dose was delivered using a single train of pulses, to which we refer in the following as "fraction", having a duration ranging from 1.7 s to 10.2 s in order to target a dose range between 1 Gy and 6 Gy (single fraction mode, Fig. 6.7.a) in six steps.

As mentioned, we also investigated the effect of dose fractionation on cell survival. In the irradiations performed for the fractionation assay, the samples were irradiated with the same total dose, delivered in 5 fractions (fractionated mode, Fig. 6.7.b). A dose of 5 Gy, corresponding to an expected surviving fraction of ∼0.1 was targeted. The delay between fractions was kept constant during the irradiation of each sample, but was varied between samples. The delays used in the experiment were 30 s, 10 s and 5 s, which is the range of values where an oscillatory behaviour of cell survival was observed with laser-plasma accelerated proton bunches (see section 2.5). The pulsed structure was obtained with a programmable shutter, having an opening and closure time of few tens of ms, placed in the laser chain to block the laser pulse.

[5]The COVID pandemic crisis prevented us from calibrating the film batch at the University hospital of Lausanne before the experiment.

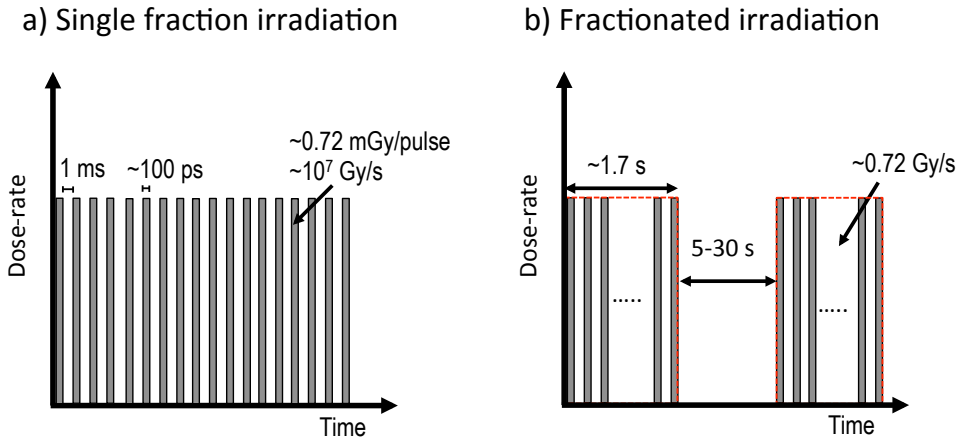

Figure 6.7: a) Temporal structure used for the survival assay. b) Temporal structure used for the fractionation assay. The duration of the fraction was adapted depending on the dose-rate measured before each irradiation series.

The duration of fractions, both in the single fraction and in the fractionated mode, was adapted at each irradiation series according to the dose-rate[6] measured with the double film arrangement. However, since the EBT3 calibration used during the experiment underestimated the dose (or the dose-rate) of ∼25%, the range of dose finally applied for the survival was between ∼1.3 Gy and ∼7.5 Gy whereas the dose delivered in the fractionation assay was ∼ 6.5 Gy.

An irradiation series, dedicated to a given cell line and a given cell structure (monolayer or spheroids), consisted in 6 single fraction irradiations for the cell survival assays and 3 fractionated irradiations for the fractionation assay. Fig. 6.8 shows the values of dose-rate at the cell position measured before the 12 irradiation series. The dose-rate between series was rather stable except for the first two irradiation series. These two series have been performed in the first day of the experimental campaign, in which the interaction conditions (laser intensity and gas pressure) had not yet been optimised to obtain the highest charge at the source. The spectrum corresponding to these two irradiation series is shifted at higher energies in comparison with the spectra used for the rest of the irradiations (see Fig. 6.9), which entails a decrease of the total accelerated charge per bunch of about a factor of two, from 9.8 pC to 5 pC. The average dose-rate is, excluding the first two points, 0.78 Gy/s with a variation of ±8.8% (standard deviation). This corresponds to a fraction duration of 1.28 ± 0.11 s to deliver 1 Gy[7].

[6]With the term dose-rate we refer to the total dose delivered by a continuous train of pulses divided by its duration. Therefore, its value expressed in Gy/s is equivalent to the dose-per-pulse expressed in mGy/pulse, since the repetition rate of the electron bunches is 1 kHz.

[7]Since the dose-rate during the experiment was underestimated of 25%, as explained in section 6.2.3 the duration of a fraction was set to 1.7 ± 0.15 s and the dose delivered in a fraction was, according to

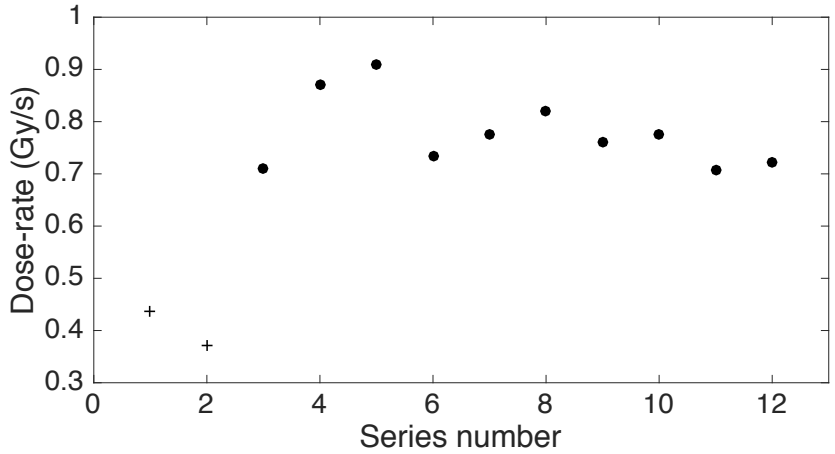

Figure 6.8: Dose-rate measured with the EBT3 placed at the cell position prior to each irradiation series.

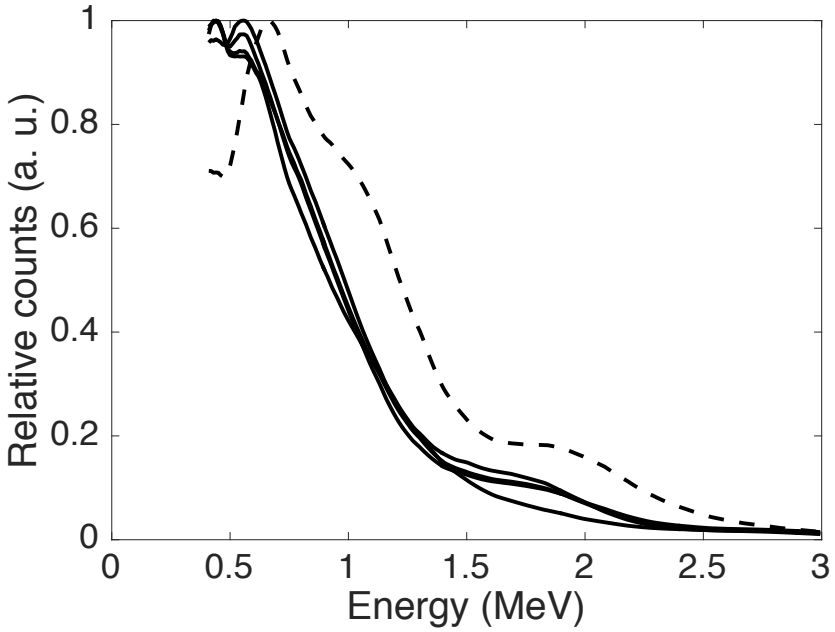

Figure 6.9: Comparison between the spectrum used for the first two irradiation series in the first day (dashed line) and the spectra used for the rest of the experimental campaign taken in four different days (continuous lines).

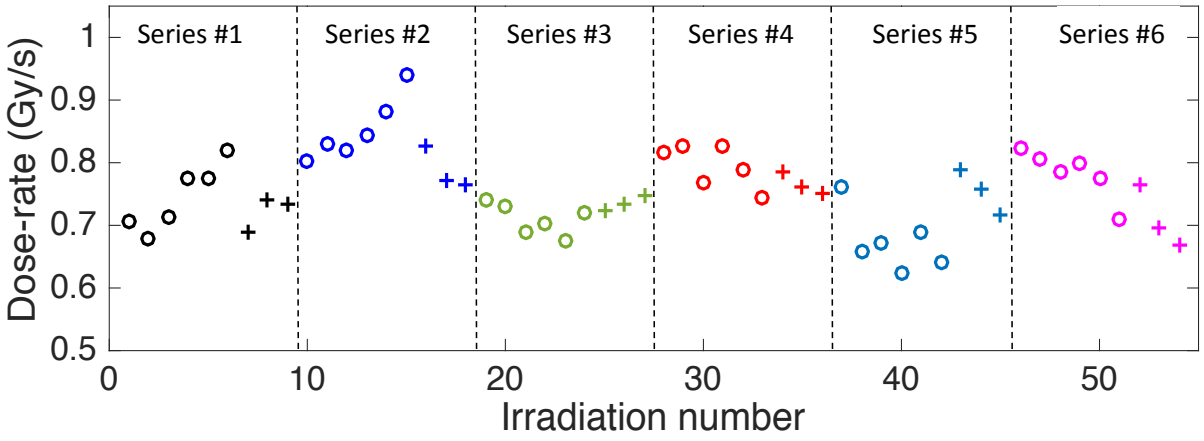

Figure 6.10: Dose-rate (or dose-per-pulse expressed in mGy/pulse) for six different irradiation series performed in four different days. The circular symbols represent the six irradiations performed in single fraction mode for the survival curves. The plus symbols represent the three irradiations carried out in fractionated mode (6.5 Gy delivered in 5 fractions) with varying delay between fractions (30 s, 10 s, 5 s).

6.3 Irradiation conditions

The use of an EBT3 film at each irradiation allowed to precisely evaluate the dose absorbed by each sample and to characterise the stability of both the dose distribution and of the dose-rate between irradiations, as described in this section.

Dose-rate Figure 6.10 shows the dose-rate at the cell position[8] for six representative irradiation series, each of which includes the six irradiations performed in single fraction mode for the survival assay (circular symbol) and the three irradiations performed in fractionated mode for the fractionation assay (cross symbol). As it is shown, in some series, such as in series #3, the dose-rate remained stable and no significant trend was observed. In other series, such as in series #4 to #6, a descending trend was observed. The phenomenon might be due to both a continuous slow drift of the laser pointing[9] and to the temporal structure of the beam, i.e. to the time during which the shutter is kept open or closed. Indeed, in the series where we observe a decrease of the dose-rate between single fraction irradiations performed for the survival assay (circular symbol), such as in series #4 to #6, the exposure time was increased from 1.7 s in the first irradiation to 10.2 s in the last irradiation. On the contrary, in two of the twelve series (series #1 and #2 in the figure), dose escalation was performed in the opposite way, i.e. the first sample was irradiated for

post-processing of the films after calibration, 1.33 ± 0.12 Gy.

[8]The dose absorbed by the film, corrected using the $R_{cells/EBT3}$ and divided by the fraction duration.

[9]During the experiment we observed a slow drift of the laser alignment over few hours.

10.2 s and the last sample for 1.7 s. In these series we observe an increase of the dose-rate between single fraction irradiations. This suggests that the dose-rate, and therefore the charge per bunch, is affected by the period during which the shutter is kept open after it has been kept closed during the time required to replace the biological sample (∼min). In addition, in some of the irradiations performed in fractionated mode (cross symbols) we observe a decrease of the dose-rate as the delay between fractions decreases (30 s, 10 s, 5 s), as shown in series #4 to #6. All together, these results suggest that the shutter placed in the laser chain may have an impact on the laser properties and, as a consequence, on the interaction conditions[10]. Indeed, we noticed during the experiment that the electron beam properties obtained by optimising the interaction conditions between the laser and the gas-jet in a continuous mode (shutter always open) were slightly different compared to the properties obtained if the optimisation was performed in a pulsed mode, i.e. by keeping the shutter closed and opening it for a small amount of time (∼1 s)[11]. These phenomena might be due to thermal effects in the optics placed after the shutter[12], however further tests would be required to elucidate the causes. Nevertheless, the instability of the dose-rate during an irradiation series did not exceed 15% (standard deviation).

If on the one hand the slight dose-rate drift does not affect the accuracy of the dose evaluation, which was measured at each irradiation, on the other hand it prevented the delivery of the target dose with a high accuracy during the experiment. This has a major impact on the precision of the fractionation assay (see next section), in which a precise control of the dose is necessary to compare the cell survival obtained with different delays between fractions for the same total dose.

Overall, considering all of the irraditions (except those performed in the first day with a higher energy spectrum), the average value of the dose-rate is 0.72 Gy/s (corresponding to a DPP of 0.72 mGy/pulse) with a standard deviation of 13%. Considering this reference value of dose-rate, the mean dose-rate during the fractionated irradiations (total delivered dose divided by the exposure time) varied from a minumum of 0.048 Gy/s (2.86 Gy/min) with a 30 s delay between fractions to 0.21 Gy/s (12.32 Gy/min) with a 5 s delay. As anticipated in the introduction of this chapter, the dose-rate obtained with such a kHz LPAE beam is higher than the typical dose-rate reported in literature with J-class lasers

[10]The dose distribution on the EBT3 film placed on the cells does not show significant changes with the temporal structure (see Fig. 6.11), which indicates that the observed trends are more likely a consequence of a change in the spectrum or in the charge per bunch.

[11]This latter was the approach used to optimise the interaction conditions prior to an experimental run, since during irradiation of the biological samples the shutter is kept closed for most of the time (sample replacement).

[12]Four optics and the focusing parabola were placed after the shutter.

running at 10 Hz (∼Gy/min) [78, 10, 118, 150, 21, 147].
A rough estimate of the peak dose-rate, i.e. the DPP divided by the pulse duration, can be obtained by considering the temporal stretch of the beam energy components between 0.5 MeV and 1 MeV at the cell position. The calculation leads to a pulse duration of 100 ps and a peak dose-rate of 0.72×10^7 Gy/s.

Dose distribution As previously mentioned, the electron beam was aligned with the cell sample by adjusting the incidence angle of the laser on the gas-jet during optimisation of the interaction-conditions before the beginning of the irradiation series[13]. The electron beam pointing was monitored with the on-line imaging diagnostic using a reference position corresponding to the center of the cell sample placed behind. Once the beam pointing was optimised to an acceptable level (∼mm precision on the beam imaging diagnostic), the alignment between the electron beam and the cell sample was verified with the double film measurement prior to the beginning of the series.
Figure 6.11 shows the dose distribution measured with the EBT3 film in nine consecutive irradiations (series #4 in Fig. 6.10). The beam pointing and shape were rather stable during irradiations. We succeeded in keeping the maximum error on the dose distribution[14] below 10% in more than half of the irradiations and below 15% in 85% of the irradiations (see Fig. 6.12)[15]. The dose inhomogeneity, evaluated at each irradiation, is reported as horizontal error bar in the survival curves discussed in the next section.
The good homogeneity of the dose distribution ensures a low sensitivity of the dose measurement to a misalignment between the ROI and the cell sample placed behind the film. The uncertainty on dose evaluation associated to a misalignment between the ROI and the cell sample of ~ 1 mm[16] is of the order of 0.5%, except for the irradiations in which the electron beam was not perfectly aligned with the cell sample (first day of the experimental campaign), in which the error due to a misalignment of the ROI reaches 2%.

[13] A misalignment of 10 mrad causes a shift of the beam center of 3.8 mm at the cell position.

[14] The error is defined as the difference between the maximum and minimum dose values within the ROI, reported as a percentage of the maximum dose. In other words, for an error of X%, the cells are within the $100-X$ isodose surface.

[15] The statistical anlysis does not take into consideration the first day of the experimental campaign, in which the alignement procedure had not yet been optimised. The maximum error on the dose distribution, due to a misalignment of ∼5 mm, was around 22% this day.

[16] The uncertainty was evaluated by comparing the dose within different circular ROI (10 mm diameter) whose center was shifted of 1 mm with the dose measured within the reference ROI used for the dose evaluation

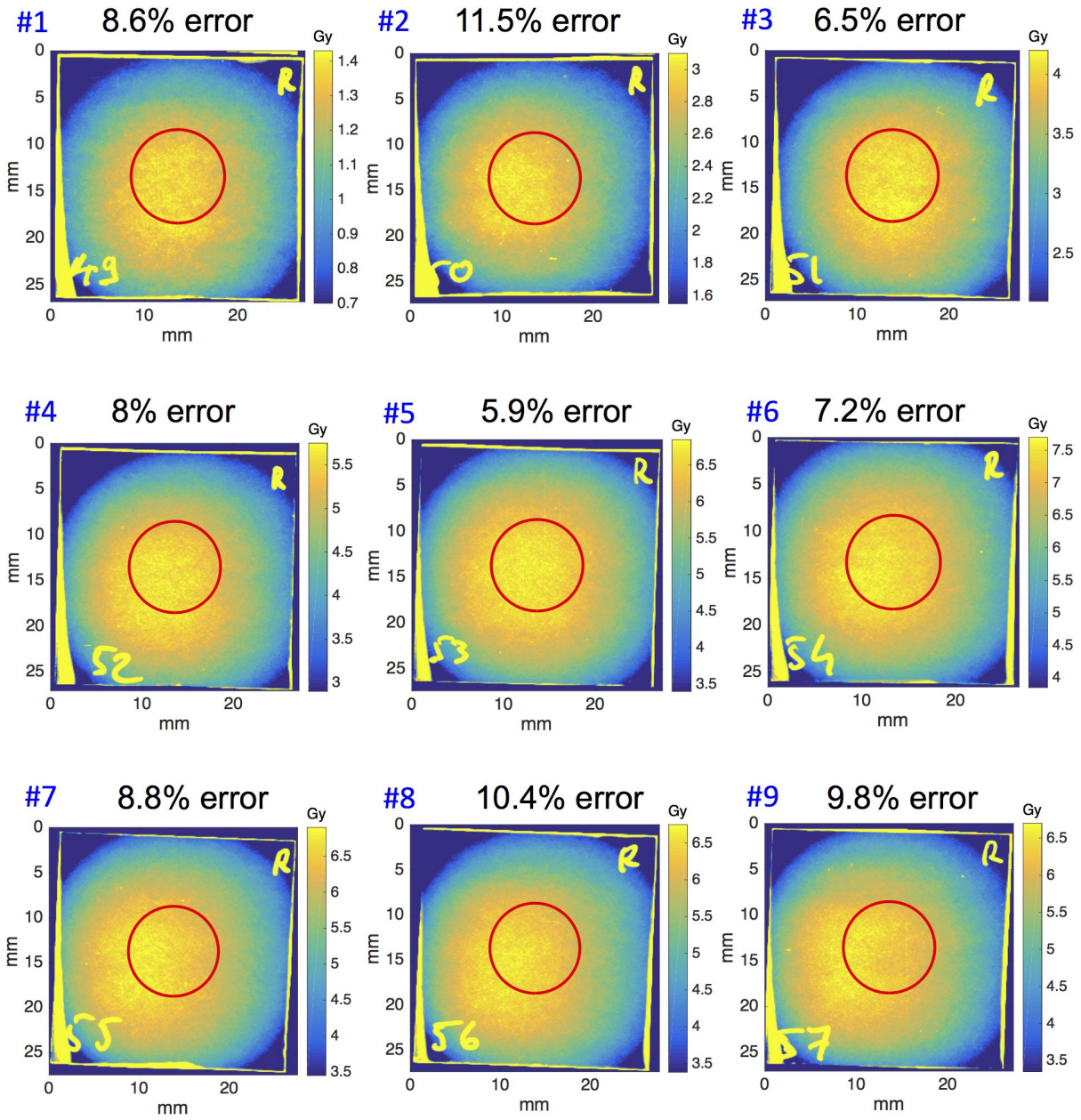

Figure 6.11: Dose distribution measured with the EBT3 film stucked on the cell plastic support for one irradiation series (nine points of series #4 in Fig. 6.10). The colormap interval is set between the maximum value and the 50% percent level in all images. In the first six irradiations (continuous mode), the exposure time was increased from 1.72 s to 10.34 s for the survival assay, whereas in the last three irradiations (fractionated mode), five fractions of a duration of 1.72 s were delivered with a different delay between fractions. The error represent the maximum error on the dose distribution within the ROI (10 mm diameter red cirle).

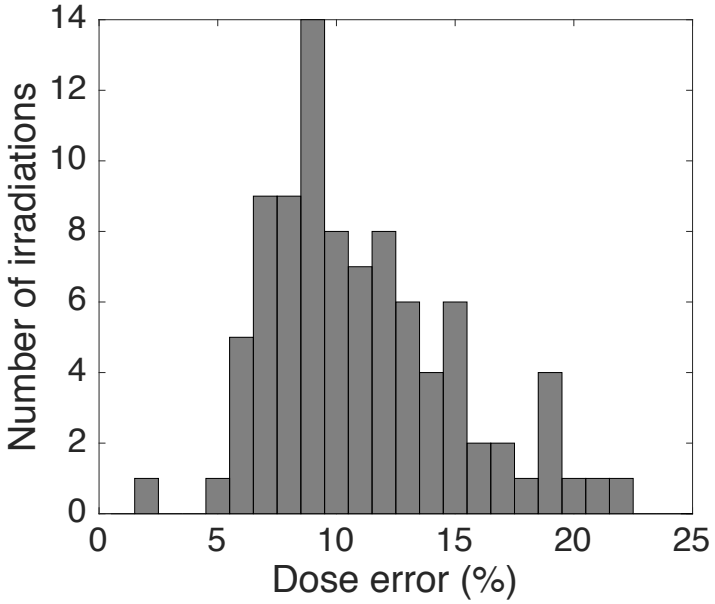

Figure 6.12: Histrogram representing the maximum error on the dose distribution over the analysed surface considering all irradiation series except those performed in the first day, in which the alignment procedure had not yet been optmised.

6.4 Experimental results

6.4.1 Survival assay

Monolayers The survival curves obtained for the HCT116 WT and HCT116 $p53^{-/-}$ cell lines grown as monolayers are reported in Fig.6.13. The surviving fraction decreases with the delivered dose and the curves exhibit the typical shoulder shape of low LET radiations (see section 1.4.3), as shown by the fitting curves obtained with a linear quadratic model. Furthermore, the curve of the WT cell line lies well below the curve of the more radioresistant counterpart $p53^{-/-}$, which confirms the quality of both the dosimetry and the biological analysis. The close match between the linear quadratic fit and the experimental points reflects the stability of the irradiation conditions, i.e. the dose-rate and the energy spectrum. The data points in the graph do not include the irradiations performed in the first day, since we observed that the surviving fraction of the majority of samples irradiated in this day differs from the overall behaviour, as shown in Fig. 6.14. This can be due to the different irradiation conditions, as discussed in section 6.3.
It is relevant to compare the D_{10} values[17] obtained with the LPAE beam with those previ-

[17] D_{10} is the dose corresponding to a 10% surviving fraction and it is often used as an indicator of the radiosensitivity of a cell line to a given radiation quality.

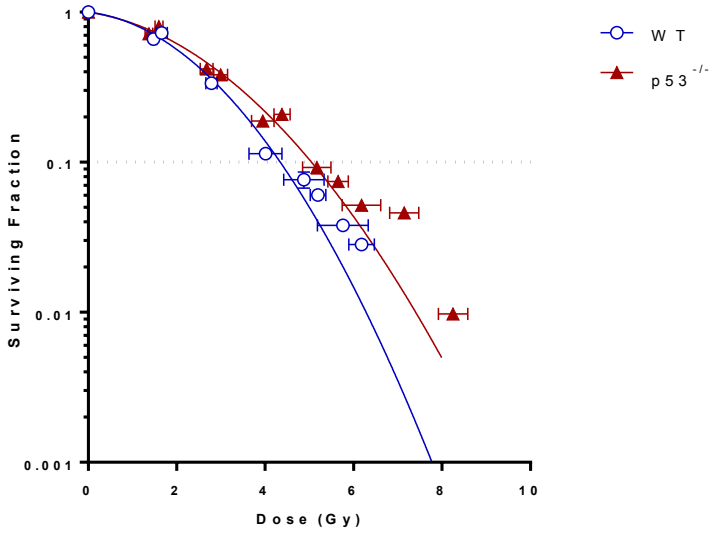

Figure 6.13: Survival curves for the HCT116 cell line, both WT and $p53^{-/-}$, grown as monolayers. The data points are obtained in two independent experiments. In both graphs each point represents the mean of three radiobiological analysis carried out on the same irradiated sample (see section 6.2.2) and the vertical error bar corresponds to the standard deviation of the survival fraction obtained in the three analysis. The horizontal error bars represent the error on the dose distribution within the analysed surface of the sample (circular surface of 1 cm diameter).

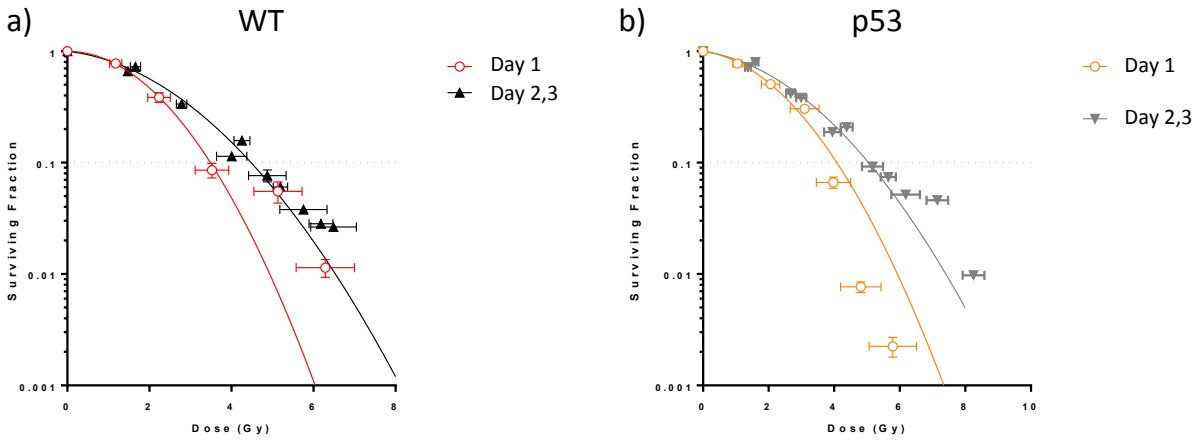

Figure 6.14: Difference between the survival curves obtained in the first day and in the other two days.

Table 6.1: D_{10} values for *in-vitro* HCT116 cell lines, grown as monolayers, obtained with laser-plasma accelerated electrons (from the survival curves of Fig. 6.13) and with 662 keV photons of a ^{137}Cs source at a conventional dose-rate, taken from Pommarel et al. (2017)[163].

Cell line	LPAE	Photons ^{137}Cs 662 keV
HCCT116 WT	4.34 Gy	3.8 ± 0.4 Gy
HCCT116 p53	5.05 Gy	5 ± 0.4 Gy

ously obtained with low-LET[18] 662 keV photons at a conventional dose-rate of 1.4 Gy/min produced by a ^{137}Cs source (integrated in an IBL 637 n°9418 device manufactured by CIS Bio)[163]. The D_{10} values for the two cell types (WT and $p53^{-/-}$) are reported in Table 6.1. The D_{10} obtained with laser-plasma accelerated electrons are close to the values obtained with the ^{137}Cs source, which is in line with the results reported in literature showing no remarkable difference in the RBE of LPAE in comparison with conventional sources of comparable LET.

Spheroids As performed for the cell monolayers, we measured the survival curves of HCT116 cells grown as spheroids in three independent experiments. The interest in irradiating spheroids lies in the oxygen distribution that reproduces more closely the physiological distribution in tumours. Tumours are indeed volumetric and their response to radiation may be different in comparison with monolayer cell samples, since the innermost cells are more hypoxic than external cells and, therefore, less sensitive to radiation. The surviving curves for the HCT116 cell line, WT and $p53^{-/-}$, are shown in Fig. 6.15. Due to incomplete cell dissociation, cell counting analysis lead to unreliable results for some samples that have been removed from the graph. However, the typical shoulder shape seems to emerge and both curves are shifted towards the right in comparison with the monolayer surviving curves (Fig. 6.13), reflecting the lower radiosensitivity of 3D cell structure. Precisely, the D_{10} values are 5.10 and 6.43 for the WT and p53 cell lines, respectively.

6.4.2 Fractionation assay

As explained in section 6.2.1, we also investigated the effect of different delays between fractions (trains of kHz pulses delivering 0.72 ± 0.09 mGy/pulse) on the cell survival. A dose of ~6.5 Gy was applied in 5 fractions, separated by a variable delay of 30 s,

[18]The LET is ~0.2 keV/µm and 0.8 keV/µm for 0.5-1 MeV electrons and the ^{137}Cs γ rays, respectively.

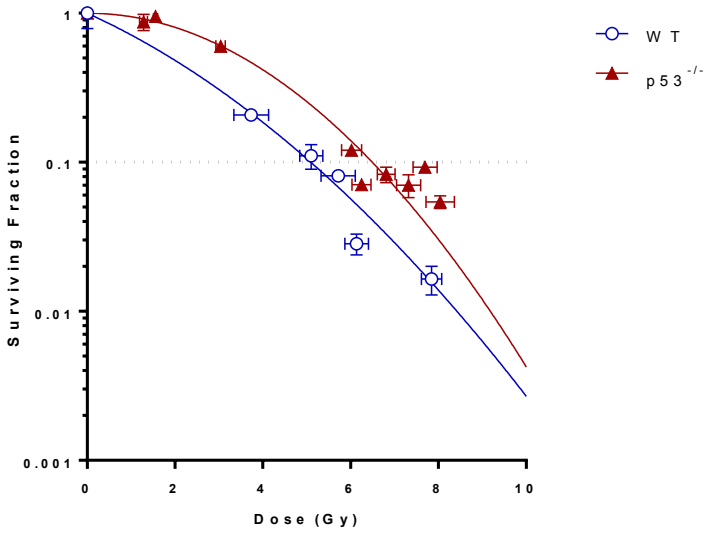

Figure 6.15: Survival curves for the HCT116 cell line, both WT and $p53^{-/-}$, grown as spheroids of 300 µm. Each point represents the mean of three radiobiological analysis carried out on the same irradiated sample (see section 6.2.2) and the vertical error bar corresponds to the standard deviation of the survival fraction obtained in the three analysis. The horizontal error bars represent the error on the dose distribution within the analysed surface of the sample (circular surface of 1 cm diameter).

10 s and 5 s and delivering a dose of 1.3 Gy each. The assays have been carried out for both monolayer and spheroid samples. The results are shown in Fig. 6.16 and include irradiations performed in three different days. The graphs also include the cell survival obtained in continous mode (single fraction), i.e. the cell survival corresponding to an applied dose of 6.5 Gy in the survival curves of Fig. 6.13.

As discussed in section 6.3, the drift of the dose-rate during the irradiation series hindered a fine control of the delivered dose during the fractionation essay. To reduce the error on the surviving fraction due to the difference in the dose applied in different replica (3 irradiations with varying delays performed in one day), the surviving fraction has been normalised to the value obtained in single fraction mode in the same day.

No oscillation is observed for the monolayer cell samples, whereas a similar oscillating trend seems to emerge in both HCT116 WT and p53 cell lines grown as spheroids. The absence of oscillation in cell monolayers might be due to the applied dose of 6.5 Gy. The surviving fraction of monolayers at 6.5 Gy is indeed lower than 0.05 (Fig. 6.13), which might be too low for an oscillation to emerge. This is not the case for spheroids, that exhibit a survival closer to 0.1 at 6.5 Gy. Although the first two points of the spheroid curves are well separated, the large errorbars do not allow definitive conclusions to be drawn. Neverthless, the results are promising and prompt to carry out further

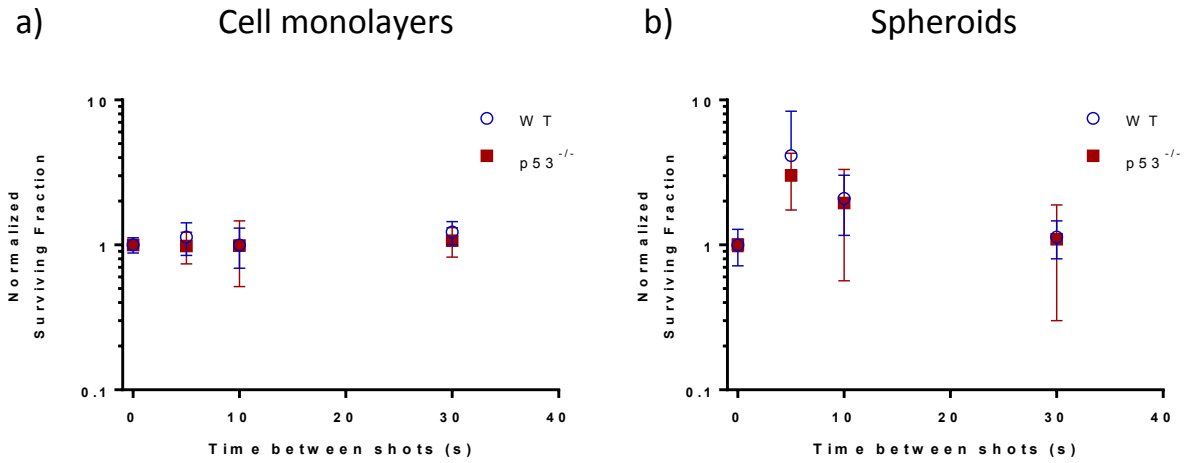

Figure 6.16: Normalised cell survival as a function of the delay between fractions for HCT116 cells grown as monolayers (a) and spheroids (b). The samples were irradiated with a total dose of ∼6.5 Gy, delivered in 5 fractions. Each point represents the mean of three irradiations performed in different days. The vertical error bars represent the standard deviation of the survival fraction corresponding to the three irradiations and is mostly due to the inaccuracy of the delivered dose.

measurements.

6.5 Conclusions

The first dosimetric characterisation and application to radiation biology of kHz Laser-Plasma Accelerated Electrons (LPAE) was presented in this chapter. While both the spectrum and the dose distribution (or the beam pointing) at the sample showed a good stability, the major challenge during the experiment was a precise control of the total delivered dose, hindered by a slight drift of the dose-rate during the irradiation series, probably due to thermal effects introduced by the laser shutter. Further experiments must look to improve the control on the delivered dose by identifying the causes of the observed dose-rate drift and/or by increasing the number of dose-rate measurements between irradiations. This is mandatory to reduce the errobars in the fractionation assay and study the effect of the temporal modality of dose delivery. Overall, the dosimetric characterisation is promising and indicates that such a laser-plasma accelerator could ensure a high degree of stability and repeatability for systematic radiobiology studies compared to other LPAE beams.

Regarding the radiobiological outcome, the survival curves obtained with HCCT116 monolayer samples indicate no significant difference in the radiobiological response

between kHz LPAE and conventional sources with similar LET. Although the results of the fractionation assays are affected by significant errors, a similar pattern seems to emerge in the HCCT116 WT and $p53^{-/-}$ spheroid samples and encourages further studies.

Future experiments should also explore the response of healthy cells. As discussed in section 2.4, the response of *in-vitro* cancer cells alone is not a full indicator of the radiobiological outcome *in-vivo*. A comparison between the response of cancer and healthy cells would provide a more complete indication of the therapeutic potential of such sources.

Conclusions and perspectives

Research conducted during this thesis, partly in collaboration with medical physicists and biologists, addressed some of the main challenges related to the application of Laser-Driven Particle (LDP) beams to radiation biology studies. The needed steps towards LDP sources more suitable for applications in biology and medicine are described in this manuscript and reviewed in this section together with future prospects.

Definite strategies must be found to cope with the peculiar properties of Laser-Accelerated Protons (LAPs). The energy dependent divergence requires to develop dedicated approaches to characterise the source. The knowledge of the total spectral intensity at the source and of the energy-dependent divergence is necessary to design transport beamlines adapted to such beams. A stack of radiochromic films placed behind the source can be used to obtain this information. The deconvolution technique developed to reconstruct the spectrum allowed an accurate characterisation of LAP sources and the design of beamlines dedicated to radiation biology studies.
Furthermore, the large divergence and the polychromatic spectrum require the use of transport systems to collect as much charge as possible and perform spatial and spectral shaping of the beam to reach the desired dose distribution in the biological target. The approach adopted in this thesis, consisting in coupling permanent magnet quadrupoles with Scattering Systems (SSs), was shown to succesfully shape LAP beams for irradiation of both 2D and 3D biological targets (chapter 4). Simulation of the entire beamline (beam transport and interaction with matter) with a Monte Carlo code (Geant4) allowed to optimise, with a single software, the beamline parameters according to the desired irradiation conditions at the biological target. The approach enables the study of more complex shaping techniques, shuch as the genetic approach described in section 3.3, used to optimise the coupling between non-flat SSs and the transport system to shape the dose distribution in the biological sample [43]. Experimental investigation of the benefits of a non-flat SS designed with the described method should be carried out to further validate the approach. Other uses of the genetic approach, such as optimization

of energy-selection systems, can be envisaged.

LAPs produced by commercially available J-class lasers running at 10 Hz and multi-joule lasers firing a shot every hour can be used for different radiobiology applications.
J-class lasers can accelerate nC proton bunches up to ∼10 MeV and deliver doses of the order of 1 Gy/pulse (on a 1 cm^2 surface), which is comparable to the dose delivered in clinics in a single fraction (typically 2 Gy are delivered in fractions separated by ∼24 hours). The experiments performed at the *Salle Saphir* of the LOA (section 2.5) showed oscillation of the cell survival as a function of the delay between proton bunches, pointing out that the temporal structure of such beams may play a role in the radiobiological response [17]. Future studies should investigate the effect of different dose fractionation modalities and precise the conditions at which a fractionation effect emerges, e.g. the minimal or maximal total dose to be delivered in a fraction or the influence of the dose-rate within the fraction. Moreover, next experiments should seek to compare the response of healthy and cancer cells and to evaluate other biological end-points, such as the inflammatory response [39], which would help to obtain a full indication of the therapeutic potential of these sources and of different irradiation protocols.
Multi-J class lasers do represent a viable option to reach FLASH-like conditions with LAPs. As presented in section 4.2, such lasers can accelerate tens of nC per proton bunch and deliver a therapeutic dose (>10 Gy) in a single pulse, i.e. in a time shorter than few nanoseconds. The cut-off energy, higher than 10 MeV, enables *in-vivo* irradiation of thin targets (<1 mm thick), such as zebrafish embryos. The experiment scheduled for the end of 2020 at the LULI laboratory's pico2000 laser facility aims at demonstrating the reach of FLASH conditions with such laser-based accelerators. If successful, the experiment could pave the way for future studies under these conditions. Future PW class lasers could also be relevant for similar studies.
The main limit of LAP sources is the low proton energy which is not sufficient to irradiate large volumes *in-vivo*. However, the rapid development of the laser technology will boost the energy-per-pulse of the next generation of commercially available PW lasers. Although it is still debated what is the best scaling law to model the cut-off energy as a function of the laser intensity on target, the reach of laser intensities greater than 10^{21} W/cm^2 should lead to cut-off energies above ∼100 MeV [212, 30].

The recent discovery of FLASH effect pointed out the importance of *in-vivo* assays to establish the therapeutic potential of an irradiation protocol. Contrary to protons, Laser-Accelerated Electrons (LAEs) are already mature in terms of beam

energy (few MeV up to hundreds of MeV) to investigate the outcome of high dose-rate irradiation *in-vivo*. One of the main issues associated with LAEs is the shot-to-shot pointing instability in the order of the beam divergence, which hinders the reach of stable irradiation conditions (section 5.5). Therefore, investigation of the phenomena behind the LAE shot-to-shot fluctuations, and in particular of pointing instabilities, is a mandatory step to improve the stability of such beams and approach the standards required in clinics.

LAEs generated with low energy lasers running at 1 kHz represent a promising option to conduct radiation biology studies, since the high repetition rate significantly decreases the impact of shot-to-shot fluctuations. The first dosimetric characterisation of such a source was performed at the *Salle noire* of the LOA. The results, presented in chapter 6, indicate that kHz LAEs could ensure a higher degree of stability and repeatability for systematic radiobiology studies compared to other LAE beams. Radiobiology assays on HCT116 cancer cells, grown as monolayers and spheroids, have been succesfully carried out. The results show a radiobiological effectiveness (RBE) of such beam close to that of conventional sources, in line with the findings reported in literature for LAEs generated by J-class lasers. The effect of a dose fractionation was also investigated and an oscillation of cell survival with the delay between fractions seems to emerge for spheroid samples. Future experiments should aim at improving the control of the delivered dose, by investigating the causes of the observed slow drift of the charge per bunch (section 6.3). Boosting the energies up to few MeV without a significant decrease of the charge per bunch would allow to irradiate *in-vivo* biological targets such as mice and would increase the peak dose-rate in the pulse, estimated to 0.72×10^7 Gy/s, by reducing the pulse stretch due to the different velocity of the spectral components from $\sim$100 ps to few ps.

Altough LAEs produced by J-class lasers running at 10 Hz are strongly affected by shot-to-shot instabilities, the ability to produce quasi-monoenergetic electrons at energies of hundreds of MeV might open the way for future studies on the therapeutic benefits of Very High Energy Electrons (VHEE). At the time of writing, theoretical studies reported in literature shown better dose uniformity and sparing of healthy tissues compared to photons [71, 123] but no experiments have been performed with such sources.

The definition of high dose-rate dosimetry protocols represents a crucial issue that needs to be addressed to perform precise radiation biology studies with LDP beams. Dosimetry at high dose-rate is a challenging aspect since Ionisation Chambers (ICs), which are the reference instrument for clinical dosimetry, exhibit saturation due to

recombination of secondary particles produced by radiation in the sensitive volume. As discussed in chapter 5, recombination in ICs is a complex phenomenon that depends on both the chamber geometry and beam parameters, such as the pulse duration and dose-per-pulse. Therefore, the calibration obtained for a given chamber with a clinical accelerator needs to be corrected at the typical dose-rate and dose-per-pulse achieved with LDP beams. The work carried out on the calibration of an IBA Razor Nano Chamber with 6 MeV, µs electron bunches generated by the ert6 Oriatron LINAC prototype showed that the small active volume ensures a higher collection efficiency compared to larger chambers. However, the chamber response becomes more sensitive to the pulse duration at a ∼µs time scale. Preliminary results obtained with fs LAE bunches, presented in section 5.5, suggest that the chamber response is not significantly affected by a further reduction of the pulse duration to fs time scales at dose-per-pulses of tens of mGy. Further work is required to characterise this chamber over a wide range of dose-per-pulse (up to few Gy/pulse) with LAEs. High-charge, low-energy LAEs produced by J-class lasers running at 10 Hz [86] might be used to this scope.
In view of the transfer of ICs to LAE dosimetry, future experiments at the Oriatron should aim at characterising recombination in different chamber types as a function of the pulse duration and for a given DPP, over the whole range of achievable pulse duration (from few µs to a fraction of µs). The results would indicate what is the most appropriate choice for LAE dosimetry. If, on the one hand, the Razor Nano Chamber seems to be capable of measuring higher DPP than larger chambers, such as the Markus type, on the other hand, larger chambers may be more suitable for LAE dosimetry, since they are less sensitive to the pulse duration below a few µs and they could be calibrated at a modified LINAC, such as the Oriatron, with µs pulses.
Parallel research should focus on the identification of alternative reliable systems for high dose-rate dosimetry. This is particularly relevant for LAPs, as there are no other proton accelerators capable of delivering high DPP (∼Gy) in bunches shorter than few µs, as it is the case for electrons. Therefore, future dosimetry protocols for LAPs should rely on the use of other devices insensitive to the dose-rate. ICs might be used as on-line dose monitors once they have been calibrated under LAP irradiation conditions using a dose-rate independent device as dose reference. For instance, radiochromic films are widely used for FLASH-RT dosimetry, since many studies reported in literature demonstrated their dose-rate independence at different dose-rate levels. A comprehensive study of the film response over the entire dose-rate spectrum, from clinical to FLASH and LDP conditions, should be carried out to definitely confirm their dose-rate independence. Other passive devices, such as alanine or termoluminescent detectors, are reported to be insensitive to

the dose-rate [11] and might represent a viable option for future LDP dosimetry protocols.

Laser-based accelerator facilities entirely dedicated to radiation biology applications are needed to address the aforementioned challenges and foster close collaborations with the medical community.

Bibliography

[1] Report 16. *Journal of the International Commission on Radiation Units and Measurements*, volume os9(1):NP–NP, 1970. ISSN 1742-3422, 1473-6691. doi: 10.1093/jicru/os9.1.Report16. 25

[2] Absorbed Dose Determination in External Beam Radiotherapy. Number 398 in Technical Reports Series. INTERNATIONAL ATOMIC ENERGY AGENCY, Vienna, 2001. ISBN 92-0-102200-X. 137, 141, 142, 145

[3] Dosimetry of Small Static Fields Used in External Beam Radiotherapy. Number 483 in Technical Reports Series. INTERNATIONAL ATOMIC ENERGY AGENCY, Vienna, 2017. ISBN 978-92-0-105916-1. 148

[4] G. Adrian, E. Konradsson, M. Lempart, S. Bäck, C. Ceberg, et al. The FLASH effect depends on oxygen concentration. *The British Journal of Radiology*, volume 93(1106):20190702, 2020. ISSN 0007-1285, 1748-880X. doi:10.1259/bjr.20190702. 37

[5] S. Agostinelli, J. Allison, K. Amako, J. Apostolakis, H. Araujo, et al. Geant4—a simulation toolkit. *Nuclear Instruments and Methods in Physics Research Section A: Accelerators, Spectrometers, Detectors and Associated Equipment*, volume 506(3):250–303, 2003. ISSN 01689002. doi:10.1016/S0168-9002(03)01368-8. 92, 97

[6] T. Akagi, A. Higashi, H. Tsugami, H. Sakamoto, Y. Masuda, et al. Ridge filter design for proton therapy at Hyogo Ion Beam Medical Center. *Physics in Medicine and Biology*, volume 48(22):N301–N312, 2003. ISSN 0031-9155, 1361-6560. doi: 10.1088/0031-9155/48/22/N01. 20

[7] A. M. Allen, T. Pawlicki, L. Dong, E. Fourkal, M. Buyyounouski, et al. An evidence based review of proton beam therapy: The report of ASTRO's emerging technology committee. *Radiotherapy and Oncology*, volume 103(1):8–11, 2012. ISSN 01678140. doi:10.1016/j.radonc.2012.02.001. 21

[8] J. Allison, K. Amako, J. Apostolakis, P. Arce, M. Asai, et al. Recent developments in Geant4. *Nuclear Instruments and Methods in Physics Research Section A: Accelerators, Spectrometers, Detectors and Associated Equipment*, volume 835:186–225, 2016. ISSN 01689002. doi:10.1016/j.nima.2016.06.125. 97

[9] D. Alloni, L. Mariotti, A. Ottolenghi. Early Events Leading to Radiation-Induced Biological Effects. In Comprehensive Biomedical Physics, pages 1–22. Elsevier, 2014. ISBN 978-0-444-53633-4. doi:10.1016/B978-0-444-53632-7.00801-7. 23

[10] M. G. Andreassi, A. Borghini, S. Pulignani, F. Baffigi, L. Fulgentini, et al. Radiobiological Effectiveness of Ultrashort Laser-Driven Electron Bunches: Micronucleus Frequency, Telomere Shortening and Cell Viability. *Radiation Research*, volume 186(3):245–253, 2016. ISSN 0033-7587. doi:10.1667/RR14266.1. 44, 52, 178

[11] M. R. Ashraf, M. Rahman, R. Zhang, B. B. Williams, D. J. Gladstone, et al. Dosimetry for FLASH Radiotherapy: A Review of Tools and the Role of Radioluminescence and Cherenkov Emission. *Frontiers in Physics*, volume 8:328, 2020. ISSN 2296-424X. doi:10.3389/fphy.2020.00328. 191

[12] D. Baatar, M. Ehrgott, H. W. Hamacher, I. M. Raschendorfer. Minimizing the number of apertures in multileaf collimator sequencing with field splitting. *Discrete Applied Mathematics*, volume 250:87–103, 2018. ISSN 0166218X. doi:10.1016/j.dam.2018.04.016. 18

[13] N. Babayan, G. Hovhannisyan, B. Grigoryan, R. Grigoryan, N. Sarkisyan, et al. Dose-rate effect of ultrashort electron beam radiation on DNA damage and repair in vitro. *Journal of Radiation Research*, volume 58(6):894–897, 2017. ISSN 0449-3060, 1349-9157. doi:10.1093/jrr/rrx035. 44

[14] M. Barberio, M. Scisciò, S. Vallières, F. Cardelli, S. N. Chen, et al. Laser-accelerated particle beams for stress testing of materials. *Nature Communications*, volume 9(1):372, 2018. ISSN 2041-1723. doi:10.1038/s41467-017-02675-x. 42

[15] G. W. Barendsen. Responses of cultured cells, tumours, and normal tissues to radiations of different linear energy transfer. *Current Topics in Radiation Research*, pages 293–356, 1968. 31

[16] E. Bayart, F. Pouzoulet, L. Calmels, J. Dadoun, F. Allot, et al. Enhancement of IUdR Radiosensitization by Low-Energy Photons Results from Increased and

Persistent DNA Damage. *PLOS ONE*, volume 12(1):e0168395, 2017. ISSN 1932-6203. doi:10.1371/journal.pone.0168395. 57

[17] E. Bayart, A. Flacco, O. Delmas, L. Pommarel, D. Levy, et al. Fast dose fractionation using ultra-short laser accelerated proton pulses can increase cancer cell mortality, which relies on functional PARP1 protein. *Scientific Reports*, volume 9(1):10132, 2019. ISSN 2045-2322. doi:10.1038/s41598-019-46512-1. xx, 53, 57, 69, 104, 112, 188

[18] M. Bazalova-Carter, M. Liu, B. Palma, M. Dunning, D. McCormick, et al. Comparison of film measurements and Monte Carlo simulations of dose delivered with very high-energy electron beams in a polystyrene phantom: Measurements and MC simulations of VHEE beams. *Medical Physics*, volume 42(4):1606–1613, 2015. ISSN 00942405. doi:10.1118/1.4914371. 139

[19] M. Bazalova-Carter, B. Qu, B. Palma, B. Hårdemark, E. Hynning, et al. Treatment planning for radiotherapy with very high-energy electron beams and comparison of VHEE and VMAT plans: Treatment planning for VHEE radiotherapy. *Medical Physics*, volume 42(5):2615–2625, 2015. ISSN 00942405. doi:10.1118/1.4918923. 22

[20] R. J. Berry, E. J. Hall, D. W. Forster, T. H. Storr, M. J. Goodman. Survival of mammalian cells exposed to X rays at ultra-high dose-rates. *The British Journal of Radiology*, volume 42(494):102–107, 1969. ISSN 0007-1285, 1748-880X. doi:10.1259/0007-1285-42-494-102. 33, 52

[21] E. Beyreuther, W. Enghardt, M. Kaluza, L. Karsch, L. Laschinsky, et al. Establishment of technical prerequisites for cell irradiation experiments with laser-accelerated electrons: Laser-accelerated electrons for cell irradiation experiments. *Medical Physics*, volume 37(4):1392–1400, 2010. ISSN 00942405. doi:10.1118/1.3301598. 44, 52, 178

[22] E. Beyreuther, M. Brand, S. Hans, K. Hideghéty, L. Karsch, et al. Feasibility of proton FLASH effect tested by zebrafish embryo irradiation. *Radiotherapy and Oncology*, volume 139:46–50, 2019. ISSN 01678140. doi:10.1016/j.radonc.2019.06.024. 35

[23] M. T. Bhoskar, M. O. K. Kulkarni, M. N. K. Kulkarni, M. S. L. Patekar, G. Kakandikar, et al. Genetic Algorithm and its Applications to Mechanical Engineering: A Review. *Materials Today: Proceedings*, volume 2(4-5):2624–2630, 2015. ISSN 22147853. doi:10.1016/j.matpr.2015.07.219. 101

[24] J. Bin, K. Allinger, W. Assmann, G. Dollinger, G. A. Drexler, et al. A laser-driven nanosecond proton source for radiobiological studies. *Applied Physics Letters*, volume 101(24):243701, 2012. ISSN 0003-6951, 1077-3118. doi:10.1063/1.4769372. 48

[25] J. W. Boag. Ionization Measurements at Very High Intensities—Part I. *The British Journal of Radiology*, volume 23(274):601–611, 1950. ISSN 0007-1285, 1748-880X. doi:10.1259/0007-1285-23-274-601. 143

[26] J. W. Boag, J. Currant. Current collection and ionic recombination in small cylindrical ionization chambers exposed to pulsed radiation. *The British Journal of Radiology*, volume 53(629):471–478, 1980. ISSN 0007-1285, 1748-880X. doi:10.1259/0007-1285-53-629-471. 145

[27] J. W. Boag, E. Hochhäuser, O. A. Balk. The effect of free-electron collection on the recombination correction to ionization measurements of pulsed radiation. *Physics in Medicine and Biology*, volume 41(5):885–897, 1996. ISSN 0031-9155, 1361-6560. doi:10.1088/0031-9155/41/5/005. 146, 147

[28] G. Boissonnat. Chambres d'ionisation en Protonthérapie et Hadronthérapie. Ph.D. thesis, Université Caen Normandie, 2015. 158

[29] P. Bolton, M. Borghesi, C. Brenner, D. Carroll, C. De Martinis, et al. Instrumentation for diagnostics and control of laser-accelerated proton (ion) beams. *Physica Medica*, volume 30(3):255–270, 2014. ISSN 11201797. doi:10.1016/j.ejmp.2013.09.002. 66, 67

[30] M. Borghesi. Laser-driven ion acceleration: State of the art and emerging mechanisms. *Nuclear Instruments and Methods in Physics Research Section A: Accelerators, Spectrometers, Detectors and Associated Equipment*, volume 740:6–9, 2014. ISSN 01689002. doi:10.1016/j.nima.2013.11.098. 188

[31] T. Bortfeld, R. Schmidt-Ullrich, W. De Neve, D. E. Wazer. Image Guided IMRT. 2006. 18

[32] J. Bourhis, P. Montay-Gruel, P. Gonçalves Jorge, C. Bailat, B. Petit, et al. Clinical translation of FLASH radiotherapy: Why and how? *Radiotherapy and Oncology*, volume 139:11–17, 2019. ISSN 01678140. doi:10.1016/j.radonc.2019.04.008. 36, 37, 127

[33] J. Bourhis, W. J. Sozzi, P. G. Jorge, O. Gaide, C. Bailat, et al. Treatment of a first patient with FLASH-radiotherapy. *Radiotherapy and Oncology*, volume 139:18–22, 2019. ISSN 01678140. doi:10.1016/j.radonc.2019.06.019. xvii, 37, 149

[34] A. L. Boyer. The Physics of Intensity-Modulated Radiation Therapy. *Physics Today*, volume 55(9):38–43, 2002. ISSN 0031-9228, 1945-0699. doi:10.1063/1.1522214. 17, 18

[35] E. Breschi, M. Borghesi, M. Galimberti, D. Giulietti, L. Gizzi, et al. A new algorithm for spectral and spatial reconstruction of proton beams from dosimetric measurements. *Nuclear Instruments and Methods in Physics Research Section A: Accelerators, Spectrometers, Detectors and Associated Equipment*, volume 522(3):190–195, 2004. ISSN 01689002. doi:10.1016/j.nima.2003.11.199. 69, 72, 73

[36] S. Bright, M. Kadhim. The future impacts of non-targeted effects. *International Journal of Radiation Biology*, volume 94(8):727–736, 2018. ISSN 0955-3002, 1362-3095. doi:10.1080/09553002.2018.1454617. 23

[37] A. Buck, J. Wenz, J. Xu, K. Khrennikov, K. Schmid, et al. Shock-Front Injector for High-Quality Laser-Plasma Acceleration. *Physical Review Letters*, volume 110(18):185006, 2013. ISSN 0031-9007, 1079-7114. doi:10.1103/PhysRevLett.110.185006. 42

[38] S. V. Bulanov, V. S. Khoroshkov. Feasibility of using laser ion accelerators in proton therapy. *Plasma Physics Reports*, volume 28(5):453–456, 2002. ISSN 1063-780X, 1562-6938. doi:10.1134/1.1478534. 52

[39] M. Buonanno, V. Grilj, D. J. Brenner. Biological effects in normal cells exposed to FLASH dose rate protons. *Radiotherapy and Oncology*, volume 139:51–55, 2019. ISSN 01678140. doi:10.1016/j.radonc.2019.02.009. 37, 188

[40] T. Burris-Mog, K. Harres, F. Nürnberg, S. Busold, M. Bussmann, et al. Laser accelerated protons captured and transported by a pulse power solenoid. *Physical Review Special Topics - Accelerators and Beams*, volume 14(12):121301, 2011. ISSN 1098-4402. doi:10.1103/PhysRevSTAB.14.121301. 49

[41] F. Böhle, M. Kretschmar, A. Jullien, M. Kovacs, M. Miranda, et al. Compression of CEP-stable multi-mJ laser pulses down to 4 fs in long hollow fibers. *Laser Physics Letters*, volume 11(9):095401, 2014. ISSN 1612-2011, 1612-202X. doi:10.1088/1612-2011/11/9/095401. 165

[42] V. Calugaru, C. Nauraye, G. Noël, N. Giocanti, V. Favaudon, et al. Radiobiological Characterization of Two Therapeutic Proton Beams With Different Initial Energy Spectra Used at the Institut Curie Proton Therapy Center in Orsay. *International Journal of Radiation Oncology*Biology*Physics*, volume 81(4):1136–1143, 2011. ISSN 03603016. doi:10.1016/j.ijrobp.2010.09.003. 57

[43] M. Cavallone, A. Flacco, V. Malka. Shaping of a laser-accelerated proton beam for radiobiology applications via genetic algorithm. *Physica Medica*, volume 67:123–131, 2019. ISSN 11201797. doi:10.1016/j.ejmp.2019.10.027. 187

[44] C. Chargari, N. Magne, J.-B. Guy, C. Rancoule, A. Levy, et al. Optimize and refine therapeutic index in radiation therapy: Overview of a century. *Cancer Treatment Reviews*, volume 45:58–67, 2016. ISSN 03057372. doi:10.1016/j.ctrv.2016.03.001. 2, 30

[45] P. Chaudhary, T. I. Marshall, F. M. Perozziello, L. Manti, F. J. Currell, et al. Relative Biological Effectiveness Variation Along Monoenergetic and Modulated Bragg Peaks of a 62-MeV Therapeutic Proton Beam: A Preclinical Assessment. *International Journal of Radiation Oncology*Biology*Physics*, volume 90(1):27–35, 2014. ISSN 03603016. doi:10.1016/j.ijrobp.2014.05.010. 22, 29

[46] G. Cirrone, G. Cuttone, F. Di Rosa, S. Guatelli, B. Mascialino, et al. Validation of Geant4 Physics Models for the Simulation of the Proton Bragg Peak. In 2006 IEEE Nuclear Science Symposium Conference Record, pages 788–792. IEEE, San Diego, CA, USA, 2006. ISBN 978-1-4244-0560-2. doi:10.1109/NSSMIC.2006.355969. 92

[47] G. Cirrone, G. Cuttone, F. Di Rosa, S. Mazzaglia, F. Romano, et al. Hadrontherapy: An open source, Geant4-based application for proton-ion therapy studies. In 2009 IEEE Nuclear Science Symposium Conference Record (NSS/MIC), pages 4186–4189. IEEE, Orlando, FL, 2009. ISBN 978-1-4244-3961-4. doi:10.1109/NSSMIC.2009.5402279. 92

[48] G. Cirrone, G. Petringa, B. Cagni, G. Cuttone, G. Fustaino, et al. Use of radiochromic films for the absolute dose evaluation in high dose-rate proton beams. *Journal of Instrumentation*, volume 15(04):C04029–C04029, 2020. ISSN 1748-0221. doi:10.1088/1748-0221/15/04/C04029. 138

[49] G. A. P. Cirrone, G. Cuttone, L. Pandola, D. Margarone, G. Petringa. Particles Simulation Through Matter in Medical Physics Using the Geant4 Toolkit: From Conventional to Laser-Driven Hadrontherapy. In L. A. Gizzi, R. Assmann, P. Koester,

A. Giulietti, editors, Laser-Driven Sources of High Energy Particles and Radiation, volume 231, pages 187–208. Springer International Publishing, Cham, 2019. ISBN 978-3-030-25849-8 978-3-030-25850-4. doi:10.1007/978-3-030-25850-4_9. Series Title: Springer Proceedings in Physics. 92

[50] G. A. P. Cirrone, G. Cuttone, S. E. Mazzaglia, F. Romano, D. Sardina, et al. Hadrontherapy: a Geant4-Based Tool for Proton/Ion-Therapy Studies. *Progress in Nuclear Science and Technology*, volume 2(0):207–212, 2011. ISSN 2185-4823. doi:10.15669/pnst.2.207. 92

[51] M. Dalui, M. Kundu, T. M. Trivikram, R. Rajeev, K. Ray, et al. Bacterial cells enhance laser driven ion acceleration. *Scientific Reports*, volume 4(1):6002, 2015. ISSN 2045-2322. doi:10.1038/srep06002. 66

[52] S. Demaria, S. C. Formenti. Role of T lymphocytes in tumor response to radiotherapy. *Frontiers in Oncology*, volume 2, 2012. ISSN 2234-943X. doi:10.3389/fonc.2012.00095. 37

[53] O. Desouky, N. Ding, G. Zhou. Targeted and non-targeted effects of ionizing radiation. *Journal of Radiation Research and Applied Sciences*, volume 8(2):247–254, 2015. ISSN 1687-8507. doi:10.1016/j.jrras.2015.03.003. 23, 27

[54] C. DesRosiers, V. Moskvin, M. Cao, C. J. Joshi, M. Langer. Laser-plasma generated very high energy electrons in radiation therapy of the prostate. page 688109. San Jose, CA, 2008. doi:10.1117/12.761663. 22

[55] M. Desrosiers, L. DeWerd, J. Deye, P. Lindsay, M. K. Murphy, et al. The Importance of Dosimetry Standardization in Radiobiology. *Journal of Research of the National Institute of Standards and Technology*, volume 118:403, 2013. ISSN 2165-7254. doi:10.6028/jres.118.021. 13, 55

[56] S. Devic, N. Tomic, D. Lewis. Reference radiochromic film dosimetry: Review of technical aspects. *Physica Medica*, volume 32(4):541–556, 2016. ISSN 11201797. doi:10.1016/j.ejmp.2016.02.008. 138, 171

[57] S. Devic, N. Tomic, C. G. Soares, E. B. Podgorsak. Optimizing the dynamic range extension of a radiochromic film dosimetry system: Optimizing dynamic range of radiochromic film system. *Medical Physics*, volume 36(2):429–437, 2009. ISSN 00942405. doi:10.1118/1.3049597. 79

[58] D. Doria, K. F. Kakolee, S. Kar, S. K. Litt, F. Fiorini, et al. Biological effectiveness on live cells of laser driven protons at dose rates exceeding 10 ^{9} Gy/s. *AIP Advances*, volume 2(1):011209, 2012. ISSN 2158-3226. doi:10.1063/1.3699063. 44, 48, 51

[59] M. Durante, E. Brauer-Krisch, M. Hill. Faster and safer? FLASH ultra-high dose rate in radiotherapy. *The British Journal of Radiology*, page 20170628, 2017. ISSN 0007-1285, 1748-880X. doi:10.1259/bjr.20170628. 33, 60

[60] J. Eduardo Villarreal-Barajas, R. F. Khan. Energy response of EBT3 radiochromic films: implications for dosimetry in kilovoltage range. *Journal of Applied Clinical Medical Physics*, volume 15(1):331–338, 2014. ISSN 15269914. doi:10.1120/jacmp.v15i1.4439. 77, 138

[61] E. R. Epp, H. Weiss, B. Djordjevic, A. Santomasso. The Radiosensitivity of Cultured Mammalian Cells Exposed to Single High Intensity Pulses of Electrons in Various Concentrations of Oxygen. *Radiation Research*, volume 52(2):324, 1972. ISSN 00337587. doi:10.2307/3573572. 52

[62] J. Faure, C. Rechatin, A. Norlin, A. Lifschitz, Y. Glinec, et al. Controlled injection and acceleration of electrons in plasma wakefields by colliding laser pulses. *Nature*, volume 444(7120):737–739, 2006. ISSN 0028-0836, 1476-4687. doi:10.1038/nature05393. 42

[63] J. Faure, C. Rechatin, A. F. Lifschitz, X. Davoine, E. Lefebvre, et al. Experiments and Simulations of the Colliding Pulse Injection of Electrons in Plasma Wakefields. *IEEE Transactions on Plasma Science*, volume 36(4):1751–1759, 2008. ISSN 0093-3813. doi:10.1109/TPS.2008.927430. 42, 46

[64] V. Favaudon, L. Caplier, V. Monceau, F. Pouzoulet, M. Sayarath, et al. Ultra-high dose-rate FLASH irradiation increases the differential response between normal and tumor tissue in mice. *Science Translational Medicine*, volume 6(245):245ra93–245ra93, 2014. ISSN 1946-6234, 1946-6242. doi:10.1126/scitranslmed.3008973. xvii, 2, 33, 34

[65] E. D.-A.-M. Fernet, V. Ponette. Poly(ADP-ribose) polymerase, a major determinant of early cell response to ionizing radiation. *International Journal of Radiation Biology*, volume 76(12):1621–1629, 2000. ISSN 0955-3002, 1362-3095. doi:10.1080/09553000050201118. 60

[66] M. Ferrario, M. Migliorati, L. Palumbo. Space Charge Effects. 2014. doi:10.5170/CERN-2014-009.331. Publisher: CERN. 94

[67] S. Field, D. Bewley. Effects of Dose-rate on the Radiation Response of Rat Skin. *International Journal of Radiation Biology and Related Studies in Physics, Chemistry and Medicine*, volume 26(3):259–267, 1974. ISSN 0020-7616. doi:10.1080/09553007414551221. 33

[68] F. Fiorini, D. Kirby, M. Borghesi, D. Doria, J. C. G. Jeynes, et al. Dosimetry and spectral analysis of a radiobiological experiment using laser-driven proton beams. *Physics in Medicine and Biology*, volume 56(21):6969–6982, 2011. ISSN 0031-9155, 1361-6560. doi:10.1088/0031-9155/56/21/013. 44, 48, 51

[69] C. Fouillade, V. Favaudon, M.-C. Vozenin, P.-H. Romeo, J. Bourhis, et al. Les promesses du haut débit de dose en radiothérapie. *Bulletin du Cancer*, volume 104(4):380–384, 2017. ISSN 00074551. doi:10.1016/j.bulcan.2017.01.012. 33

[70] J. Fuchs, P. Audebert, P. Antici, E. Brambrink, E. DâtmHumières, et al. Review of high-brightness proton & ion acceleration using pulsed lasers. pages 319–323. 2006. 97

[71] T. Fuchs, H. Szymanowski, U. Oelfke, Y. Glinec, C. Rechatin, et al. Treatment planning for laser-accelerated very-high energy electrons. *Physics in Medicine and Biology*, volume 54(11):3315–3328, 2009. ISSN 0031-9155, 1361-6560. doi:10.1088/0031-9155/54/11/003. 22, 53, 189

[72] C. G. R. Geddes, K. Nakamura, G. R. Plateau, C. Toth, E. Cormier-Michel, et al. Plasma-Density-Gradient Injection of Low Absolute-Momentum-Spread Electron Bunches. *Physical Review Letters*, volume 100(21):215004, 2008. ISSN 0031-9007, 1079-7114. doi:10.1103/PhysRevLett.100.215004. 42

[73] C. Geng, D. Gates, L. Bronk, D. Ma, F. Guan. Physical parameter optimization scheme for radiobiological studies of charged particle therapy. *Physica Medica*, volume 51:13–21, 2018. ISSN 11201797. doi:10.1016/j.ejmp.2018.06.001. 19

[74] A. Ghaheri, S. Shoar, M. Naderan, S. S. Hoseini. The Applications of Genetic Algorithms in Medicine. *Oman Medical Journal*, volume 30(6):406–416, 2015. ISSN 1999768X, 20705204. doi:10.5001/omj.2015.82. 101

[75] A. Ghaith, D. Oumbarek, C. Kitégi, M. Valléau, F. Marteau, et al. Permanent Magnet-Based Quadrupoles for Plasma Acceleration Sources. *Instruments*, volume 3(2):27, 2019. ISSN 2410-390X. doi:10.3390/instruments3020027. 87

[76] M. Ghorbanpour Besheli, I. Simiantonakis, K. Zink, W. Budach. Determination of the ion recombination correction factor for intraoperative electron beams. *Zeitschrift für Medizinische Physik*, volume 26(1):35–44, 2016. ISSN 09393889. doi:10.1016/j.zemedi.2015.06.011. 145

[77] A. Giulietti, N. Bourgeois, T. Ceccotti, X. Davoine, S. Dobosz, et al. Intense - Ray Source in the Giant-Dipole-Resonance Range Driven by 10-TW Laser Pulses. *Physical Review Letters*, volume 101(10):105002, 2008. ISSN 0031-9007, 1079-7114. doi:10.1103/PhysRevLett.101.105002. 44, 50

[78] L. Gizzi, L. Labate, F. Baffigi, F. Brandi, G. Bussolino, et al. Laser–plasma acceleration of electrons for radiobiology and radiation sources. *Nuclear Instruments and Methods in Physics Research Section B: Beam Interactions with Materials and Atoms*, volume 355:241–245, 2015. ISSN 0168583X. doi:10.1016/j.nimb.2015.03.050. 42, 44, 178

[79] L. Gizzi, C. Altana, F. Brandi, P. Cirrone, G. Cristoforetti, et al. Role of laser contrast and foil thickness in target normal sheath acceleration. *Nuclear Instruments and Methods in Physics Research Section A: Accelerators, Spectrometers, Detectors and Associated Equipment*, volume 829:144–148, 2016. ISSN 01689002. doi:10.1016/j.nima.2016.01.036. 112

[80] L. Gizzi, D. Giove, C. Altana, F. Brandi, P. Cirrone, et al. A New Line for Laser-Driven Light Ions Acceleration and Related TNSA Studies. *Applied Sciences*, volume 7(10):984, 2017. ISSN 2076-3417. doi:10.3390/app7100984. 112

[81] L. Gizzi, F. Baffigi, F. Brandi, G. Bussolino, G. Cristoforetti, et al. Light Ion Accelerating Line (L3IA): Test experiment at ILIL-PW. *Nuclear Instruments and Methods in Physics Research Section A: Accelerators, Spectrometers, Detectors and Associated Equipment*, volume 909:160–163, 2018. ISSN 01689002. doi:10.1016/j.nima.2018.03.016. 66, 112, 126

[82] Y. Glinec, J. Faure, V. Malka, T. Fuchs, H. Szymanowski, et al. Radiotherapy with laser-plasma accelerators: Monte Carlo simulation of dose deposited by an experimental quasimonoenergetic electron beam: Radiotherapy with quasimonoenergetic

electron beam from laser-plasma interaction. *Medical Physics*, volume 33(1):155–162, 2005. ISSN 00942405. doi:10.1118/1.2140115. 22

[83] G. Golovin, S. Chen, N. Powers, C. Liu, S. Banerjee, et al. Tunable monoenergetic electron beams from independently controllable laser-wakefield acceleration and injection. *Physical Review Special Topics - Accelerators and Beams*, volume 18(1):011301, 2015. ISSN 1098-4402. doi:10.1103/PhysRevSTAB.18.011301. 42

[84] M. Gondré, P. G. Jorge, M.-C. Vozenin, J. Bourhis, F. Bochud, et al. Optimization of Alanine Measurements for Fast and Accurate Dosimetry in FLASH Radiation Therapy. *Radiation Research*, page RR15568.1, 2020. ISSN 0033-7587. doi:10.1667/RR15568.1. 138

[85] M. Gotz, L. Karsch, J. Pawelke. A new model for volume recombination in plane-parallel chambers in pulsed fields of high dose-per-pulse. *Physics in Medicine & Biology*, volume 62(22):8634–8654, 2017. ISSN 1361-6560. doi:10.1088/1361-6560/aa8985. 147, 159

[86] E. Guillaume, A. Döpp, C. Thaury, A. Lifschitz, J.-P. Goddet, et al. Physics of fully-loaded laser-plasma accelerators. *Physical Review Special Topics - Accelerators and Beams*, volume 18(6):061301, 2015. ISSN 1098-4402. doi:10.1103/PhysRevSTAB.18.061301. 42, 44, 46, 47, 190

[87] D. Gustas. High-repetition-rate relativistic electron acceleration in plasma wakefields driven by few-cycle laser pulses. Ph.D. thesis, Université Paris-Saclay, 2018. 166, 167

[88] D. Gustas, D. Guénot, A. Vernier, S. Dutt, F. Böhle, et al. High-charge relativistic electron bunches from a kHz laser-plasma accelerator. *Physical Review Accelerators and Beams*, volume 21(1):013401, 2018. ISSN 2469-9888. doi:10.1103/PhysRevAccelBeams.21.013401. xxi, 44, 166

[89] G. Güngör, G. Aydın, T. Z. Mustafayev, E. Özyar. Output factors of ionization chambers and solid state detectors for mobile intraoperative radiotherapy (IORT) accelerator electron beams. *Journal of Applied Clinical Medical Physics*, volume 20(2):13–23, 2019. ISSN 15269914. doi:10.1002/acm2.12522. 157

[90] D. C. Hall, A. Makarova, H. Paganetti, B. Gottschalk. Validation of nuclear models in Geant4 using the dose distribution of a 177 MeV proton pencil beam. *Physics*

in Medicine and Biology, volume 61(1):N1–N10, 2016. ISSN 0031-9155, 1361-6560. doi:10.1088/0031-9155/61/1/N1. 92

[91] E. J. Hall. Radiation Dose-Rate: A Factor of Importance in Radiobiology and Radiotherapy. *The British Journal of Radiology*, volume 45(530):81–97, 1972. ISSN 0007-1285, 1748-880X. doi:10.1259/0007-1285-45-530-81. 33, 60

[92] E. J. Hall, A. J. Giaccia. Radiobiology for the radiologist. Wolters Kluwer Health, 2012. ISBN 978-1-86094-135-1. 3, 25, 28, 33, 61

[93] F. Hanton, P. Chaudhary, D. Doria, D. Gwynne, C. Maiorino, et al. DNA DSB Repair Dynamics following Irradiation with Laser-Driven Protons at Ultra-High Dose Rates. *Scientific Reports*, volume 9(1):4471, 2019. ISSN 2045-2322. doi:10.1038/s41598-019-40339-6. 44, 55

[94] K. Harres, M. Schollmeier, E. Brambrink, P. Audebert, A. Blažević, et al. Development and calibration of a Thomson parabola with microchannel plate for the detection of laser-accelerated MeV ions. *Review of Scientific Instruments*, volume 79(9):093306, 2008. ISSN 00346748. doi:10.1063/1.2987687. 68

[95] K. Harres, I. Alber, A. Tauschwitz, V. Bagnoud, H. Daido, et al. Beam collimation and transport of quasineutral laser-accelerated protons by a solenoid field. *Physics of Plasmas*, volume 17(2):023107, 2010. ISSN 1070-664X, 1089-7674. doi:10.1063/1.3299391. 50

[96] Z.-H. He, B. Hou, J. A. Nees, J. H. Easter, J. Faure, et al. High repetition-rate wakefield electron source generated by few-millijoule, 30 fs laser pulses on a density downramp. *New Journal of Physics*, volume 15(5):053016, 2013. ISSN 1367-2630. doi:10.1088/1367-2630/15/5/053016. 44, 165

[97] E. Hochhauser, O. A. Balk. The influence of unattached electrons on the collection efficiency of ionisation chambers for the measurement of radiation pulses of high dose rate. *Physics in Medicine and Biology*, volume 31(3):223–233, 1986. ISSN 0031-9155, 1361-6560. doi:10.1088/0031-9155/31/3/002. 146

[98] I. Hofmann. Performance of solenoids versus quadrupoles in focusing and energy selection of laser accelerated protons. *Physical Review Special Topics - Accelerators and Beams*, volume 16(4):041302, 2013. ISSN 1098-4402. doi:10.1103/PhysRevSTAB.16.041302. 50

[99] K. M. Hofmann, U. Masood, J. Pawelke, J. J. Wilkens. A treatment planning study to assess the feasibility of laser-driven proton therapy using a compact gantry design: A treatment planning study to assess the feasibility of laser-driven proton therapy. *Medical Physics*, volume 42(9):5120–5129, 2015. ISSN 00942405. doi: 10.1118/1.4927717. 49

[100] K. M. Hofmann, S. Schell, J. J. Wilkens. Laser-driven beam lines for delivering intensity modulated radiation therapy with particle beams. *Journal of Biophotonics*, volume 5(11-12):903–911, 2012. ISSN 1864063X. doi:10.1002/jbio.201200078. 49

[101] S. Hornsey, D. Bewley. Hypoxia in Mouse Intestine Induced by Electron Irradiation at High Dose-rates. *International Journal of Radiation Biology and Related Studies in Physics, Chemistry and Medicine*, volume 19(5):479–483, 1971. ISSN 0020-7616. doi:10.1080/09553007114550611. 33

[102] A. Hussain, Y. S. Muhammad, M. Nauman Sajid, I. Hussain, A. Mohamd Shoukry, et al. Genetic Algorithm for Traveling Salesman Problem with Modified Cycle Crossover Operator. *Computational Intelligence and Neuroscience*, volume 2017:1–7, 2017. ISSN 1687-5265, 1687-5273. doi:10.1155/2017/7430125. 101

[103] G. Iliakis, E. Mladenov, V. Mladenova. Necessities in the Processing of DNA Double Strand Breaks and Their Effects on Genomic Instability and Cancer. *Cancers*, volume 11(11):1671, 2019. ISSN 2072-6694. doi:10.3390/cancers11111671. 26

[104] M. Jaccard, K. Petersson, T. Buchillier, J.-F. Germond, M. T. Durán, et al. High dose-per-pulse electron beam dosimetry: Usability and dose-rate independence of EBT3 Gafchromic films. *Medical Physics*, volume 44(2):725–735, 2017. ISSN 00942405. doi:10.1002/mp.12066. 139, 149

[105] M. Jaccard, M. T. Durán, K. Petersson, J.-F. Germond, P. Liger, et al. High dose-per-pulse electron beam dosimetry: Commissioning of the Oriatron eRT6 prototype linear accelerator for preclinical use. *Medical Physics*, volume 45(2):863–874, 2018. ISSN 00942405. doi:10.1002/mp.12713. xx, 149, 153, 154

[106] L. Jagannathan, S. Cuddapah, M. Costa. Oxidative Stress Under Ambient and Physiological Oxygen Tension in Tissue Culture. *Current Pharmacology Reports*, volume 2(2):64–72, 2016. ISSN 2198-641X. doi:10.1007/s40495-016-0050-5. 52

[107] M. Joiner, A. v. d. Kogel, editors. Basic clinical radiobiology. Hodder Arnold, London, 4th ed edition, 2009. ISBN 978-0-340-92966-7. 23, 57

[108] P. G. Jorge, M. Jaccard, K. Petersson, M. Gondré, M. T. Durán, et al. Dosimetric and preparation procedures for irradiating biological models with pulsed electron beam at ultra-high dose-rate. *Radiotherapy and Oncology*, volume 139:34–39, 2019. ISSN 01678140. doi:10.1016/j.radonc.2019.05.004. 138, 149

[109] C. P. Karger, G. H. Hartmann. Correction of ionic recombination for pulsed radiation according to DIN 6800-2 and TRS-398. *Zeitschrift für Medizinische Physik*, volume 14(4):260–266, 2004. ISSN 09393889. doi:10.1078/0939-3889-00224. 143

[110] L. Karsch, E. Beyreuther, T. Burris-Mog, S. Kraft, C. Richter, et al. Dose rate dependence for different dosimeters and detectors: TLD, OSL, EBT films, and diamond detectors: Dose rate dependence for different dosimeters an detectors. *Medical Physics*, volume 39(5):2447–2455, 2012. ISSN 00942405. doi:10.1118/1.3700400. 139

[111] D. Kirby, S. Green, F. Fiorini, D. Parker, L. Romagnani, et al. Radiochromic film spectroscopy of laser-accelerated proton beams using the FLUKA code and dosimetry traceable to primary standards. *Laser and Particle Beams*, volume 29(2):231–239, 2011. ISSN 0263-0346, 1469-803X. doi:10.1017/S0263034611000206. 69, 72

[112] A. Klyachko. GEM-based Dose Imaging Detectors for Proton Therapy Quality Assurance and Proton Radiography. 2017. 20

[113] G. F. Knoll. Radiation Detection and Measurement. John Wiley & sons, Inc., 3 edition, 2000. 4, 7

[114] A.-C. Knopf, A. Lomax. *In vivo* proton range verification: a review. *Physics in Medicine and Biology*, volume 58(15):R131–R160, 2013. ISSN 0031-9155, 1361-6560. doi:10.1088/0031-9155/58/15/R131. 21

[115] K. Kokurewicz, E. Brunetti, G. H. Welsh, S. M. Wiggins, M. Boyd, et al. Focused very high-energy electron beams as a novel radiotherapy modality for producing high-dose volumetric elements. *Scientific Reports*, volume 9(1):10837, 2019. ISSN 2045-2322. doi:10.1038/s41598-019-46630-w. 22

[116] S. D. Kraft, C. Richter, K. Zeil, M. Baumann, E. Beyreuther, et al. Dose-dependent biological damage of tumour cells by laser-accelerated proton beams. *New Journal of Physics*, volume 12(8):085003, 2010. ISSN 1367-2630. doi:10.1088/1367-2630/12/8/085003. 13, 44, 45, 48, 51, 55

[117] R. F. Laitano, A. S. Guerra, M. Pimpinella, C. Caporali, A. Petrucci. Charge collection efficiency in ionization chambers exposed to electron beams with high dose per pulse. *Physics in Medicine and Biology*, volume 51(24):6419–6436, 2006. ISSN 0031-9155, 1361-6560. doi:10.1088/0031-9155/51/24/009. 147

[118] M. F. L'Annunziata. Radiation Physics and Radionuclide Decay. In Handbook of Radioactivity Analysis, pages 1–162. Elsevier, 2012. ISBN 978-0-12-384873-4. doi:10.1016/B978-0-12-384873-4.00001-3. 25, 44, 178

[119] L. Laschinsky, M. Baumann, E. Beyreuther, W. Enghardt, M. Kaluza, et al. Radiobiological Effectiveness of Laser Accelerated Electrons in Comparison to Electron Beams from a Conventional Linear Accelerator. *Journal of Radiation Research*, volume 53(3):395–403, 2012. ISSN 0449-3060, 1349-9157. doi:10.1269/jrr.11080. 44, 46, 52, 53

[120] K. Ledingham, P. Bolton, N. Shikazono, C.-M. Ma. Towards Laser Driven Hadron Cancer Radiotherapy: A Review of Progress. *Applied Sciences*, volume 4(3):402–443, 2014. ISSN 2076-3417. doi:10.3390/app4030402. 52

[121] K. Levy, S. Natarajan, J. Wang, S. Chow, J. T. Eggold, et al. FLASH irradiation enhances the therapeutic index of abdominal radiotherapy for the treatment of ovarian cancer. preprint, Cancer Biology, 2019. doi:10.1101/2019.12.12.873414. 34

[122] M. Lomax, L. Folkes, P. O'Neill. Biological Consequences of Radiation-induced DNA Damage: Relevance to Radiotherapy. *Clinical Oncology*, volume 25(10):578–585, 2013. ISSN 09366555. doi:10.1016/j.clon.2013.06.007. 25

[123] O. Lundh, C. Rechatin, J. Faure, A. Ben-Ismaïl, J. Lim, et al. Comparison of measured with calculated dose distribution from a 120-MeV electron beam from a laser-plasma accelerator: Laser-plasma accelerated high-energy electron beams for radiotherapy. *Medical Physics*, volume 39(6Part1):3501–3508, 2012. ISSN 00942405. doi:10.1118/1.4719962. 53, 189

[124] A. Macchi, M. Borghesi, M. Passoni. Ion acceleration by superintense laser-plasma interaction. *Reviews of Modern Physics*, volume 85(2):751–793, 2013. ISSN 0034-6861, 1539-0756. doi:10.1103/RevModPhys.85.751. 42, 69

[125] V. Malka. Laser plasma accelerators. *Physics of Plasmas*, volume 19(5):055501, 2012. ISSN 1070-664X, 1089-7674. doi:10.1063/1.3695389. 42

[126] V. Malka, S. Fritzler, E. Lefebvre, E. d'Humières, R. Ferrand, et al. Practicability of protontherapy using compact laser systems. *Medical Physics*, volume 31(6):1587–1592, 2004. ISSN 00942405. doi:10.1118/1.1747751. 52

[127] D. M. Marcus, A. B. Jani, K. Godette, P. J. Rossi. A Review of Low-Dose-Rate Prostate Brachytherapy—Techniques and Outcomes. *Journal of the National Medical Association*, volume 102(6):500–510, 2010. ISSN 00279684. doi:10.1016/S0027-9684(15)30559-9. 33

[128] E. Y. L. Marroquin, J. A. Herrera González, M. A. Camacho López, J. E. V. Barajas, O. A. García-Garduño. Evaluation of the uncertainty in an EBT3 film dosimetry system utilizing net optical density. *Journal of Applied Clinical Medical Physics*, volume 17(5):466–481, 2016. ISSN 15269914. doi:10.1120/jacmp.v17i5.6262. 79

[129] U. Masood, M. Bussmann, T. E. Cowan, W. Enghardt, L. Karsch, et al. A compact solution for ion beam therapy with laser accelerated protons. *Applied Physics B*, volume 117(1):41–52, 2014. ISSN 0946-2171, 1432-0649. doi:10.1007/s00340-014-5796-z. 49, 116

[130] U. Masood, T. E. Cowan, W. Enghardt, K. M. Hofmann, L. Karsch, et al. A light-weight compact proton gantry design with a novel dose delivery system for broad-energetic laser-accelerated beams. *Physics in Medicine & Biology*, volume 62(13):5531–5555, 2017. ISSN 0031-9155, 1361-6560. doi:10.1088/1361-6560/aa7124. 49, 50

[131] J. Matthews, B. Meeker, J. Chapman. Response of human tumor cell lines in vitro to fractionated irradiation. *International Journal of Radiation Oncology*Biology*Physics*, volume 16(1):133–138, 1989. ISSN 03603016. doi:10.1016/0360-3016(89)90020-5. 32

[132] I. Mavragani, Z. Nikitaki, M. Souli, A. Aziz, S. Nowsheen, et al. Complex DNA Damage: A Route to Radiation-Induced Genomic Instability and Carcinogenesis. *Cancers*, volume 9(12):91, 2017. ISSN 2072-6694. doi:10.3390/cancers9070091. 23

[133] J. McCall. Genetic algorithms for modelling and optimisation. *Journal of Computational and Applied Mathematics*, volume 184(1):205–222, 2005. ISSN 03770427. doi:10.1016/j.cam.2004.07.034. 102

[134] C. McGuffey, A. G. R. Thomas, W. Schumaker, T. Matsuoka, V. Chvykov, et al. Ionization Induced Trapping in a Laser Wakefield Accelerator. *Physical Review*

Letters, volume 104(2):025004, 2010. ISSN 0031-9007, 1079-7114. doi:10.1103/PhysRevLett.104.025004. 42

[135] S. J. McMahon. The linear quadratic model: usage, interpretation and challenges. *Physics in Medicine & Biology*, volume 64(1):01TR01, 2018. ISSN 1361-6560. doi:10.1088/1361-6560/aaf26a. 30

[136] M. McManus, F. Romano, N. D. Lee, W. Farabolini, A. Gilardi, et al. The challenge of ionisation chamber dosimetry in ultra-short pulsed high dose-rate Very High Energy Electron beams. *Scientific Reports*, volume 10(1):9089, 2020. ISSN 2045-2322. doi:10.1038/s41598-020-65819-y. 145

[137] G. Milluzzo, J. Pipek, A. Amico, G. Cirrone, G. Cuttone, et al. Transversal dose distribution optimization for laser-accelerated proton beam medical applications by means of Geant4. *Physica Medica*, volume 54:166–172, 2018. ISSN 11201797. doi:10.1016/j.ejmp.2018.07.008. 92, 99

[138] M. Mirzaie, G. Zhang, S. Li, K. Gao, G. Li, et al. Effect of injection-gas concentration on the electron beam quality from a laser-plasma accelerator. *Physics of Plasmas*, volume 25(4):043106, 2018. ISSN 1070-664X, 1089-7674. doi:10.1063/1.5008561. 46, 47

[139] R. Mohan, D. Grosshans. Proton therapy – Present and future. *Advanced Drug Delivery Reviews*, volume 109:26–44, 2017. ISSN 0169409X. doi:10.1016/j.addr.2016.11.006. 19, 21

[140] P. Montay-Gruel, L. Meziani, C. Yakkala, M.-C. Vozenin. Expanding the therapeutic index of radiation therapy by normal tissue protection. *The British Journal of Radiology*, page 20180008, 2018. ISSN 0007-1285, 1748-880X. doi:10.1259/bjr.20180008. 31, 37

[141] P. Montay Gruel, B. Petit, F. Bochud, V. Favaudon, J. Bourhis, et al. PO-0799: Normal brain, neural stem cells and glioblastoma responses to FLASH radiotherapy. *Radiotherapy and Oncology*, volume 115:S400–S401, 2015. ISSN 01678140. doi:10.1016/S0167-8140(15)40791-1. 34

[142] P. Montay-Gruel, K. Petersson, M. Jaccard, G. Boivin, J.-F. Germond, et al. Irradiation in a flash: Unique sparing of memory in mice after whole brain irradiation with dose rates above 100 Gy/s. *Radiotherapy and Oncology*, volume 124(3):365–369, 2017. ISSN 01678140. doi:10.1016/j.radonc.2017.05.003. 34

[143] P. Montay-Gruel, A. Bouchet, M. Jaccard, D. Patin, R. Serduc, et al. X-rays can trigger the FLASH effect: Ultra-high dose-rate synchrotron light source prevents normal brain injury after whole brain irradiation in mice. *Radiotherapy and Oncology*, volume 129(3):582–588, 2018. ISSN 01678140. doi:10.1016/j.radonc.2018.08.016. 35

[144] P. Mora. Plasma Expansion into a Vacuum. *Physical Review Letters*, volume 90(18):185002, 2003. ISSN 0031-9007, 1079-7114. doi:10.1103/PhysRevLett.90.185002. 42

[145] P. Mora. Thin-foil expansion into a vacuum. *Physical Review E*, volume 72(5):056401, 2005. ISSN 1539-3755, 1550-2376. doi:10.1103/PhysRevE.72.056401. 42

[146] M. Mori, M. Kando, A. S. Pirozhkov, Y. Hayashi, A. Yogo, et al. New Detection Device for Thomson Parabola Spectrometer for Diagnosis of the Laser-Plasma Ion Beam. *Plasma and Fusion Research*, volume 1:042–042, 2006. ISSN 1880-6821. doi:10.1585/pfr.1.042. 66

[147] M. Nicolai, A. Sävert, M. Reuter, M. Schnell, J. Polz, et al. Realizing a laser-driven electron source applicable for radiobiological tumor irradiation. *Applied Physics B*, volume 116(3):643–651, 2014. ISSN 0946-2171, 1432-0649. doi:10.1007/s00340-013-5747-0. 44, 178

[148] D. L. Nile, C. Rae, I. J. Hyndman, M. N. Gaze, R. J. Mairs. An evaluation in vitro of PARP-1 inhibitors, rucaparib and olaparib, as radiosensitisers for the treatment of neuroblastoma. *BMC Cancer*, volume 16(1):621, 2016. ISSN 1471-2407. doi:10.1186/s12885-016-2656-8. 62

[149] F. Nürnberg, M. Schollmeier, E. Brambrink, A. Blažević, D. C. Carroll, et al. Radiochromic film imaging spectroscopy of laser-accelerated proton beams. *Review of Scientific Instruments*, volume 80(3):033301, 2009. ISSN 0034-6748, 1089-7623. doi:10.1063/1.3086424. 69, 73

[150] M. Oppelt, M. Baumann, R. Bergmann, E. Beyreuther, K. Brüchner, et al. Comparison study of in vivo dose response to laser-driven versus conventional electron beam. *Radiation and Environmental Biophysics*, volume 54(2):155–166, 2015. ISSN 0301-634X, 1432-2099. doi:10.1007/s00411-014-0582-1. 33, 44, 46, 52, 60, 178

[151] R. Orecchia, U. Veronesi. Intraoperative electrons. *Seminars in Radiation Oncology*, volume 15(2):76–83, 2005. ISSN 10534296. doi:10.1016/j.semradonc.2004.10.009. 22

[152] H. Paganetti. Relative biological effectiveness (RBE) values for proton beam therapy. Variations as a function of biological endpoint, dose, and linear energy transfer. *Physics in Medicine and Biology*, volume 59(22):R419–R472, 2014. ISSN 0031-9155, 1361-6560. doi:10.1088/0031-9155/59/22/R419. 28

[153] A. Pak, K. A. Marsh, S. F. Martins, W. Lu, W. B. Mori, et al. Injection and Trapping of Tunnel-Ionized Electrons into Laser-Produced Wakes. *Physical Review Letters*, volume 104(2):025003, 2010. ISSN 0031-9007, 1079-7114. doi:10.1103/PhysRevLett.104.025003. 42

[154] B. Palma, M. Bazalova-Carter, B. Hårdemark, E. Hynning, B. Qu, et al. Assessment of the quality of very high-energy electron radiotherapy planning. *Radiotherapy and Oncology*, volume 119(1):154–158, 2016. ISSN 01678140. doi:10.1016/j.radonc.2016.01.017. 22

[155] L. Papiez, T. Bortfeld, W. R. Hendee. Very high energy electromagnetically-scanned electron beams are an attractive alternative to photon IMRT. *Medical Physics*, volume 31(7):1945–1948, 2004. ISSN 00942405. doi:10.1118/1.1760769. 22

[156] W. Parwaie, S. Refahi, M. Ardekani, B. Farhood. Different dosimeters/detectors used in small-field dosimetry: Pros and cons. *Journal of Medical Signals & Sensors*, volume 8(3):195, 2018. ISSN 2228-7477. doi:10.4103/jmss.JMSS_3_18. 148

[157] A. Patriarca, C. Fouillade, M. Auger, F. Martin, F. Pouzoulet, et al. Experimental Set-up for FLASH Proton Irradiation of Small Animals Using a Clinical System. *International Journal of Radiation Oncology*Biology*Physics*, volume 102(3):619–626, 2018. ISSN 03603016. doi:10.1016/j.ijrobp.2018.06.403. 127

[158] G. C. Pereira, M. Traughber, R. F. Muzic. The Role of Imaging in Radiation Therapy Planning: Past, Present, and Future. *BioMed Research International*, volume 2014:1–9, 2014. ISSN 2314-6133, 2314-6141. doi:10.1155/2014/231090. 30

[159] K. Petersson, M. Jaccard, J.-F. Germond, T. Buchillier, F. Bochud, et al. High dose-per-pulse electron beam dosimetry - A model to correct for the ion recombination in the Advanced Markus ionization chamber. *Medical Physics*, volume 44(3):1157–1167, 2017. ISSN 00942405. doi:10.1002/mp.12111. 141, 145, 148, 149, 152, 154, 157, 158

[160] A. Pilar, M. Gupta, S. Ghosh Laskar, S. Laskar. Intraoperative radiotherapy: review of techniques and results. *ecancermedicalscience*, volume 11, 2017. ISSN 17546605. doi:10.3332/ecancer.2017.750. 22

[161] J. Polz, A. P. L. Robinson, A. Kalinin, G. A. Becker, R. A. C. Fraga, et al. Efficient Laser-Driven Proton Acceleration from a Cryogenic Solid Hydrogen Target. *Scientific Reports*, volume 9(1):16534, 2019. ISSN 2045-2322. doi:10.1038/s41598-019-52919-7. 66

[162] L. Pommarel. Transport and control of a laser-accelerated proton beam for application to radiobiology. Ph.D. thesis, Université Paris-Saclay, 2017. 4, 26, 49, 54, 55, 65, 77, 80, 95, 96, 118, 141

[163] L. Pommarel, B. Vauzour, F. Mégnin-Chanet, E. Bayart, O. Delmas, et al. Spectral and spatial shaping of a laser-produced ion beam for radiation-biology experiments. *Physical Review Accelerators and Beams*, volume 20(3), 2017. ISSN 2469-9888. doi:10.1103/PhysRevAccelBeams.20.032801. xviii, 44, 45, 53, 54, 56, 81, 104, 112, 182

[164] E. D.-V. Ponette, C. Le Péchoux. Hyperfast, early cell response to ionizing radiation. *International Journal of Radiation Biology*, volume 76(9):1233–1243, 2000. ISSN 0955-3002, 1362-3095. doi:10.1080/09553000050134465. 60

[165] Y. Prezado, G. R. Fois. Proton-minibeam radiation therapy: A proof of concept: Proton-minibeam radiation therapy: A proof of concept. *Medical Physics*, volume 40(3):031712, 2013. ISSN 00942405. doi:10.1118/1.4791648. 15

[166] T. T. Puck, P. I. Marcus. ACTION OF X-RAYS ON MAMMALIAN CELLS. *The Journal of Experimental Medicine*, volume 103(5):653–666, 1956. ISSN 1540-9538, 0022-1007. doi:10.1084/jem.103.5.653. 26

[167] S. Raschke, S. Spickermann, T. Toncian, M. Swantusch, J. Boeker, et al. Ultra-short laser-accelerated proton pulses have similar DNA-damaging effectiveness but produce less immediate nitroxidative stress than conventional proton beams. *Scientific Reports*, volume 6(1):32441, 2016. ISSN 2045-2322. doi:10.1038/srep32441. 50, 51

[168] G. Reggiori, A. Stravato, P. Mancosu, F. Lobefalo, L. Paganini, et al. Small field characterization of a Nanochamber prototype under flattening filter free photon beams. *Physica Medica*, volume 49:139–146, 2018. ISSN 11201797. doi:10.1016/j.ejmp.2017.08.007. 148

[169] J. u. Rehman, Zahra, N. Ahmad, M. Khalid, H. Noor ul Huda Khan Asghar, et al. Intensity modulated radiation therapy: A review of current practice and future outlooks. *Journal of Radiation Research and Applied Sciences*, volume 11(4):361–367, 2018. ISSN 1687-8507. doi:10.1016/j.jrras.2018.07.006. 17

[170] T. J. Roberts, D. M. Kaplan. G4beamline simulation program for matter-dominated beamlines. In 2007 IEEE Particle Accelerator Conference (PAC), pages 3468–3470. IEEE, Albuquerque, NM, 2007. ISBN 978-1-4244-0916-7. doi:10.1109/PAC.2007.4440461. 97, 104

[171] F. Romano, A. Attili, G. A. P. Cirrone, M. Carpinelli, G. Cuttone, et al. Monte Carlo simulation for the transport beamline. pages 63–69. Catania, Italy, 2013. doi:10.1063/1.4816608. 92

[172] F. Romano, F. Schillaci, G. Cirrone, G. Cuttone, V. Scuderi, et al. The ELIMED transport and dosimetry beamline for laser-driven ion beams. *Nuclear Instruments and Methods in Physics Research Section A: Accelerators, Spectrometers, Detectors and Associated Equipment*, volume 829:153–158, 2016. ISSN 01689002. doi:10.1016/j.nima.2016.01.064. 49, 92

[173] L. Roso. High repetition rate Petawatt lasers. *EPJ Web of Conferences*, volume 167:01001, 2018. ISSN 2100-014X. doi:10.1051/epjconf/201816701001. 45

[174] M. Roth, M. Schollmeier. Ion Acceleration—Target Normal Sheath Acceleration. *CERN Yellow Reports*, page 231 Pages, 2016. doi:10.5170/CERN-2016-001.231. Artwork Size: 231 Pages Publisher: CERN, Geneva. 46

[175] T. F. Rösch, P. Hilz, J. Bin, F. Englbrecht, Y. Gao, et al. Considerations on employing a PMQ-doublet for narrow and broad proton energy distributions. *Current Directions in Biomedical Engineering*, volume 3(2):339–342, 2017. ISSN 2364-5504. doi:10.1515/cdbme-2017-0069. 118

[176] T. F. Rösch, Z. Szabó, D. Haffa, J. Bin, S. Brunner, et al. A feasibility study of zebrafish embryo irradiation with laser-accelerated protons. *Review of Scientific Instruments*, volume 91(6):063303, 2020. ISSN 0034-6748, 1089-7623. doi:10.1063/5.0008512. 46, 127

[177] H. Safigholi, W. Y. Song, A. S. Meigooni. Optimum radiation source for radiation therapy of skin cancer. *Journal of Applied Clinical Medical Physics*, volume 16(5):219–227, 2015. ISSN 15269914. doi:10.1120/jacmp.v16i5.5407. 22

[178] F. Salehi, A. J. Goers, G. A. Hine, L. Feder, D. Kuk, et al. MeV electron acceleration at 1 kHz with <10 mJ laser pulses. *Optics Letters*, volume 42(2):215, 2017. ISSN 0146-9592, 1539-4794. doi:10.1364/OL.42.000215. 44, 165

[179] D. Sanchez Parcerisa, C. Ainsley, A. Carabe. Fast Range Switching of Passively Scattered Proton Beams Using a Modulation Wheel and Dynamic Beam Current Modulation. *International Journal of Radiation Oncology*Biology*Physics*, volume 87(2):S742, 2013. ISSN 03603016. doi:10.1016/j.ijrobp.2013.06.1966. 20

[180] D. Schardt, T. Elsässer, D. Schulz-Ertner. Heavy-ion tumor therapy: Physical and radiobiological benefits. *Reviews of Modern Physics*, volume 82(1):383–425, 2010. ISSN 0034-6861, 1539-0756. doi:10.1103/RevModPhys.82.383. 19, 20

[181] S. Schell. Dose delivery and treatment planning methods for efficient radiation therapy with laser-driven particle beams. Ph.D. thesis, 2011. 43

[182] F. Schillaci, M. Maggiore, D. Rifuggiato, G. Cirrone, G. Cuttone, et al. Errors and optics study of a permanent magnet quadrupole system. *Journal of Instrumentation*, volume 10(05):T05001–T05001, 2015. ISSN 1748-0221. doi:10.1088/1748-0221/10/05/T05001. 54, 92, 104, 128

[183] F. Schillaci, L. Pommarel, F. Romano, G. Cuttone, M. Costa, et al. Characterization of the ELIMED Permanent Magnets Quadrupole system prototype with laser-driven proton beams. *Journal of Instrumentation*, volume 11(07):T07005–T07005, 2016. ISSN 1748-0221. doi:10.1088/1748-0221/11/07/T07005. 49, 54, 92, 94, 118, 128

[184] A. Schipler, G. Iliakis. DNA double-strand-break complexity levels and their possible contributions to the probability for error-prone processing and repair pathway choice. *Nucleic Acids Research*, volume 41(16):7589–7605, 2013. ISSN 0305-1048, 1362-4962. doi:10.1093/nar/gkt556. 26

[185] K. Schmid, A. Buck, C. M. S. Sears, J. M. Mikhailova, R. Tautz, et al. Density-transition based electron injector for laser driven wakefield accelerators. *Physical Review Special Topics - Accelerators and Beams*, volume 13(9):091301, 2010. ISSN 1098-4402. doi:10.1103/PhysRevSTAB.13.091301. 42

[186] M. Schollmeier, M. Geissel, A. B. Sefkow, K. A. Flippo. Improved spectral data unfolding for radiochromic film imaging spectroscopy of laser-accelerated proton beams. *Review of Scientific Instruments*, volume 85(4):043305, 2014. ISSN 0034-6748, 1089-7623. doi:10.1063/1.4870895. 69, 72

[187] D. R. Spitz, G. R. Buettner, M. S. Petronek, J. J. St-Aubin, R. T. Flynn, et al. An integrated physico-chemical approach for explaining the differential impact of FLASH versus conventional dose rate irradiation on cancer and normal tissue responses. *Radiotherapy and Oncology*, volume 139:23–27, 2019. ISSN 01678140. doi:10.1016/j.radonc.2019.03.028. 37

[188] D. Strickland, G. Mourou. Compression of amplified chirped optical pulses. *Optics Communications*, volume 56(3):219–221, 1985. ISSN 00304018. doi:10.1016/0030-4018(85)90120-8. 40

[189] A. Subiel, V. Moskvin, G. H. Welsh, S. Cipiccia, D. Reboredo, et al. Dosimetry of very high energy electrons (VHEE) for radiotherapy applications: using radiochromic film measurements and Monte Carlo simulations. *Physics in Medicine and Biology*, volume 59(19):5811–5829, 2014. ISSN 0031-9155, 1361-6560. doi:10.1088/0031-9155/59/19/5811. 22

[190] C. Thaury, E. Guillaume, A. Lifschitz, K. Ta Phuoc, M. Hansson, et al. Shock assisted ionization injection in laser-plasma accelerators. *Scientific Reports*, volume 5(1):16310, 2015. ISSN 2045-2322. doi:10.1038/srep16310. 42, 46

[191] J. Thomson. XXVI. *Rays of positive electricity. The London, Edinburgh, and Dublin Philosophical Magazine and Journal of Science*, volume 21(122):225–249, 1911. ISSN 1941-5982, 1941-5990. doi:10.1080/14786440208637024. 66

[192] X. Tian, K. Liu, Y. Hou, J. Cheng, J. Zhang. The evolution of proton beam therapy: Current and future status (Review). *Molecular and Clinical Oncology*, 2017. ISSN 2049-9450, 2049-9469. doi:10.3892/mco.2017.1499. 21

[193] A. Tramontana, G. Candiano, M. Carpinelli, G. A. P. Cirrone, G. Cuttone, et al. The Energy Selection System for the laser-accelerated proton beams at ELI-Beamlines. *Journal of Instrumentation*, volume 9(05):C05065–C05065, 2014. ISSN 1748-0221. doi:10.1088/1748-0221/9/05/C05065. 92

[194] S. Tudisco, C. Altana, G. Lanzalone, A. Muoio, G. A. P. Cirrone, et al. Investigation on target normal sheath acceleration through measurements of ions energy distribution. *Review of Scientific Instruments*, volume 87(2):02A909, 2016. ISSN 0034-6748, 1089-7623. doi:10.1063/1.4934691. 114

[195] M. Vadrucci, G. Esposito, C. Ronsivalle, R. Cherubini, F. Marracino, et al. Calibration of GafChromic EBT3 for absorbed dose measurements in 5 MeV proton beam

and ^{60}Co -rays: Calibration of GafChromic EBT3 for absorbed dose measurements in 5 MeV proton beam and ^{60}Co -rays. *Medical Physics*, volume 42(8):4678–4684, 2015. ISSN 00942405. doi:10.1118/1.4926558. 93

[196] B. P. Venkatesulu, A. Sharma, J. M. Pollard-Larkin, R. Sadagopan, J. Symons, et al. Ultra high dose rate (35 Gy/sec) radiation does not spare the normal tissue in cardiac and splenic models of lymphopenia and gastrointestinal syndrome. *Scientific Reports*, volume 9(1):17180, 2019. ISSN 2045-2322. doi: 10.1038/s41598-019-53562-y. 35

[197] H. von Boehmer, P. Kisielow. Self-nonself discrimination by T cells. *Science*, volume 248(4961):1369–1373, 1990. ISSN 0036-8075, 1095-9203. doi:10.1126/science.1972594. 37

[198] M.-C. Vozenin, J. Hendry, C. Limoli. Biological Benefits of Ultra-high Dose Rate FLASH Radiotherapy: Sleeping Beauty Awoken. *Clinical Oncology*, volume 31(7):407–415, 2019. ISSN 09366555. doi:10.1016/j.clon.2019.04.001. 33, 34

[199] M.-C. Vozenin, P. De Fornel, K. Petersson, V. Favaudon, M. Jaccard, et al. The Advantage of FLASH Radiotherapy Confirmed in Mini-pig and Cat-cancer Patients. *Clinical Cancer Research*, volume 25(1):35–42, 2019. ISSN 1078-0432, 1557-3265. doi:10.1158/1078-0432.CCR-17-3375. 34

[200] R. L. Warters, K. G. Hofer, C. R. Harris, J. M. Smith. Radionuclide toxicity in cultured mammalian cells: elucidation of the primary site of radiation damage. *Current Topics in Radiation Research Quarterly*, volume 12(1-4):389–407, 1978. ISSN 0011-3964. 23

[201] S. Webb. The physical basis of IMRT and inverse planning. *The British Journal of Radiology*, volume 76(910):678–689, 2003. ISSN 0007-1285, 1748-880X. doi: 10.1259/bjr/65676879. 17

[202] H. Wei, X. Yu. Functions of PARylation in DNA Damage Repair Pathways. *Genomics, Proteomics & Bioinformatics*, volume 14(3):131–139, 2016. ISSN 16720229. doi:10.1016/j.gpb.2016.05.001. 61

[203] H. Wiedemann. Particle accelerator physics. Springer, Berlin, 3. ed edition, 2007. ISBN 978-3-540-49043-2. OCLC: 180961933. 86, 88

[204] S. C. Wilks, A. B. Langdon, T. E. Cowan, M. Roth, M. Singh, et al. Energetic proton generation in ultra-intense laser–solid interactions. *Physics of Plasmas*, volume 8(2):542–549, 2001. ISSN 1070-664X, 1089-7674. doi:10.1063/1.1333697. 42

[205] J. D. Wilson, E. M. Hammond, G. S. Higgins, K. Petersson. Ultra-High Dose Rate (FLASH) Radiotherapy: Silver Bullet or Fool's Gold? *Frontiers in Oncology*, volume 9:1563, 2020. ISSN 2234-943X. doi:10.3389/fonc.2019.01563. 35, 36

[206] P. Wołowiec, P. Kukołowicz. The analysis of the measurement uncertainty with application of small detectors made of Gafchromic EBT films for the range of doses typical for in vivo dosimetry in teleradiotherapy. *Radiation Measurements*, volume 92:72–79, 2016. ISSN 13504487. doi:10.1016/j.radmeas.2016.08.001. 77, 138

[207] X. H. Xu, Q. Liao, M. J. Wu, Y. X. Geng, D. Y. Li, et al. Detection and analysis of laser driven proton beams by calibrated Gafchromic HD-V2 and MD-V3 radiochromic films. *Review of Scientific Instruments*, volume 90(3):033306, 2019. ISSN 0034-6748, 1089-7623. doi:10.1063/1.5049499. 69, 73

[208] C. M. Yashar. Basic Principles in Gynecologic Radiotherapy. In Clinical Gynecologic Oncology, pages 586–605.e3. Elsevier, 2018. ISBN 978-0-323-40067-1. doi:10.1016/B978-0-323-40067-1.00023-1. 24

[209] C. Yeboah, G. A. Sandison. Optimized treatment planning for prostate cancer comparing IMPT, VHEET and 15 MV IMXT. *Physics in Medicine and Biology*, volume 47(13):2247–2261, 2002. ISSN 00319155. doi:10.1088/0031-9155/47/13/305. 22

[210] A. Yogo, K. Sato, M. Nishikino, M. Mori, T. Teshima, et al. Application of laser-accelerated protons to the demonstration of DNA double-strand breaks in human cancer cells. *Applied Physics Letters*, volume 94(18):181502, 2009. ISSN 0003-6951, 1077-3118. doi:10.1063/1.3126452. 44, 45, 48, 51

[211] A. Yogo, T. Maeda, T. Hori, H. Sakaki, K. Ogura, et al. Development of laser-driven quasi-monoenergetic proton beam line for radiobiology. *Nuclear Instruments and Methods in Physics Research Section A: Accelerators, Spectrometers, Detectors and Associated Equipment*, volume 653(1):189–192, 2011. ISSN 01689002. doi:10.1016/j.nima.2010.12.016. 44, 45, 48, 51

[212] K. Zeil, S. D. Kraft, S. Bock, M. Bussmann, T. E. Cowan, et al. The scaling of proton energies in ultrashort pulse laser plasma acceleration. *New Journal of Physics*,

volume 12(4):045015, 2010. ISSN 1367-2630. doi:10.1088/1367-2630/12/4/045015. 188

[213] K. Zeil, M. Baumann, E. Beyreuther, T. Burris-Mog, T. E. Cowan, et al. Dose-controlled irradiation of cancer cells with laser-accelerated proton pulses. *Applied Physics B*, volume 110(4):437–444, 2013. ISSN 0946-2171, 1432-0649. doi:10.1007/s00340-012-5275-3. 44, 45, 49, 51

[214] J. F. Ziegler. Stopping of energetic light ions in elemental matter. *Journal of Applied Physics*, volume 85(3):1249–1272, 1999. ISSN 0021-8979, 1089-7550. doi:10.1063/1.369844. 5

[215] O. Zlobinskaya, C. Siebenwirth, C. Greubel, V. Hable, R. Hertenberger, et al. The Effects of Ultra-High Dose Rate Proton Irradiation on Growth Delay in the Treatment of Human Tumor Xenografts in Nude Mice. *Radiation Research*, volume 181(2):177–183, 2014. ISSN 0033-7587, 1938-5404. doi:10.1667/RR13464.1. 34, 37

ECOLE DOCTORALE

Titre : Application des faisceaux de particules accélérées par laser à la biologie des rayonnements à haut débit de dose

Mots clés : Radiobiologie à haut débit de dose, mise en forme de faisceaux de particules, simulations Monte Carlo, dosimétrie à haut débit de dose

Résumé : Les faisceaux de particules accélérées par laser sont produits en focalisant une impulsion laser ultra-courte ($<$ps) et ultra-intense ($>10^{19}\,\mathrm{W/cm^2}$) sur une cible mince solide ou gazeuse ($\sim$µm). Ces faisceaux de particules ont une durée de l'impulsion allant de la picoseconde à la femtoseconde, ce qui permet d'atteindre un débit de dose dans l'impulsion de l'ordre de $10^9\,\mathrm{Gy/s}$, supérieur de plusieurs ordres de grandeur au débit de dose typiquement utilisé en radiothérapie conventionnelle (Gy/min). L'effet du débit de dose élevé sur la réponse biologique a fait l'objet de nombreux travaux de recherche dans les dernières années. Notamment, plusieurs études *in-vivo* menés avec un protocol d'irradiation FLASH, c'est-à-dire en administrant la dose en un temps très court ($<500\,\mathrm{ms}$) et avec un débit de dose élevé ($>40\,\mathrm{Gy/s}$), ont montré une réduction du risque d'effets secondaires sur les tissus sains, tout en gardant le même effet sur la tumeur. Cependant, les caractéristiques temporelles de l'irradiation déclanchant l'effet FLASH (débit de dose, dose par impulsion, durée de l'irradiation), ainsi que les mécanismes physiques, font toujours l'objet de discussions. Dans ce contexte, les faisceaux de particules accélérées par laser représentent un outil unique pour jeter de la lumière sur les processus qui régissent la réponse biologique suite à une irradiation à haut débit de dose.
Cette thèse porte sur l'application à la radiobiolgoie des protons et des électrons produits par différents types de laser à haute puissance, ce qui a permis d'explorer différentes modalités temporelles d'administration de la dose. L'objectif est de traiter certains des principaux problèmes liés à l'application de telles sources de particules à la radiobiologie et de montrer des solutions et des techniques viables pour mener des études de radiobiologie solides. Cela demande une caractérisation précise de ces faisceaux, l'optimisation de la distribution de dose dans la cible biologique à travers l'utilisation de systèmes de transport et mise en forme du faisceau adaptées et, enfin, l'étude de la réponse des instruments de dosimétrie à haut débit de dose.

Title : Application of laser-plasma accelerated beams to high dose-rate radiation biology

Keywords : High dose-rate radiation biology, LPA beam shaping, Monte Carlo simulations, high dose-rate dosimetry

Abstract : Laser-Plasma Accelerated (LPA) beams are produced by focusing an ultra-short ($<$ps) and ultra-intense ($>10^{19}\,\mathrm{W/cm^2}$) laser pulse on a solid or gaseous thin target ($\sim$µm), leading to proton and electron bunches with duration of a few picoseconds and a few femtoseconds respectively. These characteristics allow the reach of extremely high peak dose-rates in the pulse of the order of $10^9\,\mathrm{Gy/s}$, which are order of magnitudes greater than the typical dose rate employed in conventional radiotherapy (Gy/min). Recent *in-vivo* experiments on FLASH-RT protocols, consisting in delivering the therapeutic dose in a time shorter than hundreds of milliseconds and at a dose-rate higher than $40\,\mathrm{Gy/s}$, demonstrated sparing of the healthy tissues for the same tumour control. However, the beam temporal features triggering the FLASH effect (dose-rate, dose-per-pulse, irradiation time) as well as the underlying physical mechanisms are still being debated. In this scenario, LPA beams represent a unique tool to shed some light on the radiobiological response following high-dose rate irradiation.
This thesis discusses the potential of both protons and electrons produced by different types of high-power lasers systems. In particular, it presents experimental and theoretical studies carried out with three different types of beam enabling different temporal modalities of dose delivery. The goal is to address some of the main issues related to the application of such sources to radiation biology and show viable solutions and irradiation protocols to perform systematic radiobiology studies. Such issues include accurate characterisation of the source, optimisation of the dose distribution at the biological target through the design of adapted transport beamlines and investigation of the behaviour of dosimetric instruments for high dose-rate dosimetry.

Institut Polytechnique de Paris
91120 Palaiseau, France